Abuhaimed, Abdullah Abdulaziz (2015) Dosimetric investigations of kilovoltage cone beam computed tomography (kV-CBCT) utilized in image guided radiation therapy (IGRT) using Monte Carlo simulations. PhD thesis.

http://theses.gla.ac.uk/6751/

Copyright and moral rights for this thesis are retained by the author

A copy can be downloaded for personal non-commercial research or study, without prior permission or charge

This thesis cannot be reproduced or quoted extensively from without first obtaining permission in writing from the Author

The content must not be changed in any way or sold commercially in any format or medium without the formal permission of the Author

When referring to this work, full bibliographic details including the author, title, awarding institution and date of the thesis must be given.

Glasgow Theses Service
http://theses.gla.ac.uk/
theses@gla.ac.uk

Dosimetric Investigations of Kilovoltage Cone Beam Computed Tomography (kV-CBCT) Utilized in Image Guided Radiation Therapy (IGRT) using Monte Carlo Simulations

Abdullah Abdulaziz Abuhaimed
BSc (Physics), MSc (Medical Physics)

Submitted in fulfilment of the requirements for the degree of Doctor of Philosophy.

School of Medicine
College of Medical, Veterinary & Life Sciences
University of Glasgow

September 2015

Abstract

Many studies have shown that the computed tomography dose index ($CTDI_{100}$) which is considered to be the main dose descriptor for CT dosimetry fails to provide a realistic reflection of the dose involved in cone beam CT (CBCT) scans. The main reason for this failure is that $CTDI_{100}$ measurements are performed within standard head and body phantoms made of polymethyl methacrylate (PMMA) that are only 150 cm long, which is less than or similar to beam widths used for CBCT scans. Therefore, much of the scatter that would contribute to the dose received by a patient is not recorded. Several practical approaches have been proposed to overcome drawbacks of the $CTDI_{100}$. The aim of this project was to investigate the various dose indices based on the approaches proposed. The dose indices studied were: (1) $CTDI_{IEC}$ proposed by the International Electrotechnical Commission (IEC) and based on measuring $CTDI_{100}$ using a reference beam and the application of a correction factor based on free-in-air CTDI measurements, (2) $f(0,150)$ the cumulative dose measured with a small ionization chamber within the standard PMMA phantoms, (3) $f_{100}(150)$ the cumulative dose measured in the standard PMMA phantoms with a 100 mm pencil ionization chamber, (4) $f(0,\infty)$ proposed by the American Association of Physicists in Medicine (AAPM) TG - 111 and similar to $f(0,150)$, but measured in infinitely long phantoms made of PMMA, polyethylene, and water, (5) $f_{100}(\infty)$ similar to $f_{100}(150)$, but measured in infinitely long phantoms. The project also aimed to facilitate the use of indices defined in long phantoms through the generation of correction factors that could be applied to measurements in standard phantoms.

This project was based on the use of the Monte Carlo (MC) technique. MC EGSnrc-based user codes namely BEAMnrc and DOSXYZnrc were used to simulate the On-Board-Imager (OBI) imaging system mounted on a Varian TrueBeam linear accelerator. The MC model was benchmarked against experimental measurements and good agreement shown. PMMA, polyethylene, and water head and body phantoms of various lengths and diameters were simulated including a new polyethylene phantom named ICRU/AAPM phantom made by the International Commission on Radiation

Units and Measurements (ICRU) and AAPM. A wide range of beam widths with different beam qualities were employed. Four scanning protocols using two acquisition modes (full and half), employed in routine clinical practice, were utilized. In addition, organ doses resulting from three CBCT scans (head, thorax, and pelvis) were evaluated in terms of absorbed dose to organs and tissues using MC simulations on the International Commission on Radiological Protection (ICRP) 110 adult male and female reference computational phantoms. The suitability of the dose indices for CBCT dosimetry was investigated by taking three factors into consideration: (1) the efficiency of the approach as a dose descriptor to report $CTDI_{\infty}$, which is close to the dose received by body tissues near to the middle of a CBCT scan of a patient, (2) the simplicity of the application of the approach in the clinical environment in terms of availability of the measuring instruments, simplicity of the technique, and the number of the scans required to accomplish a quality assurance (QA) assessment, i.e. the QA time, and (3) the ability of the approach in providing an evaluation of organ doses resulting from CBCT scans. To facilitate the use of long phantoms, the relationship between $f(0{,}150)$ and $f_{100}(150)$ measurements obtained within the standard PMMA phantoms and those for $f(0,\infty)$ obtained within longer phantoms of different compositions were studied.

Considering the three factors for the dose indices investigated, all the dose indices were found to be comparable, but each index has advantages and disadvantages. Overall, $f(0{,}150)$ was considered to be the most suitable with $f_{100}(150)$ providing an alternative for wider beams. Therefore, the dose indices $f(0{,}150)$ followed by $f_{100}(150)$ are recommended for practical CBCT dosimetry. In addition, a function called $G_x(W)_{100}$ was proposed for evaluating the cumulative dose in long phantoms, and correction factors were also provided to avoid the use of long phantoms. The $G_x(W)_{100}$ function did not vary significantly with tube potential, but the tube potential did influence the correction factors. The use of the $G_x(W)_{100}$ function is recommended for estimation of $f(0,\infty)$ values from $f_{100}(150)$ measurements taken in the standard PMMA phantoms.

Table of Contents

List of Tables

List of Figures

Acknowledgement

First of all, I would like to thank Almighty Allah for his guidance and mercy for making this thesis possible.

I would like to thank many people who have supported me to complete my PhD project. First, I would express my sincere gratitude to my supervisor Dr. Colin J Martin. He was always available to assist me to carry out my research and answer all my questions. Through his guidance, enthusiasm, encouragement, attention, friendship and respect, I have learned many scientific aspects and obtained research skills. I was lucky to work with him to gain from his deep understanding of many aspects in the medical physics field, and from his long experience, over 40 years, in the field. Without his support, this thesis would not have been possible. I was and will be proud to work under his supervision.

I would also like to think my research team Mr. Marimuthu Sankaralingam, Head of Imaging in Radiotherapy section of the Radiotherapy Physics Department of the Beatson West of Scotland Cancer Centre. I am deeply indebted and thankful for his support in many areas, particularly those related to the technical aspects. He was always happy to help me and to assist in conducting experimental measurements outside his work hours. I am also grateful to Dr. David J Gentle, consultant physicist in the Health Physics Department, Gartnavel Royal Hospital for his valuable contributions, ideas and comments.

My thanks are extended to Dr. Mark McJury, Head of Research and Development section, Dr Mohamed.Metwaly and Dr. Kurian Oomen of the Radiotherapy Physics Department of the Beatson West of Scotland Cancer Centre for their contributions at different stages of my PhD project.

I would like to thank the administrators, Mr. Garry Currie and Mr. Martin Glegg, and all the staff and trainees at Radiotherapy Physics Department of the Beatson West of Scotland Cancer Centre for their hospitality, support and friendship during my PhD project. I gratefully acknowledge the

assistance I have had from my colleagues at the department, and their kindness in answering questions in various aspects.

I wish to thank the support team of Scottish Grid Service (ScotGrid) at the University of Glasgow, Dr Gareth Roy, Dr David Crooks, Mr Stuart Purdie and Mr Mark Mitchell, for their support in using ScotGrid to run the MC codes. I would also thank Prof. David Keating, Head of the Department of Clinical Physics and Bio-engineering in the University of Glasgow for his support and friendship. My thanks are extended to Dr. Supawitoo Sookpeng, Mr Matthew J Carter, and Mr David Robertson of Health Physics department, Gartnavel Royal Hospital for their assistance in various aspects of the project.

I would also like to thank Dr. Mukhtar Alshanqity, consult of Medical Physics at King Fahad Medical City, Riyadh, Saudi Arabia, formerly a PhD student at the University of Surrey, for his kindness in answering questions related to the Monte Carlo technique during the early stages of the project. I also gratefully acknowledge the assistance of Dr Xinhua Li of Massachusetts General Hospital, Boston, Massachusetts in sharing some of his data for comparison with my results obtained in this project, and for his sharing experiences and discussion. My thanks are extended to Prof. John Boone of University of California Davis Medical Centre for his permission to use photographs of the ICRU/AAPM phantom and for the useful discussion related to the ICRU practical method presented in ICRU report-85, and Prof. Robert Dixon of Wake Forest University for his permission to use the photograph of the water phantom, and for the useful discussion related to the AAPM practical method presented in TG – 111.

I would also like to thank Varian Medical systems for providing specifications of the OBI system simulated in this project, and King Abdulaziz City for Science and Technology (KACST) for the scholarship.

Last but not least, I would like to thank all my family for all their prayers and support, and for the love they showed during my period of study abroad.

Dedication

To soul of my father Abdulaziz, who passed away during my second year of the study,

To my mother Norah,

To my wife Hutoon and my son Abdulaziz,

To my brothers and sisters.

Author's Declaration

I declare that this dissertation is the result of my own work and has not been submitted for any other degree at the University of Glasgow or any other institution.

Permissions to reproduce published articles had been granted by institute of physics (IOP) publishing.

Signature _____

Printed name Abdullah A. Abuhaimed

Publications Arising from this Work

- **Peer-Reviewed Articles**

Abuhaimed, A., Martin, C. J., Sankaralingam, M., Gentle, D. J. & Mcjury, M. 2014. An assessment of the efficiency of methods for measurement of the computed tomography dose index (CTDI) for cone beam (CBCT) dosimetry by Monte Carlo simulation. *Phys Med Biol*, 59, 6307-26.

Abuhaimed, A., Martin, C. J., Sankaralingam, M. & Gentle, D. J. 2015. A Monte Carlo investigation of cumulative dose measurements for cone beam computed tomography (CBCT) dosimetry. *Phys Med Biol*, 60, 1519-1542.

Abuhaimed, A., Martin, C. J., Sankaralingam, M. & Gentle, D. J. 2015. Investigation of practical approaches to evaluating cumulative dose for cone beam computed tomography (CBCT) from standard CT dosimetry measurements: A Monte Carlo study. *Phys Med Biol*, 60, 5413-5438.

Abuhaimed, A., Martin, C. J., Sankaralingam, M. & Gentle, D. J. 2015. Evaluation of cumulative dose for cone beam computed tomography (CBCT) scans within phantoms made from different compositions using Monte Carlo simulations. *J. Appl. Clin. Med. Phys.*, (In Press).

Abuhaimed, A., Martin, C. J., Sankaralingam, M., Metwaly, M. & Gentle, D. J. 2015. Evaluation of organ doses from cone beam computed tomography (CBCT) scans using various dose indices. (In Review).

- **Abstracts (Oral Presentations)**

Abuhaimed, A., Martin, C., Sankaralingam, M. & Gentle, D. 2014. A comparison of two practical approaches for cone beam computed tomography (CBCT) dosimetry using Monte Carlo technique. *Physica Medica: European Journal of Medical Physics,* 30**,** e27-e28. Presented in the 8th European Conference on Medical Physics, Athens, Greece.

Abuhaimed, A., Martin, C., Sankaralingam, M. & Gentle, D. 2014. Evaluation of a modified computed tomography dose index (CTDI) used for cone-beam computed tomography (CBCT) dosimetry: A Monte Carlo study. Presented in the Medical Physics and Engineering and Biennial Radiotherapy Physics Conference, Glasgow, UK

Definitions/Abbreviation

4DCT	Four Dimensions Computed Tomography
AAPM	The American Association of Physicists in Medicine
AE	Lower Energy Thresholds for Creation of Secondary Electrons
AOI	Area of Interest
AP	Lower Energy Thresholds for Creation of Secondary Photons
BCA	Boundary Crossing Algorithm
CBDI	Cone Beam Dose Index
CDF	Cumulative Distribution Function
CH technique	Condensed History Technique
CM	Component Modules
CT	Computed Tomography
CTDI	Computed Tomography Dose Index
$CTDI_{vol}$	Volume Weighted Computed Tomography Dose Index
$CTDI_{w}$	Weighted Computed Tomography Dose Index
DBS	Directional Bremsstrahlung Splitting
DI	Dose Index
DICOM	The Digital Imaging and Communications in Medicine
DLP	Dose Length Product
ECUT	Cut-Off Electron Energy
EGS	Electron Gamma Shower
EPID	Electronic Portal Imaging Devices
FIA	Free in Air
FOV	Field of View
GPU	Graphics Processing Unit
H(a)	Approach to Equilibrium Function
HVL	Half Value Layer

IAEA	The International Atomic Energy Agency
ICRU	The International Commission on Radiation Units and Measurements
ICRP	The International Commission on Radiological Protection
IEC	The International Electrotechnical Commission
IGRT	Imaged Guided Radiation Therapy
ImPACT	Imaging Performance and Assessment of Ct
IMRT	Intensity Modulated Radiation Therapy
IPEM	The Institute of Physics and Engineering in Medicine
kV-CBCT	Kilo-Voltage Cone Beam Computed Tomography
KVision	Siemens Imaging System
LINAC	Linear Accelerator
MC	Monte Carlo
MCNP	Monte Carlo N-Particle
MCNPX	Monte Carlo N-Particle Extended
MOSFETS	Metal Oxide Semiconductor Field Effect Transistors
MU	Monitor Unit
MV-CBCT	Mega-Voltage Cone Beam Computed Tomography
NRC	The National Research Council of Canada
OAR	Organs at Risk
OBI	Varian On Board Imager
OD	Optical Density
ODs	Organ Doses
OMEGA	Ottawa Madison Electron Gamma Algorithm
OSLDS	Optically Stimulated Luminescence Dosimeters
PCUT	Cut-Off Photon Energy
PCXMC	PC-Based Monte Carlo Program
PDF	Probability Distribution Function
PENELOPE	Penetration and Energy Loss of Positrons and Electrons

PHSP	Phase Space
PMMA	Polymethyl Methacrylate
QA	Quality Assurance
ROI	Region of Interest
RPV	Red Pixel Value
SABR	Stereotactic Ablative Radiotherapy
SBS	Selective Bremsstrahlung Splitting
SID	Source-Isocentre-Distance
SLAC	Stanford Linear Accelerator Centre
SSD	Source-to-Surface Distance
TLDs	Thermoluminescent Dosimeters
TPS	Treatment Planning Systems
UBS	Uniform Bremsstrahlung Splitting
UE	Upper Energy Thresholds for Creation of Secondary Electrons
UP	Upper Energy Thresholds for Creation of Secondary Photons
VMAT	Volumetric Modulated Arc Therapy
VRT	Variance Reduction Technique
W	Beam Width
XVI	Elekta Synergy X-Ray Volume Imager

Chapter 1

Introduction

1.1 Rationale

Medical imaging is the basis for a wide range of medical applications, which play a critical role in diagnosis and treatment of numerous diseases. One of these applications is the use of imaging for cancer treatment. The imaging is considered an essential part of cancer treatment over all the treatment stages from diagnosis of the disease using different imaging modalities through the treatment stage to the inspection of treatment output and follow up of patients after the treatment. The treatment stage is different for each patient, but for patients undergoing radiotherapy, an essential part of the treatment is to scan patients to localize the position of the tumour and organs at risk (OAR) and upon this treatment planning is developed. The imaging is also utilized in this stage to enhance the treatment output by using a procedure known as image guided radiation therapy (IGRT) (Bujold et al., 2012). IGRT is based on using various imaging modalities to precisely position patients prior to radiotherapy treatment and hence assist practitioners to deliver the prescribed doses to patients with a high level of accuracy. Moreover, IGRT is important for adaptive radiotherapy, which is based on re-planning the treatment plan used in earlier fractions to account for the change in patient geometry and tumour shrinkage (Ding et al., 2007a).

Although the continued development in the imaging modalities and their utilization in the different treatment stages are considered to have enabled a paradigm shift in the treatment outcome, there is a cost, as the majority of these modalities employ ionizing radiation. Therefore, the extensive use for imaging over the treatment course becomes a concern, particularly those employed for IGRT procedures (AAPM, 2007a). At the present time, the use of IGRT with modern radiotherapy delivery modalities has become essential in most of the major radiotherapy departments worldwide. IGRT

is different for each patient, and the number of scans required over the treatment course is based on different factors such as the type of treatment, the treatment site, and the availability of the imaging modalities. The number of scans is also based on the clinical protocol applied in each department.

One of the imaging modalities commonly used for IGRT procedures at the present time is cone beam computed tomography (CBCT) in the kilo-voltage (kV–CBCT) and mega-voltage (MV-CBCT) ranges (Midgley et al., 1998, Jaffray and Siewerdsen, 2000, Siewerdsen and Jaffray, 2001, Jaffray et al., 2002). CBCT scans are acquired for patients prior to the treatment fractions, and the scans are then compared with the CT scans obtained for the treatment planning, which are considered as reference images. Based on this comparison, a correction for the patient's position is applied by shifting the treatment couch according to the difference between the CBCT and CT scans. These scans have great benefits in guiding the practitioners, enabling them to minimize the potential set-up errors associated with positioning the patients for the treatment. However, as a CBCT scan is acquired multiple times or on a daily basis for some patients, the cumulative dose resulting from these scans becomes non-negligible. For example in our centre, a daily kV–CBCT scan prior to each treatment fraction is acquired for patients undergoing Stereotactic Ablative Radiotherapy (SABR) treatment, whereas multiple kV–CBCT scans are obtained over the treatment course for patients undergoing Intensity Modulated Radiation Therapy (IMRT) or Volumetric Modulated Arc Therapy (VMAT) treatments. The doses resulting from IGRT procedures and those delivered to patients by other imaging modalities such as CT and 4DCT scans obtained at the different stages of the treatment may increase the risk of developing second malignancy cancer, thus a trade-off between the benefits and the risk should be taken into consideration (AAPM, 2007a, Brenner and Hall, 2007, Hall and Brenner, 2008, Fazel et al., 2009, Pearce et al., 2012, Spezi et al., 2012).

In order to utilize the significant benefits of employing IGRT procedures in enhancement of the treatment output (Bujold et al., 2012), and optimizing

the larger concomitant doses resulting from these scans at the same time, inclusion of these doses in the treatment dose using the treatment planning systems (TPS) has been suggested (Miften et al., 2007, Ding et al., 2008b, Alaei et al., 2010, Ding et al., 2010a). Inclusion doses from MV-CBCT scans to the treatment dose has been shown to be possible due to the capability of TPS calculating doses in the MV range (Miften et al., 2007). The TPS, however, is unable to calculate doses resulting from kV-CBCT scans accurately. The differences between organ doses measured experimentally with a Varian CBCT scanner and those calculated with the Philips PINNACLE TPS were found up to 20% for soft tissues and 68% for bony structures (Alaei et al., 2010), and between a Siemens CBCT scanner and the Philips PINNACLE TPS were <10% and 30%, respectively (Dzierma et al., 2014). Moreover, organ doses calculated with the Philips PINNACLE TPS were within ±17% of those measured experimentally with an Elektra CBCT scanner for soft tissues and body structures (Alaei and Spezi, 2012). To avoid this limitation, several calculation algorithms have been developed with the aim of extending the TPS to account for doses not only for kV-CBCT but also for other imaging modalities in the kV range such as conventional kV radiographic images (Ding et al., 2008b, Pawlowski and Ding, 2011, Pawlowski and Ding, 2014). The ability of calculating doses resulting from all IGRT procedures using TPS is still unavailable, but this feature may be introduced in the near future (AAPM, 2015b).

Besides the inability of the TPS in calculating kV-CBCT doses, the dosimetric methods used in quality assurance (QA) procedures to monitor performance of CBCT scanners and to estimate doses received by patients are also problematic. Note that CBCT from now on refers to kV-CBCT. This issue is not only associated with CBCT employed in IGRT procedures, but also with the other imaging modalities acquired with wide beams such as conventional CT scans, dental CBCT scans, and interventional radiology and cardiology scans acquired with C-arm CBCT scanners. As the ionizing radiation involved in these various CBCT applications may involve a risk of initiating a cancer not only for cancer patients undergoing IGRT procedures but also for non-cancer patients who are scanned with other CBCT devices (Brenner and Hall, 2007, Hall and Brenner, 2008, Fazel et al., 2009, Pearce

et al., 2012), monitoring the doses involved for the CBCT scans is necessary (AAPM, 2007a, COMARE, 2014). Therefore, it is important to have effective ways for evaluating doses from CBCT scans and hence estimating the risks to patients.

The dose descriptor that has been employed for CT dosimetry for many years is known as the CT dose index (CTDI) (Shope et al., 1981). The CTDI concept is based on integrating the axial dose profile resulting from a single axial rotation over an arbitrary length at the middle of the scan (z = 0). The CTDI has been adapted several times to accommodate advances in CT scanner technology. Different derivatives of the CTDI concept have been developed based on the CTDI measured with a 100 mm long pencil ionization chamber known as ($CTDI_{100}$). The $CTDI_{100}$ is the main index, from which other derivatives are derived such as the weighted CTDI ($CTDI_w$), volume weighted CTDI ($CTDI_{vol}$), and dose-length product (DLP) (IEC, 2001, McNitt-Gray, 2002, Kalender, 2014). The $CTDI_{100}$ characterises a CT scanner by integrating a dose profile resulting from a single axial rotation using the pencil ionization chamber set up free in air at the isocentre parallel to the rotation axis (IEC, 2001). The $CTDI_{100}$ is also used as an indicator for the dose received by a patient undergoing a CT scan by performing the dose measurements within standard cylindrical polymethyl methacrylate (PMMA) phantoms of length 150 mm with diameters of 160 mm representing an adult head or a paediatric body, and 320 mm representing an adult body. The dose measurements within these phantoms are made on the central axis and at four peripheral positions 1 cm below the phantom surfaces set up at a specific source isocentre distance (SID).

With the continued evolution of CT scanner technology, preservation of the $CTDI_{100}$ as a dose index becomes problematic (Dixon, 2003, Brenner, 2005, Dixon and Ballard, 2007, Boone, 2009), as the main concept of CBCT scans is to use an x-ray beam, which is usually wider than the length of the 100 mm ionization chamber and sometimes wider than the standard 150 mm long PMMA phantoms (Mori et al., 2005, Boone, 2007, Kyriakou et al., 2008, Geleijns et al., 2009). Moreover, the efficiency of the $CTDI_{100}$, which is the ratio of the $CTDI_{100}$ parameter measured in a PMMA phantom of standard

length to the equivalent $CTDI_{\infty}$ parameter measured in an infinitely long phantom, is limited even for narrow beams (Boone, 2007). The $CTDI_{\infty}$ includes the dose from all the scattered radiation generated within a phantom undergoing a CT or CBCT scan that reaches the measurement chamber, and will be closer to the radiation level from a scan within a human trunk. The efficiency values are approximately constant for beams of width ≤ 40 mm at ~75% and ~60% at the centre of the standard PMMA head and body phantoms, respectively, and ~84% at the periphery of the phantoms (Boone, 2007, Dixon and Ballard, 2007, Perisinakis et al., 2007, Ruan et al., 2010, Martin et al., 2011, Li et al., 2011, Li et al., 2012). The efficiency values, however, decrease with increasing beam width reaching ~25% of $CTDI_{\infty}$ for wide beams for both the head and body phantoms (Boone, 2007, Kyriakou et al., 2008). As a result, the $CTDI_{100}$ concept is no longer appropriate for CBCT scans. The main shortcoming is its inability to accommodate and record the whole primary beam and the scattered radiation.

In order to avoid the underestimation of dose associated with the use of $CTDI_{100}$ for wide beams, various practical methods have been suggested (Mori et al., 2005, Islam et al., 2006, Fahrig et al., 2006, Amer et al., 2007, Kyriakou et al., 2008, Geleijns et al., 2009, IEC, 2010, AAPM, 2010). Two methods have been proposed by international organisations. One by the International Electrotechnical Commission (IEC) (IEC, 2010) is based on modifications to measurement of the $CTDI_{100}$, and this has been recommended by the International Atomic Energy Agency (IAEA) (IAEA, 2011) and the Institute of Physics and Engineering in Medicine (IPEM) (Platten et al., 2013). However, the methodology proposed by the American Association of Physicists in Medicine (AAPM) Task Group TG–111 (AAPM, 2010) aimed to replace the $CTDI_{100}$ with a concept based on measuring the cumulative dose under a scatter equilibrium condition by using an infinitely long cylindrical phantom made of PMMA, polyethylene, or water. The International Commission on Radiation Units and Measurements (ICRU) Report-87 has recommended the cumulative dose concept proposed by AAPM, but a practical method has been suggested to overcome the difficulty of using the long phantoms in the clinical environment (ICRU,

2012). All these methods will be discussed and described in detail in the thesis chapters.

1.2 Project Objectives

Dosimetric methods for CBCT are still not yet well established, as are those employed for dosimetry of standard multi-slice CT (MSCT) scanners, $CTDI_{vol}$ and DLP. Moreover, different approaches have been recommended by various international organizations to tackle the problem. For example, IPEM has recommended the IEC method to be followed in the UK, whereas the AAPM TG-111 method has been recommended for use in the USA.

The project was based on Monte Carlo technique, which is a valuable tool for assessing not only the doses received by patients undergoing CT or CBCT scans, but also dose distributions within phantoms for evaluation of the performance of different dosimetry techniques. The project had two main objectives:

1. To investigate the various possible dosimetric methods for CBCT including the IEC and AAPM methods proposed for CBCT dosimetry. This required several studies to investigate features and limitations of each method. This included various aspects such as the consistency of the evaluations, the inclusion of all the radiation exposure, and the ability of the method to evaluate organ doses resulting from CBCT scans. Subsequently, results of these investigations were used to recommend a method that is more practical in the clinical environment.

2. To facilitate utilizing some methods such as the AAPM method that requires using infinitely long phantoms by developing functions and conversion factors, from which doses within long phantoms made of different compositions can be estimated using the standard PMMA phantoms that are widely available in hospitals worldwide.

The aim has been to make the study generic and as comprehensive as possible so that the method recommended is not only suitable for CBCT scans employed in IGRT procedures, but also for other CBCT applications.

Therefore, a wide range of parameters such the beam widths and tube potentials were studied. It is hoped that the results arising from this project will add beneficial content to the body of knowledge on CBCT dosimetry, make an effective contribution to the literature, and provide some evidence to assist the scientific community and international organizations in reaching consensus on CBCT dosimetry methods. The recommendation of an agreed specific dosimetric method suitable for all CBCT applications would be beneficial at this time with the rapid development of CBCT applications.

1.3 Thesis Structure

The project was divided into five different subprojects, which are presented in five chapters. The thesis is comprised of ten chapters:

- Chapter 1: gives an introduction and overview for the project. It also presents the research problem and objectives of the project.

- Chapter 2: provides a background for the main concepts in the project and a literature review for studies related to the project topic. The kV system employed to generate CBCT scans and parameters of the scanning protocols studied in this project are described. An overview of the dose index CTDI used for CT dosimetry and its limitations in CBCT scans are explained. The various dosimetric methods proposed for CBCT dosimetry are discussed in detail.

- Chapter 3: gives an overview for the Monte Carlo (MC) technique and some historical overview for the technique. It also presents an overview for the way of transporting particles using the MC technique to study quantities of interest. Different MC codes used for Medical Physics applications are discussed. A description for the MC code utilized in the project is given, and the MC parameters used for theses codes are described briefly.

- Chapter 4: describes the methodology of designing the kV system with the MC code. Various experimental measurements performed to validate the MC model are presented. In addition, the calibration method, which was

required to convert the MC output to absolute absorbed dose values in (Gy), is described.

- Chapter 5: presents the first subproject, which investigated the efficiency of the IEC method and $CTDI_{100}$ for evaluating CBCT scan doses with beams of width 20 – 300 mm using four different head and body scanning protocols. The failure of $CTDI_{100}$ for CBCT scans and overcoming the drawbacks obtained with the IEC method are shown. Dose measurements for the IEC method and $CTDI_{100}$ were also measured experimentally using three scanning protocols commonly used in the clinic.

- Chapter 6: shows the results conducted for the second subproject, which studied the efficiency of four different dosimetric methods based on the cumulative dose concept, one of which was the AAPM method, using beams of width 40 – 300 mm and four different head and body scanning protocols. In addition, experimental measurements using the methods studied were made for three scanning protocols commonly used in the clinic. The influence of measuring the cumulative dose with the standard 100 mm pencil ionization chamber and a small ionization chamber of an active length of 20 mm was investigated. Additionally, the influence of using the long and short phantoms on the cumulative dose measurements was studied. A comparison between the methods investigated in this subproject and those studied in the first subproject is presented.

- Chapter 7: investigates the practical method proposed by ICRU to utilize the AAPM method, but avoiding the use of the long phantoms. The ICRU method was proposed for conventional CT scanners, thus the third subproject investigated the suitability of extending the ICRU method for CBCT scans. Simulations were conducted for two different head and body scanning protocols using phantoms of different compositions namely PMMA, polyethylene, and water. A wide range of CBCT scans with beams of width 40 – 500 mm and tube potentials of 80 – 140 kV were studied. The suitability of using this method to the other CBCT scanners was also discussed.

- Chapter 8: presents the fourth subproject, which studied the possibility of using a small ionization chamber within the standard PMMA head and body

phantoms to measure the cumulative dose and evaluate the result based on the AAPM method within infinitely long head and body phantoms of different compositions made of PMMA, polyethylene and water. The study was conducted with two different head and body scanning protocols and a wide range of CBCT scans for beams of width 40 – 500 mm and tube potentials of 80 – 140 kV. The feasibility of using short polyethylene head and body phantoms 150 mm in length to estimate doses within the long polyethylene phantoms was also investigated. The suitability of using this method for other types of CBCT scanners was also discussed.

- Chapter 9: the fifth subproject is presented in this chapter, and it aimed to study the ability of the dosimetric quantities proposed for CBCT dosimetry and investigated in the first and second subprojects to be used for evaluation of organ doses resulting from CBCT scans. Organ doses for three scanning protocols employed in the clinic were calculated using MC simulations on the ICRP-110 adult male and female reference computational phantoms. This study covered a wide range of organs, and more attention was paid for those with weightier coefficients in effective dose.

- Chapter 10: gives the main conclusions resulting from the five subprojects presented in Chapters 4 – 8. These conclusions included a recommendation for a dosimetric method that was considered to be more practical in terms of the simplicity of the implementation in the clinical environment and estimating organ doses for patients undergoing CBCT scans. In addition, possible future works were suggested.

Chapter 2

Background and Related Works

2.1 CBCT in Image Guided Radiation Therapy (IGRT)

The use of CBCT in IGRT procedures was initially developed by Jaffray and Siewerdsen in early 2000's (Jaffray and Siewerdsen, 2000, Siewerdsen and Jaffray, 2001, Jaffray et al., 2002), and was characterized and implemented in radiotherapy departments during the mid 2000's (Létourneau et al., 2005, Islam et al., 2006, Amer et al., 2007, Wen et al., 2007, Ding et al., 2007). The kV imaging system used for CBCT scans is mounted on the treatment machine, i.e. the linear accelerator (Linac), with retractable arms as shown in Figure 2.1. It consists of the kV source, i.e. x-ray tube, which is similar to those employed for conventional CT scanners, and a flat panel detector. The movement of the kV source and the detector are controlled by the retractable arms, and a CBCT scan is acquired with the kV source and the detector being placed at 90° to the treatment source and perpendicular to the axis of the treatment couch.

The main difference between CT and CBCT scans is the acquisition technique. The CT scan reconstructs a 3D image for a patient by scanning an area of interest (AOI) slice by slice using a fan beam with a width of ≤40 mm and a multi-detector array of similar width. The acquisition of CT slices is accomplished by using acquisition modes known as axial or helical modes. The axial mode scans a patient over the AOI in multiple rotations, each of which is acquired with a stationary table but at a different axial position, i.e. step and shoot. The helical scan is also obtained with multiple rotations but with a table moving at constant speed, so that the x-ray beam scans the patient continuously to cover the AOI. The reconstruction of a 3D image from a CBCT scan is entirely different from that applied for a CT scan. A 3D image for a CBCT scan is formed from a large number of conventional kV radiographic images acquired with the 2D flat panel detector and a wide beam width usually ~200 mm. Each radiographic image is projected and

collected at a different angle, and the number of projections is different for each scanning protocol. Unlike conventional CT scans, CBCT scans are acquired only using the axial scan mode with a fixed patient table position, and the kV source rotates around the patient over arcs of 360° or 200°.

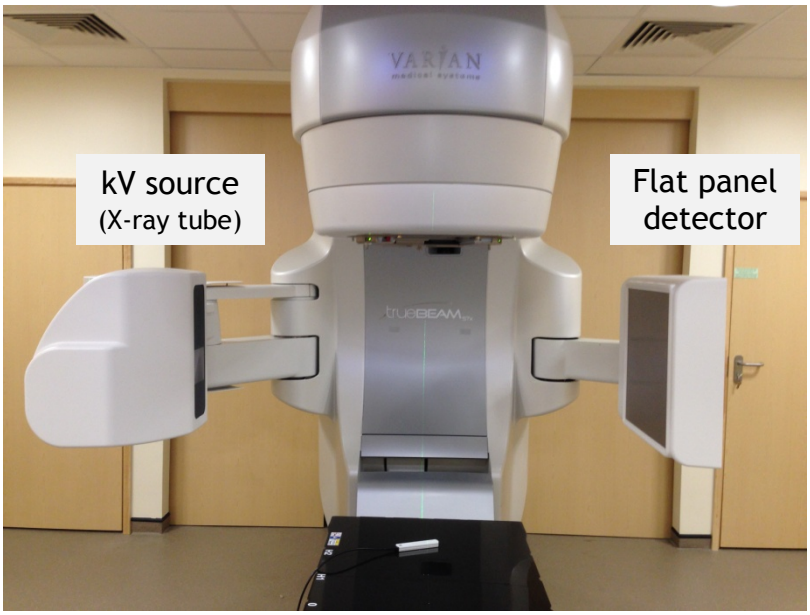

Figure 2.1: The kV system, On Board Imager (OBI), mounted on a Varian TrueBeam linear accelerator.

2.2 On Board Imager (OBI) System

At the present time, several kV systems are commercially available and utilized in IGRT procedures to acquire CBCT scans: (1) On Board Imager (OBI) by (Varian Medical systems, Palo Alto, CA), (2) Synergy X-ray Volume Imager (XVI) by (Elekta, Crawley, UK), and (3) kVision by (Siemens Healthcare, Erlangen, Germany), with the first two systems being more common. This project was based on using the OBI system mounted on a Varian TrueBeam linear accelerator (Figure 2.1). The OBI system can be operated in various imaging modes namely radiography, fluoroscopy and CBCT mode, and with a tube potential between 40 and 140 kV. In addition, two focal spots of size 0.4 mm used for the radiography and fluoroscopy modes and 1.0 mm used for the CBCT mode are used. Two different types of aluminium bowtie filter, full and half as shown in Figure 2.2, are used to improve the quality of the CBCT images by reducing the range of x-ray intensities to be recorded.

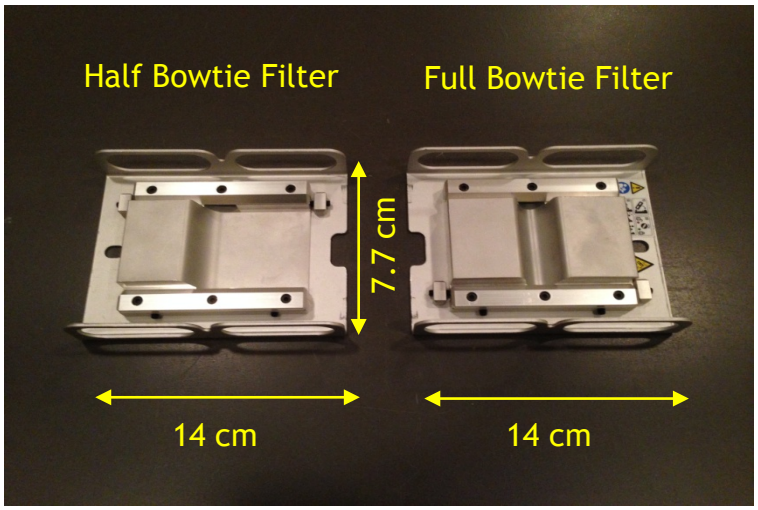

Figure 2.2: Half and Full bowtie filters used on the OBI system.

The OBI is manufactured with four collimator blades X1, X2, Y1, and Y2. The collimator blades work independently to enable delivery of a symmetrical or an asymmetrical field with minimum and maximum field sizes of 20 mm × 20 mm and 500 mm × 500 mm at the isocentre. The collimator blades X1 and X2 set the lateral extent of the beam that control the field of view (FOV) of a scan, while Y1 and Y2 select the length of the scan in the axial direction, i.e. beam width of the scan. Therefore, each blade can be opened from 10 mm to 250 mm. The maximum image size that can be collected by the detector is 400 mm × 300 mm, i.e. the active area of the detector. The source-detector distance is set to 150 cm so that the distance between the treatment couch and the detector is 50 cm.

Either of two acquisition modes: the full-fan and the half-fan can be employed depending on the size of the scanned target region. For a smaller target such as the head, the full-fan mode is employed with the full bowtie filter, and for larger regions such as the chest or pelvis, the half-fan mode is employed with the half bowtie filter (Figure 2.3).

1. The full-fan mode: scans the target symmetrically with a diameter of 264 mm at the isocentre. The collimator blades X_1 and X_2 are set to 132 mm to give a field of 264 mm at the isocentre, and Y1 and Y2 to 99 mm to give 198 mm. The flat panel detector is placed at 150 cm from the kV source and is set so that its centre matches that of the region to be imaged. The kV source and the flat panel detector

are rotated simultaneously around a patient lying on a stationary table in axial mode to acquire a volumetric image for the target as shown in (Figure 2.3 (a - b)).

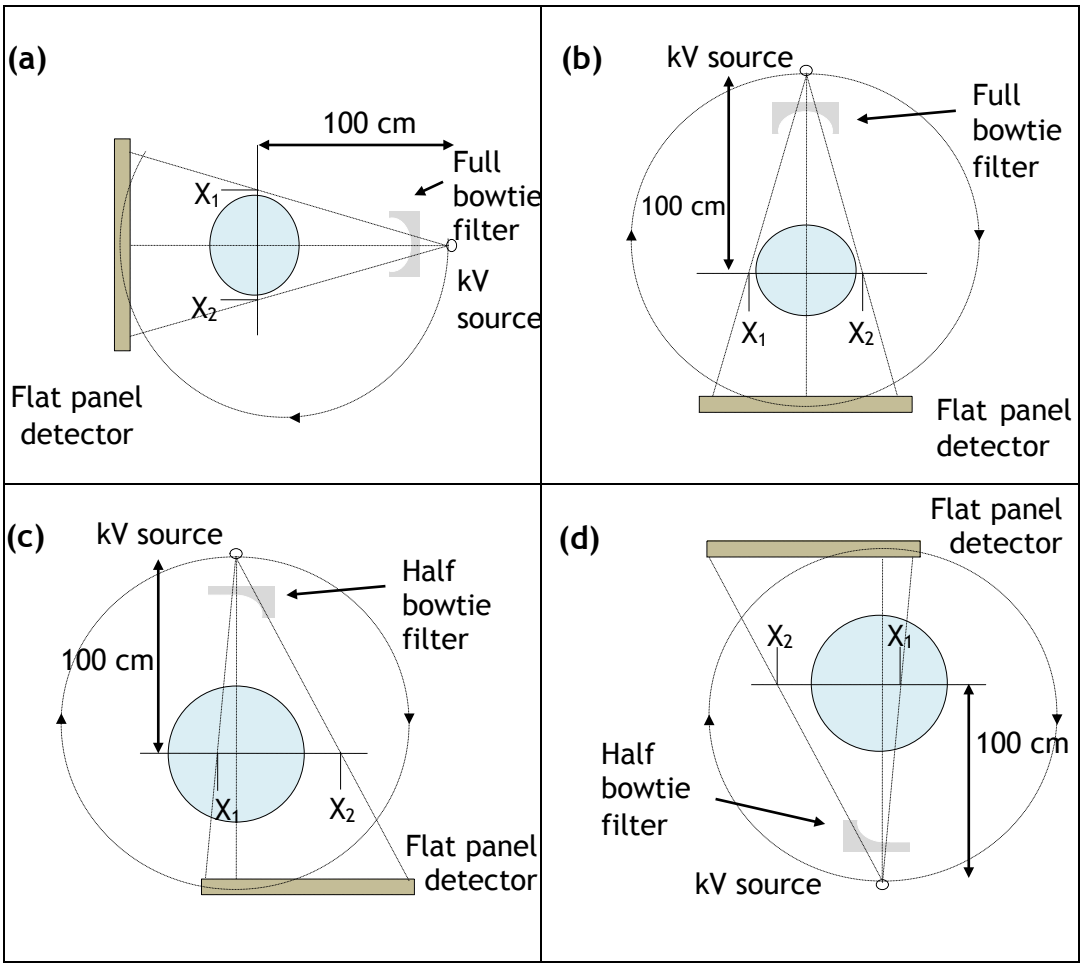

Figure 2.3: Diagrammatic representations of the TrueBeam scanning modes. (a - b) The full-fan mode is employed for scanning smaller targets such as the head through (a) a partial scan (200°; 90° to 290°) and (b) a full 360° scan. (c - d) The half-fan mode is used for scans of the trunk though a full 360° scan, with c and d each covering the two halves of the scan.

2. The half-fan mode: allows a larger scan diameter by scanning target volumes asymmetrically, where the X1 and X2 blades are set to 25 mm and 239 mm, respectively, and the Y1 and Y2 ones are set similar to those used for the full-fan mode. As the maximum active area of the detector is 400 mm for the X blades, 200 mm to each side, setting X2 to 239 mm makes the beam width larger than the active length in the X2 direction. In order to avoid this issue, the detector is shifted laterally by 148 mm to accommodate the beam width in the X2 direction within the active area as shown in (Figure 2.3 (c - d)), and

hence acquiring a scan with a lateral extent of 478 mm at the isocentre.

Although the reconstructed images for both the modes are different, the field size of the head and body scans is similar 264 mm × 198 mm. The full-fan mode can be acquired with a rotation of 200° or 360°, while only the full 360° rotation is used for the half-fan mode. Only a single rotation is used for both the modes.

2.3 Clinical Scanning Protocols

Several pre-configured scanning protocols such as head, thorax, pelvis and pelvis spot light are employed in the clinic for IGRT procedures using the OBI system version (V 1.6), with the first three protocols being commonly used. The parameters are different for each protocol and are listed in Table 2.1. The head scan is different from that used for CT scans, as a partial 200° scan is acquired. For the majority of the patients, the head scan rotates beneath the patient's head to minimize the imaging dose and to avoid irradiating sensitive organs and tissues directly such as the eye lens. The thorax and pelvic scans, however, rotate a full 360° scan, and cover the AOI fully. The pelvic spot light scan, which acquires an image for a target in the pelvic region posterior of a patient with a partial 200° scan mode, is obtained for some patients. Similar to the head scan, the pelvic spot light is utilized to minimize the imaging dose delivered to organs and tissues lying closer to the anterior surface in the pelvic region, and is considered as an alternative scanning protocol for the pelvic scan, which requires higher mAs (Table 2.1). The full-fan mode with the full bowtie filter is employed for the head and pelvic spot light scans, whereas the half-fan mode with the half bowtie filter is used for the thorax and pelvic scans.

Table 2.1: Parameters of the scanning protocols employed for the OBI system (V 1.6) in IGRT procedures.

	Head	Thorax	Pelvis spot light	Pelvis
X-ray tube potential (kV)	100	125	125	125
X-ray current (mA)	20	20	80	80
X-ray millisecond (ms)	20	20	25	20
Exposures (mAs)	147	264	733	1056
Acquisition mode	full-fan	half-fan	full-fan	half-fan
Scan Arc Gantry rotation (degrees) [(a)]	200°	360°	200°	360°
	90°-290°	0°-360°	90°-290°	0°-360°
Bowtie filter	Full	Half	Full	Half
No of Projections	367	660	367	660
X1 and X2 (mm)	132, 132	25, 239	132 , 132	25, 239
Y1 and Y2 (mm)	99, 99			
The lateral extent of the scan (mm)	264	478	264	478
The axial extent of the scan (mm)	198			

(a) Left side-90°, right side-270°.

2.4 $CTDI_{100}$, $CTDI_w$, and $CTDI_\infty$

$CTDI_{100}$ is the main dose index used for CT dosimetry and the basis for other CT dosimetry quantities. $CTDI_{100}$ is defined as:

$$CTDI_{100} = \frac{1}{N \times T} \int_{-50\,mm}^{+50\,mm} D(z)\, dz \qquad (2.1)$$

where $D(z)$ is the dose profile resulting from a single axial scan at a specific position at the rotation axis (z-axis), N is the number of slices acquired in a single scan, and T is the nominal thickness of a single slice. The product of $(N \times T)$ is equal to the nominal beam width involved in the scan. In CBCT scans, the region of interest is scanned with a single detector and a single rotation. Therefore, the nominal beam width of the scan (W) is used instead of $(N \times T)$ in Eq.(2.1).

The $CTDI_{100}$ measurements are made at the centre of the scan ($z = 0$) within the standard head and body PMMA phantoms, which are known as CTDI phantoms and shown in Figure 2.4.

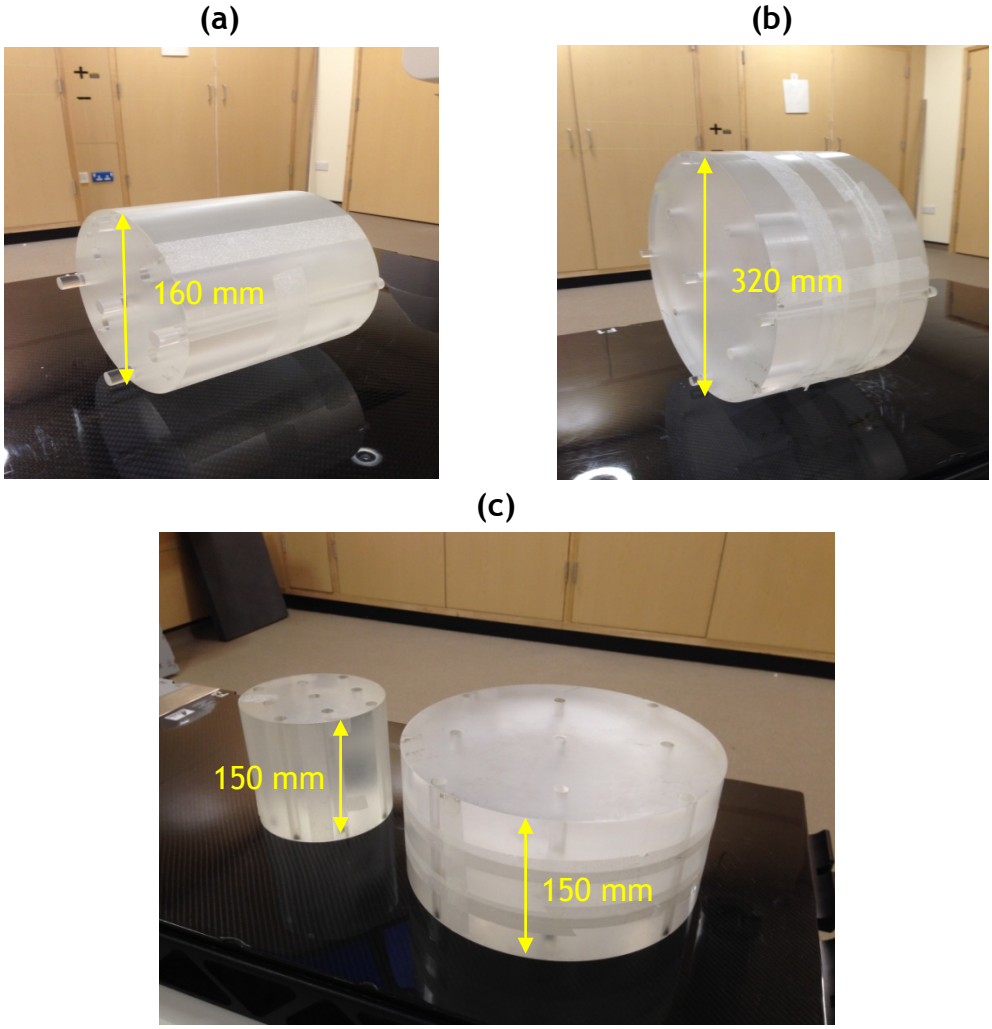

Figure 2.4: The standard head and body PMMA phantoms known as CTDI phantoms. (a) the head phantom 160 mm in diameter, and (b) the body phantom 320 mm in diameter. (c) Both the phantoms are 150 mm in length.

The phantoms are manufactured with removable PMMA plugs at the central and four peripheral positions so that a pencil ionization chamber can be inserted in these positions. Measurements are performed with the phantoms set up at a SID of 100 cm at the middle of the central axis ($CTDI_{100,c}$) and at the four peripheral axes situated 10 mm below the phantom surface ($CTDI_{100,p}$). The weighted $CTDI_{100}$ known as $CTDI_w$ accounts for inhomogeneity of the dose distribution over the axial scan plane, and is defined as:

$$CTDI_{100,w} = \frac{1}{3} CTDI_{100,c} + \frac{2}{3} CTDI_{100,p} \quad (2.2)$$

where $CTDI_{100,p}$ is the average of the four dose measurements made at the peripheral positions, ($CTDI_{100,p} = 1/4 \sum_{n=1}^{4} CTDI_{100,pn}$). For MSCT scans, ($CTDI_{vol} = CTDI_w / pitch$) is used to quantify the dose along the scan axis to allow for differences in the beam width and pitch of the tube rotation, where the pitch is the ratio of the table movement for a single rotation (b) to the nominal beam width ($N \times T$), i.e. ($pitch = b/N \times T$). In addition, ($DLP = CTDI_{vol} \times scan\ length$) is employed in assessment of dose for patients undergoing MSCT scans.

In order to estimate the total amount of radiation to which a patient is exposed during a CT scan, the $CTDI_\infty$ concept has been proposed (Shope et al., 1981, Li et al., 2011). $CTDI_\infty$ takes into account all the contributions resulting from the primary beam and the scattered radiation by integrating the dose from a scan of an infinitely long phantom as:

$$CTDI_\infty = \frac{1}{N \times T} \int_{-\infty}^{+\infty} D(z) dz \quad (2.3)$$

and weighed $CTDI_\infty$ is defined in manner similar to that for $CTDI_{100,w}$ as:

$$CTDI_{\infty,w} = \frac{1}{3} CTDI_{\infty,c} + \frac{2}{3} CTDI_{\infty,p} \quad (2.4)$$

2.5 $CTDI_{100}$ for CBCT Dosimetry

As $CTDI_{100}$ is evaluated with a chamber and phantoms of arbitrary lengths 100 mm and 150 mm, respectively, the beam width used for a scan plays a major role in determining the $CTDI_{100}$ measurement values (Eq.(2.1)). The ability of $CTDI_{100}$ in estimating $CTDI_\infty$, which is defined as the efficiency of $CTDI_{100}$, has been investigated in a number of studies (Mori et al., 2005, Boone, 2007, Dixon and Ballard, 2007, Perisinakis et al., 2007, Kyriakou et al., 2008, Ruan et al., 2010, Martin et al., 2011, Li et al., 2011, Li et al., 2012). Most of these studies were conducted for beams of width ($N \times T \leq$

$40\ mm$), which are commonly used for MSCT scans. However, the studies conducted by (Mori et al., 2005, Boone, 2007, Kyriakou et al., 2008) have been extended to investigate the efficiency of $CTDI_{100}$ for cone beams.

Mori et al. (2005) have investigated the efficiency of $CTDI_{100}$ for five beam widths (20, 42, 74, 106 and 138 mm) using a conventional CT scanner. The standard 150 mm and 900 mm long head and body PMMA phantoms were used to measure dose profiles resulting from the beam widths studied, where the length of 900 mm was considered to be a sufficient length to measure $CTDI_{\infty}$. Dose profiles of the scans were integrated using pin photodiode sensors placed along axes of the short and long phantoms in specified intervals. For the long phantoms, the dose profiles were measured over a detection length of 900 mm, which was equal to the lengths of the phantoms involved, i.e. the chamber and phantoms had the same length. Therefore, $CTDI_{\infty}$ was represented by $CTDI_{900}$ measurements, i.e. $CTDI_{900} \equiv CTDI_{\infty}$. A 300 mm long ionization chamber was also used within the long phantoms. It has been found that $CTDI_{100,w}$ underestimated $CTDI_{900,w}$ by 24 – 40 % in the head and body phantoms for the beam widths studied, with the underestimation values being larger in the body phantom. However, $CTDI_{300,w}$ measured in a manner similar to those for $CTDI_{100}$ Eqs.(2.1) and (2.2), but over a detection length of 300 mm at the centre and periphery of the long phantoms as:

$$CTDI_{300} = \frac{1}{N \times T} \int_{-150\ mm}^{+150\ mm} D(z)\, dz \qquad (2.5)$$

gave estimates of over 90% of the $CTDI_{\infty,w}$ for all beam widths and phantoms, i.e. the underestimation values dropped to <10%. Therefore, it has been concluded that weighted $CTDI_L$, provides an alternative dose index suitable for wide beams, where $CTDI_L$ is defined as:

$$CTDI_L = \frac{1}{N \times T} \int_{-L/2}^{+L/2} D(z)\, dz \qquad (2.6)$$

and $CTDI_{L,w}$ is equal to:

$$CTDI_{L,w} = \frac{1}{3} CTDI_{L,c} + \frac{2}{3} CTDI_{L,p} \quad (2.7)$$

where L is the detection length, The detection length needs to be ≥ 300 mm to minimize the $CTDI_{100,w}$ underestimation for CBCT scans by ~14 – 30%.

Boone (2007) used Monte Carlo simulations to study the efficiency of $CTDI_{100}$ for beam widths up to 400 mm and tube potentials of 80, 100, 120 and 140 kV. A conventional CT scanner was simulated, and the efficiency values were calculated within the standard and 500 mm long head and body PMMA phantoms, where $CTDI_{\infty}$ was evaluated within the long phantom. It has been found that at 120 kV for beams of width up to 40 mm, the efficiency values were approximately constant at 82% and 90% at the centre and periphery of the head phantom, respectively, and at 63% and 88% for the centre and periphery of the body phantom, respectively. Subsequently, the efficiency values declined steadily as beam width increased up to 80 mm, and then dropped significantly as the beam width was increased further, reaching ~25% for a beam of width 400 mm at the central and peripheral axes of phantoms. The efficiency values calculated for 120 kV differed only slightly from those calculated for the other tube potentials, i.e. the tube potential showed a minimal impact on the efficiency values.

Kyriakou et al. (2008) investigated the efficiency of $CTDI_{100}$ for a C-arm scanner equipped with a flat panel detector using Monte Carlo simulations. The efficiency values were investigated for beams of widths ranging from 20 to 200 mm, and two tube potentials of 70 kV and 125 kV. Two acquisition modes partial 200° and full 360° scans, and the standard and 900 mm long head and body PMMA phantoms were used. It has been found that the relationship between the efficiency and the beam width for the head and body phantoms were varying in a manner similar to those reported by (Boone, 2007). It has also been shown that the influence of the acquisition mode and the tube potential on the efficiency values was minimal, where the efficiency values were similar under the different conditions. The efficiency values were ~80% and ~85% at the centre and periphery of the head phantom, respectively, for a beam of width 20 mm, and declined to ~50% for a beam of width 200 mm. This also occurred for the body phantom,

where the efficiency values declined from ~62% and ~82% to ~42% and ~55% at the centre and periphery of the phantom, respectively.

In addition to investigation of the $CTDI_{100}$ efficiency, Kyriakou et al. (2008) also studied the influence of the detection length on the $CTDI_{100}$ measurement using the same scanning parameters, but only for beams of width 20 and 200 mm. The influence of the detection length was studied by evaluating $CTDI_L$, as given in Eq.(2.6), for the head and body phantoms using detection of lengths ranging from 150 to 900 mm with an increment of 150 mm, i.e. $CTDI_{150}$, $CTDI_{300}$, $CTDI_{450}$, $CTDI_{600}$, $CTDI_{750}$, and $CTDI_{900}$. The phantom length for each $CTDI_L$ was similar to the detection length (L). $CTDI_{900}$ was considered to represent $CTDI_\infty$, thus all CTDI measured with the different detection lengths were normalized by $CTDI_{900}$. They found that the underestimation decreased with increasing detection length, and lengths of 600 mm or more, i.e. $CTDI_{600}$, were needed to assess $CTDI_\infty$ within ±1% for wide beams within the head and body phantoms under different conditions.

2.6 Methods for CBCT Dosimetry

From the studies conducted by (Mori et al., 2005, Boone, 2007, Kyriakou et al., 2008), it has been clearly shown that the $CTDI_{100}$ has a shortcoming for the evaluation of imaging doses for CBCT scans. The total amount of radiation delivered to the body is underestimated, and this underestimation increases with the beam width used for the scan. To overcome this limitation, several methods have been proposed for CBCT dosimetry:

2.6.1 $CTDI_L$ Method

$CTDI_L$, as given in Eq.(2.6) was proposed by (Mori et al., 2005) and (Kyriakou et al., 2008) as an alternative dose index for $CTDI_{100}$ that is suitable for CBCT dosimetry. $CTDI_L$, as illustrated in Figure 2.5, extends the use of the $CTDI_{100}$ concept to provide a better estimate of $CTDI_\infty$ for CBCT scans. Mori et al. (2005) recommended the detection length to be ≥300 mm, whereas Kyriakou et al. (2008) suggested 600 mm. As measurement of $CTDI_L$ requires different equipment from that used for $CTDI_{100}$ measurements, i.e. longer

chambers and phantoms, which are impractical for routine measurements in the clinical environment, Kyriakou et al. (2008) suggested the application of correction factors to $CTDI_{100}$ measurements to allow the assessments.

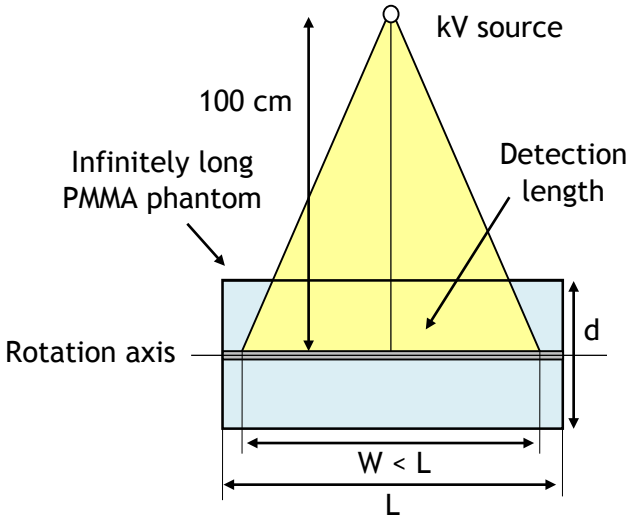

Figure 2.5: A diagrammatic representation of the experimental configuration used to assess $CTDI_L$ for a CBCT scan with a beam of width (W). $CTDI_L$ is measured using infinitely long head and body PMMA phantoms with a diameter of (d) over a detection length of (L). $CTDI_L$ measurements are made at the centre and periphery of the phantom.

2.6.2 $f(0,150)$ Method

Dixon (2003) has proposed a dosimetric method to replace the $CTDI_{100}$ concept for MSCT scans obtained with conventional CT scanners. It is based on the cumulative dose concept, and requires measuring cumulative dose resulting from a complete MSCT scan. This method involves using a small ionization chamber positioned at the middle of a phantom that is long enough to provide the scatter equilibrium condition, i.e. further extending the length of the phantom will have a negligible effect on the measurement. Fahrig et al. (2006) have investigated the use of the cumulative dose concept for CBCT scans obtained with a C-arm scanner equipped with a flat panel detector. They have adapted the cumulative dose concept for CBCT scans, and assumed that the contribution of scattered radiation arising from longer phantoms at the central point, at which the cumulative dose is measured, is minimal. Therefore, it has been proposed that the cumulative dose $D(0)$ for a CBCT scan can be measured

within the standard PMMA phantoms as illustrated in Figure 2.6 with minimal differences from results obtained with longer phantoms.

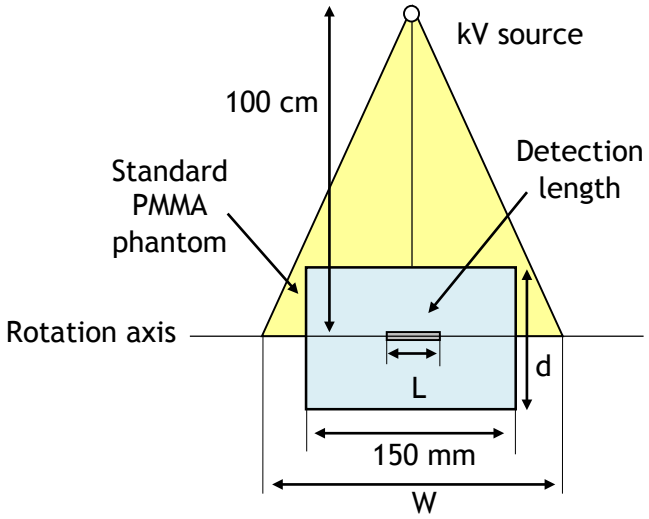

Figure 2.6: A diagrammatic representation of the experimental configuration used to assess $D(0)$ for a CBCT scan with a beam of width (W). The measurements are performed using the standard head and body PMMA phantoms with a diameter of (d) and a small ionization chamber with an active length of (L) positioned at the centre of the scan. $D(0)$ measurements are made at the centre and periphery of the phantoms.

$D(0)$ can be averaged over the axial plane in a manner similar to that used for $CTDI_w$ (Eq.(2.2)) as:

$$D(0)_w = \frac{1}{3} D(0)_c + \frac{2}{3} D(0)_p \qquad (2.8)$$

The $D(0)$ method has been utilized to evaluate imaging doses from CBCT scans in various studies (Song et al., 2008, Kim et al., 2008, Osei et al., 2009, Kim et al., 2010a, Cheng et al., 2011).

In order to distinguish between this method and that proposed by AAPM TG-111, which is discussed in section 2.6.4, the expression $f(0,150)$ was used in this project, where (0) represents the measurement position at the centre of the scan ($z = 0$), and (150) represents the length of the standard PMMA phantoms.

2.6.3 $f_{100}(150)$ Method

Amer et al. (2007) introduced an alternative dose index called cone beam dose index (CBDI). It is based on measurement of the average cumulative dose resulting from a CBCT scan using the $CTDI_{100}$ equipment as illustrated in Figure 2.7. The CBDI is slightly different from $f(0,150)$ in that a 100 mm long chamber is used, and it is defined as:

$$CBDI = \frac{1}{100} \int_{-50mm}^{+50mm} D(z)\, dz \tag{2.9}$$

Although CBDI is not based on the beam width as that for $CTDI_{100}$ Eq.(2.1), partial or full chamber irradiation plays a role in CBDI values. When a beam of width < 100 mm is used, the chamber is irradiated partially and that is then averaged over length of the chamber. This leads to a minimizing of the cumulative dose due to averaging the dose from a given beam over a larger detection length. However, when a wider beam > 100 mm is used, the chamber is fully irradiated, and the cumulative dose from the scan is detected properly. In contrast, $CTDI_{100}$ depends on the beam width, thus the dose is underestimated if a beam > 100 mm is used, i.e. full chamber irradiation. This is because the dose measured over the chamber length is normalized with respect to a beam that has a nominal width longer than the chamber length. However, in the partial chamber irradiation with beams < 100 mm, $CTDI_{100}$ normalizes the dose with respect to the same width measured over the chamber. Therefore, based on the CBDI definition Eq.(2.9), the full chamber irradiation by using a beam width > 100 mm gives the best estimation for the cumulative dose. This has been discussed in detail in Chapter 6.

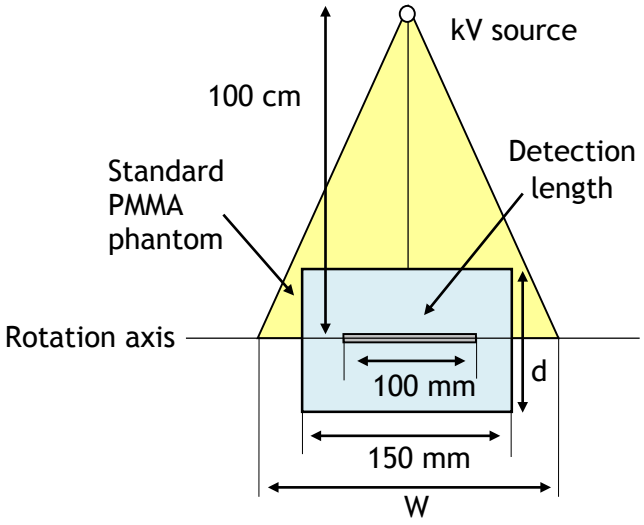

Figure 2.7: A diagrammatic representation of the experimental configuration used to assess CBDI for a CBCT scan with a beam of width (W). The measurements are performed using the standard head and body PMMA phantoms with a diameter of (d) and a 100 mm long pencil ionization chamber positioned at the centre of the scan. CBDI measurements are made at the centre and periphery of the phantoms.

Amer et al. (2007) used a XVI imaging system mounted on an Elekta linear accelerator. CBDI was investigated using three beams of width 160, 210, and 260 mm. CBDI was measured at the centre and periphery of the standard PMMA phantoms as well as a 290 mm long head PMMA phantom and a 440 mm long body PMMA phantom. It has been found that CBDI measured within the standard phantoms using the beam of width 260 mm underestimated CBDI measured within the longer phantoms by 31% and 8% at the centre and periphery, respectively. This underestimation reduced by 6% and 12% for the weighted CBDI ($CBDI_w$), calculated as for the $CTDI_w$, when beams of width 210 and 160 mm, respectively, were used.

Geleijns et al. (2009) studied five dose indices $CTDI_{100}$, $CTDI_{300}$, $CTDI_{600}$, $\overline{D_{100}}$ and $\overline{D_{24}}$ for a conventional CT scanner using a beam of width 160 mm. The $\overline{D_x}$ forms use chambers that fit within the width of the beam and are not normalized with respect to the beam width. $CTDI_{300}$ and $CTDI_{600}$ were based on the $CTDI_L$ method (Eq.(2.6)), and $\overline{D_{100}}$ was similar to CBDI (Eq.(2.9)). $\overline{D_{24}}$ was based on the cumulative dose $f(0,150)$ proposed by (Fahrig et al., 2006), and was evaluated over a detection length of 24 mm. The dose indices were assessed using experimental measurements and Monte Carlo simulations.

First, $CTDI_{100}$, $CTDI_{300}$ and $\overline{D_{100}}$ were measured experimentally using ionization chambers inserted into head and body PMMA phantoms 150 mm long for $CTDI_{100}$ and $\overline{D_{100}}$, and 350 mm for $CTDI_{300}$ measurements. Beam qualities for tube potentials of 80 – 135 kV and head and body bowtie filters of different sizes were used. The study found that under different scanning conditions, $\overline{D_{100,w}}$ values were in the range 0.90 – 0.93 of $CTDI_{300,w}$ for the head phantom, and 0.93 – 1.02 for the body phantom. Whereas $CTDI_{100,w}$ values were only 0.56 – 0.58 of $CTDI_{300,w}$ for the head phantom and 0.58 – 0.63 for the body phantom.

Second, Monte Carlo simulations were used to assess all the dose indices at 120 kV using head and body PMMA phantoms 150, 350, and 700 mm in length. $CTDI_{100}$, $\overline{D_{100}}$ and $\overline{D_{24}}$ were calculated within all the phantoms of different lengths, whereas $CTDI_{300}$ was only evaluated within the 350 mm and 700 mm long phantoms, and $CTDI_{600}$ was only evaluated within the 700 mm long phantom. It has been found that $CTDI_{300,w}$ values calculated within the 350 mm long phantoms were within 1% of those calculated within the 700 mm long phantoms. $\overline{D_{24,w}}$ values were in the range of 0.91 – 0.93 of $CTDI_{300,w}$ for the head phantom, and 0.99 – 1.02 for the body phantom, while $\overline{D_{100,w}}$ values were in the ranges of 0.89 – 0.91 and 0.95 – 0.99 for the head and body phantoms, respectively. $CTDI_{100,w}$ values, however, underestimated $CTDI_{300,w}$ values by 43 – 45 % for the head phantoms and 38 – 41 % for the body phantoms. $CTDI_{600,w}$ values were larger than $CTDI_{300,w}$ values by 1% and 4% for the head and body phantoms, respectively.

The expression $f_{100}(150)$ was used in the project for the CBDI concept, where (100) and (150) represent the length of the standard pencil ionization chamber and the standard PMMA phantoms, respectively.

2.6.4 $f(0,\infty)$ Method

AAPM TG–111 (AAPM, 2010) adapted the cumulative dose concept proposed by (Dixon, 2003), and introduced a dosimetric method for measurement in MSCT and CBCT scans. For a MSCT scan acquired with the moving table mode using the axial or helical modes over a given scan length, the cumulative dose $D_L(0)$ at the centre of the scan $(z = 0)$ is measured using

a small ionization chamber placed at the centre of the phantom. $D_L(0)$ resulting from multiple rotations is assessed as:

$$D_L(z=0) = \frac{1}{b}\int_{-L/2}^{+L/2} D(z)\,dz \qquad (2.10)$$

where the detection length is equal to the scan length, which covers the range from $-L/2$ to $+L/2$. The small chamber is transferred over the scan length L to integrate the dose profile accumulated from the multiple rotations. Subsequently, $D_L(0)$ is normalized with respect to b, which is the table increment for a single rotation. This means that $D_L(0)$ measures the cumulative dose within the $(-b/2\,,+b/2)$ interval, where $b = (N \times T) \times pitch$ and $b << L$. Figure 2.8 shows an example for a dose profile accumulated from a scan acquired with five axial scans and pitch = 1, i.e. $N \times T = b$, within an infinitely long body PMMA phantom. Each axial scan is acquired with a beam of width $N \times T = 40\,mm$, therefore the scan length $L = 200\,mm$. The small chamber is placed at the centre of the phantom, and then the phantom is moved from -100 mm to +100 mm to integrate the dose profile. The cumulative dose $D_{L=200mm}(\mathrm{z}=0)$, then, is normalized with respect to $b = 40\,mm$.

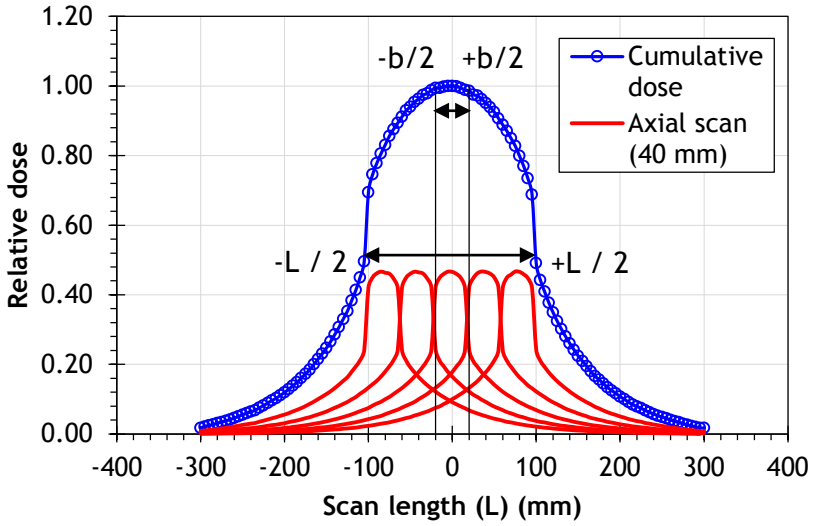

Figure 2.8: A dose profile accumulated from five axial scans, each of which is obtained with a beam of width 40 mm. The scan is acquired with a pitch of 1, and a scan length of 200 mm.

However, for scans obtained with the stationary table mode such as those employed for CBCT scans, the cumulative dose, which is analogous to that for MSCT scans $D_L(0)$ obtained with the moving table mode, is evaluated as:

$$D_N(z = 0) = Nf(0) \tag{2.11}$$

where N is the number of rotations involved in a CBCT scan, which is $(N = 1)$ in most cases, and $f(0)$ is the peak value of a dose profile resulting from a single CBCT rotation at the centre of the scan $(z = 0)$. $f(0)$ is measured as a point dose using a small ionization chamber at the middle of an infinitely long phantom ≥ 450 mm, which is sufficiently long to create the scatter equilibrium condition as illustrated in Figure 2.9 (a). Figure 2.9 (b) shows an example of a dose profile for a cumulative dose resulting from a CBCT scan obtained with a single rotation and a beam width of 200 mm within an infinitely long body PMMA phantom.

The International Commission on Radiation Units and Measurements (ICRU) Report–87 recommended the AAPM method, but proposed a practical measurement methodology to avoid the difficulty of using the long phantoms (ICRU, 2012). This method is based on the application of a function called $G_x(L)$, and is discussed in detail in Chapter 6.

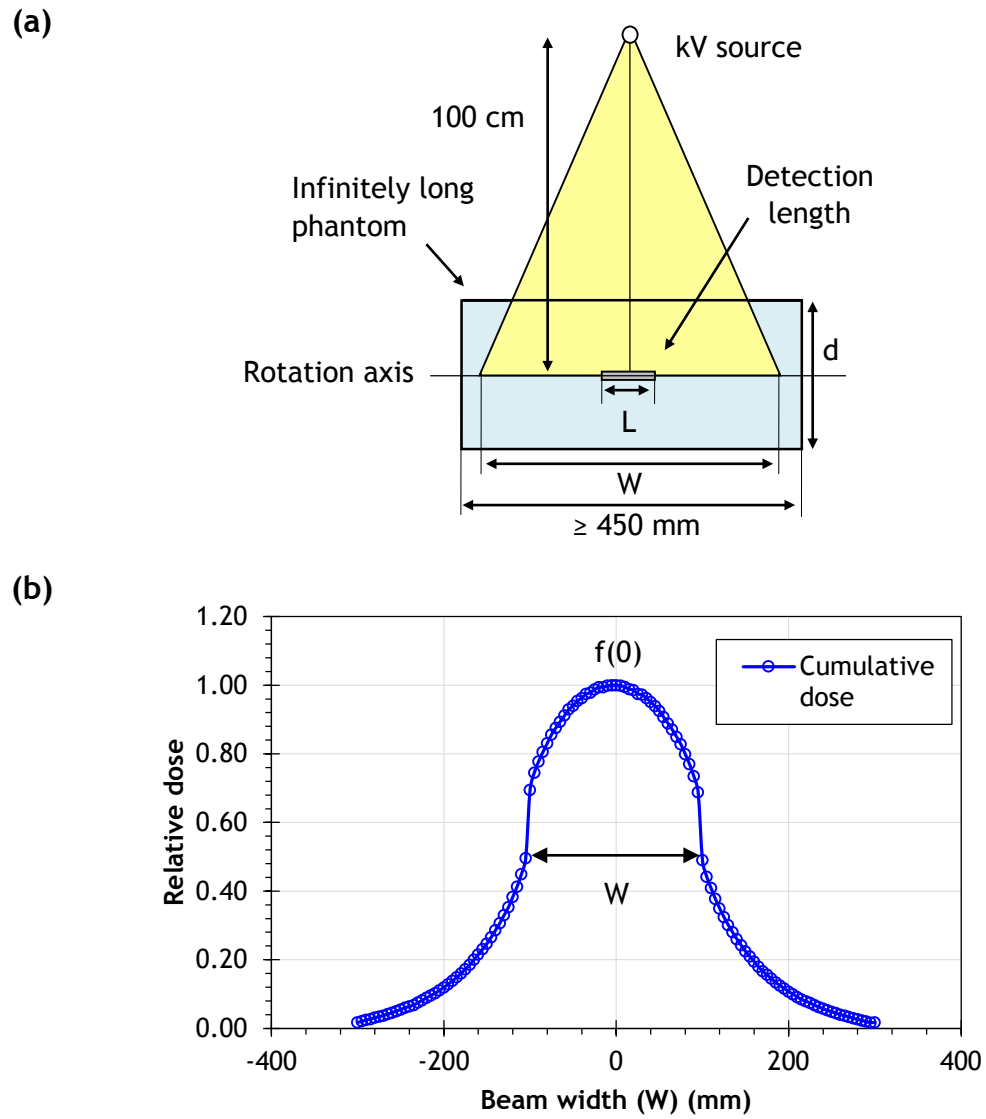

Figure 2.9: (a) A diagrammatic representation of the experimental configuration used to assess $f(0)$ for a CBCT scan with a beam of width (W). The measurements are performed using infinitely long head and body phantoms with a diameter of (d) and a small ionization chamber with an active length of L positioned at the centre of the scan. $f(0)$ measurements are made at the centre and periphery of the phantoms. (b) Dose profile for cumulative dose resulting from a CBCT scan with a single rotation and W = 200 mm.

$D_L(0)$ and $f(0)$ measurements can also be performed in infinitely long head and body phantoms made of polyethylene or water as shown in Figure 2.10. AAPM TG-111 (AAPM, 2010) recommended that the measurements are made in a water phantom (Figure 2.10 (a)), 300 mm in diameter and 500 mm in length. However, the ICRU in cooperation with the AAPM TG-200 (AAPM, 2015a) introduced a new cylindrical phantom named the ICRU/AAPM phantom, within which the cumulative dose is measured. This phantom is shown in Figure 2.10 (b), and is designed to emulate an adult body. The

ICRU/AAPM phantom is made of a polyethylene cylinder, 300 mm in diameter and 600 mm in length.

The expression $f(0,\infty)$ was used in the project for the AAPM method, where (0) and (∞) represent the position of the measurement and the infinitely long phantom, respectively.

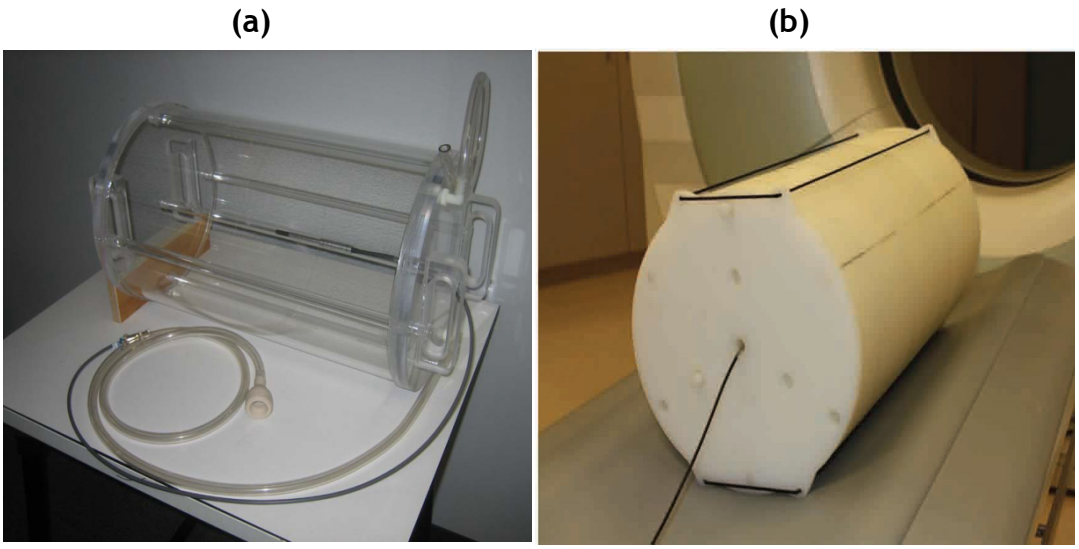

Figure 2.10: (a) The water filled phantom recommended by AAPM TG–111. (b) The ICRU/AAPM phantom. Both the phantoms represent an adult body. (a) Reprinted with a permission of John Boone, (b) reprinted with a permission of AAPM and Robert Dixon.

2.6.5 $CTDI_{IEC}$ Method

The IEC method ($CTDI_{IEC}$) extends the $CTDI_{100}$ concept, and is based on the use of $CTDI_{100}$ equipment. Note that the expression IEC has been used with CTDI to distinguish this method from the $CTDI_{100}$ and $CTDI_L$. The $CTDI_{IEC}$ is designed to be employed for beams of width > 40 mm and involves the application of a correction factor to measurements of $CTDI_{100}$ for a narrow reference CT beam. The correction factor is a ratio of two CTDI measurements free in air (FIA) for the beam width of interest ($CTDI_{FIA,N\times T}$) and the reference beam width ($CTDI_{FIA,ref}$). $CTDI_{IEC}$ is defined as follows:

$$CTDI_{IEC} = CTDI_{100,ref} \times \left(\frac{CTDI_{FIA,N\times T}}{CTDI_{FIA,ref}}\right) \quad (2.12)$$

where $CTDI_{100,ref}$ is the $CTDI_{100}$ of a narrow reference beam width (≤ 40 mm) measured within the standard PMMA phantoms and $CTDI_{FIA}$ is equal to:

$$CTDI_{FIA} = \frac{1}{N \times T} \int_{-L/2}^{+L/2} D(z)\, dz \qquad (2.13)$$

where L is the minimum integration length and depends on $(N \times T)$; (1) if $N \times T \leq 60\,mm$ then $L = 100\,mm$, or (2) if $N \times T > 60\,mm$, then $L = N \times T + 40\,mm$. For the beam widths that fall within the first range, measurements of $CTDI_{FIA}$ are made in a manner similar to that for the standard $CTDI_{100}$, but for wider beams, a longer ionization chamber that covers $L = N \times T + 40\,mm$ is required. If a long ionization chamber is not available, a standard 100 mm ionization chamber can be used by implementing a practical technique (IAEA 2011). This technique involves moving the chamber across the entire beam width in 100 mm steps to achieve the required length L. Utilizing this technique, integration lengths are multiples of 100 mm (i.e. 200, 300, etc). The sum of the dose resulting from these steps is then multiplied by the ionization chamber length 100 mm and divided by the width of the beam of interest to calculate $CTDI_{FIA}$.

Therefore, performing measurements for $CTDI_{IEC}$ using $CTDI_{100}$ equipment requires three steps as illustrated in Figure 2.11. Step 1: measuring $CTDI_{100,ref}$ using a reference beam width within the standard PMMA phantoms. Step 2: measuring $CTDI_{FIA,ref}$ for the same reference beam width free in air. Step 3: measuring $CTDI_{FIA,N\times T}$ for the beam of interest free in air, $CTDI_{FIA,W}$ in the case of CBCT scans. Number of the chamber movement required for $CTDI_{FIA,W}$ is mainly based on the beam width W. For example, three movements are needed for the clinical beam width W = 198 mm as shown in step 3. The measurements within the phantoms in the first step are made at the centre and periphery of the phantoms, whereas free in air measurements in the second and third steps are only performed at the centre, i.e. at the rotation axis.

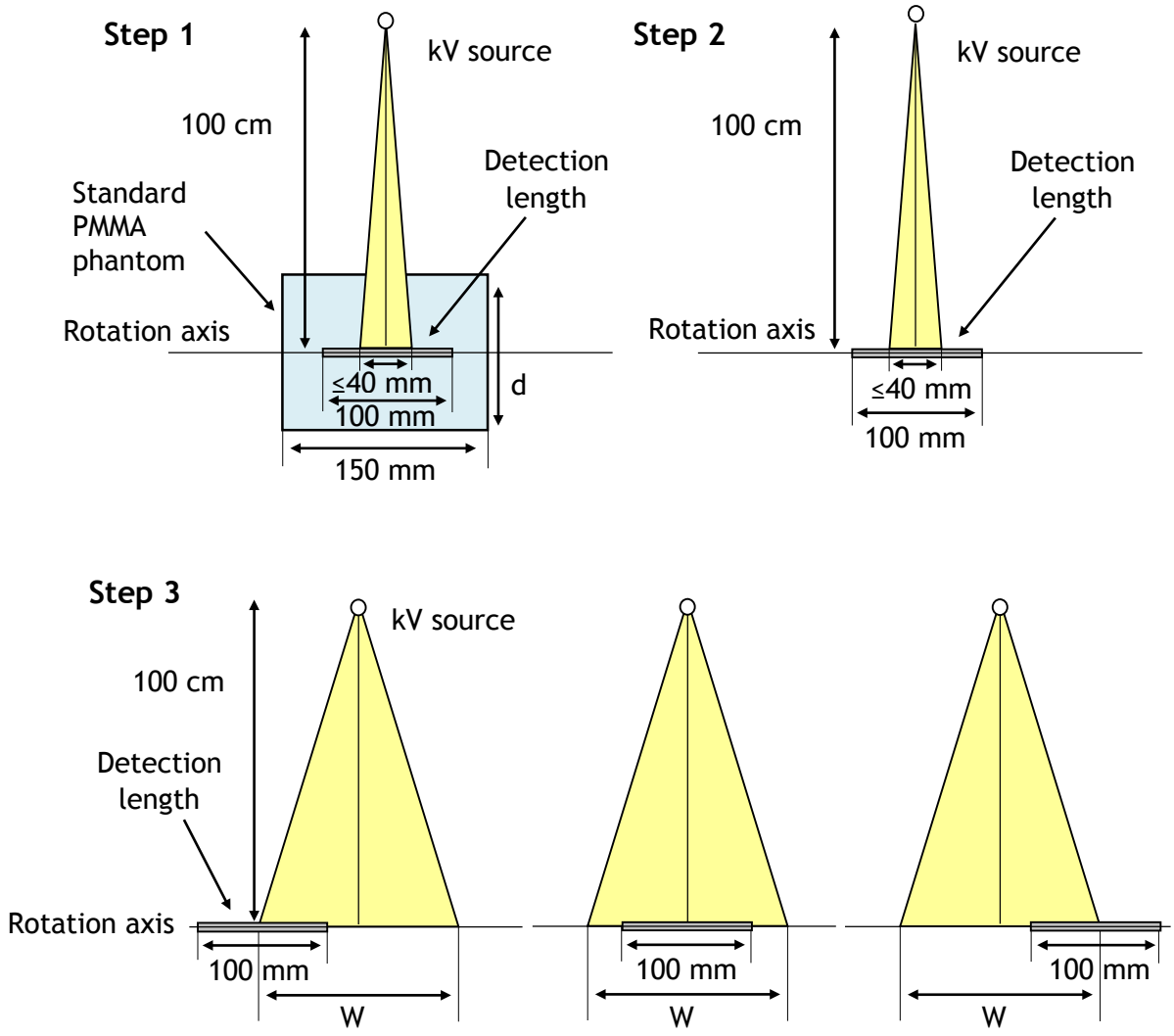

Figure 2.11: Diagrammatic representations of the experimental configuration used to assess $CTDI_{IEC}$ through three different steps for a CBCT scan with a beam of width (W = 198 mm). The measurements are performed with the standard head and body PMMA phantoms with a diameter of (d) (step 1) and free in air (steps 2 and 3) using a 100 mm long pencil ionization chamber positioned at the centre of the scan in steps 1 and 2, and moved over the scan range in step 3.

2.7 Organ Doses from CBCT Scans

Organ doses resulting from CBCT scans utilized in IGRT procedures using the different CBCT systems under different conditions have been investigated extensively in many studies in the literature. Table 2.2 shows a summary for some of these studies. Although all these studies investigated imaging and organ doses from CBCT scans, the aims and methods were different in each study. For example, some studies estimated organ doses from the scans, while other studies assessed imaging doses at the patient surface, i.e. skin dose, and the dose distribution within the patient body. The early

studies, which were conducted at the time of implementation of the CBCT systems in the clinic such as those published by (Ding et al., 2007, Wen et al., 2007, Walter et al., 2007, Amer et al., 2007, Ding et al., 2008a), aimed to characterize and assess imaging and organ doses from the scans. Organ doses outside the scans field were also investigated (Perks et al., 2008), and some studies conducted to evaluate imaging and organ doses for paediatric patients (Ding and Coffey, 2009, Kim et al., 2010b, Zhang et al., 2012b, Deng et al., 2012). The dose distribution within the body from the scans was also investigated (Tomic et al., 2010, Nobah et al., 2014).

2.7.1 Methods for Organ Dose Evaluation

From Table 2.2, it can be seen that the majority of the studies were conducted experimentally using anthropomorphic phantoms and dosimeters or by using Monte Carlo simulations on CT images of adult and paediatric patients or computational phantoms. The Monte Carlo method is discussed in Chapters 3 and 9. However, for experimental measurements, different dosimeters placed inside or at the surface of an anthropomorphic phantom are utilized to measure organ doses. Thermoluminescent dosimeters (TLDs), which were involved in most of the experimental studies (Table 2.2), are considered as the standard dosimeter used to measure organ doses. Some studies, however, utilized different dosimeters such as metal oxide semiconductor field effect transistors (MOSFETs) (Kim et al., 2010b), and Gafchromic film to measure the dose distribution within the phantom, i.e. the dose profile (Tomic et al., 2010, Nobah et al., 2014).

Table 2.2: A summary of studies conducted for patients dosimetry from CBCT scans.

Investigators	Methodology	CBCT system	Results
(Wen et al., 2007)	- TLDs on prostate cancer patients' skin - An adult anthropomorphic phantom with TLDs	OBI	Skin and in vivo doses from prostate scans
(Amer et al., 2007)	- An adult anthropomorphic phantom with TLDs - TLDs on patients' skin - ImPACT calculator	XVI	Organ doses from head, lung, and pelvic scans
(Walter et al., 2007)	- Ionization chambers at the surface and inside of five patients (rectum)	XVI	Dose for rectum and at the patients surface from MV EPID images and pelvic CBCT scans
(Kan et al., 2008)	- An adult anthropomorphic phantom with TLDs	OBI	Effective dose and organ doses from head and neck, chest, and pelvic scans
(Gu et al., 2008)	- MC on an adult phantom	Not mentioned	Effective dose and organ doses for kV and MV CBCT head and prostate scans
(Ding et al., 2008a)	- MC on CT images of adult patients	OBI	Organ doses from head and neck, lung, prostate, and pelvic scans
(Perks et al., 2008)	- An adult anthropomorphic phantom with TLDs	XVI	Imaging doses outside the scan field from pelvic scans

(Osei et al., 2009)	- An adult anthropomorphic phantom with TLDs - TLDs on patients' skin	OBI	Imaging doses and skin doses from head and body scans
(Downes et al., 2009)	- MC on CT images of adult patients	XVI	Organ doses from head and neck, lung, and pelvic scans
(Ding and Coffey, 2009)	- MC on CT images of paediatric and adult patients	OBI	Organ doses from head and neck, chest, and abdominal scans
(Walters et al., 2009)	- MC on adult phantoms	OBI	Red bone marrow and bone surface cells doses from head and neck, chest, and pelvic scans
(Chow, 2009)	- MC on anthropomorphic phantoms	XVI	Organ doses from head and neck, chest, and pelvic scans
(Ding et al., 2010a)	- MC on CT images of adult patients	OBI	Organ doses from CBCT and MSCT scans from prostate scans
(Hyer et al., 2010)	- An adult anthropomorphic phantom with fibre-optic coupled dosimetry system	OBI and XVI	Effective dose and organ doses from head, chest and pelvic scans
(Hyer and Hintenlang, 2010)	- ImPACT calculator and comparison with measurements obtained with an adult anthropomorphic phantom	OBI and XVI	Organ doses from head, chest and pelvic scans
(Kim et al., 2010b)	- A paediatric anthropomorphic phantom with MOSFETs	OBI	Effective dose and organ doses from abdominal scans

(Palm et al., 2010)	- An adult anthropomorphic phantom with TLDs	OBI	Imaging doses from head, thorax and pelvic scans using two different versions of OBI
(Tomic et al., 2010)	- An adult anthropomorphic phantom with Gafchromic film	OBI	Skin and imaging doses from head, thorax and pelvic scans
(Alaei et al., 2010)	- An adult anthropomorphic phantom with TLDs - A treatment planning system	XVI	Imaging doses from pelvic scan
(Ding et al., 2010b)	- MC on CT images of paediatric and adult patients	OBI	Organ doses from head, thorax, and pelvic scans using two different versions of OBI
(Dufek et al., 2011)	- An adult anthropomorphic phantom with TLDs	OBI and XVI	Effective dose and organ doses from head and neck and pelvic scans using (1) two different versions of OBI, (2) MV EPID, and (3) kV images
(Cheng et al., 2011)	- An adult anthropomorphic phantom with TLDs	OBI	Effective dose and organ doses from head and neck and pelvic scans using two different versions of OBI
(Qiu et al., 2012)	- MC on CT images of adult patients	OBI	Equivalent doses from pelvic scans
(Shah et al., 2012)	- An adult anthropomorphic phantom with TLDs	OBI and XVI	Imaging and organ doses from thorax and pelvic scans using (1) two different CBCT systems and (2) MVCT
(Zhang et al., 2012b)	- MC on CT images of paediatric patients	OBI	Organ doses from head and neck, and pelvic scans

(Spezi et al., 2012)	- MC on CT images of adult patients	XVI	Organ doses from head and neck, chest, and pelvic scans
(Deng et al., 2012)	- MC on CT images of paediatric patients	OBI	Organ doses from head and pelvic scans
(Alaei and Spezi, 2012)	- A treatment planning system and MC on anthropomorphic phantoms - An adult anthropomorphic phantom with TLDs	XVI	Imaging doses from head and neck, chest, and pelvic scans
(Stock et al., 2012)	- An adult anthropomorphic phantom with TLDs	XVI	Imaging doses from MV EPID images, kV radiographic images, MSCT, and CBCT using from head and neck and pelvic scans.
(Ding and Malcolm, 2013)	- An anthropomorphic phantom with and OSLDs - MC on CT images of adult patients	OBI	Skin and imaging doses from head and neck, thorax and pelvic scans
(Giaddui et al., 2013)	- An anthropomorphic phantom with Gafchromic film and OSLDs	OBI and XVI	Imaging doses from head and neck, thorax and pelvic scans
(Ding and Munro, 2013)	- MC on CT images of adult patients	OBI	Organ doses from MV EPID images, kV radiographic images and CBCT using from head, thorax and pelvic scans
(Montanari et al., 2014)	- MC on CT images of adult patients	OBI	Organ doses from head and pelvic scans

(Son et al., 2014)	- MC on adult phantoms	OBI	Organ doses from head and neck, chest, abdomen, and pelvic scans
(Nelson and Ding, 2014)	- MC on CT images of paediatric and adult patients	OBI	Organ doses from head and neck, chest, abdomen, and pelvic scans
(Nobah et al., 2014)	- An anthropomorphic phantom with Gafchromic film	OBI	Skin and imaging doses from head and neck, lung and prostate scans using (1) two different OBI systems, (2) MVCT, and (3) kV images
(Dzierma et al., 2014)	- An adult anthropomorphic phantom with TLDs - A treatment planning system	kVision	Organ doses from head and neck, thorax, and pelvic scans
(Alaei et al., 2014)	- A treatment planning system	XVI	Organ doses from head and neck, and pelvic scans
(Brochu et al., 2014)	- MC on CT images of adult patients	XVI	Imaging doses from chest scans
(Wood et al., 2015)	- An adult anthropomorphic phantom with TLDs - PCXMC program	OBI	Organ doses from pelvic scans

OBI: Varian On Board Imager, XVI: Elekta X-ray Volume Imager, kVision: Siemens imaging system, TLDs: Thermoluminescent Dosimeters, MC: Monte Carlo simulations, MOSFETs: Metal Oxide Semiconductor Field Effect Transistors, OSLDs: Optically Stimulated Luminescence Dosimeters, ImPACT: Imaging Performance and Assessment of CT, PCXMC: PC-based Monte Carlo program.

In addition, Ding and Malcolm (2013) investigated the suitability of using optically stimulated luminescence dosimeters (OSLDs), which are a relatively recent alternative dosimeter to TLDs. OSLDs were used to measure CBCT scans doses from the OBI system at the surface and selected points inside an anthropomorphic phantom. The experimental measurements were then compared against values calculated with Monte Carlo simulations. They found that OSLDs can be used as an alternative dosimeter for TLDs, but correction factors are required for the photon energy distribution. For the OBI system used in their study, the correction factors were in the range 0.88 – 1.13 for tube potentials of 60 – 125 kV.

2.7.2 Programs for Organ Dose Calculations

Various dose calculation programs have been developed to estimate organ doses for x-ray procedures. A dose calculator known as Imaging Performance and Assessment of CT (ImPACT) is commonly used to calculate organ doses from conventional CT scans. Hyer and Hintenlang (2010) studied the suitability of utilizing ImPACT to estimate organ doses from CBCT scans. Organ doses calculated with ImPACT for the head, chest and pelvic scans were compared to experimental measurements with an anthropomorphic phantom and TLDs using the OBI and XVI systems. They found significant differences between the measurements and the calculated values within ±551% and ±101% for the OBI and XVI systems, respectively.

Another dose calculation program developed to assess organ doses from x-ray examinations is known as PC-based Monte Carlo (PCXMC) (Tapiovaara and Siiskonen, 2008). Wood et al. (2015) investigated the use of this program to estimate organ doses from pelvic scans using the OBI system. Organ doses calculated with PCXMC program were found to differ by 1% to -80% from those measured experimentally using an anthropomorphic phantom and TLDs. The suitability of using TPS for evaluating organ doses from CBCT scans have also been studied by (Alaei et al., 2010, Alaei and Spezi, 2012, Dzierma et al., 2014), and they found differences between experimental measurements and those from TPS as discussed in the introduction chapter.

Recently, Montanari et al. (2014) showed that organ doses from CBCT scans can be estimated efficiently for each patient, i.e. patient-specific, by a dose calculation package named gCTD. This package is based on Monte Carlo simulations and uses a graphics processing unit (GPU), which decreases the time required for the simulations significantly. This allowed accurate calculation of organ doses for each patient within less than five minutes. This approach is still in the early stage of development and associated with some challenges such as the possibility of contouring the organs of interest automatically. This approach, however, might provide a practical solution to evaluating organ doses from CBCT scans easily as it is more practical in the clinical environment. Also it may give a solution to overcome the TPS limitation in the kV range.

2.7.3 Development of Hardware and Software for the OBI System

Since introduction of the CBCT systems, the hardware and software have been developed over time. For example, the Varian OBI system was upgraded from version of 1.0 to 1.6, and recently, a new version of 2.0 and 2.5 were released. For some new upgraded versions, new scanning protocols with different parameters from the early versions are configured by Varian. Therefore, some studies have investigated the differences between old and new scanning protocols, .i.e. different system versions (Ding et al., 2010b, Palm et al., 2010, Dufek et al., 2011, Cheng et al., 2011). Generally, the studies showed that more optimisation of radiation protection has been introduced in new scanning protocols, which has reduced imaging doses delivered to the patents. For example, Palm et al. (2010) found that imaging doses for head, thorax, pelvic spot light and pelvic scans of the OBI system with a version of 1.3 were reduced significantly to less than half when a version of 1.4 with different parameters was used. Moreover, Cheng et al. (2011) compared between organ doses and effective dose resulting from two different versions V1.4.11 and V1.4.13 of the OBI system. They also found that, overall, doses reduced significantly to less than half.

In addition, the hardware of the OBI system was changed slightly for new machines such as those integrated in TrueBeam linac. The main difference

between hardware of the OBI systems was the introduction of a filter made of titanium in addition to an internal aluminium filter. This was found to reduce organ doses from the head, thorax and pelvic scans to about the half compared to the scans acquired without the filter, as well as it enhanced the image quality for the scans (Ding and Munro, 2013). For instance, doses to heart and lung resulting from a thorax scan declined from 4.2 mGy and 5.2 mGy to 2.0 mGy and 2.7 mGy, respectively.

2.7.4 Differences between Imaging Modalities Used in IGRT

As various imaging modalities are used in IGRT procedures, some studies compared doses resulting from the different modalities (Gu et al., 2008, Ding et al., 2010a, Dufek et al., 2011, Shah et al., 2012, Ding and Munro, 2013, Nobah et al., 2014). For example, Ding and Munro (2013) evaluated organ doses from conventional radiographic kV images, CBCT scans, and MV images obtained with Electronic Portal Imaging Devices (EPID) using 6 MV for head, thorax and pelvic scans. Doses from CBCT scans were found to be lower than those delivered by MV EPID images, but higher than kV images. Doses to the brain stem, for instance, resulting from a head scan using MV EPID images, CBCT scans without the titanium filter and with the filter, and radiographic kV images were 37 mGy, 2.4 mGy, 1.6 mGy and 0.3 mGy, respectively. These findings were in agreement with other studies conducted by (Walter et al., 2007, Dufek et al., 2011, Stock et al., 2012). Nobah et al. (2014) also compared doses from CBCT scans, kV images from a kV system mounted on a CyberKnife unit, and MVCT from TomoTherapy linac. It has been found that, generally, doses from head, thorax, and pelvic CBCT scans were lower than those of the other modalities, followed by MVCT scans and kV images from the CyberKnife unit.

2.7.5 Organ Doses from OBI and XVI Systems

The differences between the OBI and XVI CBCT systems that are commonly used in the clinic have also been investigated in various studies (Hyer et al., 2010, Shah et al., 2012, Giaddui et al., 2013). Hyer et al. (2010) found that organ doses from the head scan obtained with the XVI system were about half of those for the OBI system, but larger for the thorax scan. Organ

doses from the pelvic scan were found to be comparable for both the systems. Shah et al. (2012) also found organ doses from the XVI system were larger than those for the OBI system for the thorax scan, but organ doses were comparable for the pelvic scan as shown in Table 2.3. Giaddui et al. (2013) used Gafchromic film and optically stimulated luminescence dosimeters (OSLDs) to estimate imaging doses at the surface and inside the patients delivered from both the systems. They found that the surface and internal doses from the head scan of the OBI system were higher than those from the XVI system, but doses from the thorax scan delivered by the XVI system were larger. Doses from the pelvic scans were found to be comparable for both the systems. These findings were in agreement with organ doses measurements conducted by (Hyer et al., 2010, Shah et al., 2012).

Table 2.3: Results for organ doses resulting from thorax and pelvic scans using the OBI and XVI systems. Organ doses were measured experimentally by (Shah et al., 2012) using anthropomorphic phantoms and TLDs.

	OBI		XVI	
Organ	Thorax scan (mGy)			
Breast	6.8	(6.4–7.4)	20.1	(18.6–23.2)
Breast surface	6.4	(6.3–6.5)	19.4	(18.8–19.4)
Heart	7.4	(6.9–7.9)	20.6	(19.6–21.6)
Lung	5.8	(1.7–8.4)	14.4	(3.0–22.8)
Abdomen	5.3	(3.8–7.0)	9.9	(3.6–16.5)
Sternum	14.7	(4.3–22.8)	33.2	(5.1–54.5)
Rib	13.9	(9.2–16.2)	35	(8.2–48.6)
Thyroid	0.9		1.0	
	Pelvic scan (mGy)			
Prostate	21.9	(21.0–22.8)	25.5	(24.3–26.5)
Bladder	23.2	(19.3–29.5)	25.4	(21.2–31.1)
Rectum	20.7	(19.4–21.6)	23.9	(22.9–25.6)
Sigmoid	17.9	(17.6–18.1)	19	(17.3–20.7)
Left femoral head	37.9	(36.8–39.1)	42	(40.4–43.5)
Right femoral head	37.2	(36.7–37.7)	50.6	(49.7–51.4)

2.7.6 Daily CBCT Scan

Spezi et al. (2012) used Monte Carlo simulations to simulate the XVI system and investigate the influence of using CBCT scans on a daily basis during a treatment course of 40 fractions. They calculated organ doses resulting from head and neck, chest and pelvic scans for 6 adult patients. They found that mean doses to organs within the imaging field from daily head and neck scans taken throughout treatment were in the range of 0.07 – 0.12 Gy. This range, however, increased to 0.79 - 1.90 Gy and 0.45 – 1.27 Gy, for the chest and pelvic scans, respectively. They suggested that the doses to the target tissues are significant and should be taken into account if daily scans are acquired. The doses accumulated during the course of treatment might also increase the risk of developing a secondary cancer in adjacent tissues for the patients. In addition, Nelson and Ding (2014) also used Monte Carlo simulations to simulate the OBI system. They calculated organ doses resulting from head and neck, thorax and pelvic scans for 30 paediatric and adult patients. For 40 fractions, organ doses from daily head and neck scans were in the range of 0.01 – 0.44 Gy. This range also increased in the OBI system for the thorax and pelvic scans to 0.11 – 0.69 Gy and 0.47 – 1.58 Gy, respectively.

2.7.7 Organ Doses and Scan Isocentre

In most cases, the isocentre of CBCT scans is set at the centre of the area of interest, i.e. (0, 0, 0). However, some of CBCT scanning protocols are based on using the treatment isocentre, i.e. the centre of the tumour. The arrangement varies between cancer centres, and in the Beatson Centre the practice adopted is to use the centre of the patient as the isocentre for the scan. Chow (2009) used the XVI system to investigate the influence of movement of the scan isocentre on the imaging doses. It has been shown that the imaging doses varied by up to 15% for the head scans when the isocentre was shifted across the x-y plan by up to 6 cm compared to those acquired at the centre of the patient. The difference increased by up to 19% and 22% for the thorax and pelvic scans, respectively, when shifts of up to 10 cm were applied. Moreover, Nelson and Ding (2014) used the OBI system and showed that the shift of the scan isocentre by 5 cm led to

differences in organ dose of less than 1 mGy for the head scan, and in the range of -7.7 to 4.7 mGy for the pelvic scan when the isocentre was shifted by 8 cm.

Chapter 3

The Monte Carlo Technique

3.1 Introduction

The Monte Carlo (MC) technique was used in this project as the main method to conduct different dosimetric studies by simulating the OBI system. The MC technique enables a wide range of studies that would be more difficult and time-consuming to investigate experimentally. It also allows simulating a system with a high level of accuracy, and hence obtaining accurate results. This chapter gives a general background for the MC technique and the basic concept behind the technique. It also presents an overview of the codes used in this project. This chapter is mainly based on descriptions and explanations given in the references (Hirayama et al., 2005, AAPM, 2007b, Dunn and Shultis, 2011, Seco and Verhaegen, 2013), and the manuals of the codes involved in this project (Rogers et al., 2013a, Rogers et al., 2013b, Walters et al., 2013).

3.2 Monte Carlo Technique

The MC technique is utilized in a wide range of applications such as medical and particle physics, astrophysics, and financial applications. The main concept used in all of them is the same, but the way of employing the MC technique is different in each science. Therefore, the definition of the MC technique can be divided into a general definition describing the main concept of the technique and a specific definition based on the application, for which the MC technique is used. In the literature, different general definitions for the MC technique have been given. All these definitions try to encompass the essence of the technique, and some examples are:

“The MC technique is a statistical method for performing numerical integrations.” (AAPM, 2007b),

“The analysis technique called Monte Carlo is, in essence, a methodology to use sample means to estimate population means.” (Dunn and Shultis, 2011),

“Monte Carlo is a numerical method to solve equations or to calculate integrals based on random number sampling.” (Seco and Verhaegen, 2013).

The technique was called ‘Monte Carlo’ by Stanislaw Ulam and John von Neumann in 1947 during the development of thermonuclear weapons in the Manhattan project, from which the atomic bomb was produced during the Second World War. The MC technique was employed in this project by using the first electronic computers, ENIAC, to calculate neutron transport accurately, which was one of the essential steps in the project. Since then, the term of Monte Carlo became common, and the interest of using the MC technique increased, especially with the improvement and developments in computer technology in 1950’s and 1960’s. However, for a long time before 1940’s, in which the name of Monte Carlo was used, the concept of the MC technique was known as statistical sampling. The first experiment, which used the statistical sampling concept, was conducted by Comte de Buffon in 1777, and his experiment is known as Buffon’s needle experiment. This experiment is designed as shown in Figure 3.1, and consists of a plane of a given dimension of (x, y) and has parallel lines spaced equally over the plane with a separation distance of (D). This experiment is based on tossing needles on the plane randomly, where all the needles have an equal length of (L) and $L < D$. The aim of the experiment was to find the probability of a needle dropped randomly crossing one of the parallel lines P_c, which is evaluated as:

$$P_c = \frac{N_c}{N_{tot}} \tag{3.1}$$

where N_c is the number of needles crossing one of the lines, and N_{tot} is the total number of needles dropped randomly on the plane.

Buffon found that P_c can be expressed as:

$$P_c = \frac{2L}{\pi D} \tag{3.2}$$

In 1886, Laplace suggested that Buffon's needle experiment could be used to estimate the value of π. As L and D in Eq.(3.2) are known, the π value, can be calculated as:

$$\pi = \frac{2L}{P_c D} = \frac{2L}{(N_c/N_{tot})\, D} \tag{3.3}$$

For example, if the needles shown in Figure 3.1 have a length of $L = 0.5\, D$, and 10 needles are dropped randomly on the plane, and 4 of them are found to cross the lines, then:

$$\pi = \frac{2 \times 0.5D}{(4/10)\, D} = 2.5 \tag{3.4}$$

which does not give a good estimation for $\pi = 3.1415929$. Thus, in order to overcome this difference, a large number of needles, i.e. samples or trials, are required to be dropped randomly.

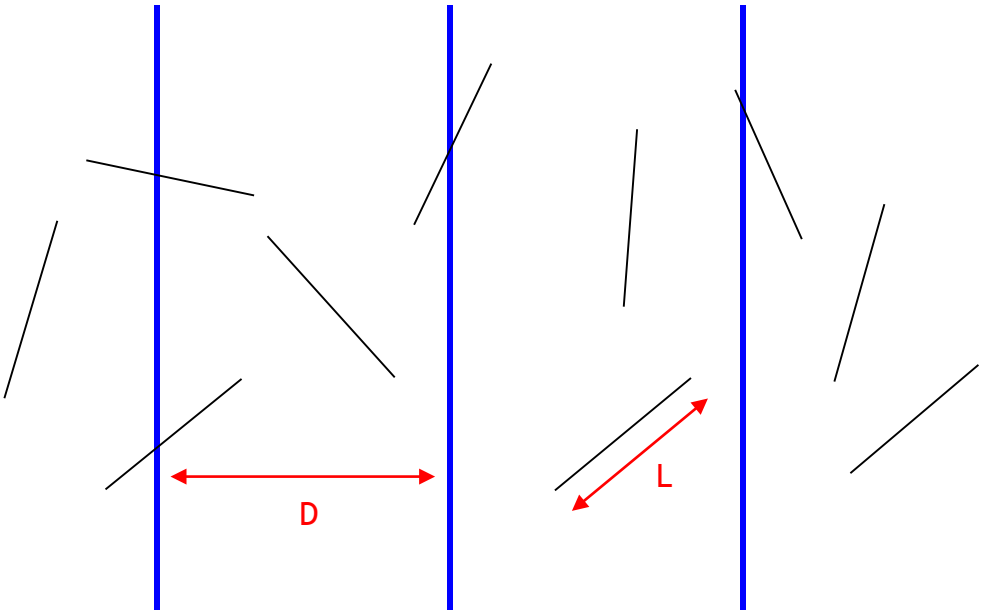

Figure 3.1: A schematic representation of Buffon's needle experiment.

Moreover, another experiment, which is used to estimate the value of π by using the random sampling concept, is shown in Figure 3.2. Assume we have a circle with a radius of (r) placed inside a square with a length of (2r). If several points located inside the square area are selected randomly, then

the probability of these points to be inside the circle as well (P_{in}) is estimated by:

$$P_{in} = \frac{N_{in}}{N_{tot}} \tag{3.5}$$

where N_{in} is the number of the random points located inside both the circle and the square, and N_{tot} is the total number of random points selected.

Theoretically, the probability of a random point (x,y) being inside the circle is calculated as:

$$P_{in} = \frac{Area\ of\ circle}{Area\ of\ square} = \frac{\pi r^2}{4r^2} = \frac{\pi}{4} \tag{3.6}$$

Thus, Eqs.(3.5) and (3.6) can be used to estimate the value of π as follows:

$$\pi = 4P_{in} = 4 \times \frac{N_{in}}{N_{tot}} \tag{3.7}$$

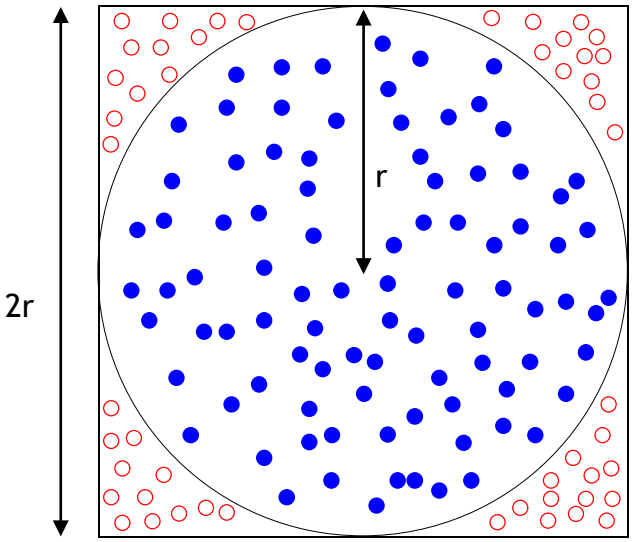

Figure 3.2: A schematic representation of an experiment used to estimate the (π) value by using the random sampling concept, which is similar to the MC concept.

For example, if 10 points are selected randomly, and 7 of these points are found to be inside the circle, i.e. $P_{in} = 0.7$, then,

$$\pi = 4P_{in} = 4 \times 0.7 = 2.8 \quad (3.8)$$

This underestimation is also affected by the total number of points selected, and the differences can be minimized by using a large number of points.

Kawrakow (2006) showed that the underestimation associated with estimation of the value of π decreased with increasing number of trials for both the experiments. 1×10^9 tossing needles and 1×10^{10} random points were required to estimate π value accurately.

3.3 Monte Carlo Technique for Medical Physics Applications

The two experiments described in the previous section are considered to be good examples to illustrate the main concept behind the MC technique. The MC technique plays a vital role in predicting output of an experiment with a stochastic output, such as a random point being inside or outside the circle. This predication is based on sampling random numbers, i.e. points in our example, repeatedly a large number of times until a reasonable estimation for the result is achieved. Therefore, one of the main bases of using the MC technique is to perform a larger number of trials. The larger number of trials we take; the closer we approach the true value. This is also the case for medical physics applications. When a particle is incident on a bulk of a given medium such as a water phantom, the behaviour of the particle inside the medium is not known as this behaviour is governed by stochastic events. For example, the distance that a particle travels inside the medium before the first interaction takes place, the trajectory of the particle inside the medium, the energy loss, the type of the interaction that a particle undergoes, the scattering angle, and so on. Such information that describes the random trajectories of individual particles is difficult to determine experimentally or analytically. Thus, the MC technique is a powerful tool and a suitable approach to solve such complex problems. The MC technique provides an average value for outputs of these stochastic events by tracking the trajectories of a large number of particles using probability distribution functions, as will be discussed in next section. The

MC output is, then, unitized to predicate the behaviour of the particles inside the medium, and hence determine the quantity of interest. Thus, the specific definition for the MC technique used for medical physics applications is defined as:

"The Monte Carlo method provides a numerical solution to a problem that can be described as a temporal evolution ("translation / reflection/ mutation") of objects ("quantum particles" [photons, electrons, neutrons, protons, charged nuclei, atoms, and molecules] in the case of medical physics) interacting with other objects based upon object–object interaction relationships ("cross sections")" (Seco and Verhaegen, 2013).

3.4 Transport Photons and Electrons using the Monte Carlo Technique

Although the main concept of the MC technique is simple as shown in the two experiments presented in section 3.2, simulating a trajectory of a particle travelling in a medium in three-dimensions (3D) is a complex process compared to a 2D experiment. In order to evaluate the quantity of interest such as estimation of the absorbed dose value at a specific depth within a medium, MC simulations known as analog simulations are employed. As this project was based on simulating photons and charged particles (electron and positron), the discussion only focuses on transporting these particles.

3.4.1 Analog Simulations

The analog simulations method is the standard approach for transporting particles inside a medium using the MC technique, and similar steps are followed for most MC codes. This method is also known as event-by-event or interaction-by-interaction simulations. To illustrate the method, assume a photon is incident on a phantom of a given medium. The analog simulations method transports this photon through the medium using four steps:

Step 1: Determination of a distance that the photon travels inside the medium before an interaction takes place. The probability of the photon travelling distance (dr) to reach the interaction site at (r) is governed by a continuous probability distribution function (PDF). This PDF is based on the linear attenuation coefficient $\mu(E)$ of the medium and the photon energy (E), as follows:

$$p(r)dr = e^{-\mu(E)r}\mu(E)dr \tag{3.9}$$

To estimate the position (r), sampling from the PDF using random numbers is the essential step. In MC simulations, the random numbers are produced by a generator known as a pseudo-random number generator. This generator distributes random numbers in the range (0 - 1) uniformly. Thus, direct sampling from the PDF in Eq.(3.9) using these random numbers is invalid as r value can be any value ≥ 0. In order to avoid this, and since the (PDF) is known, a method known as the inverse-transform method or the inverse cumulative distribution function (CDF) method is utilized. This method is based on using the CDF for the known PDF. Values for the CDF are in the range (0 - 1), which are in the same range for the random numbers distributed by the generator. Thus, CDF values can be equated to the random numbers ξ_1 values as:

$$PDF = p(r)dr \;\rightarrow\; CDF = P(r')dr' \tag{3.10}$$

so,

$$\xi_1 = CDF = P(r')dr' \tag{3.11}$$

For a given position (r):

$$\xi_1 = \int_0^r P(r')dr' = \int_0^r e^{-\mu(E)r'}\mu(E)dr' = 1 - e^{-\mu(E)r} \tag{3.12}$$

This leads to

$$r = -\frac{\ln(1-\xi_1)}{\mu(E)} \tag{3.13}$$

Thus, the r value for the particle is estimated from this equation using the random number.

Step 2: Transporting the photon for a distance dr, which is estimated in the first step, to the interaction site at r. If this site is located inside the geometry of interest, for example a phantom, then the simulation moves to the third step. If this site, however, is outside the geometry, i.e. the photon leaves the phantom, then tracking of the photon is terminated.

Step 3: Determination of the interaction type that the photon undergoes at the interaction site. This step is similar to the first step in terms of sampling from a CDF based on a known PDF using random numbers. However, when a photon enters a medium, one of four interactions is likely to occur: (1) photoelectric absorption, (2) Rayleigh (coherent) scattering, (3) Compton (incoherent) scattering, or (4) pair production. Therefore, the probability of occurrence for one of these interactions is governed by a discrete PDF. This PDF is based on the cross-section values (σ) of these interactions, which give the probability of occurrence a certain interaction for a photon with energy of E travelling inside a medium. If σ_{tot} is the total cross-section value for all the potential interactions for the photon:

$$\sigma_{tot} = \sigma_{PA} + \sigma_{RS} + \sigma_{CS} + \sigma_{PP} \tag{3.14}$$

then the probability of occurrence for the photoelectric absorption interaction is $(\sigma_{PA}/\sigma_{tot})$, and $(\sigma_{RS}/\sigma_{tot})$, $(\sigma_{CS}/\sigma_{tot})$, and $(\sigma_{PP}/\sigma_{tot})$ for the Rayleigh scattering, Compton scattering and pair production interactions, respectively. Subsequently, different random numbers ξ_2 from those used for the first step ξ_1 are generated, and are used with the CDF as follows:

Let $i = 1,\ 2,\ 3,\ 4$ represent the different interactions, if $(\xi_2 \leq \sigma_1/\sigma_{tot})$ then the first interaction is likely to occur, if $(\xi_2 \leq \sigma_1 + \sigma_2/\sigma_{tot})$ then the second interaction, if $(\xi_2 \leq \sigma_1 + \sigma_2 + \sigma_3/\sigma_{tot})$ then the third interaction, and the fourth interaction for the larger values.

Step 4: Performing the interaction determined in the third step. If the interaction type determined produces secondary particles, the four steps are, then, repeated for all the secondary particles and so on.

The four steps are repeated for a large number of primary and secondary particles using different random numbers ξ_1 and ξ_2 in the first and third steps, respectively. The random numbers are changed for each particle, thus a long cycle for the random number generator is needed to obtain unique random numbers for each particle. The use of many particles and different random numbers helps to approach the true value for the interaction position and the interaction type for a given experiment in a manner similar to the two experiments presented earlier. The simulation keeps tracking all primary and secondary particles using the four steps until (1) the particle leaves the geometry, (2) the particle is absorbed, or (3) the energy of the particle becomes lower than a user-defined cut-off energy known as PCUT and ECUT for the photon and electron, respectively. In the latter case, the MC simulation terminates tracking the particle trajectory, and its energy is absorbed locally at the site at which its energy becomes lower than PCUT and ECUT values.

The initial incident particle and all its secondary particles resulted from the different interactions are called ‘a particle history’ or ‘history’. This term is commonly used in the MC simulations to indicate the number of the initial particles used in a simulation, i.e. similar to the number of needles tossed and random points used for the two experiments.

3.4.2 Condensed History Technique

As only a few photons are transported during a given simulation, the analog simulations (event-by-event) method is practical for photons. However, this method is impractical for electrons due to the large number of interactions - the order of 10^6 - that electrons undergo during their travels in a medium. Such numbers of interactions leads to a significant increase in the time required for a MC simulation using the analog simulations method.

Therefore, in order to avoid this difficulty, another technique known as the condensed history (CH) technique has been introduced by Berger in 1963.

Electrons interact with a medium through either elastic (soft) collisions or inelastic (hard) collisions. The majority of electrons undergo the elastic collisions, through which a very small change in direction and energy of the electrons occurs. Based on this fact, the CH technique transports electrons by grouping, i.e. condensing and combining, small effect interactions, in the order of 10^3 - 10^5, into a single large effect interaction, also known as a large step. This step accounts for the effects resulting from the interactions condensed by sampling from PDFs covering the physical process involved for transporting grouped interactions. This technique decreases the time required for MC simulations significantly, by factors of hundreds. Thus, it plays a major role in MC simulations, and is considered as one of the essential techniques for implementation in almost all MC codes used at the present time.

The use of the CH technique is divided into two classes: (1) In the first class, all electrons undergoing elastic or inelastic collisions are transported by the CH technique. (2) In the second class, however, electrons undergoing elastic collisions are transported by the CH technique, but the analog simulations method is used for transporting electrons undergoing inelastic collisions. Figure 3.3 shows an example for using the CH technique. A photon is incident on the geometry of interest of a given medium. It is transported using the analog simulations method and the second class of the CH technique. First, the photon is transported using the analog simulations method. It begins when the photon reaches the surface of the medium geometry, where the first step is performed to calculate the r value. This step is followed by the second and the third steps to move the photon to the interaction site and determine the interaction type. In this example, the photon undergoes a Compton scattering interaction in the fourth step, which results in a photon and an electron: (1) For the photon resulting from the interaction, the four steps for the analog simulations method are repeated. This leads to another interaction, such as a pair production interaction. The simulation, then, continues running for the

secondary particles (electron and positron) until one of the four things mentioned earlier occurs. (2) For the electron, on the other hand, the CH technique is employed to transport the electron. Then, an inelastic collision (radiative interaction) with the atomic nucleus occurs, at which point the analog simulations method is used. Subsequently, the secondary particles (electron and bremsstrahlung photon) resulting from the inelastic collision are simulated in a manner similar to that for the secondary particles in (1). It should be noted that the particle trajectory shown in Figure 3.3 is an example given for an illustration purpose. However, the real particle trajectory is predicted by simulating a large number of histories, and is affected by various factors, mainly the particle type and energy and the medium of the interest.

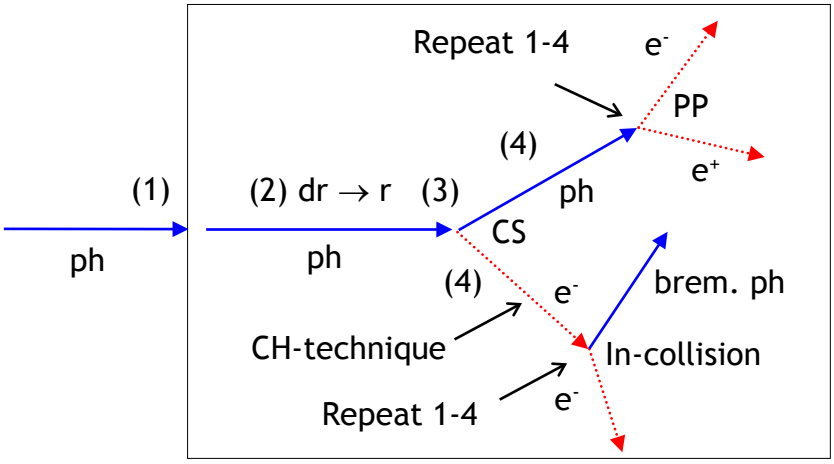

Figure 3.3: An example for the trajectory of a particle transported inside a medium using the analog simulations method and the second class of the CH technique. (r: the interaction site, ph: photon, CS: Compton scattering interaction, PP: pair production interaction, CH-technique: condensed history technique, brem ph: bremsstrahlung photon, and In-collision: Inelastic collision)

3.5 Selection of a Monte Carlo Code to Simulate the OBI System

With the evolution of computer technology, many general purpose MC codes have been developed for particles transport. One of the earliest codes written to transport particles using the MC technique was called SHOWER1 code. This code was written by Nagel at Stanford Linear Accelerator Centre (SLAC) at Stanford University in the early-to-mid 1960s to transport high energy electrons. In addition, another code named ETRAN code was written by Berger and Seltzer in 1968 to transport electrons and photons.

Performance of the different codes written in the early days has improved remarkably over time, which has led to the use of the MC technique extensively to conduct accurate studies in various aspects of many different fields. Some of the general purpose codes were developed for a wide range of applications including medical physics for interactions of both low and high energies of different particles.

At the present time, there are a number of codes that can be utilized for medical physics applications. For example, Electron Gamma Shower (EGSnrc) code from the National Research Council of Canada (NRC) (Kawrakow, 2000a, Kawrakow et al., 2013), Monte Carlo N-Particle (MCNP), which was originated from ETRAN code, and the extended version of MCNP (MCNPX) codes from Los Alamos National Laboratory (Team, 2008, Pelowitz, 2008), GEANT4 code from an international collaboration (Agostinelli et al., 2003), and Penetration and Energy Loss of Positrons and Electrons (Penelope) code from University of Barcelona (Salvat et al., 2011). The main difference between MCNP and MCNPX codes is in the type of particles they transport, where MCNPX has the ability to transport particles of all types. Many studies investigated the differences between these codes such as those conducted by (Faddegon et al., 2009, Maigne et al., 2011, Koivunoro et al., 2012, Archambault and Mainegra-Hing, 2015).

As shown in Chapter 2 Table 2.2, MC played a major role in conducting many studies carried out with the OBI system. EGSnrc code was found to be the most popular code, where the majority of these studies employed EGSnrc code. This is due to the user codes based on EGSnrc such as BEAMnrc (Rogers et al., 1995) and DOSXYZnrc (Walters et al., 2013) codes, which were developed to be utilized in various areas of medical physics and are common in radiotherapy applications. Moreover, EGSnrc showed a good accuracy at low and high energies (Kawrakow, 2000b, Mainegra-Hing and Kawrakow, 2006, Ali and Rogers, 2007, Ali and Rogers, 2008). The other codes were also utilized for simulating the OBI system such as GEANT4 (Brochu et al., 2014), and GATE code (Son et al., 2014), where GATE is a user code based on GEANT4 and commonly used for nuclear medicine applications (Jan et al., 2004, Jan et al., 2011, Sarrut et al., 2014).

Additionally, McMillan et al. (2013) and Poirier et al. (2014) used MCNPX and MCNP, respectively, for the OBI system. All the studies have shown good accuracy in evaluating results for the different codes at low energies. Therefore, any of the codes available can be utilized for simulating the OBI system. In this project, EGSnrc was used by utilizing different user codes based on EGSnrc (see section 3.7).

3.6 EGSnrc

As mentioned previously, SHOWER1 code was one of the first codes developed in the early 1960s by Nagel. Subsequently, Nicoli improved the code in 1966 and called it SHOWER2 code. This was followed by other improved versions SHOWER3/PREPRO code in 1972 and SHOWER4/SHINP code in 1974. Ford and Nelson continued to develop the code at SALC, and they re-named the code as Electron Gamma Shower (EGS1) in the mid 1970s. This was followed by further improvements, and the new versions of the code were called EGS2 in 1975, and EGS3 in 1978 (Ford and Nelson, 1978). In 1985, another version of EGS code (EGS4) was released in collaboration between Nelson from SALC, Rogers from NRC, and Hirayama from the High Energy Accelerator Research Organization in Japan (KEK) (Nelson et al., 1985). EGS4 code was then used extensively for a relatively long time. In 2000, Kawrakow at NRC developed EGS4 code and re-named it as EGSnrc code (Kawrakow, 2000a, Kawrakow, 2000b). Since then, EGSnrc code has been improved by NRC, and the last version of the code was EGSnrc V4 2.4.0 released in 2013, which was used in this project. Figure 3.4 shows a summary for the development of EGSnrc code.

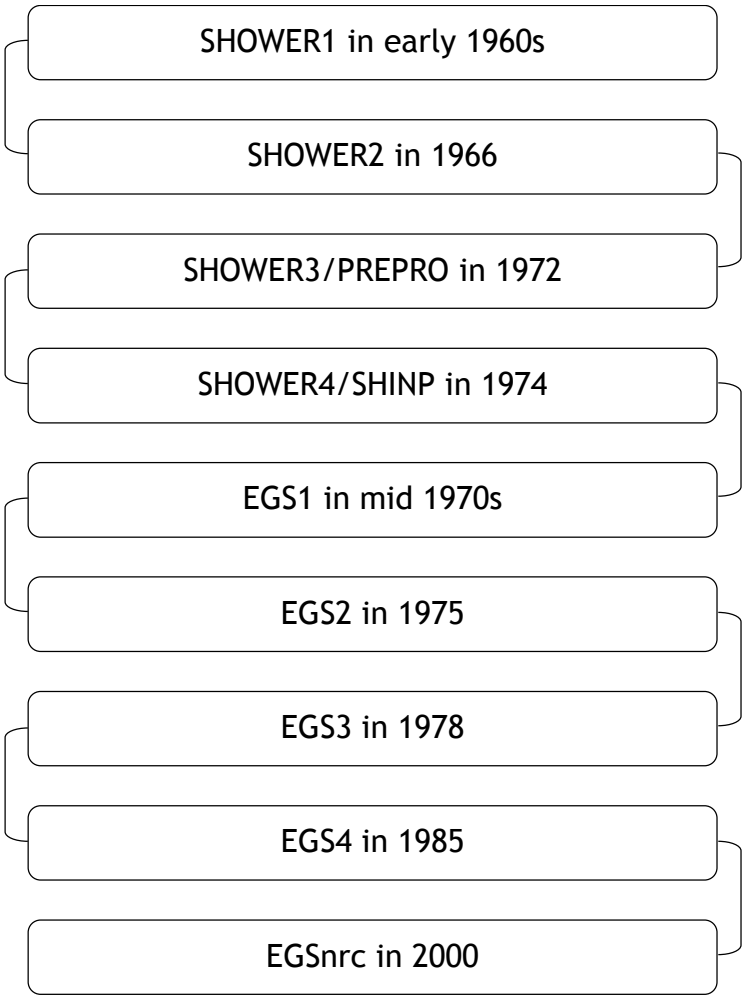

Figure 3.4: The development of EGSnrc code (Hirayama et al., 2005).

SHOWER codes and subsequently EGS have been improved significantly over the time to transport electrons and photons in the range of a few keV up to several hundreds of GeV with a high level of accuracy (Kawrakow et al., 2013). Initially, the different versions of SHOWER code and the early versions of EGS code were developed for shielding design for high energy particles. However, since 1985, the use of EGS4 code and after that EGSnrc code became more popular for medical physics applications. This is mainly due to the release of user codes used for medical physics applications such as studying an ionization chamber dosimetry and simulating a linear accelerator head (Rogers, 2006).

3.7 EGSnrc-Based User Codes

A number of user codes have been developed based on EGSnrc, each designed for a specific purpose. These codes have played a vital role in simplifying the use of the MC technique, by providing pre-coded routines. There has been further simplification in the development of friendly graphical user interfaces for some user codes, by which one can model a given geometry accurately. As a result, the use of EGSnrc-based user codes has increased and allowed large numbers of studies to be conducted based on simulations using the MC technique (Rogers, 2006). EGSnrc is a flexible code that allows a user to modify the user codes provided, if necessary, as well as creating a new user code if needed. In this project, three different user codes were used, namely BEAMnrc (Rogers et al., 1995, Rogers et al., 2013b), DOSXYZnrc (Walters et al., 2013) and CAVRZnrc (Rogers et al., 2013a).

3.7.1 BEAMnrc

BEAMnrc is considered to be one of the main user codes distributed with EGSnrc code. Originally, BEAMnrc was developed in collaboration between NRC and the University of Wisconsin in the early-mid 1990s in a collaborative project named Ottawa Madison Electron Gamma Algorithm (OMEGA) (Rogers et al., 1995). The aim of the project was to develop a 3D treatment planning system based on the MC technique using EGS4. Thus, the code was initially developed to model a linear accelerator head and to calculate 3D absorbed doses for patients undergoing radiotherapy treatment. Beside BEAMnrc, other codes were also developed such as DOSXYZnrc. These codes were made available publically for research and educational purposes. This has given medical physics researchers worldwide the opportunity to utilize the codes, and hence the increase of MC studies, especially in the radiotherapy field (Seco and Verhaegen, 2013). Currently, the user codes are based on EGSnrc, and are being improved continuously at NRC.

The steps of running a simulation in BEAMnrc can be divided into three main steps:

Step1: Specifying the geometry, i.e. designing the system of interest. This step is the essential step, upon which the accuracy of the simulation is largely based. It requires the geometrical specifications of each component of the system to be obtained accurately. This includes material, dimensions in (x, y, z) directions, the position of each component inside the system, and so on. In most cases, such information can be obtained from the manufacturer. More than 20 pre-coded components known as component modules (CMs) were implemented in BEAMnrc to simplify modelling components of the system of interest with a high degree of accuracy. Each CM is utilized for a specific purpose, for example, CMs known as XTUBE and SLABS are used to simulate an x-ray target (anode) and a filter of a specific thickness and material, respectively. Also some CMs are used to model complex geometries such as DYNJAWS, which is utilized to simulate the dynamic jaws used during a radiotherapy treatment.

All the geometrical data used for designing the system are then listed in an input file in (.egsinp) extension to be involved in the second step. This input file also contains information and parameters specified by the user for the simulation. For example, it includes the number of histories to be simulated, parameters of the variance reduction techniques (see section 3.8), values for PCUT and ECUT, and database names from which cross-section data are obtained. For instance, bremsstrahlung cross-section data can be obtained from Bethe-Heitler, the National Institute of Standards and Technology (NIST), or NRC.

Step 2: Running the simulation. In this step, a set of files including the input file prepared by the user in the first step, the code files, and the data file in (.pegs4dat) extension containing the cross-section date, densities, mediums compositions, etc. for the system materials used in the first step are compiled. The data file is created from a stand-alone code PEGS4 distributed with EGSnrc code (Kawrakow et al., 2006). This code allows the user to create a data file for all the materials involved in the simulation over a range of energies for photons and electrons. This range starts from the lower energy thresholds for creation of secondary electrons (AE) and photons (AP), and ends at the upper thresholds (UE) and (UP). These

thresholds are determined by the user, and typically AE and AP values are equated to ECUT and PCUT values, respectively. When all the files required are compiled successfully, the simulation begins to run.

The simulation runs in BEAMnrc using one of more than 15 per-coded sources called source routines (ISOURCE). These sources are employed to determine the parameters of the incident beam, and it depends on the simulation type. For example, (ISOURCE = 10: Parallel Circular Beam Incident from Side), which was used in this project, is employed for x-ray tube simulations such as those used to simulate CT and CBCT scanners. This ISOURCE allows an electron beam with a given energy and diameter to hit the anode of the x-ray tube from the side at a specific angle. The ISOURCE is selected by the user in the first step, and is incorporated into the input file. The simulation could be run as a single job using a single computer, or it could be split into N jobs running in parallel, where each job is run by a separate computer simultaneously.

Step 3: Collecting the simulation results. In most cases, outputs from the simulation are stored in a file called a phase space (PHSP) file. The PHSP file records information related to all the particles resulting from the simulation and passing a plane defined by the user at a specific distance from the source. This information includes the charge, the total energy, the position and the direction, the statistical weigh for each particle, and the position of the last interaction site for photons and creation of electrons by a photon moving in the z direction towards the target. Subsequently, the particles stored in the PHSP file are used as a source in another code to run another simulation such as DOSXYZnrc to calculate 3D absorbed dose. The PHSP file can also be analyzed by another code called BEAMDP to extract information from the PHSP file such as obtaining the spectrum resulting from the simulation (Ma and Rogers, 2013).

Usually, the PHSP file has a large size, the order of Gigabytes, and this size depends on factors such as the number of histories, the beam diameter and energy, and geometry of the system. This means that the PHSP file requires a relatively large disk storage space in most cases. In the case of a lack of storage capacity, a shared library from BEAMnrc code is created. The shared

library allows making BEAMnrc the source for the simulation, and running another code such as DOSXYZnrc simultaneously without a need to record an intermediate PHSP file. However, this needs longer simulation time (Kawrakow and Walters, 2006, Bazalova et al., 2009), and it requires running a new simulation from BEAMnrc, if the simulation with the second code, DOSXYZnrc in this example, needs to be repeated. This is different from the use of a PHSP file, where the simulation is only repeated for the second code. Moreover, in some cases, the same PHSP file is used repeatedly in anther code under different conditions, such as for different phantoms in DOSXYZnrc for the same PHSP file. The differences between doses calculated with PHSP files and BEAMnrc (shared library) as sources were minimal at high energies (Kawrakow and Walters, 2006), but the use of PHSP files was 54 -1.6 times more efficient than using BEAMnrc as a source at low energies (Bazalova et al., 2009). Thus, recording a PHSP file is recommended, as this can overcome the need to run the same simulation in BEAMnrc each time, hence minimizing the time required for all simulations. Also, it increases the efficiency of the simulation. Therefore, the method of using the PHSP file as a source was employed in this project. For some simulations, however, neither a PHSP file nor using another code are required such as obtaining a depth dose curve in BEAMnrc using the CM CHAMBER. In this case, the simulation results are listed in a file in (.egslst) extension. Figure 3.5 shows the main steps used in this project to run a simulation in BEAMnrc.

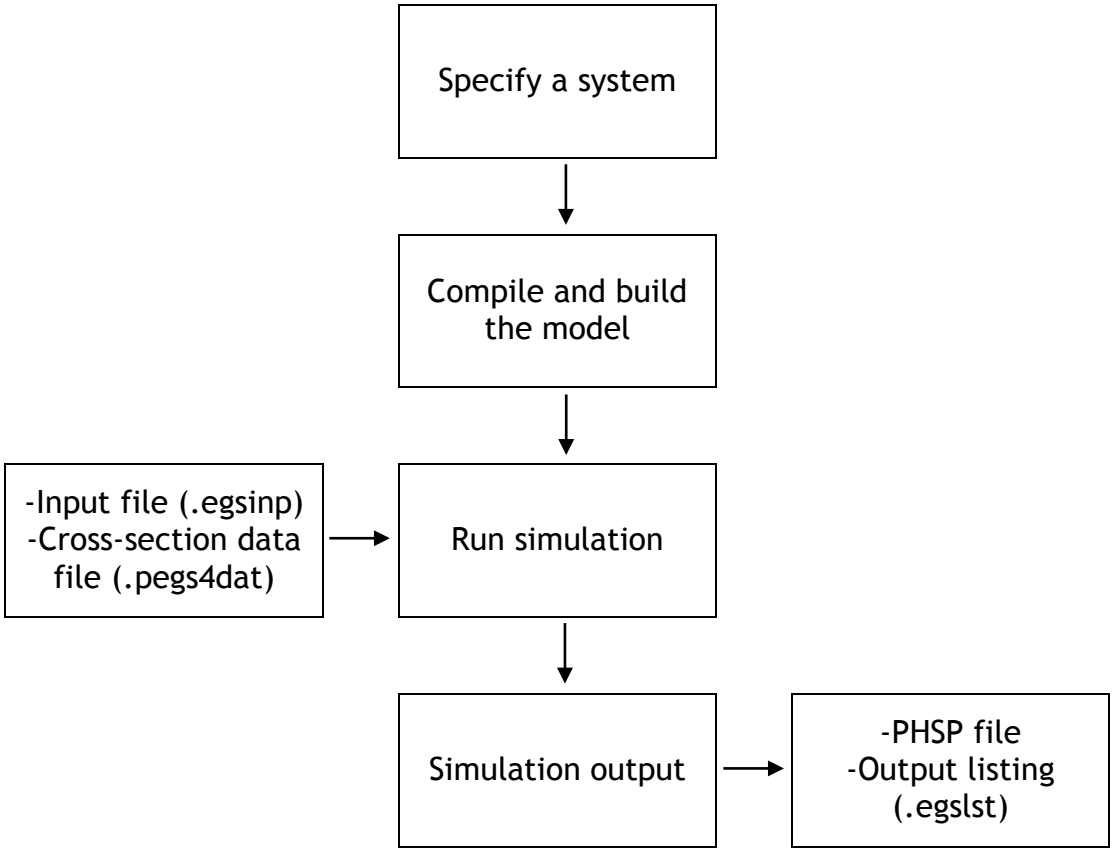

Figure 3.5: The main steps used in this project to run a simulation in BEAMnrc.

3.7.2 DOSXYZnrc

Beside BEAMnrc, DOSXYZnrc is also considered to be one the main user codes distributed with EGSnrc code. DOSXYZnrc calculates 3D absorbed dose in phantoms of simple geometries designed in the code or in complex geometries extracted from CT images. The geometries are obtained from CT images by converting the format (DICOM) to DOSXYZnrc format. This conversion is accomplished by using another code called CTCREATE (Walters et al., 2013). The geometry of a phantom designed in DOSXYZnrc or converted from CT images is divided into voxels of specific size. This means that DOSXYZnrc format is based on voxels. Subsequently, the absorbed dose at an area of interest is calculated from the voxels of this area.

The steps required for DOSXYZnrc simulations are similar to those followed in BEAMnrc (section 3.7.1). Figure 3.6 shows the main steps used in this project to run a simulation in DOSXYZnrc.

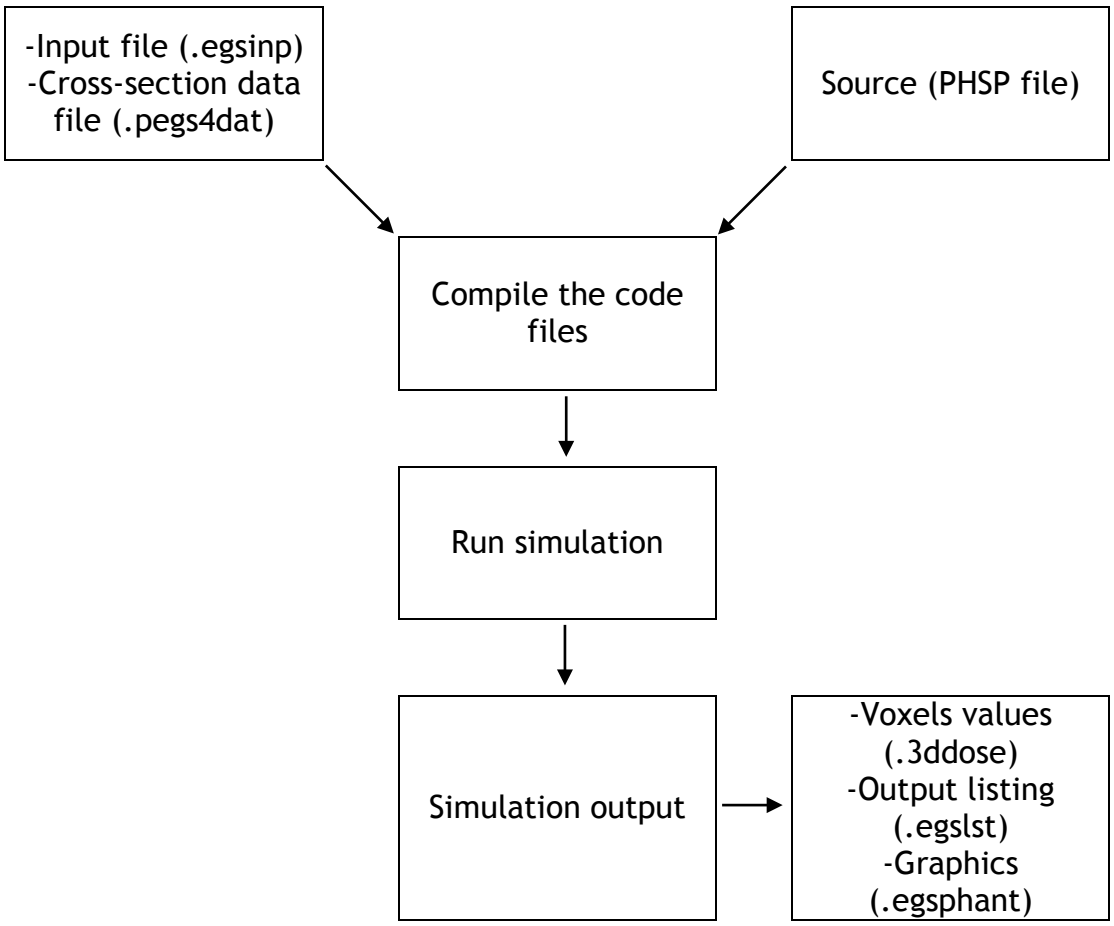

Figure 3.6: The main steps used in this project to run a simulation in DOSXYZnrc.

In the first step, the input file is created by the user, and this file includes the geometry of the phantom including the size of the voxels. It also includes the source of the particles such as the PHSP file or BEAMnrc (shared library), and other parameters such as the number of histories and parameters of the variance reduction techniques (see section 3.8). In the second step, all files required for the simulation are compiled and the simulation begins to run using one of more than 10 pre-coded sources (ISOURCE). Similar to BEAMnrc, each ISOURCE works differently and depends on the simulation. For example, (ISOURCE = 2: Phase-Space Source Incident from Any Direction) delivers the particles from a PHSP file to a phantom from a specific direction and angle determined by the user,

whereas (ISOURCE = 8: Phase-Space Source Incident from Multiple Directions) delivers the particles from various directions at different angles determined by the user. In this step, the cross-section data for the phantom materials are also obtained from the data file. In the third step, DOSXYZnrc outputs are given in a file in (.3ddose) extension. The results can also be listed in the (.egslst) file. The (.3ddose) file is, then, analyzed by a code called STATDOSE (McGowan et al., 2013) or a specific code developed by the user such as a MATLAB code. DOSXYZnrc allows the user to output the phantom geometry in a file in (.egsphant) extension. This file can then be used with the (.3ddose) file to show the dose distribution inside the phantom using dosxyz_show code (Kawrakow, 2013).

3.7.3 CAVRZnrc

Simulations in CAVRZnrc code are run in a manner similar to those for DOSXYZnrc. CAVRZnrc is used to calculate various factors of interest related to an ionization chamber dosimetry such as the chamber response and correction factors for a chamber wall. CAVRZnrc simulates the cavity of an ionization chamber with a diameter of (r) and a length of (z) as well as the wall and electrode of the chamber. More than 15 pre-coded sources are implemented in CAVRZnrc, and they are used to simulate the source. Outputs of the simulations are given in a (.egslst) file.

3.8 Variance Reduction Techniques

As mentioned previously, the use of a large number of histories for a simulation assists in approaching the true value for the quantity of interest. This leads to a reduction in the statistical variance of the simulation, also known as the statistical uncertainty, and is estimated by:

$$S(N) = \sqrt{\frac{\langle f^2(N)\rangle - \langle f(N)\rangle^2}{N-1}} \tag{3.15}$$

where N is number of histories simulated, f is value of the quantity of interest, and $\langle f(N)\rangle$ and $\langle f^2(N)\rangle$ are mean values, calculated by using a method called “history-by-history” as:

$$\langle f(N)\rangle = \frac{1}{N}\sum_{i=1}^{N} f_i \quad and \quad \langle f^2(N)\rangle = \frac{1}{N}\sum_{i=1}^{N} f_i^2 \tag{3.16}$$

where f_i is calculated for each history (i).

The $S(N)$ value becomes virtually constant as the number of histories increases, where any increase above a specific number of histories leads to a very small change in $S(N)$. Such a value is desirable for any simulation. However, this comes at the cost of increasing the time required for the simulation.

The efficiency (ε) for a given simulation is estimated by:

$$\varepsilon = \frac{1}{S(N)^2\, T(N)} \tag{3.17}$$

where $T(N)$ is the time required to simulate N histories. Thus, obtaining a small value for the statistical uncertainty $S(N)$ and minimizing the simulation time $T(N)$ are required to improve the efficiency of the simulation. Besides the use of ECUT and PCUT values, techniques called the variance reduction techniques (VRTs) are employed to speed up the simulation, and hence achieve a high efficiency for a simulation. Various VRTs were implemented in EGSnrc-based user codes. For example, four different VRTs are available in BEAMnrc code. One of these VRTs is called bremsstrahlung splitting, upon which three different techniques are based: uniform bremsstrahlung splitting (UBS), selective bremsstrahlung splitting (SBS), and directional bremsstrahlung splitting (DBS). Each VRT works differently. In this project, three VRTs were used namely DBS, photon splitting, and HOWFARLESS.

3.8.1 Directional Bremsstrahlung Splitting

The main concept behind the bremsstrahlung (brem) splitting technique is to increase the number of photons in the field of interest in order to minimize the $S(N)$ value and complete the simulation within a shorter time. To illustrate this technique, assume an electron is incident on the target of a system, and this electron interacts in the target and produces several brem photons, one of which is able to reach the field of interest and

contribute to the quantity of interest. This means that, approximately, X numbers of electrons are required to be simulated to produce X number of brem photons that reach the field of interest. However, the electron may or may not produce brem photons. Moreover, the brem photon produced may or may not reach the field of interest. In the range of kV energies, only a relatively small number of brem photons are produced by the electrons. This is due to the low probability of brem photon emission in the kV range, being less than 10% and 5% for tungsten and molybdenum targets, respectively, at 100 keV, and less than 20% at 250 keV (Ali and Rogers, 2007). Therefore, simulating a large number of electrons to increase the number of brem photons at the field on interest is required to gain a small $S(N)$ value, which increases the simulation time. The splitting technique saves the time required for these transports by splitting brem photons produced by fewer electrons into many photons. This splitting can be made using one of three different techniques implemented in BEAMnrc UBS, SBS, or DBS. Comparison of these techniques has shown DBS to be the efficient technique at low and high energies (Kawrakow et al., 2004, Mainegra-Hing and Kawrakow, 2006). Mainegra-Hing and Kawrakow (2006) showed that DBS technique increases the efficiency of an x-ray simulation at kV energies up to 5 - 6 times compared to that for a simulation without a splitting technique and 60 times higher than a simulation with the UBS technique. Therefore, the DBS technique was employed in this project. DBS is not only employed for brem photons, but also used to split photons resulting from other interactions such as annihilation (Mainegra-Hing and Kawrakow, 2006).

In order to utilize the DBS technique for photon splitting, three main parameters should be provided by the user: (1) the splitting number (NBRSPL), (2) the radius of the field of splitting (FS), i.e. the field of interest, and (3) the source to surface distance (SSD) at the FS. When a photon is produced, DBS splits it into NBRSPL photons each of which is given a statistical weight of $(w = 1/NBRSPL)$ in the final result. DBS, then, examines the split photons individually, and determines whether the photon is aiming inside or outside the FS specified by the user. If it is inside, the photon is kept and simulated with the given weight, and this photon is

called (non-fat) photon. However, for photons aiming outside the FS, a technique called Russian roulette is employed. This technique is considered as the opposite of the splitting technique. It is based on using a value known as a survival threshold, or a survival probability, equal to $(1/NBRSPL)$, and a random number (ξ) distributed uniformly in the range (0 - 1). If $(\xi < 1/NBRSPL)$, then the photon is kept and its weight is multiplied by NBRSPL to be $(w = 1)$, and it is called a (fat) photon. However, If $(\xi > 1/NBRSPL)$, the photon is terminated. If the surviving (fat) photons undergo interactions and produce secondary photons, the DBS technique is repeated for the secondary photons, and so on. By the end of the simulation, all the split photons reaching the field of interest are non-fat photons and have similar weight $(w = 1/NBRSPL)$. The use of this technique means that the majority of the simulation time is spent on tracking the particles that contribute to the quantity of interest, and avoids wasting time in simulating the other particles. So the splitting technique saves the time required to simulate a large number of electrons to obtain many photons. Thus, the use of a VRT improves the efficiency of a simulation significantly.

Figure 3.7 shows an example to illustrate the DBS technique and to show importance of the technique. In Figure 3.7 (a), four electrons are incident on a target. Two photons are resulted from these electrons, where one of the photons is aiming inside the FS, thus it contributes to the quantity of interest. This means that only a single photon is resulted from four electrons, which requires a long simulation time. However, if the DBS technique is used, larger number of photons are reaching the FS, and hence contribute to the quantity of interest within a shorter time and lower number of electros as shown in Figure 3.7 (b), where each photon is split to five photons $(NBRSPL = 5)$.

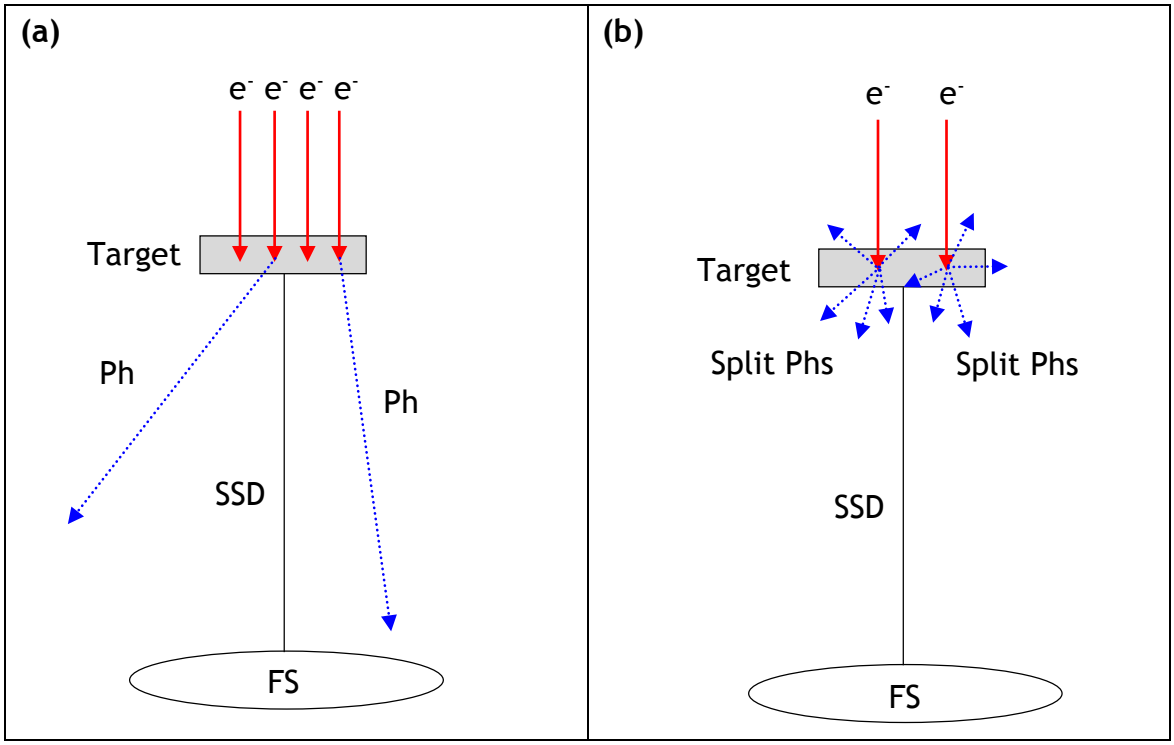

Figure 3.7: An example for a simulation (a) without and (b) with the DBS technique. (Ph: photon).

3.8.2 Photon Splitting

Photon splitting technique was implemented in DOSXYZnrc and CAVRZnrc codes. This technique has the same concept as that for the DBS technique. A user-defined splitting number (n_split) is used to split the photon n_split times when it enters the DOSXYZnrc or CAVRZnrc geometry. Thus, split photons are given a weight of $(w = 1/n\_split)$. The use of DBS in BEAMnrc and photon splitting in DOSXYZnrc was found to increase the simulation efficiency by a factor of up to 6.5 and ~2 for high and low energies, respectively (Kawrakow and Walters, 2006, Bazalova et al., 2009). The encashment in the simulation efficiency showed dependencies on various factors such as beam energy and diameter, field size, and voxel size.

3.8.3 HOWFARLESS

The HOWFARLESS technique is only used in DOSXYZnrc code, and it is utilized for simulations carried out with phantoms made of a homogeneous medium (Walters and Kawrakow, 2007). As mentioned previously, phantoms used in DOSXYZnrc are formed of voxels of specific sizes. The phantom consists of outer boundaries, i.e. the phantom size, and inner boundaries,

i.e. the voxel size. When a charged particle is transported inside the phantom, its step is restricted to the inner boundaries. The charged particle is stopped at each boundary to calculate the dose deposited inside the voxel during its transport, and this increases the time required for the simulation remarkably. In order to overcome this, the HOWFARLESS technique is used. It is based on transporting the charged particle without a restriction to the inner boundaries, i.e. ignoring the voxels boundaries, and only considering the outer boundaries. Thus, the charged particle is transported in steps freely without the need to stop at each inner boundary. Subsequently, the dose deposited at each voxel is calculated by the HOWFARLESS algorithm using the total curved path, through which the charged particle travels inside the phantom. The HOWFARLESS technique is only used for charged particles and not employed for photons. This is because no dose is deposited as photons cross over voxels. Thus, the photon step is not restricted to the voxel boundaries. The HOWFARLESS technique has been shown to be dependent on different factors such as beam energy and the boundary crossing algorithm (BCA), which is used in EGSnrc-based user codes to control the transport of electrons. The simulation efficiency was found to increase by a factor of 2.9 – 5.4 when the HOWFARLESS technique was used with a BCA called EXACT, and by 51% – 89% with PRESTA-I BCA (Walters and Kawrakow, 2007).

Chapter 4

Monte Carlo Modelling, Validation, and Calibration

4.1 Introduction

In the previous chapter, the theoretical aspects of the MC technique were discussed. The MC user codes used in this project and parameters employed for these codes were also presented. This chapter discusses the practical aspects concerning the use of the MC technique followed in this project. The chapter is divided into three main parts: (1) Modelling: this part discusses the method and component modules employed to model the OBI system. (2) Validation: this part presents the measurements carried out to validate the MC model designed in the first part. The validation tasks were (a) to validate the geometrical and beam properties of the model and (b) to validate dose calculations reported by the MC simulation for the quantities of interest. (3) Calibration: in this part, calibration factors were obtained to convert outputs of the MC results from Gy/incident particle to Gy. These factors were required for the study related to organ doses calculations reported in Chapter 9.

4.2 Modelling of the OBI System

The components of the OBI system were modelled in detail using BEAMnrc. The geometrical specifications of the system were obtained from the manufacturer under a non-disclosure agreement. Five component modules implemented in BEAMnrc, listed in Table 4.1, were utilized to model the system. Figures 4.1 - 4.2 show the model designed for the full-fan and half-fan modes, respectively.

Table 4.1: Component modules and materials used to model the OBI system involved in this project.

CM order	Component modules of BEAMnrc	Component of the OBI system	Material
1	XTUBE	x-ray target (anode)	95% Tungsten and 5% Rhodium
2	CONESTAK	Tube window and inherent filter	Beryllium and Aluminium
3	PYRAMIDS	Port	Lead
4	PYRAMIDS	Primary collimator	Lead
5	JAWS	Blades	Lead and Steel
6	SLABS	Beam hardening filter	Titanium
7	PYRAMIDS	Half and Full bowtie filters	Aluminium
8	SLABS	Housing window	Polycarbonate

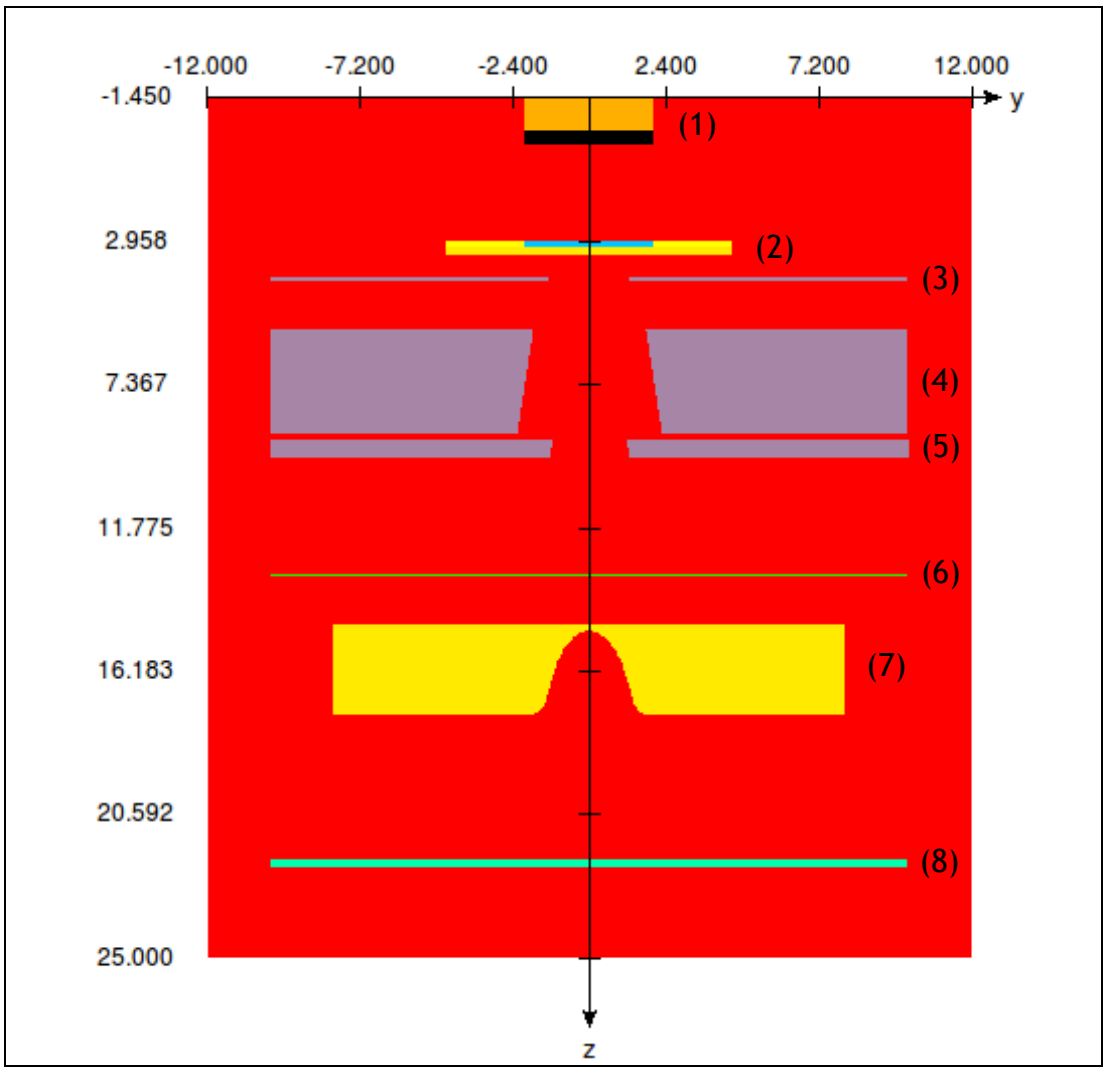

Figure 4.1: The MC model for the OBI system representing the full-fan mode with full bowtie filter. The model was designed using the CMs listed in Table 4.1. The dimensions are in cm.

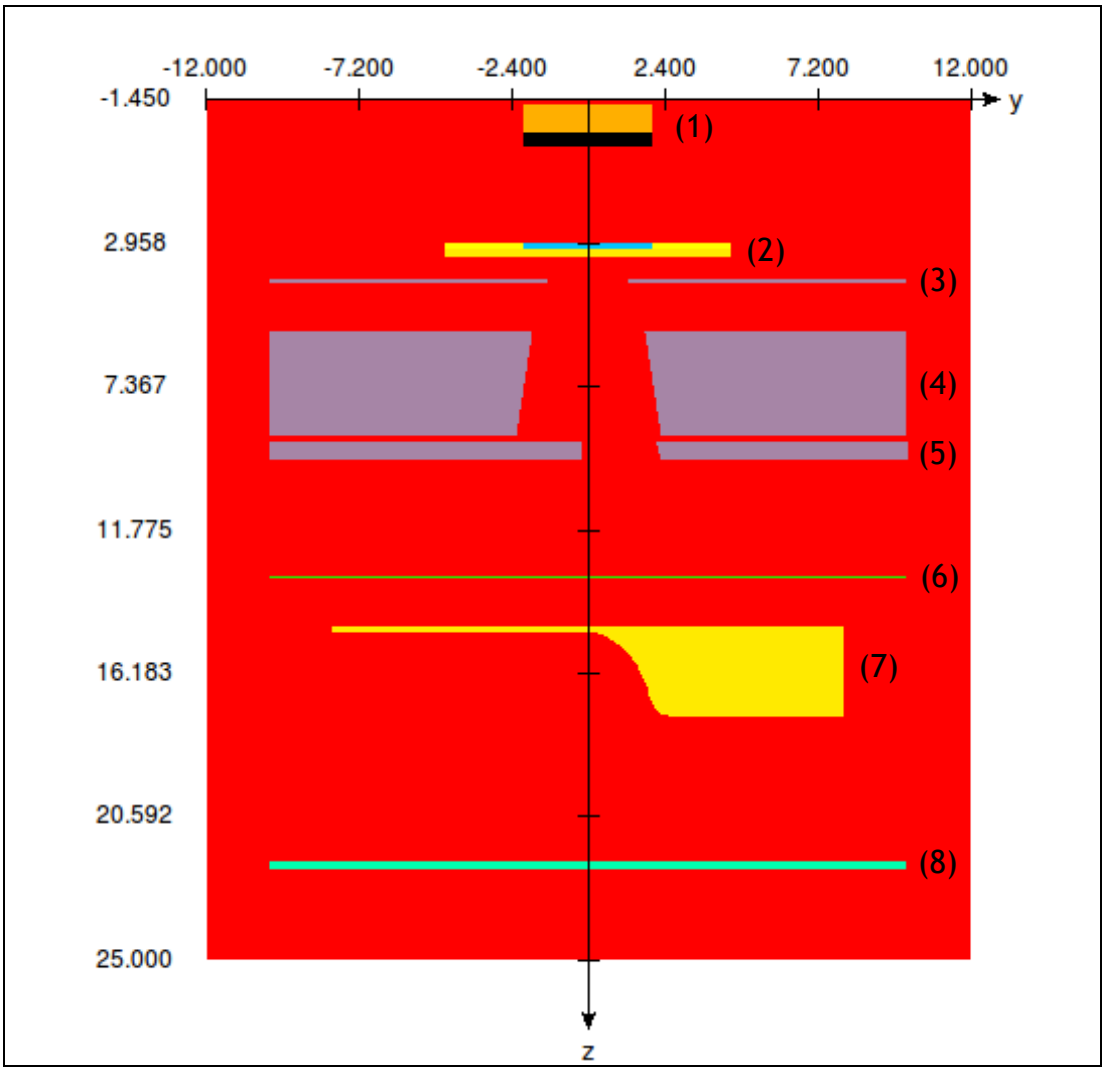

Figure 4.2: The MC model for the OBI system representing the half-fan mode with half bowtie filter. The model was designed using the CMs listed in Table 4.1. The dimensions are in cm.

4.3 Validation of the OBI System Model

In order to validate the geometrical and beam properties of the MC models designed in BEAMnrc, shown in Figures 4.1 - 4.2, five experimental measurements namely (1) x-ray spectra, (2) half value layer (HVL), (3) lateral (in-plane), (4) axial (cross-plane) and (5) depth dose profiles were performed. Subsequently, results of these experiments were compared against MC results calculated under the same conditions. All the materials and cross sectional data used in the simulations were obtained from PEGS4 code.

4.3.1 Experimental Measurements

4.3.1.1 X-ray Spectra

X-ray spectra were obtained from a MATLAB-based code SPEKTR (V2.1) (Siewerdsen et al., 2004). The SPEKTR code is based on experimental measurements obtained with parameters almost similar to those used for the OBI system. The code allows the user to generate an x-ray spectrum for a wide range of keV energies using filters of different materials and thicknesses. The x-ray spectra were generated for tube potentials 100 kV and 125 kV, which are used for the OBI scanning protocols listed in Table 2.1 Chapter 2. The x-ray spectra were obtained with all the internal filters, except the bowtie filters, which cannot be model in SPEKTR due to their shapes (see Chapter 2 Figure 2.2).

4.3.1.2 Measurements of HVL

To examine the beam quality for the designed MC model, the HVL measurements were made in terms of air kerma using two tube potentials 100 kV and 125 kV. The radiographic mode which allows the system to be operated with a stationary source was used to deliver a beam with a field of size 5 × 5 cm^2 without a bowtie filter at a source-isocentre-distance (SID) of 100 cm. Different thicknesses of aluminium (Al) layers ranging from 0.5 – 5.5 mm were applied to filter the beam. The Al thicknesses were incremented in steps of 0.5 mm over the full range studied, and by 0.1 mm or 0.2 mm in the region of the expected HVL. To minimize the effect of scattered radiation arising from the Al layers and the kV system housing, the Al layers were set up at a source-to-surface distance (SSD) of 65 cm. A plane parallel ionization chamber (Fluke model 96020C (150 CC), US) with a calibration traceable to a standard dosimetry laboratory was involved and placed at an SID of 100 cm as shown in Figure 4.3. An exponential curve from the measurements for each tube potential was, then, obtained, from which the HVL was estimated.

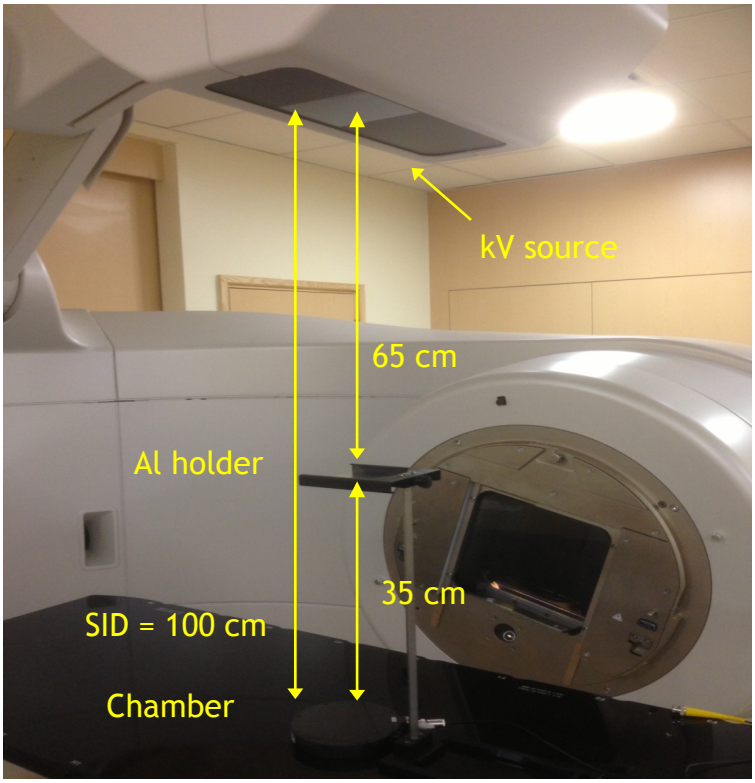

Figure 4.3: The experimental set up used for HVL measurements.

4.3.1.3 Measurements of Dose Profiles

Measurements for the lateral, axial, and depth dose profiles were used to validate the geometric design of the MC model. The dose profiles were measured by using two settings: 100 kV with the full bowtie filter and 125 kV with the half bowtie filter. The measurements were made within a 30 × 30 × 30 cm^3 solid water phantom (Gammex, Middleton, WI, US) using sheets of Gafchromic film (International Specialty Products—Advanced Materials, New Jersey, US) XR-QA model (lot No. 10121202). The dose profiles measurements were completed in two stages:

Stage 1: Calibration of the Gafchromic film. XR-QA model is manufactured to be used at low energies in the range of 20 – 200 kV. It consists of a 25 μm thick active layer with sensitivity ranges from 1 – 200 mGy. The film was calibrated using a local calibration protocol, which was described in (Martin et al., 2011). A Gulmay superficial x-ray therapy unit operated at 110 kV was used to calibrate the film. This tube potential gives a calibration curve almost similar to those for 100 kV and 125 kV (Giaddui et al., 2012). At the beginning, a number of measurements were made to determine the

dose values corresponding to the monitor unit (MU) settings at the position used for the film exposure as shown in Figure 4.4. 20 pieces of the film with a size of 2 x 2 cm^2 were exposed to doses ranging from 0.27 to 197.6 mGy. The film pieces were left for 24 hours after the exposure process to allow the optical density (OD) of the film to reach equilibrium status.

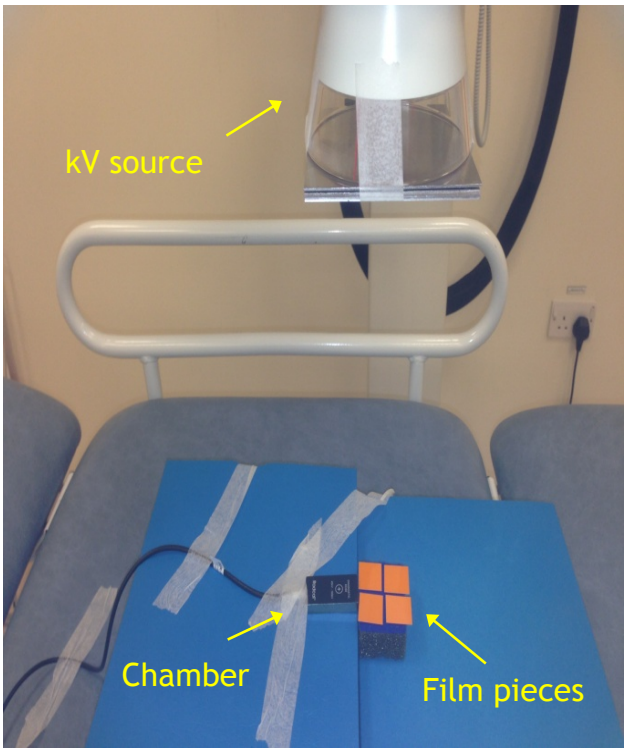

Figure 4.4: The experimental set up used to calibrate the Gafchromic film.

Subsequently, an Epson V700 flatbed colour scanner was employed to scan the 20 exposed pieces and a single unexposed piece using the reflection mode at 72 dpi resolution as shown in Figure 4.5. Images of the scanned pieces were saved in (.tiff) format so that they could be analyzed using ImageJ software. The red channel of the software was selected, and a macro built in house was used to automatically select a region of interest (ROI) with a size of 1 x 1 cm^2 at the centre of each piece of film. The ROIs selected were, then, analysed to obtain the red pixel value (RPV) for each piece.

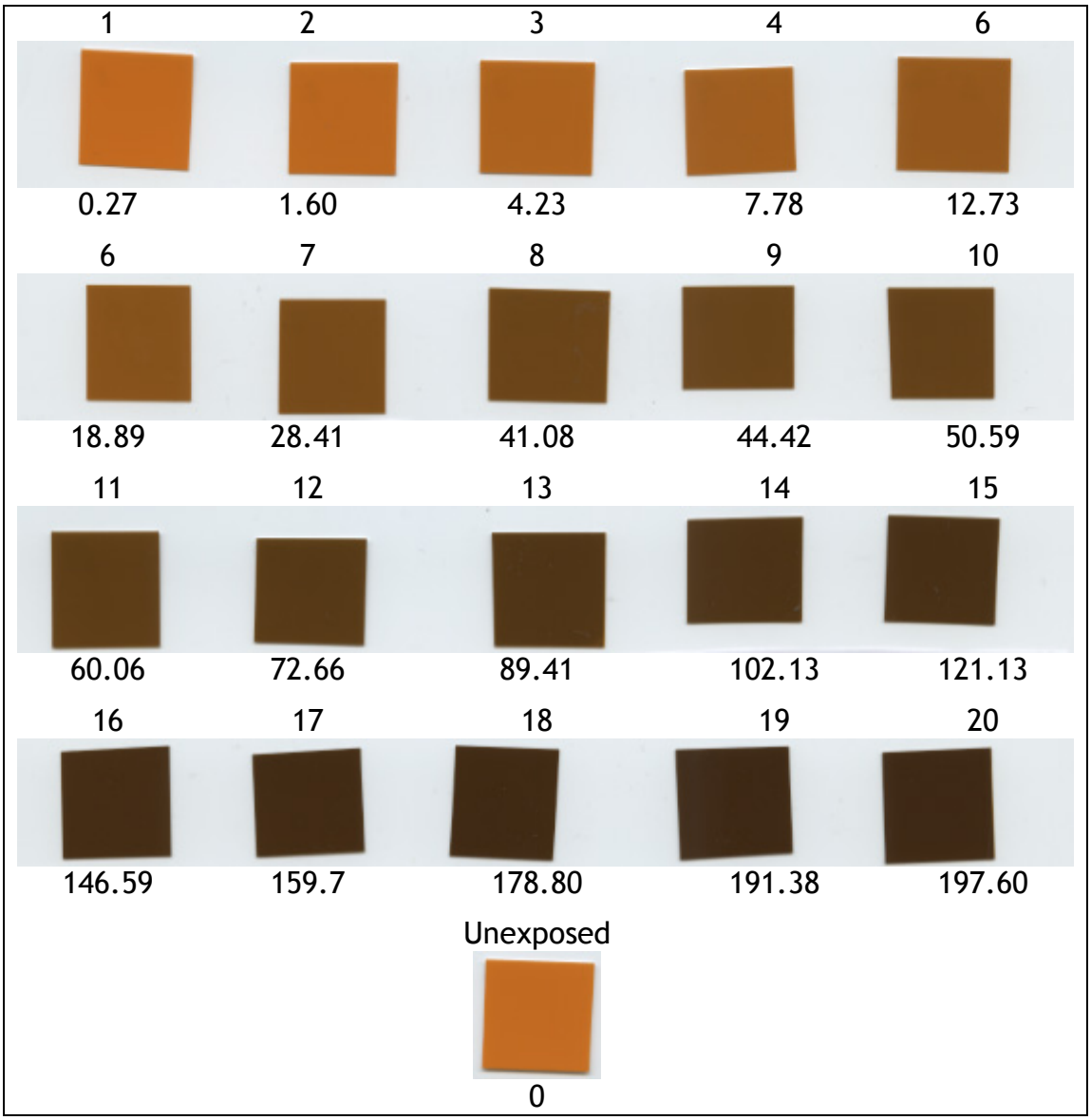

Figure 4.5: The 21 film pieces scanned with Epson V700 flatbed colour scanner. Doses used to calibrate the film ranged from 0.27 - 197.6 mGy.

The RPV values were used to calculate the OD for each piece as follows:

$$OD = log_{10}\left(\frac{RPV_{unexposed}}{RPV_{exposed}}\right) \tag{4.1}$$

ImageJ was used to obtain a curve fit for the dose values used in Gulmay and the corresponding OD values calculated in Eq.(4.1). The curve was fitted using the Rodbard function, which is defined as:

$$y = d + (a - d)/\left(1 + \left(\frac{x}{c}\right)^{b}\right) \tag{4.2}$$

where a, b, c, and d are parameters of the fitted curve. Thus:

$$OD = d + (a - d)/\left(1 + \left(\frac{Dose}{c}\right)^{b}\right) \quad (4.3)$$

which leads to

$$Dose = c \times \left(\left(\frac{a - d}{OD - d}\right) - 1\right)^{1/b} \quad (4.4)$$

Stage 2: Performing dose profile measurements. Once the film was calibrated, a sheet of film was cut into strips of size 3 × 30 cm^2 and 3 × 15 cm^2. The fluoroscopy mode was employed for all the measurements to deliver a continuous beam for 5 - 6 minutes to minimize fluctuations that may arise from the different responses of film from low exposure times. For the lateral and axial dose profiles, the solid water phantom was set up at an SSD of 100 cm, and the strips were placed at a depth of 0.5 cm inside the phantom along the x-axis for the lateral profiles and along the y-axis for the axial profiles as shown in Figure 4.6 (a - b). In order to ensure that the beam widths used in the MC calculations were set up properly by the MC model, a lateral dose profile and four axial dose profiles of different beam widths were measured for each setting. A field of size 280 × 280 mm^2 was used for the lateral dose profile, while 280 × 20 mm^2, 280 × 100 mm^2, 280 × 198 mm^2, and 280 × 280 mm^2 were used for the axial dose profiles. The film strips of size 3 × 15 cm^2 were employed for the beams of width 20 mm and 100 mm, and the strips 3 × 30 cm^2 for 198 mm and 280 mm.

For the depth dose profiles, the kV source was moved 90°, and a film strip with a size of 3 × 30cm^2 was placed parallel to the beam at a depth of 15 cm inside the phantom along the z-axis. The film strip was centred within a field of size 280 × 280 mm^2 at an SSD of 100 cm as shown in Figure 4.6 (c - d) (Fletcher and Mills, 2008). After the exposure, all the strips were left for more than 24 hours to reach the equilibrium status. The strips were, then, analyzed in a manner similar to that described in the first stage. Once the OD values were obtained, dose profiles for the strips were calculated using the calibration curve as in Eq.(4.4).

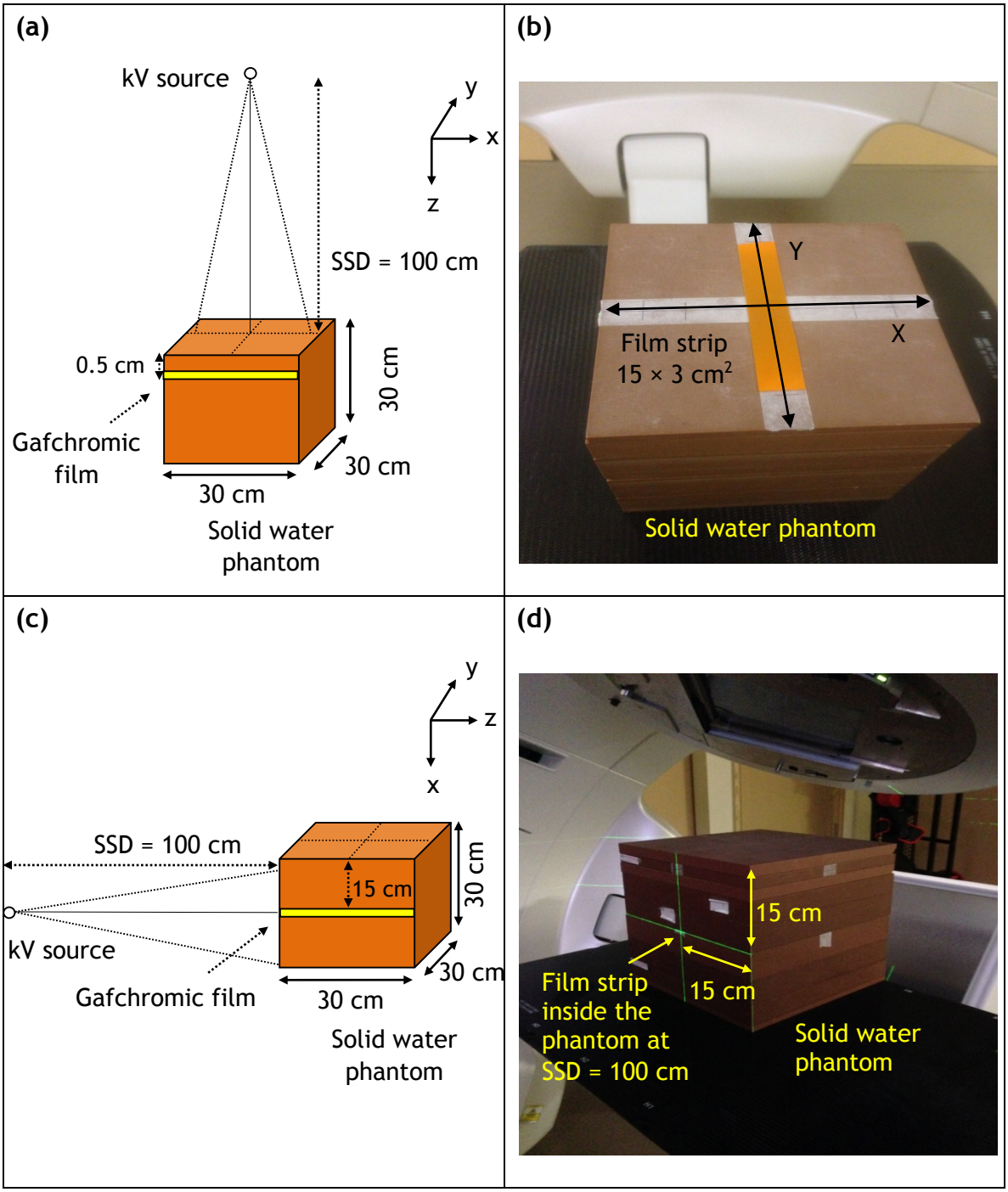

Figure 4.6: The experimental set up for (a - b) axial and lateral dose profiles measurements, and (c - d) for depth dose profiles.

4.3.2 Monte Carlo Simulations

The five measurements described in the previous section were calculated in MC through two steps: First, PHSP files were generated from BEAMnrc, and second, the files generated were utilized to obtain x-ray spectra using BEAMDP, HVL values using CAVRZnrc, and lateral, axial, and depth dose profiles using DOSXYZnrc. All these quantities were calculated using the

same parameters and set up used for the experimental measurements. In this project, almost all the MC simulations were run in the Scottish Grid Service (ScotGrid) at the University of Glasgow.

4.3.2.1 PHSP Files from BEAMnrc

The parameters used to generate the PHSP files from BEAMnrc were the same for all the different experiments, apart from three parameters: the number of histories, the SSD, at which the PHSP file is stored, and the field size for the beam. These parameters depended on the experiment type, thus they are given in the relevant sections. The DBS technique with a splitting number NBRSP of 1 - 2 × 10^4 were employed for all simulations (Ding and Coffey, 2010). ISOURCE = 10 of BEAMnrc (Parallel Circular Beam Incident from Side) was selected to allow an electron beam with a diameter of 0.4 mm or 1 mm to hit the anode of the OBI system from the side at an angle of 14^0. The electron beam was specified as a mono-energetic beam of energies either 100 keV or 125 keV. The low energy thresholds for creation of secondary electrons (AE) and photons (AP) were set to 0.516 MeV and 0.001 MeV, respectively, and these values were also set to the cut-off energies for transport of electrons (ECUT) and photons (PCUT) (Ding and Munro, 2013). The default boundary crossing algorithm (EXACT) and electron step algorithm (PRESTA-II) were used. Spin effect, the electron impact ionization, Rayleigh scattering, and atomic relaxations were included in the simulations (Ding and Coffey, 2010). The cross-section data of the National Institute of Standards and Technology (NIST) was used for bremsstrahlung cross sections, Koch–Motz for bremsstrahlung angular sampling, and NIST XCOM for photon cross sections (Mainegra-Hing and Kawrakow, 2006). The default cross-section data for all other interactions were used.

4.3.2.2 Calculations of X-ray Spectra

8×10^8 histories were run in BEAMnrc with a field of size 50 × 50 cm^2 without the bowtie filters and with the presence of the internal filters. Two PHSP files for energies 100 kV and 125 kV were recorded at an SID of 100 cm.

These files were, then, analyzed by BEAMDP to acquire x-ray spectra for the two simulations.

4.3.2.3 Calculations of HVL

The HVL calculation for the MC model was accomplished by calculating the dose in an air cavity using CAVRZnrc (Ding et al., 2007, Kim et al., 2012). First, 1×10^9 histories with a field of size 5×5 cm^2 were run in BEAMnrc for tube potentials 100 kV and 125 kV. PHSP files for the simulations were recorded at an SSD of 65 cm, similar to the experimental set up. Second, the plane parallel ionization chamber used in the experimental measurements was modelled in CAVRZnrc using specifications of the chamber obtained from the manufacturer. The PHSP files were used to run $2 - 3 \times 10^7$ histories using a photon splitting number 100 and source No. 22 of CAVRZnrc (Full Beam Phase-Space Beam Data from Any Angle, Inside or Outside). Al layers of thicknesses 0.5 – 6 mm with an increment of 0.5 mm were utilized. The designed chamber was placed at an SID of 100 cm, and the dose for each Al thickness was calculated with a statistical uncertainty of less than 1%. The HVL value for each tube potential was estimated by fitting the resulting values obtained from CAVRZnrcn to exponential curves.

4.3.2.4 Calculations of Dose Profiles

The MC dose profiles were derived by DOSXYZnrc using the experimental set up shown in Figure 4.6. First, 8 PHSP files (four for each setting described in section 4.3.1.3) were recorded in BEAMnrc at an SID of 100 cm using 1×10^9 histories. Second, the PHSP files were used as sources in DOSXYZnrc to calculate the absorbed dose inside the phantom by using ISOURCE = 2 of DOSXYZnrc (Phase-Space Source Incident from Any Direction). The solid water phantom used in the experimental measurements was designed in DOSXYZnrc as a cube of size $30 \times 30 \times 30$ cm^3 and consisted of voxels of size $0.5 \times 0.5 \times 0.5$ cm^3. 5×10^8 histories with a photon splitting number 50 - 300 were used for all simulations to achieve a statistical uncertainty of less than 2% in the voxels of interest (Bazalova et al., 2009). The same ECUT and PCUT values used in BEAMnrc were also involved in DOSXYZnrc. The HOWFARLESS technique together

with the default boundary crossing algorithm (PRESTA-I) were utilized to enhance the efficiency of the simulations. The output files were in (.3ddose) format, which were analyzed subsequently by STATDOSE.

4.3.3 Results

4.3.3.1 Comparison of X-ray Spectra

Figure 4.7 shows a comparison between x-ray spectra for 100 kV and 125 kV generated by the MC model, which were obtained at an SID of 100 cm with a field of size 50 × 50 cm^2, and those generated by Spektr code. For all spectra, the number of photons at each tube potential was normalized with respect to the number of photons at the characteristic energy. The comparisons show good agreement between the spectra.

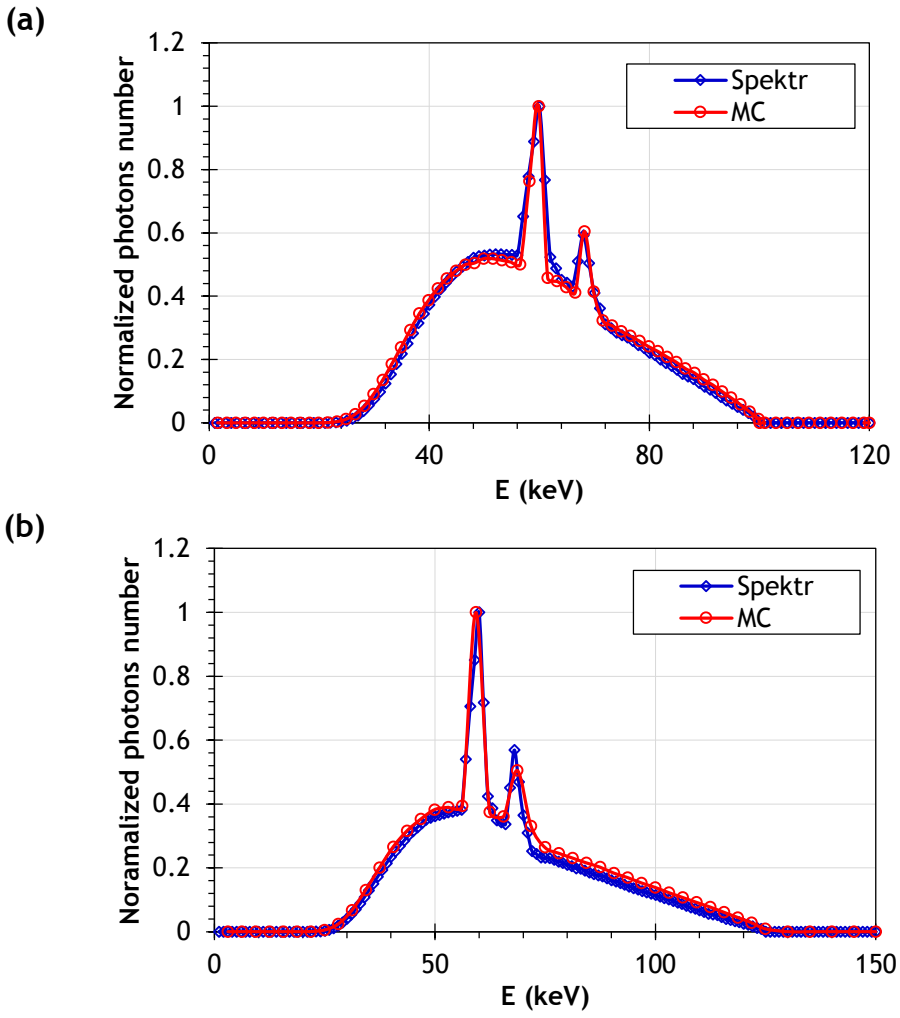

Figure 4.7: A comparison between the x-ray spectra of the MC model and Spektr normalized with respect to the number of photons at the characteristic energy. (a) 100 kV and (b) 125 kV.

4.3.3.2 Comparison of HVL Values

Figure 4.8 shows a comparison between the MC and the experimental results for the HVL experiment. The HVL values calculated in MC were 3.84 mm Al and 4.89 mm Al for 100 kV and 125 kV, respectively. These values were within 0.05 mm of the respective experimental measurements 3.79 mm Al and 4.90 mm Al, respectively. The HVL values for the MC model agreed with the experimental measurements to within 1.3% for 100 kV and 0.41% for 125 kV.

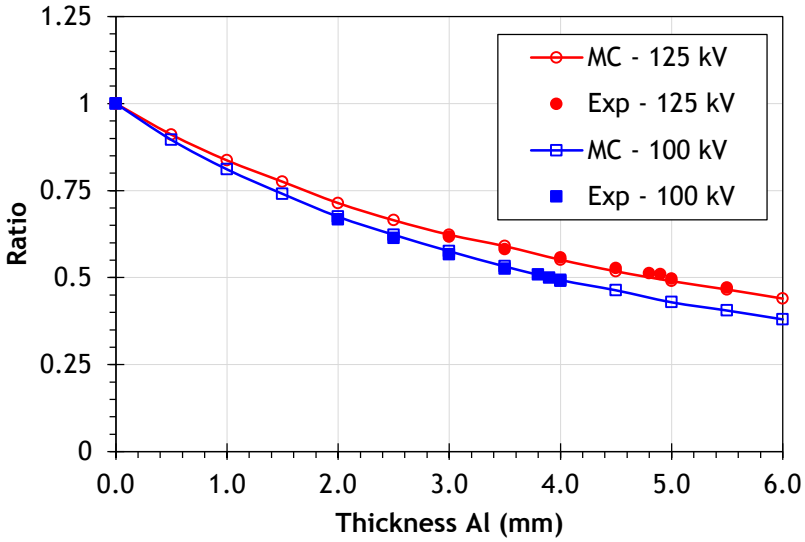

Figure 4.8: A comparison between the ratios of the dose in the air cavity with Al thicknesses (0.5 – 6.0) mm to the dose in the air cavity without a filter calculated with CAVRZnrc and those measured experimentally (Exp) at tube potentials 100 kV and 125 kV.

4.3.3.3 Comparison of Dose Profiles

Figure 4.9 shows the calibration curve for the Gafchromic film. The lateral, axial, and depth dose profiles obtained from the MC in terms of absorbed dose to the phantom showed good agreement with the experimental measurements as shown in Figures 4.10 - 4.11. The dose values for the profiles were normalized with respect to the central value, while those for the depth dose profiles were normalised to the dose at a depth of 1 cm. The lateral dose profiles (Figures 4.10 (a) - 4.11 (a)) were used to validate the geometrical design of the full and half bowtie filters, respectively. The lateral dose profiles of the MC for both settings matched to the

experimental measurements to within ±2.3%. Figures 4.10 (b) - 4.11 (b) show the comparison between the axial dose profiles for different beam widths. The MC and the experimental axial profiles agreed within 3 – 5%, on average, for both settings, but a larger variation was found at the tails of the narrower beam width (20 mm) profiles. Such variations are likely to be caused by the accuracy of blade collimation for narrower beam widths (Varian, 2010). The depth dose profiles for the energies 100 kV and 125 kV obtained from the MC model (Figures 4.10 (c) - 4.11 (c)) were within ±2.2% and ±2.9% of the experimental measurements, respectively.

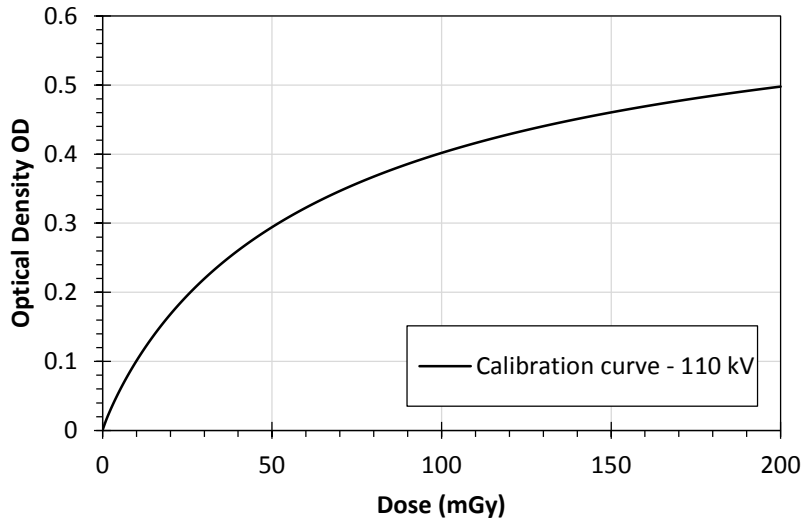

Figure 4.9: The calibration curve for the Gafchromic film used in this project calibrated at tube potential of 110 kV.

(a)

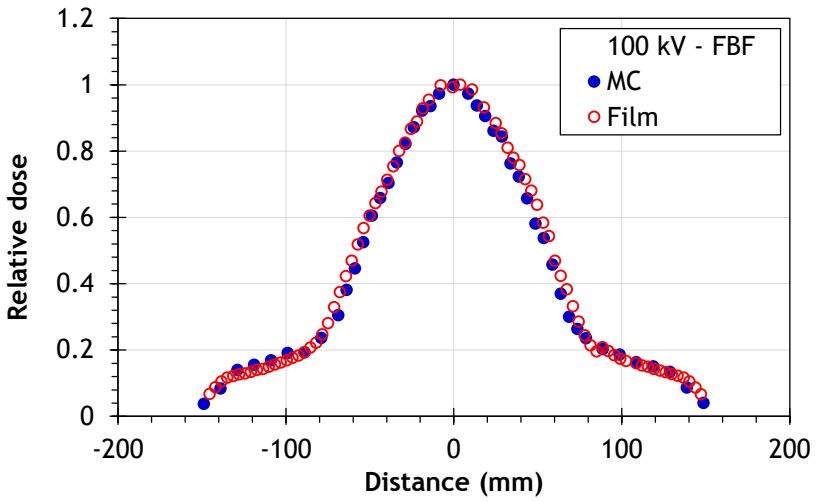

(b)

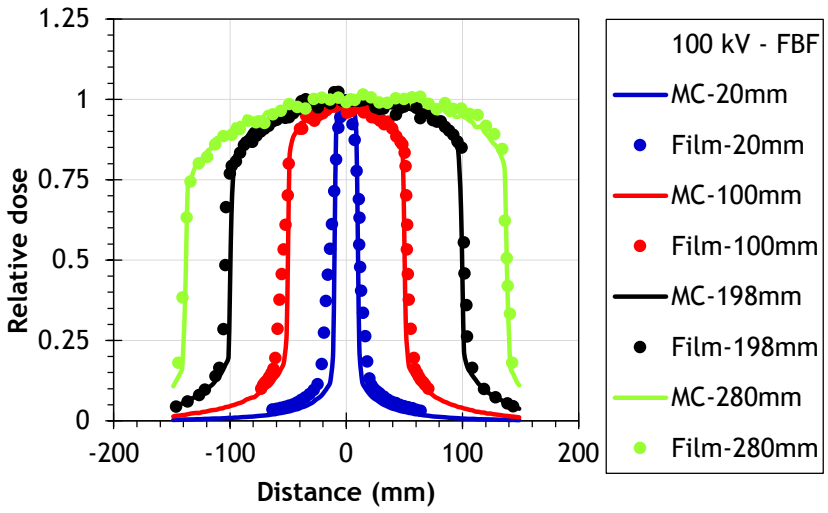

(c)

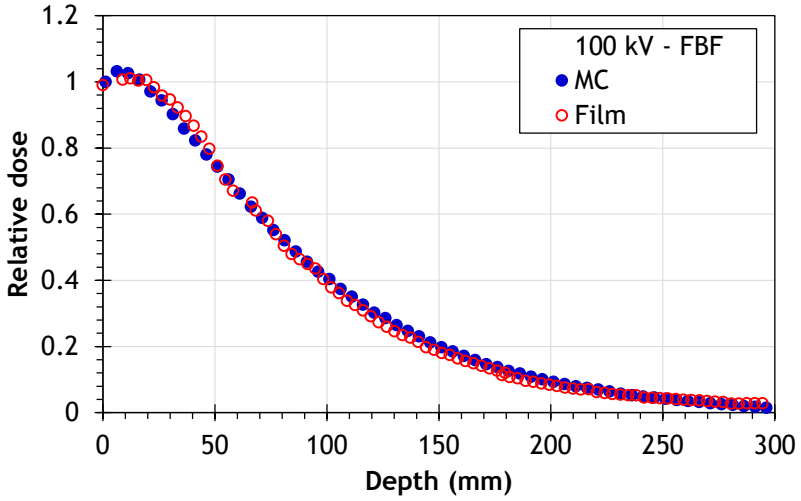

Figure 4.10: A comparison between dose profiles of the MC and the experimental measurements made within a solid water phantom with film using 100 kV and the full bowtie filter (FBF). (a) The lateral dose profiles, (b) the axial dose profiles for the beams of width 20, 100, 198, and 280 mm, and (c) the depth dose profiles.

(a)

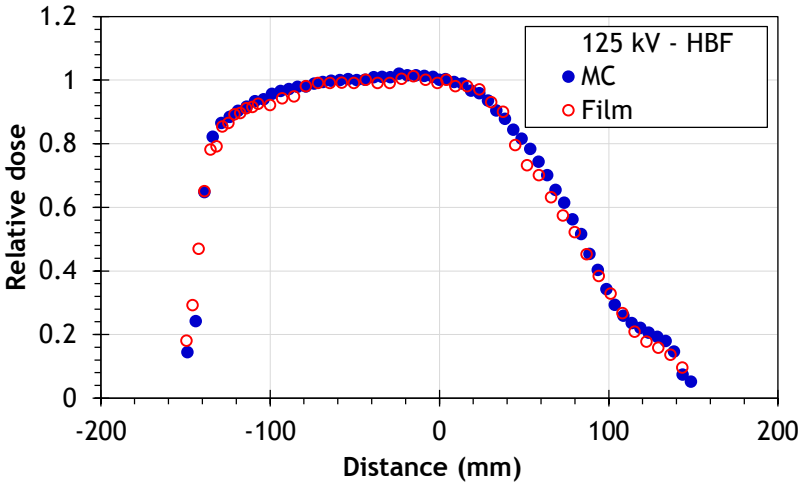

(b)

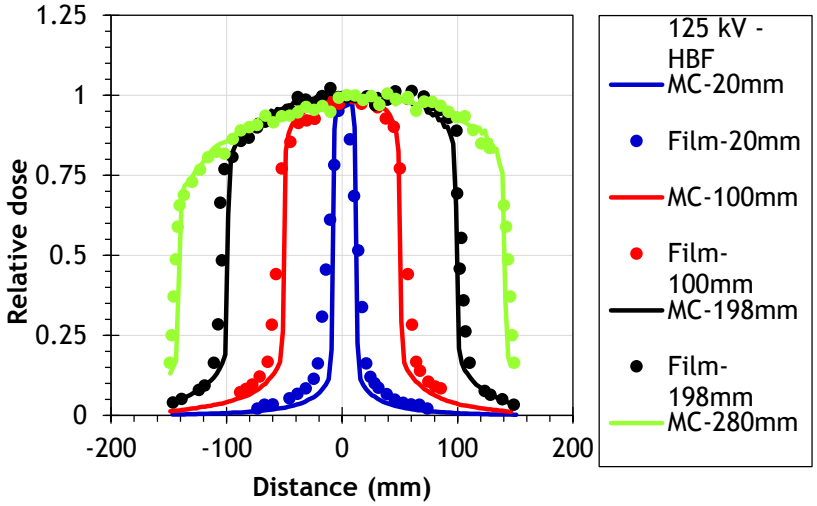

(c)

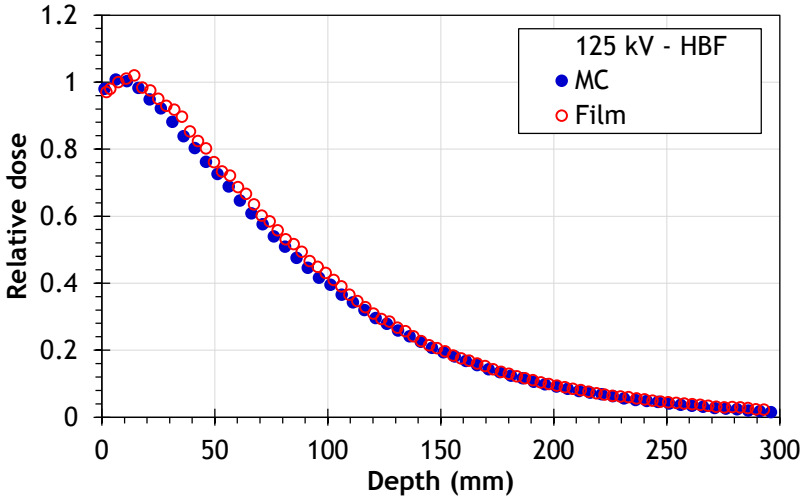

Figure 4.11: A comparison between dose profiles of the MC and the experimental measurements made within a solid water phantom with film using 125 kV and the half bowtie filter (HBF). (a) The lateral dose profiles, (b) the axial dose profiles for the beams of width 20, 100, 198, and 280 mm, and (c) the depth dose profiles.

4.4 Validation of Monte Carlo Dose Calculations

The previous section shows the measurements made to validate the geometrical and beam properties for the MC model. In this section, further validations for four dose measurements were performed. These measurements were made to ensure accuracy of the dose calculations reported by the MC for the quantities of interest. The four dose measurements (1) $CTDI_{100}$, (2) $f(0,150)$, and (3) dose distributions within the standard PMMA phantoms, and (4) $CTDI_{FIA}$ free in air were performed experimentally using pencil and small ionization chambers and Gafchromic film. Results of these measurements were subsequently compared to the MC results calculated under the same conditions and parameters. All the measurements performed experimentally and results calculated in the MC were obtained using the clinical beam width of 198 mm.

4.4.1 Experimental Measurements

4.4.1.1 Measurements of $CTDI_{100}$

Two scanning protocols (head and body) were used to measure $CTDI_{100}$ within the standard PMMA phantoms: (1) The head protocol called (Head-200): 100 kV, full bowtie filter, and 200° rotation, and (2) the body protocol called (Body-360): 125 kV, half bowtie filter, and 360° rotation. The measurements were carried out with a 100 mm pencil ionization chamber (Radcal, 20X6-3CT, US) with a calibration traceable to a standard dosimetry laboratory. The $CTDI_{100}$ values were measured at the middle of each phantom in the central and peripheral positions, with the phantoms placed at an SID of 100 cm. As measurement of $CTDI_{100}$ and $f_{100}(150)$ are obtained in a similar manner, the $CTDI_{100}$ validation was used to cover the validation required for $f_{100}(150)$.

4.4.1.2 Measurements of $CTDI_{FIA}$

The $CTDI_{FIA}$ measurements were made free in air using the same scanning protocols used for $CTDI_{100}$ measurements Head-200 and Body-360. Moreover, the $CTDI_{FIA}$ measurements were obtained using the same pencil chamber. The practical technique described in Chapter 2 section 2.6.5,

which requires stepping the chamber across the beam width in specific intervals, was employed. An integration of length 300 mm was required to cover the beam width 198 mm, thus the chamber was moved in three steps at the isocentre (IAEA, 2011). Additional experimental measurements for $CTDI_{FIA}$ were made at the peripheral positions free in air to validate the MC calculations. The 100 mm ionization chamber was set up at 15 cm away from the isocentre for the body protocol and at 7 cm for the head protocol. It should be noted that these measurements are not required for the QA procedure using the IEC method, but they have been performed for the purpose of the validation.

4.4.1.3 Measurements of $f(0,150)$

Fours scanning protocols were used for $f(0,150)$ measurements: (1) Head-200 and (2) Body-360, which are similar to those used for $CTDI_{100}$ measurements, additionally (3) Head-360: 100 kV, full bowtie filter, and 360° rotation, and (4) Body-200: 125 kV, full bowtie filter, and 200° rotation. Measurements for $f(0,150)$ were taken with a 0.6 cm^3 Farmer-type ionization chamber (10X5-0.6CT, Radcal Corporation, US) with a calibration traceable to a standard dosimetry laboratory within the standard PMMA phantoms set up at an SID of 100 cm. $f(0,150)$ measurements were made at the middle of each phantom on the central and four peripheral axes.

4.4.1.4 Measurements of Dose Distributions

The experimental measurements for dose distributions at the centre of the standard PMMA phantoms were obtained for all the four scanning protocols employed for $f(0,150)$ measurements. The phantoms were set up at an SID of 100 cm, and four film strips of size 1 × 15 cm^2 (i.e. a film strip for each scanning protocol) were inserted into the central hole of the phantom. In order to avoid an air gap resulting from removal of the central PMMA rod from the phantoms, a PMMA rod was cut in half along its length so that the film strips could be inserted in a PMMA sandwich during the measurements as shown in Figure 4.12. The resulting profiles were, then, compared against MC profiles derived within PMMA phantoms.

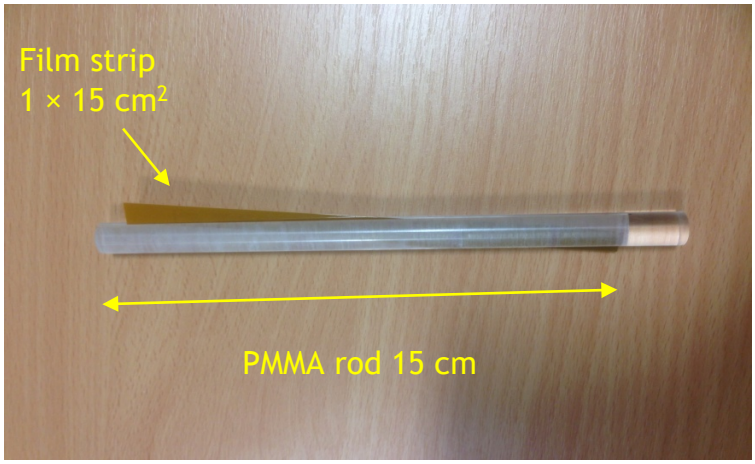

Figure 4.12: A PMMA rod 15 cm in length was used to measure dose distributions at the centre of the standard PMMA head and body phantoms using film strips of size 1 × 15 cm^2.

4.4.2 Monte Carlo Simulations

MC results for the four experiments were calculated in a manner similar to that used for validation of the MC modelling presented in section 4.3.2. PHSP files were generated from BEAMnrc using the same parameters given in section 4.3.2.1. All the experiments were calculated by DOSXYZnrc using the PHSP files. For all the simulations, the same ECUT and PCUT values used in BEAMnrc were also involved in DOSXYZnrc. Additionally, the HOWFARLESS transport algorithm and the PRESTA-I boundary crossing algorithm were used to enhance the efficiency of the dose calculation. The PHSP files were recorded at an SSD of 75 cm, which were run subsequently using ISOURCE = 8 (Phase-Space Source Incident from Multiple Directions) of DOSXYZnrc. The distance between the source, i.e. the PHSP files, and the isocentre was set to 25 cm as shown in Figure 4.13. The steps and parameters used in MC to calculate results of the four experiments were similar in all the simulations.

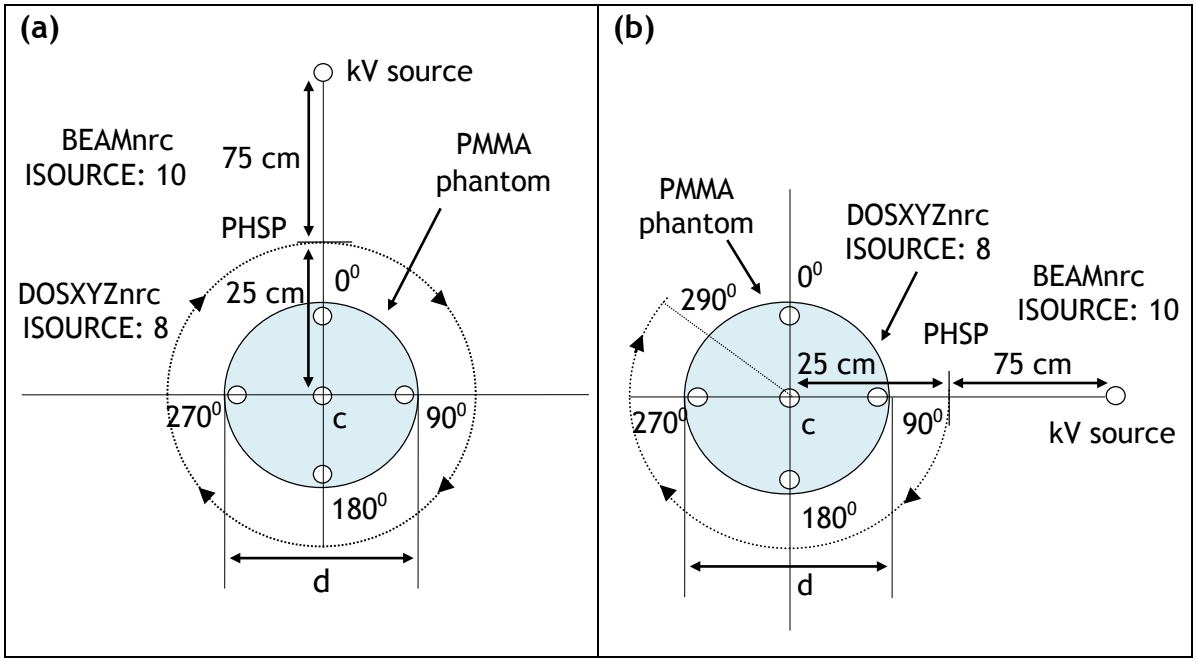

Figure 4.13: An illustration of the steps used to calculate the absorbed dose within the PMMA head and body phantoms using BEAMnrc and DOSXYZnrc. (a) Represents the steps employed to simulate scanning protocols with a 360° rotation and (b) 200° rotation.

4.4.2.1 Calculations of $CTDI_{100}$, $f(0,150)$, and Dose Distributions

1×10^9 histories were run in BEAMnrc for the four scanning protocols Head-200, Head-360, Body-200, and Body-360 using the same parameters employed for experimental measurements to generate PHSP files. This step was followed by designing two PMMA phantoms with a density of (ρ = 1.19 g/cm^3) in DOSXYZnrc to calculate $CTDI_{100}$ and $f(0,150)$ values, and to derive the dose distributions along the central axes of the phantoms. The phantoms were simulated using voxels of different sizes 0.5 × 0.5 × 0.5 cm^3 at the centre and periphery of the phantoms and larger voxels at the different sites. The use of this technique results in minimizing the time for the simulations carried out with a homogenous phantom by more than a factor of three without affecting the dose accuracy (Babcock et al., 2008). 2.4 - 3 × 10^8 histories with a photon splitting number set to 100 - 300 were run in DOSXYZnrc to obtain a statistical uncertainty of less than 2%.

4.4.2.2 Calculations of $CTDI_{FIA}$

Parameters used to calculate $CTDI_{FIA}$ values in DOSXYZnrc were similar to those used for dose calculations within the phantoms (section 4.4.2.1).

However, $CTDI_{FIA}$ values were calculated free in air by simulating a pencil chamber with a length of 300 mm instead of the phantoms shown in Figure 4.13. In addition to calculations at the isocentre, $CTDI_{FIA}$ values were also calculated at 15 cm away from the isocentre for the body protocol and at 7 cm for the head protocol in a manner similar to those obtained experimentally.

4.4.3 Results

4.4.3.1 Comparison of $CTDI_{100}$ and $CTDI_{FIA}$

Table 4.2 shows a comparison between $CTDI_{100}$ and $CTDI_{FIA}$ values measured experimentally using a beam of width 198 mm against those obtained from the MC. The results were normalised with respect to the $CTDI_{FIA}$ value at the isocentre for each protocol. The average variations between the MC and experimental values using the scanning protocols Body-360 and Head-200 were ±2.9% and ±5.8%, respectively.

Table 4.2: A comparison between the MC values and experimental measurements (Exp) for $CTDI_{100}$ and $CTDI_{FIA}$ for the scanning protocols Body-360 and Head-200 normalised with respect to the $CTDI_{FIA}$ at the isocentre. (p) indicates measurements at the periphery as shown in Figure 4.13.

	Body-360				Head-200			
	$CTDI_{FIA}$	$CTDI_{100}$	$CTDI_{FIA}$	$CTDI_{100}$	$CTDI_{FIA}$	$CTDI_{100}$	$CTDI_{FIA}$	$CTDI_{100}$
	Exp		MC		Exp		MC	
Centre	**1.00**	0.099	**1.00**	0.091	**1.00**	0.297	**1.00**	0.256
p 0°	0.307	0.143	0.316	0.142	0.608	0.113	0.589	0.117
p 90°	0.312	0.144	0.319	0.142	0.663	0.273	0.665	0.244
p 180°	0.296	0.141	0.315	0.142	0.616	0.433	0.615	0.384
p 270°	0.297	0.144	0.318	0.144	0.663	0.317	0.661	0.301
Avg. p	0.302	0.143	0.317	0.143	0.637	0.284	0.632	0.261
$CTDI_w$	0.535	0.129	0.545	0.125	0.758	0.292	0.755	0.258

The larger differences in the head protocol are thought to occur because the LINAC couch was not included in the simulations. This omission may have a greater impact on the results for the lower attenuation head phantom, and the differences between the experimental and MC results

will be enhanced by the lower tube potential (100 kV) employed for head scans.

4.4.3.2 Comparison of $f(0,150)$

Table 4.3 shows a comparison between $f(0,150)$ values measured experimentally and those obtained from the MC simulations. The values for the body protocols (Body-200 and Body-360) were normalized with respect to the central value of Body-200, and values for the head protocols were normalized with the respect to the central value of Head-200. The MC values for the body phantom were in good agreement with the experimental measurements, where the average differences for Body-200 and Body-360 were ±0.9% and ±0.8%, respectively. However, larger variations were also observed for the head protocols, for which the average differences were ±1.1% for Head-200 and ±4.1% for Head-360.

Table 4.3: A comparison between the MC results for $f(0,150)$ and experimental measurements (Exp) made within the standard PMMA phantoms using the scanning protocols Body-200, Body-360, Head-200, and Head-360, and a beam of width 198 mm. p indicates measurements at the periphery as shown in Figure 4.13.

	Body-200		Body-360		Head-200		Head-360	
	Exp	MC	Exp	MC	Exp	MC	Exp	MC
Centre	**1.00**	**1.00**	0.86	0.85	**1.00**	**1.00**	1.06	1.10
p 0°	0.10	0.10	1.20	1.22	0.38	0.34	0.99	1.01
p 90°	1.30	1.30	1.20	1.20	0.87	0.84	0.96	1.01
p 180°	2.38	2.43	1.19	1.22	1.36	1.41	0.95	0.99
p 270°	1.95	1.98	1.21	1.22	1.04	1.07	0.96	1.01
Avg. p	1.43	1.45	1.20	1.21	0.91	0.90	0.96	1.01
$f(0,150)_w$	1.29	1.30	1.09	1.10	0.94	0.94	0.99	1.03

4.4.3.3 Comparison of Dose Distributions

Figures 4.14 - 4.15 compare dose distributions derived from the MC model and experimental measurements performed at the centre of the standard PMMA phantoms set up at an SID of 100 cm. The dose values for all the profiles were normalized with respect to the central value at $(z = 0)$. The dose distributions obtained with Head-200 and Head-360 (Figure 4.14) were within ±1.7% and ±2.4% of the experimental profiles, respectively, while

Body-200 and Body-360 (Figure 4.15) were within ±2.1% and ±2.5%, respectively.

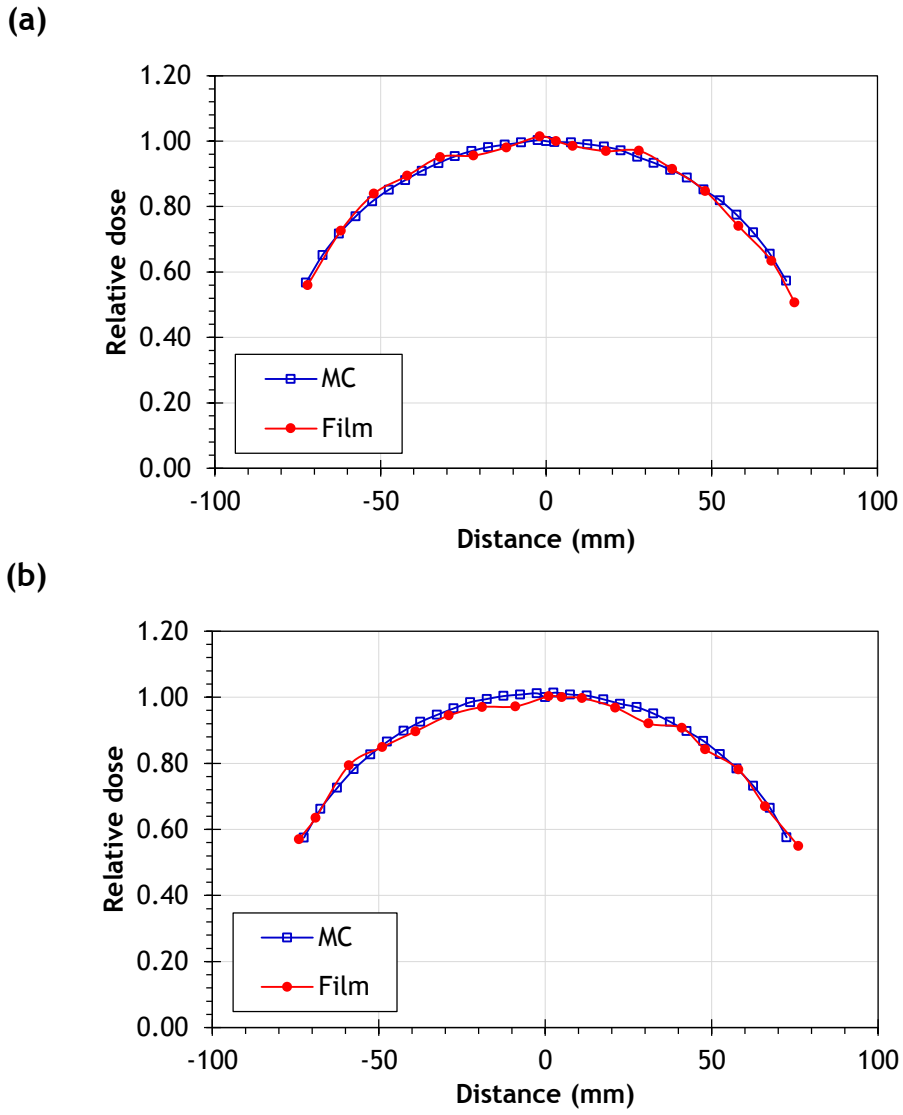

Figure 4.14: A comparison between dose distributions derived from MC simulations and those measured experimentally for the scanning protocols: (a) Head-200 and (b) Head-360.

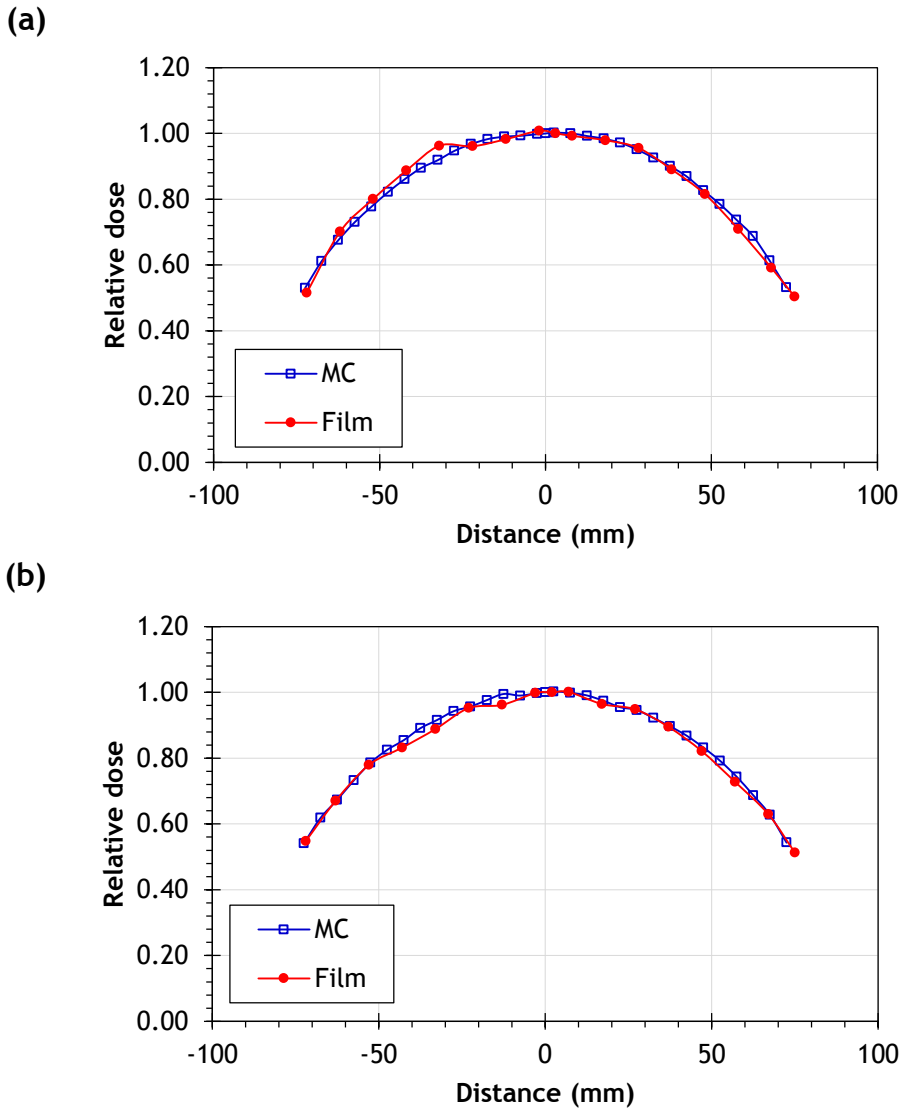

Figure 4.15: A comparison between dose distributions derived from MC simulations and those measured experimentally for the scanning protocols: (a) Body-200 and (b) Body-360.

4.5 Calibration of the Monte Carlo

The majority of the studies conducted in this project used relative dose values. However, absolute absorbed dose values were necessary for organ doses calculations. The MC user codes utilized in this project report dose values in (Gy/incident particle). Therefore in order to evaluate the absorbed dose for each organ and tissue in (Gy), the MC model developed in section 4.2 was calibrated to obtain a calibration factor (F_{MC}), which converts the MC output to (Gy). The calibration method followed in this project was described by (Qiu et al., 2012) as:

$$F_{MC} = \frac{D_{Exp}}{D_{MC} \times mAs} \quad (4.5)$$

where D_{MC} is absorbed dose calculated in MC, and D_{Exp}/mAs is absorbed dose measured experimentally in Gy per 1 mAs, thus F_{MC} is defined in (incident particle/mAs). D_{Exp} and D_{MC} are required to be determined using the same parameters and conditions.

4.5.1 Experimental Measurements

Experimental measurements for D_{Exp} were made in terms of absorbed dose to water based on the Institute of Physics and Engineering in Medicine (IPEM) code of practice (Klevenhagen et al., 1996, Aukett et al., 2005) as:

$$D_{w,z=2} = M\, N_k\, k_{ch} \left[\left(\frac{\overline{\mu_{en}}}{\rho}\right)_{w/air}\right]_{z=2,\varphi} \quad (4.6)$$

where $D_{w,z=2}$ is the absorbed dose to water at a depth of 2 cm, M is the chamber response in coulombs (C) corrected for air temperature and pressure, N_k is the air kerma calibration factor for the chamber employed in (Gy/C), k_{ch} is a correction factor which accounts for the difference between the chamber response in air and inside the water phantom, and $\left[\left(\frac{\overline{\mu_{en}}}{\rho}\right)_{w/air}\right]_{z=2,\varphi}$ is the mass energy absorption coefficient ratio water to air averaged over the photon spectrum at a depth of 2 cm within the water phantom using a field of diameter φ. D_{Exp} was measured at a depth of 2 cm within a 30 × 30 × 20 cm^3 solid water phantom (Gammex, Middleton, WI, US) set up at an SSD of 100 cm using a Farmer ionization chamber NE2611A calibrated at the National Physical Laboratory (NPL) in the UK for energies in the kV range. The measurements were performed with a stationary kV source using a field of size 10 × 10 cm^2 at an SSD of 100 cm. Two protocols were used (Head: 100 kV and full bowtie filter) and (Body: 125 kV and half bowtie filter). The measurements were repeated three times using 1000 mAs/reading for each protocol, and the average reading (M) was subsequently normalized with the respect to the mAs used for the measurements to obtain (C/mAs). N_k values were provided in the calibration certificate for the beam qualities specified in terms of half

value layer (HVL), whereas values for k_{ch} and the mass energy absorption coefficient ratio were obtained from the code of practice (Klevenhagen et al., 1996).

4.5.2 Monte Carlo Simulations

The same parameters and conditions, under which D_{Exp} values were measured, were used in the MC calculations to calculate D_{MC} values. First, the validated BEAMnrc model was used to run two simulations for the two protocols used for D_{Exp} with 1 × 10^9 histories using the same MC parameter given in section 4.3.2.1. Outputs of the simulations were recorded in PHSP files at an SSD of 100 cm. The resulting PHSP files were, then, employed as sources in DOSXYZnrc using ISOURCE = 2 of the code. The same solid water phantom was designed in DOSXYZnrc, and 3 × 10^8 histories with a photon splitting number set to 100 were run to calculate D_{MC} values at a depth of 2 cm with a statistical uncertainty of ≤ 0.2%. The HOWFARLESS transport algorithm and the default boundary crossing algorithm (PRESTA-I) were utilized

4.5.3 Results

Table 4.4 shows the values for the average D_{Exp} measured experimentally and D_{MC} calculated in MC under the same conditions for the head and body protocols. Once D_{Exp} and D_{MC} had been determined, values of F_{MC} were calculated for 1 mAs as in Eq.(4.5). Subsequently, F_{MC} was utilized to evaluate absolute absorbed dose for organ doses calculations in (Gy).

Table 4.4: Values for D_{MC} and the average D_{Exp} of three readings measured experimentally using 1000 mAs and a field size of 10 × 10 cm². The values were normalized with respect to 1 mAs, and F_{MC} is calculated as in Eq.(4.5).

Absorbed dose	Head	Body
$D_{MC}\ [Gy/incident\ particle]$	7.9680×10^{-21}	1.4921×10^{-20}
$D_{Exp}\ [Gy/mAs]$	7.9751×10^{-05}	1.5273×10^{-04}
$F_{MC}[incident\ particle/mAs]$	$1.0009\times10^{+16}$	1.0235×10^{16}

4.6 Conclusion

Specifications of the OBI system were obtained from the manufacturer Varian, which were subsequently used to model the system using BEAMnrc. A set of experiments were then used to validate the model. First, different experiments relating to x-ray spectra, HVL measurements, and lateral, axial, and depth dose profiles were used to validate the geometrical specifications and the beam properties of the model. Results of these experiments were found to be in good agreement with those obtained from the MC model. Second, results of different experimental measurements for the quantities of interest $CTDI_{100}$, $CTDI_{FIA}$, $f(0,150)$, and the dose distribution within the standard PMMA phantoms were compared with those from the MC model. The comparison again showed good agreement, which gave an indication of the validity of the model. The MC model was also calibrated to convert output of the MC from (Gy/incident particle) to (Gy) by using calibration factors F_{MC} for the head and body scanning protocols, which are used to calculate organ doses in Chapter 9.

Chapter 5

The Efficiency of $CTDI_{100}$ and $CTDI_{IEC}$

5.1 Introduction

The efficiency of the $CTDI_{100}$ is assessed as the ratio of the $CTDI_{100}$ measurement in a standard phantom to that recorded by an infinitely long chamber within an infinitely long PMMA phantom $CTDI_{\infty}$, which is close to the dose received by body tissues near the middle of a scan. The efficiency defined here should not be confused with the efficiency of the MC simulation discussed in Chapter 3 section 3.8. As mentioned previously, the efficiency of the $CTDI_{100}$ is approximately constant for beams of width ≤ 40 mm at ~75% and ~60% at the centre of the standard PMMA head and body phantoms, respectively, and at ~84% at the periphery of the phantoms. However, the values decrease with increasing beam width reaching ~25% of $CTDI_{\infty}$ for wide beams for both the phantoms. The efficiency is considered to be a good indicator for the ability of the $CTDI_{100}$ to estimate the actual tissue dose absorbed by the patient near the middle of a scan. This chapter presents an investigation conducted to evaluate the efficiency of the new IEC dosimetry arrangement described in Chapter 2 section 2.6.5 using the MC technique and compare it to the efficiency of the $CTDI_{100}$. The influence of the reference beam width on the efficiency calculation was also investigated. Results were analysed and compared with experimental measurements for three scanning protocols (head, thorax, and pelvis) frequently used in the clinic.

5.2 Materials and Methods

5.2.1 The Scanning Protocols

Four scanning protocols employed for validation of the MC dose calculations in Chapter 4 section 4.4 were used to investigate the efficiency of $CTDI_{100}$ and $CTDI_{IEC}$. The protocols were Head-200, Head-360, Body-200, and Body-360. Parameters of these protocols are listed in Table 5.1, which were

defined as they cover all scanning parameters used in the clinic. Head-200 and Head-360 are used for head scans, Body-200 covers the pelvic spot light scan, and Body-360 covers thorax and pelvic scans (Chapter 2 section 2.3).

Table 5.1: The scanning protocols employed in this study. Body-360 is used with 20 mA, 264 mAs for thorax scans and with 80 mA, 1056 mAs for pelvic scans.

	Head-200	Head-360	Body-200	Body-360
x-ray tube potential (kV)	100	100	125	125
x-ray current (mA)	20	20	80	20, 80
x-ray millisecond (ms)	20	20	25	20
Exposures (mAs)	147	264	733	264, 1056
Acquisition mode	Full-Fan	Full-Fan	Full-Fan	Half-Fan
Scan Arc Gantry rotation (degrees)[(a)]	200˚ 90˚-290˚	360˚ 0˚-360˚	200˚ 90˚-290˚	360˚ 0˚-360˚
Bowtie filter	Full	Full	Full	Half
No of Projections	367	660	367	660
Longitudinal extent of beam (mm)	20 -300			
Lateral collimator blade positions at the isocentre X1 and X2 (mm)	132, 132	132, 132	132 , 132	25, 239
Axial collimator blade positions at the isocentre Y1 and Y2 (mm)	(10 – 150), (10 – 150)			

(a) Left side-90°and right side-270°. The angles are shown in Figure 4.13 of Chapter 4.

5.2.2 Monte Carlo Calculations for the Efficiency:

The efficiency (ε) is evaluated as follows (Boone, 2007, Li et al., 2011):

$$\varepsilon = \frac{CTDI_{100}}{CTDI_{\infty}} \tag{5.1}$$

where $CTDI_{100}$ and $CTDI_{\infty}$ are defined in Chapter 2 section 2.4.

BEAMnrc and DOSXYZnrc codes were involved for the efficiency calculations. The efficiency of $CTDI_{100}$ was assessed at the centre (ε_c) and periphery (ε_p) of the phantom, and for $CTDI_w$ (ε_w)as follows:

$$\varepsilon_c(CTDI_{100}) = \frac{CTDI_{100,c}}{CTDI_{\infty,c}}$$

$$\varepsilon_p(CTDI_{100}) = \frac{CTDI_{100,p}}{CTDI_{\infty,p}} \quad (5.2)$$

$$\varepsilon_w(CTDI_{100}) = \frac{CTDI_w}{CTDI_{\infty,w}}$$

Similarly, the efficiency values for $CTDI_{IEC}$ were assessed as follows:

$$\varepsilon_c(CTDI_{IEC}) = \frac{CTDI_{IEC,c}}{CTDI_{\infty,c}}$$

$$\varepsilon_p(CTDI_{IEC}) = \frac{CTDI_{IEC,p}}{CTDI_{\infty,p}} \quad (5.3)$$

$$\varepsilon_w(CTDI_{IEC}) = \frac{CTDI_{IEC,w}}{CTDI_{\infty,w}}$$

The scanning protocols listed in Table 5.1 were used to generate PHSP files using BEAMnrc and then run in DOSXYZnrc as described in Chapter 4 section 4.4.2 to calculate values for $CTDI_{100}$, $CTDI_{IEC}$ and $CTDI_{\infty}$. Mori et al. (2005) and Kim et al. (2011) have shown that the PMMA head and body phantoms of length 600 and 900 mm, respectively, are sufficient to provide the full scatter condition, thus these lengths were designed in DOSXYZnrc and used to represent the infinite lengths for the head phantom as:

$$CTDI_{\infty}(head) = \frac{1}{W}\int_{-300}^{+300} D(z)dz \quad (5.4)$$

and

$$CTDI_{\infty}(body) = \frac{1}{W}\int_{-450}^{+450} D(z)dz \quad (5.5)$$

thus, three lengths of the phantoms were used 150, 600, and 900 mm, where 150 mm represented the standard length for the standard PMMA head and body phantoms, and the latter two were used for $CTDI_{\infty}$.

The beam widths (20 – 300) mm and (40 – 300) mm with an increment of 20 mm were applied to assess $\varepsilon(CTDI_{100})$ and $\varepsilon(CTDI_{IEC})$, respectively. A beam of width 20 mm was used as the reference beam width for evaluating $\varepsilon(CTDI_{IEC})$.

To indicate the influence of the reference beam width on $\varepsilon(CTDI_{IEC})$, the efficiency values were calculated using another reference beam of width 40 mm. The influence was estimated at the centre and periphery of the phantoms and for the weighted efficiency as the ratio of $\varepsilon(CTDI_{IEC})$ values calculated with 20 mm to those of 40 mm as follow:

$$Ratio = \frac{\varepsilon(CTDI_{IEC})_{20}}{\varepsilon(CTDI_{IEC})_{40}} \tag{5.6}$$

5.2.3 CTDI Measurements

$CTDI_{100}$ and $CTDI_{IEC}$ were assessed experimentally for three clinical scanning protocols (head, thorax, and pelvis). The clinical beam width 198 mm was used, and the protocol Head-200 was employed for the head scan, while Body-360 was used for the thorax and pelvic scans. Values for $CTDI_{\infty}$ for these protocols were estimated by the application of correction factors derived from the MC calculations.

5.3 Results and Discussion

5.3.1 Efficiency $CTDI_{100}$ and $CTDI_{IEC}$ Calculations

Figures 5.1 - 5.2 show the efficiency values for the scanning protocols used in this study (Table 5.1). $\varepsilon(CTDI_{100})$ values for all protocols were approximately stable for the beam widths (20 – 40) mm. For Head-200 (Figure 5.1 (a)), values of $\varepsilon_c(CTDI_{100})$, $\varepsilon_p(CTDI_{100})$, and $\varepsilon_w(CTDI_{100})$ for the beam widths (20 – 40) mm were 74.7 ± 0.6%, 84.6 ± 0.3%, and 80.9 ± 0.4%, respectively, whereas for Head-360 (Figure 5.1 (b)) the values were 74.3 ± 0.5%, 84.5 ± 0.3%, and 80.7 ± 0.4%, respectively. The efficiency values for the same beam widths for Body-200 (Figure 5.2 (a)) were 58.5 ± 0.3%, 82.1

± 0.1%, and 74.7 ± 0.2%, and for Body-360 (Figure 5.2 (b)) the values were 59.7 ± 0.3%, 82.1 ± 0.3%, and 74.9 ± 0.3%, respectively. When the beam width increased beyond 40 mm, the efficiency of all protocols fell steadily reaching values between ~30% and ~40% at a beam width of 300 mm.

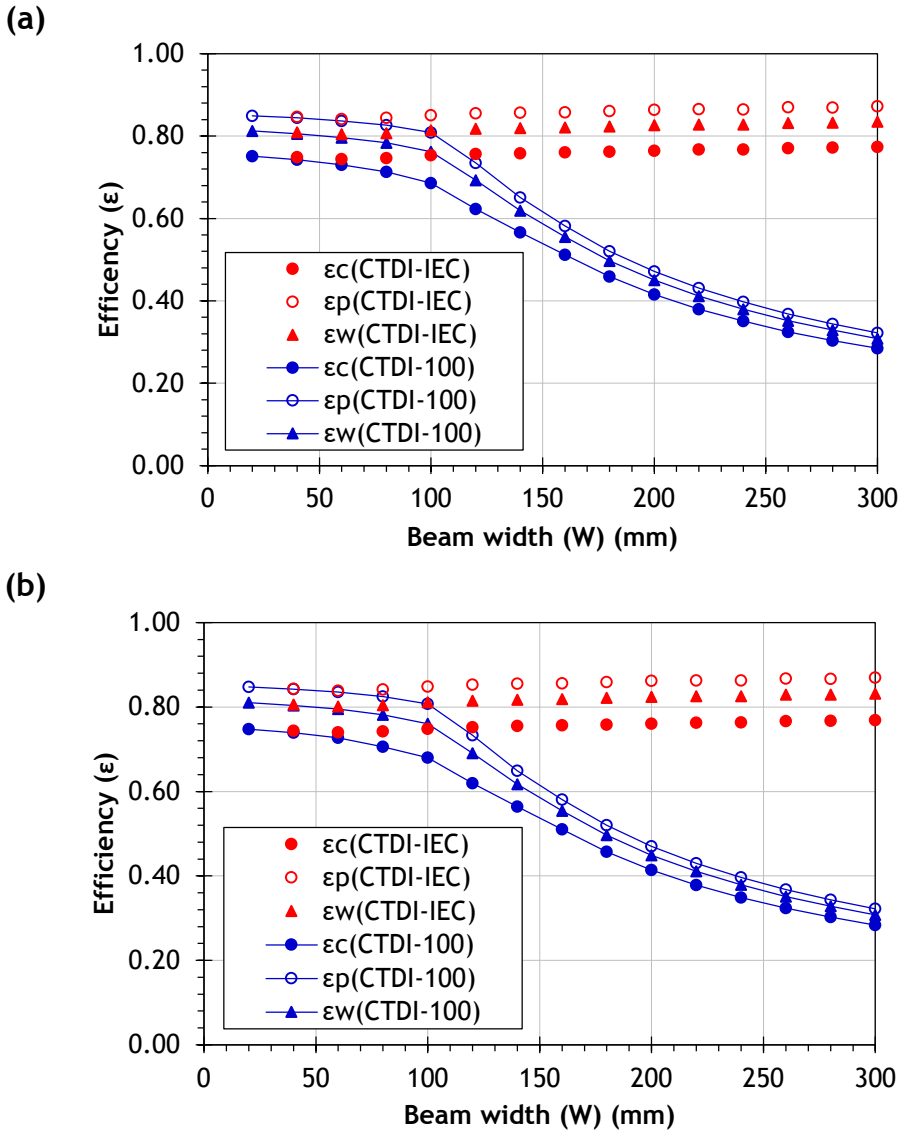

Figure 5.1: The efficiency values for $CTDI_{100}$ and $CTDI_{IEC}$ calculated with MC using (a) Head-200 and (b) Head-360. Beam widths 20 – 300 mm were used for $CTDI_{100}$, while 40 – 300 mm were used for $CTDI_{IEC}$. The reference beam width was 20 mm.

However, $\varepsilon(CTDI_{IEC})$ values for all the scanning protocols were within ±1.0% over all the beam widths (Table 5.2). The beam width was found to play a minimal role in determining the efficiency values for the IEC approach (Figures 5.1 - 5.2). Differences between the efficiency values calculated with a 200˚scan (Figure 5.1 (a)) and a 360˚scan (Figure 5.1 (b)), and full-fan with the full bowtie filter (Figure 5.2 (a)) and half-fan with the half

bowtie filter (Figure 5.2 (b)) were within 1%. Therefore, $\varepsilon(CTDI_{IEC})$ values were not affected by the type of scan or the bowtie filter significantly. Table 5.2 gives $\varepsilon(CTDI_{IEC})$ values calculated with reference beams of width 20 and 40 mm. Differences were within ±1% for head scanning protocols, and ±0.7% for body protocols.

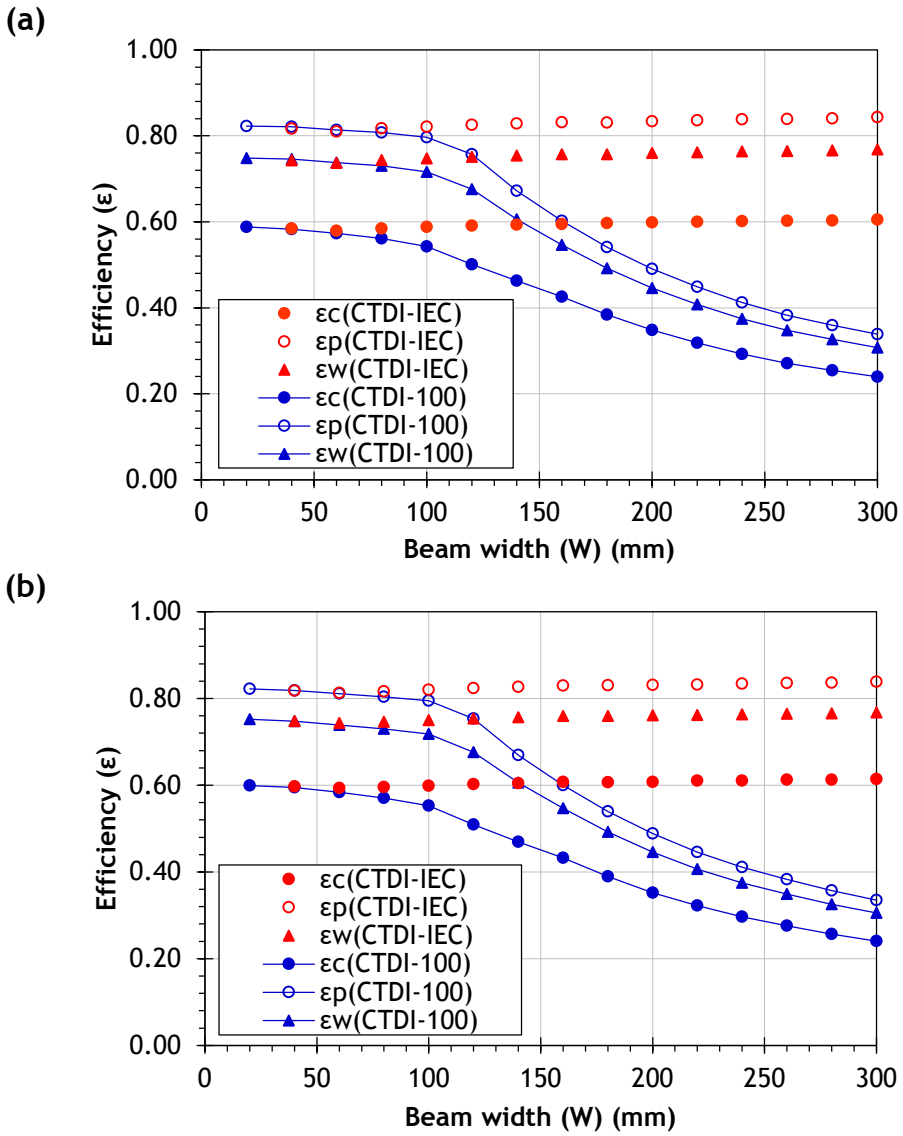

Figure 5.2: The efficiency values for $CTDI_{100}$ and $CTDI_{IEC}$ calculated with MC using (a) Body-200 and (b) Body-360. Beam widths 20 – 300 mm were used for $CTDI_{100}$, while 40 – 300 mm were used for $CTDI_{IEC}$. The reference beam width was 20 mm.

Table 5.2: The percentage $\varepsilon(CTDI_{IEC})$ values at centre and periphery of the head and body phantoms, and for the weighted efficiency using the four scanning protocols and reference beams of width 20 and 40 mm.

	Head-200 (%)	Head-360 (%)	Body-200 (%)	Body-360 (%)
$\varepsilon_c(CTDI_{IEC})_{20}$	76.1 ± 0.9	75.7 ± 0.9	59.5 ± 0.8	60.6 ± 0.7
$\varepsilon_p(CTDI_{IEC})_{20}$	85.9 ± 1.0	85.7 ± 1.0	83.1 ± 1.0	82.8 ± 0.8
$\varepsilon_w(CTDI_{IEC})_{20}$	82.2 ± 0.9	81.9 ± 1.0	75.6 ± 0.9	75.8 ± 0.7
$\varepsilon_c(CTDI_{IEC})_{40}$	75.5 ± 0.9	75.2 ± 0.9	59.4 ± 0.8	60.3 ± 0.6
$\varepsilon_p(CTDI_{IEC})_{40}$	85.7 ± 1.0	85.6 ± 1.0	83.5 ± 1.0	82.9 ± 0.8
$\varepsilon_w(CTDI_{IEC})_{40}$	81.8 ± 0.9	81.7 ± 0.9	75.9 ± 0.9	75.8 ± 0.7

5.3.2 $CTDI_{100}$ and $CTDI_{IEC}$ Measurements

The experimental values for $CTDI_{100}$ were, as expected, lower than those of $CTDI_{IEC}$ for all protocols (Table 5.3), and agreed with the MC findings (Figures 5.1 - 5.2). $CTDI_{\infty}$ values for the protocols in Table 5.3 were estimated by application of correction factors (C_f) derived from $\varepsilon(CTDI_{IEC})_{20}$ values (Table 5.2). Moreover, these correction factors were used to estimate the efficiency of $CTDI_{100}$ values measured experimentally (Table 5.3) using Eq.(5.2). $\varepsilon_c(CTDI_{100})$, $\varepsilon_p(CTDI_{100})$ and $\varepsilon_w(CTDI_{100})$ for the head scan were 42.9%, 48.8%, and 46.6%, respectively. These values agreed to within ±1.7% with the values derived from MC calculations of 41.5%, 47.1%, and 45.1%, respectively, using Head-200 (Figure 5.1 (a)). Similarly, the thorax and pelvic scans were within ±0.9% of the MC calculations, where $\varepsilon_c(CTDI_{100})$, $\varepsilon_p(CTDI_{100})$ and $\varepsilon_w(CTDI_{100})$ were 36.0%, 48.4%, and 44.6%, respectively, for the thorax scan, and 35.8%, 48.0% and 44.6%, respectively, for the pelvic scan, and the MC calculations were 35.2%, 48.9%, and 44.5%, respectively, using Body-360 (Figure 5.2 (b)).

Table 5.3: Experimental measurements for $CTDI_{100}$ and $CTDI_{IEC}$ for the head, thorax, and pelvic scans using a beam of width 198 mm. The scanning protocol Head-200 with (20 mA, 147 mAs) was used for head scan, whereas Body-360 with (20 mA, 264 mAs) and (80 mA, 1056 mAs) was used for thorax and pelvic scans, respectively. The correction factors (C_f) within parentheses can be used to derive $(CTDI_\infty = C_f \times CTDI_{IEC})$.

	$CTDI_{100}$	$CTDI_{IEC}$	$CTDI_\infty$
		Head (mGy)	
Centre	1.72	3.06 (1.31)	4.01
Average periphery	1.62	2.84 (1.17)	3.32
$CTDI_w$	1.66	2.92 (1.22)	3.56
		Thorax (mGy)	
Centre	1.73	2.95 (1.63)	4.81
Average periphery	2.47	4.24 (1.20)	5.1
$CTDI_w$	2.21	3.81 (1.30)	4.95
		Pelvis (mGy)	
Centre	6.87	11.79 (1.63)	19.21
Average periphery	9.80	16.97 (1.20)	20.40
$CTDI_w$	8.84	15.25 (1.30)	19.82

5.3.3 The Use of $CTDI_{100}$ and $CTDI_{IEC}$ for CBCT Dosimetry

The efficiency of the $CTID_{100}$ in providing a measure that collects all the radiation to which a patient is exposed has become a more important issue since the introduction of advanced CT scanners using wider beams and CBCT. The efficiency of the $CTID_{100}$ has been studied extensively using a variety of techniques, beam widths and CT scanners (Table 5.4). The MC results from the present study are in good agreement with other studies, and show that $CTID_{100,w}$ underestimates the $CTID_{\infty,w}$ by ~ 18% and ~24% for the head and body phantoms, respectively, using narrow beam widths ≤ 40 mm. This underestimation increases for wider beams, where the primary beam extends beyond the length of the chamber and phantoms (Figures 5.1 - 5.2). The variation of $\varepsilon(CTDI_{100})$ with beam width found in the present study is similar to that reported for a CT scanner (Boone, 2007) and a C-arm interventional CBCT scanner (Kyriakou et al., 2008).

The IEC approach ($CTDI_{IEC}$) addresses the dependency of the efficiency on beam width successfully, with $\varepsilon(CTDI_{IEC})$ values being essentially

independent of beam width. Moreover, $\varepsilon(CTDI_{IEC})$ values for the beam widths 40 – 300 mm were nearly identical to $\varepsilon(CTDI_{100})$ values for narrow beam widths (Figures 5.1 - 5.2, and Tables 5.2 and 5.4). Thus, the $CTDI_{IEC}$ successfully extends the application of the $CTID_{100}$ approach to CBCT scans and provides a practical solution for the use of $CTID_{100}$ dosimetry equipment that are widely available in medical imaging and therapy departments for CBCT dosimetry.

The IAEA has recommended using a reference beam with a width of about 20 mm (IAEA, 2011). Results from this study have shown that the difference between using 20 and 40 mm as the reference beam was not significant (Table 5.2). However, the use of a 40 mm beam rather than 20 mm one is recommended for CBCT scanners as these systems are manufactured for use with wide beams and use of a narrower beam width may lead to uncertainty due to the accuracy of blade collimation at narrow beams (Varian, 2010).

Although maintaining the $CTDI_{100}$ concept and equipment, the $CTDI_{IEC}$ approach does not include all the radiation contributing to the patient exposure. This is inevitable with this approach unless a much longer phantom is used, which is less practical for routine measurement because of the requirement to handle the larger weight. Moreover, using a standard 100 mm ionization chamber requires the acquisition of a relatively large number of scans (nine for 198 mm) to measure $CTDI_{IEC,w}$ for one protocol using the practical technique described earlier. Moving the 100 mm ionization chamber using the practical technique over two or three positions increases the uncertainty of the measurements, which with three steps for a beam of width 160 mm was found to be 2% (Platten et al., 2013). Therefore, use of a longer ionization chamber should be considered to minimize the number of scans and to reduce the uncertainty, and these are now becoming more readily available.

Table 5.4: Comparisons between $\varepsilon(CTDI_{100})$ values in the present study obtained from the MC simulations and those from studies conducted with different techniques, beam widths, and CT scanners.

Investigator	Beam width (mm)	Phantom	X-ray voltage (kV)	Scanner	Technique	$\varepsilon_c(CTDI_{100})$	$\varepsilon_p(CTDI_{100})$	$\varepsilon_w(CTDI_{100})$
(Li et al., 2011)	18	Head	100	Siemens SOMATOM	MC	0.76	0.87	0.83
This study	20	Head	100	OBI	MC	0.75	0.85	0.81
(Li et al., 2011)	40	Head	100	Siemens SOMATOM	MC	0.76	0.87	0.83
(Ruan et al., 2010)	40	Head	100	GE LS VCT	OSL	0.73	0.86	
This study	40	Head	100	OBI	MC	0.74	0.84	0.80
(Li et al., 2011)	18	Body	120	Siemens SOMATOM	MC	0.55	0.84	0.74
(Perisinakis et al., 2007)	18	Body	120	Siemens 16	TLD	0.63	0.78	
(Martin et al., 2011)	20	Body	120	GE Lightspeed 16	Gaf. film	0.57	0.83	
(Martin et al., 2011)	20	Body	120	GE Lightspeed 16	Gaf. film	0.55	0.81	
(Martin et al., 2011)	20	Body	120	GE Lightspeed 16	20 mm IC	0.60	0.85	
(Ruan et al., 2010)	20	Body	120	GE LS VCT	OSL	0.58	0.83	
(Boone, 2007)	20	Body	120	GE LS	MC	0.63	0.88	

(Dixon and Ballard, 2007)	20	Body	120	GE LS-16	Farmer	0.61	0.86	
(Dixon and Ballard, 2007)	20	Body	120	GE VCT-64	Farmer	0.61	0.83	
(Mori et al., 2005)	20	Body	120	Prototype 256	Photodiode			0.76
This study	20	Body	125	OBI	MC	0.59	0.82	0.75
(Mori et al., 2005)	42	Body	120	Prototype 256	Photodiode			0.74
(Martin et al., 2011)	40	Body	120	Philips Brilliance	Gaf. film	0.58	0.82	
(Li et al., 2011)	40	Body	120	Siemens SOMATOM	MC	0.55	0.83	0.74
(Ruan et al., 2010)	40	Body	120	GE LS VCT	OSL	0.56	0.81	
(Dixon and Ballard, 2007)	40	Body	120	GE VCT-64	Farmer	0.61	0.81	
(Boone, 2007)	40	Body	120	GE LS	MC	0.62	0.87	
This study	40	Body	125	OBI	MC	0.59	0.82	0.74
(Mori et al., 2005)	138	Body	120	Prototype 256	Photodiode			0.60
This study	140	Body	125	OBI				0.61
(Geleijns et al., 2009)	160	Body	120	Aquilion ONE	MC			0.59
This study	160	Body	125	OBI	MC			0.56

MC: Monte Carlo, OSL: Optically Stimulated Luminescence, TLD: Thermoluminescent Dosimeter, Gaf. film: Gafchromic film, 20 mm IC: A Farmer type ionization chamber with an active length of 20 mm.

In addition to the underestimation associated with the IEC approach, the number of measurements required to complete a quality assurance (QA) procedure (i.e. extra time and effort) and the expected uncertainty, which may arise from the accuracy of blade collimation at a narrower beam and moving the ionization chamber over several steps, may limit the acceptability of this method.

Our results together with other studies (Mori et al., 2005, Boone, 2007) (Kyriakou et al., 2008, Geleijns et al., 2009) show that the $CTDI_{100}$ underestimates $CTDI_{\infty}$ significantly. For the clinical beam width 198 mm used in this study, $CTDI_{100,w}$ underestimates $CTDI_{\infty,w}$ by ~55% for head and by ~56% for body (Figures 5.1 - 5.2). Therefore, the continued use of the standard $CTDI_{100}$ concept for CBCT scans does not provide a good reflection of the relative doses involved in the CBCT imaging procedures, as only half of the scan dose received by a patient is measured. The efficiency, maintaining the use of the $CTDI_{100}$ equipment, and the simplicity (i.e. more practical for regular use in the medical environment) may be the more important aspects for the majority of medical physicists. Moreover, the technique is used to give a measure that can be related to patient doses, rather than being used as an absolute measurement of patient dose. The IEC approach provides a practical solution for the CBCT dosimetry that overcomes some of the $CTDI_{100}$ limitations for CBCT. The efficiency of the $CTDI_{IEC,w}$ is only ~82% for head and ~76% for body, but since $CTDI_{IEC}$ is independent of beam width (Figures 5.1 - 5.2), this could be addressed by use of appropriate correction factors.

5.4 Conclusion

The MC BEAMnrc and DOSXYZnrc codes have been used to evaluate the efficiency of the $CTDI_{100}$ and $CTDI_{IEC}$ for the OBI imaging system on a TrueBeam linear accelerator for different scanning protocols and beam widths. The IEC approach successfully extends the application of the $CTDI_{100}$ to CBCT scans and provides a practical solution using existing $CTDI_{100}$ dosimetry equipment. The simulations demonstrate that the efficiency $\varepsilon_w(CTDI_{IEC})$ is essentially independent of beam width, with values of ~82% for head and ~76% for body, approximately equal to those for $\varepsilon_w(CTDI_{100})$

at narrower beam widths. Differences in values for $CTDI_{IEC}$ derived using beams with widths 20 mm and 40 mm as the reference were only ±1%. Therefore the use of a 40 mm reference beam is recommended to reduce the uncertainty associated with the accuracy of blade collimation.

$CTDI_{IEC,w}$ has the same disadvantage as the $CTDI_{100,w}$ in that $CTDI_{\infty,w}$ is underestimated by ~18% for head scans and ~24% for body scans, but unlike the $CTDI_{100,w}$, the underestimation is independent of beam width. If use of the CTDI approach, which is well established for multi-slice CT, is considered to be the best way forward for CBCT dosimetry, then use of the $CTDI_{IEC}$ method with correction factors applied to overcome the underestimation of $CTDI_{\infty}$ would be appropriate. The results of this study have been published in (Abuhaimed et al., 2014).

Chapter 6

The Efficiency of Cumulative Dose Indices

6.1 Introduction

The previous chapter presents the study that investigated the efficiency of $CTDI_{100}$ and $CTDI_{IEC}$. This chapter describes an investigation into four approaches based on the alternative concept for CBCT dosimetry proposed by AAPM and other studies as discussed in Chapter 2 section 2.6, namely the cumulative dose, using different scanning protocols and a range of beam widths. Monte Carlo simulations were used to study the four approaches: the cumulative dose (1) $f(0,150)$ (section 2.6.2) and (2) $f(0,\infty)$ (section 2.6.4) with a small ionization chamber 20 mm long, and the cumulative dose (3) $f_{100}(150)$ (section 2.6.3) and (4) $f_{100}(\infty)$ (defined in this study) with a standard 100 mm pencil ionization chamber. The $f(0,150)$ and $f_{100}(150)$ were studied within the standard PMMA phantoms, while $f(0,\infty)$ and $f_{100}(\infty)$ were within infinitely long head and body phantoms. In addition, the influence of using the 20 mm and 100 chambers on the cumulative dose measurements was investigated. Contributions to the cumulative dose measurements resulting from the primary beam and scattered radiation created under a scatter equilibrium condition were investigated. The imaging doses involved in CBCT scans for head and body scanning protocols were evaluated experimentally using the three approaches $f(0,150)$, $f_{100}(150)$, and $f(0,\infty)$, and the results were compared with those from other methodologies ($CTDI_{100}$ and $CTDI_{IEC}$) investigated in the previous chapter.

6.2 Materials and Methods

6.2.1 The Scanning Protocols

The scanning protocols presented in Chapter 5 and listed in Table 5.1, namely Head-200, Head-360, Body-200, and Body-360, which were used to calculate the efficiency of $CTDI_{100}$ and $CTDI_{IEC}$, were employed. The only

difference was in the beam width involved. In the previous chapter, the beam width (W) used in the study ranged from 20 mm to 300 mm for $CTDI_{100}$, whereas W in this study ranged from 40 – 300 mm with an increment of 20 mm for the all dose indices.

6.2.2 Monte Carlo Calculation for the Efficiency

$f_{100}(\infty)$ defined in this study was identical to $f_{100}(150)$, which is defined as:

$$f_{100}(150) = \frac{1}{100}\int_{-50mm}^{+50mm} D(z)\,dz \tag{6.1}$$

The only difference between these dose indices is in the length of the phantom involved. $f_{100}(150)$ is measured within the standard PMMA phantoms, whereas $f_{100}(\infty)$ is within infinitely long phantoms.

The efficiency values for the four dose indices were calculated using BEAMnrc and DOSXYZnrc in a manner similar to that used for $\varepsilon(CTDI_{100})$ and $\varepsilon(CTDI_{IEC})$. The efficiency values were calculated at the centre and periphery of the phantom and for the weighted value as:

$$\varepsilon_c(f(0,150)) = \frac{f(0,150)_c}{CTDI_{\infty,c}}$$

$$\varepsilon_p(f(0,150)) = \frac{f(0,150)_p}{CTDI_{\infty,p}} \tag{6.2}$$

$$\varepsilon_w(f(0,150)) = \frac{f(0,150)_w}{CTDI_{\infty,w}}$$

Similarly, $(f_{100}(150))$, $\varepsilon(f(0,\infty))$, and $\varepsilon\big(f_{100}(\infty)\big)$ were calculated in a similar manner. PMMA head and body phantoms with lengths similar to those used for the $\varepsilon(CTDI_{100})$ and $\varepsilon(CTDI_{IEC})$ study were used, and these are listed in Table 6.1.

The scanning protocols listed in Chapter 5 Table 5.1 were used to generate PHSP files using BEAMnrc. The PHSP files were, then, run in DOSXYZnrc as described in Chapter 4 section 4.4.2 to calculate values for $f(0,150)$,

$f_{100}(150)$, $f(0,\infty)$, $f_{100}(\infty)$, and $CTDI_{\infty}$. Figure 6.1 shows the configurations used to assess the five dose indices.

Table 6.1: The head and body PMMA phantoms used in this study.

Phantom	Diameter (d) (mm)	Length (mm)	Used for
Standard head	160	150	$f(0,150)$, $f_{100}(150)$
Standard body	320	150	$f(0,150)$, $f_{100}(150)$
Infinitely long head	160	600	$f(0,\infty)$, $f_{100}(\infty)$, $CTDI_{\infty}$
Infinitely long body	320	900	$f(0,\infty)$, $f_{100}(\infty)$, $CTDI_{\infty}$

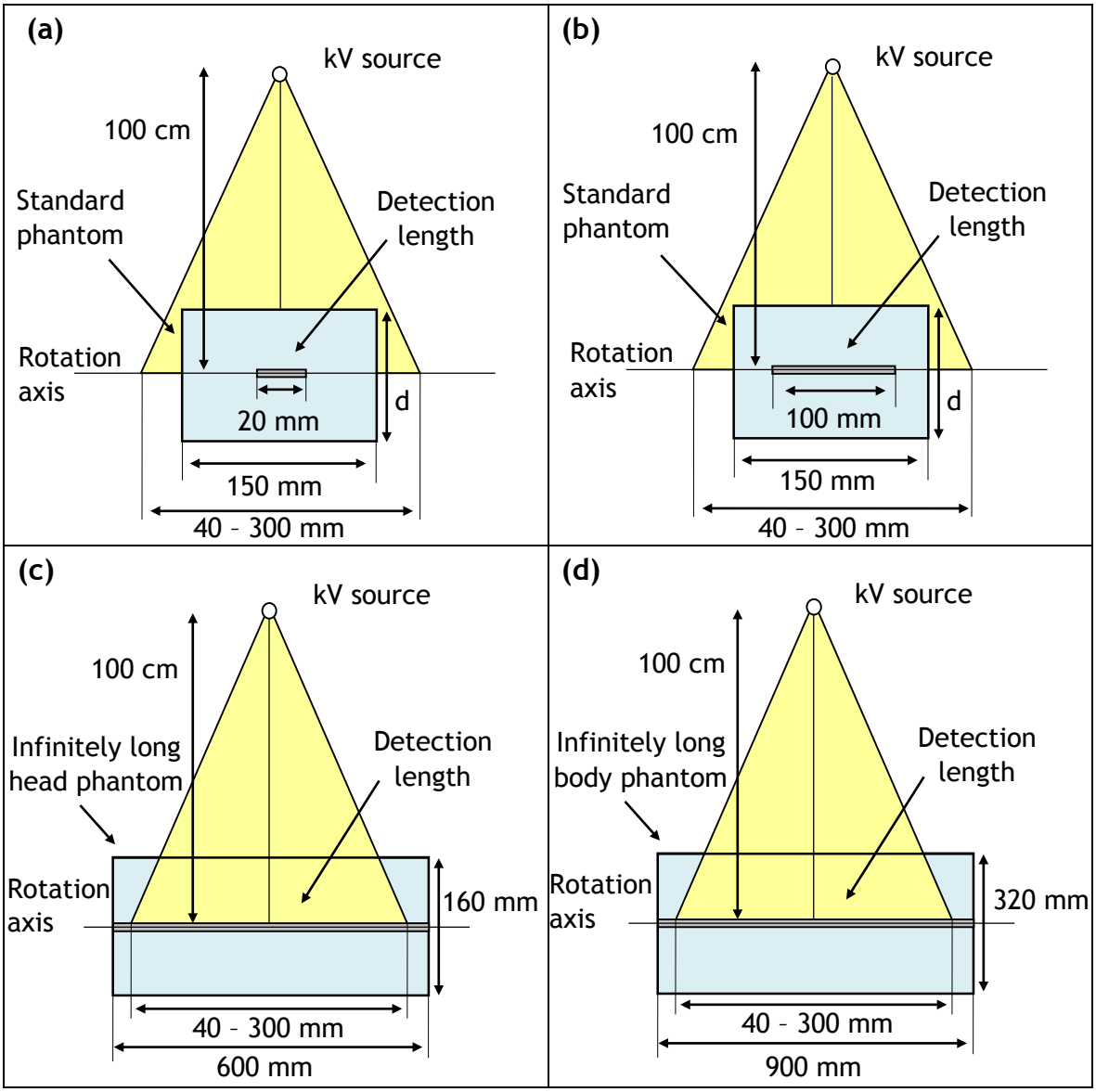

Figure 6.1: Diagrammatic representations of the configurations used to assess (a) $f(0,150)$, (b) $f_{100}(150)$, for both head and body PMMA phantoms, (c) $CTDI_{\infty}$ within the infinitely long head PMMA phantom, and (d) $CTDI_{\infty}$ within the infinitely long body PMMA phantom. The phantoms shown in (c) and (d) were also used for $f(0,\infty)$ and $f_{100}(\infty)$, but with detection lengths similar to those in (a) and (b).

6.2.3 Experimental Measurements for Dose Indices

Experimental measurements of $f(0,150)$, $f_{100}(150)$, and $f(0,\infty)$ for the CBCT scans for head and body scanning protocols used in the clinic were performed. The measurements were carried out with the clinical beam width of 198 mm. Head-200 protocol in Table 5.1 was used for the head scan, and Body-360 was employed for the body scan. $f(0,150)$ measurements were obtained as described in Chapter 4 section 4.4.1.3 , and $f_{100}(150)$ were measured in the same manner as that used for $f(0,150)$, but with the standard 100 mm pencil ionization chamber employed in Chapter 4 section 4.4.1.1. $f(0,\infty)$ measurements were obtained within head and body phantoms of length 450 mm. This length is considered sufficiently long to provide a full scatter condition for a beam width of 198 mm (AAPM, 2010). Three standard PMMA phantoms were combined together by attaching the ends to form one long phantom as shown in Figure 6.2. The phantoms were set up at an SID of 100 cm and the 0.6 cm^3 Farmer-type ionization chamber (10X5-0.6CT, Radcal Corporation, US) was placed at the middle of the central axis and the four peripheral axes to measure $f(0,\infty)$. The experimental measurements of $f(0,150)$, $f_{100}(150)$, and $f(0,\infty)$ were, then, compared with values derived from Monte Carlo simulation and with different dosimetry approaches $CTDI_{100}$ and $CTDI_{IEC}$.

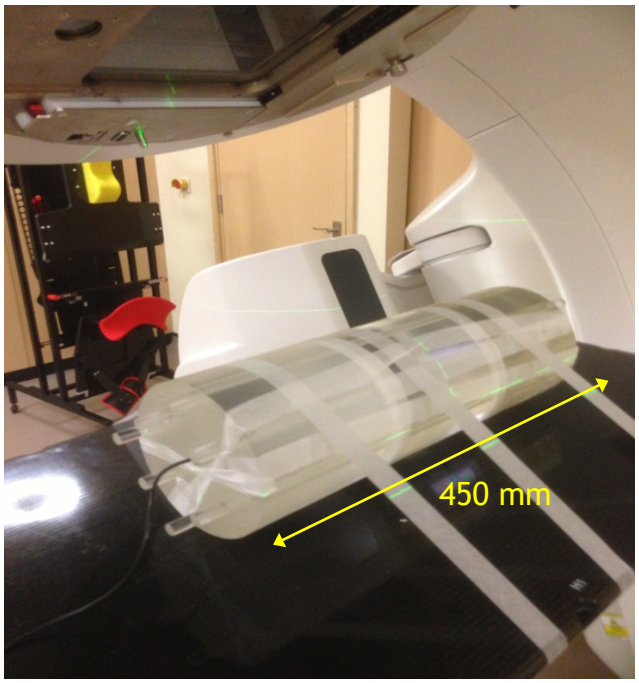

Figure 6.2: Combining three standard 150 mm long phantoms to perform $f(0,\infty)$ measurements.

6.3 Results and Discussion

6.3.1 The Efficiency for Dose Indices

The efficiency values for $f(0{,}150)$, $f_{100}(150)$, $f(0,\infty)$, and $f_{100}(\infty)$, calculated at the centre of the standard and infinitely long phantoms using Head-200, Head-360, Body-200, and Body-360 protocols are shown in Figures 6.3 - 6.6 (a), respectively. $\varepsilon_c(f(0{,}150))$ and $\varepsilon_c(f_{100}(150))$ values within the standard head and body phantoms increased with the beam width (W) until ~150 mm at which point the primary beam began to extend beyond the length of the standard phantoms (150 mm), thus the values for $\varepsilon_c(f(0{,}150))$ and $\varepsilon_c(f_{100}(150))$ remained virtually constant for W > 150 mm (Figures 6.3 - 6.6 (a)).The differences between $\varepsilon_c(f(0{,}150))$ and $\varepsilon_c(f_{100}(150))$ values for W = 160 mm and those obtained for W = 300 mm were all within 3%. The long phantoms within which $\varepsilon_c(f(0,\infty))$ and $\varepsilon_c(f_{100}(\infty))$ calculations were performed, provided a full scatter condition accommodating the whole primary beam and all scattered radiation for W = 40 – 300 mm, and as a result, values of $\varepsilon_c(f(0,\infty))$ and $\varepsilon_c(f_{100}(\infty))$ continued to increase with W.

At a narrow beam width W = 40 mm, $\varepsilon_c(f(0{,}150))$ values were larger by 20% and 13% than those for $\varepsilon_c(f_{100}(150))$ calculated within the standard head and body phantoms, respectively (Figures 6.3 - 6.6 (a)). The magnitudes of these differences declined as the beam width increased until W = 100 mm, after which the difference stabilized at ~5% for the head phantom and ~4% for the body phantom. However, the differences between $\varepsilon_c(f(0,\infty))$ and $\varepsilon_c(f_{100}(\infty))$ were similar to those found between $\varepsilon_c(f(0{,}150))$ and $\varepsilon_c(f_{100}(150))$ for W = 40 mm, and continued to decline with W reaching 1% and 2% for the head and body phantoms, respectively, for W = 300 mm. In general, the differences between $\varepsilon_c(f(0{,}150))$ and $\varepsilon_c(f_{100}(150))$ and between $\varepsilon_c(f(0,\infty))$ and $\varepsilon_c(f_{100}(\infty))$ in the head phantom were higher than those for the body phantom (Figures 6.3 - 6.6 (a)).

Figures 6.3 - 6.6 (a), also show the differences between contributions resulting from the primary beam and scattered radiation to the cumulative dose measurements under scatter equilibrium and non-equilibrium conditions. For W ≤ 140 mm, the differences were not as significant, but the differences rose steadily as W increased beyond the length of the standard phantom to be 11% between $\varepsilon_c(f(0{,}150))$ and $\varepsilon_c(f(0,\infty))$, and 15% between $\varepsilon_c(f_{100}(150))$ and $\varepsilon_c(f_{100}(\infty))$ for the head phantoms (Figures 6.3 - 6.4 (a)), and 24% and 25% respectively, for the body phantom at W = 300 mm (Figures 6.5 - 6.6 (a)).

(a)

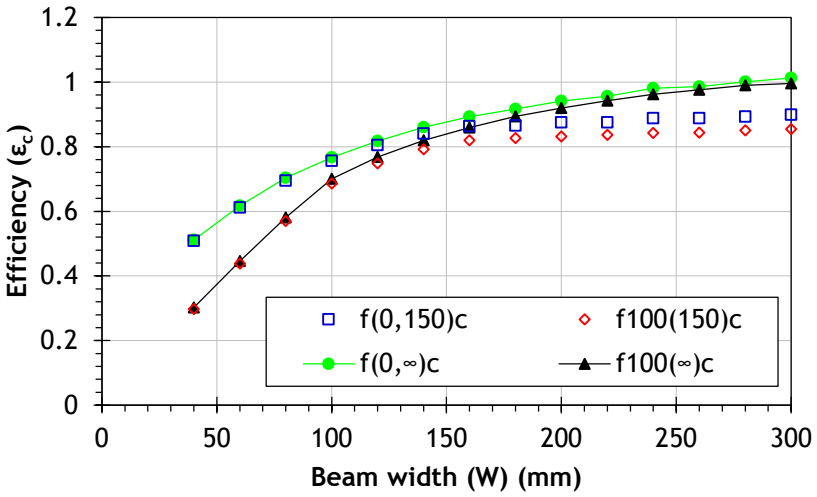

(b)

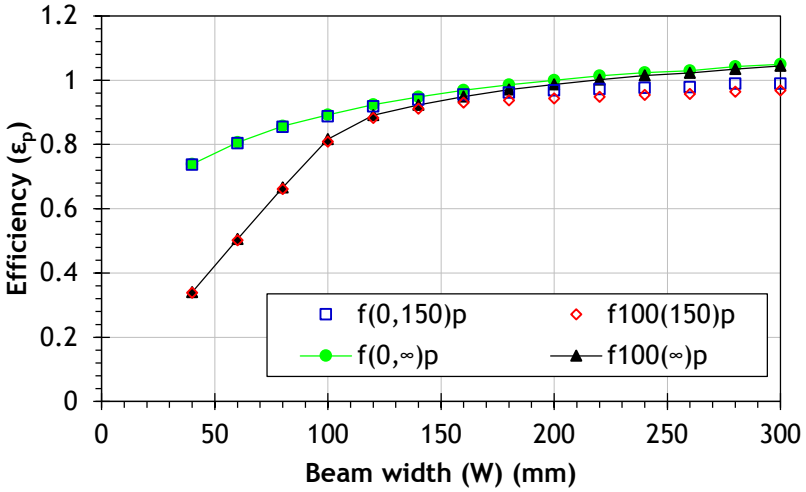

(c)

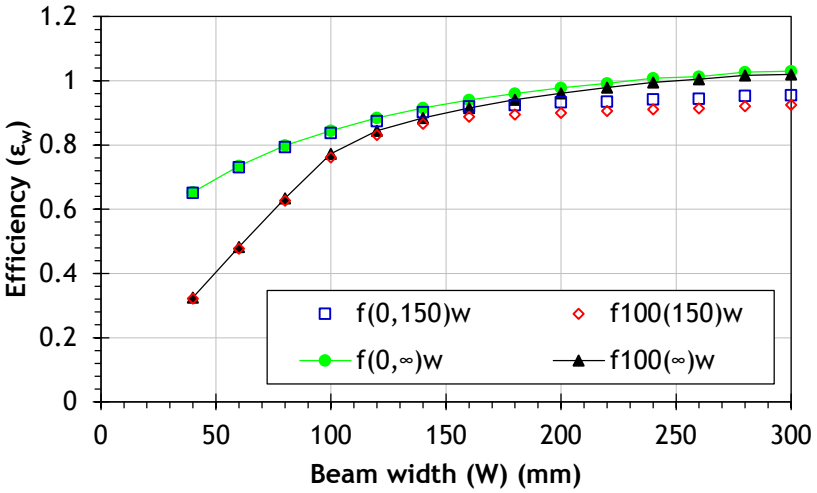

Figure 6.3: The efficiency values for $f(0,150)$, $f_{100}(150)$, $f(0,\infty)$, and $f_{100}(\infty)$ calculated at the (a) centre and (b) periphery of the head phantom, and for (c) the weighted values using Head-200 protocol derived by MC simulations.

(a)

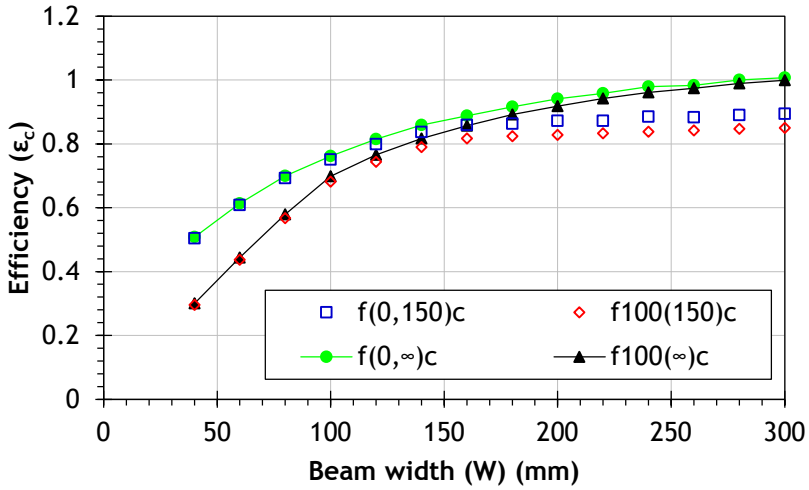

(b)

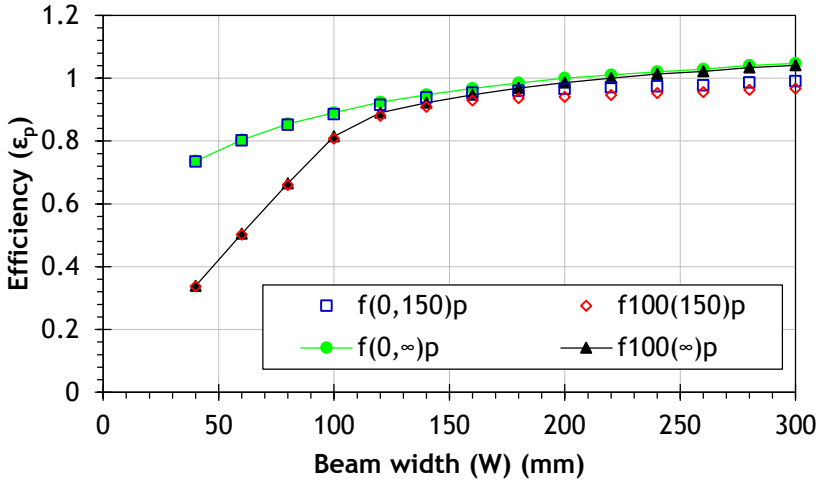

(c)

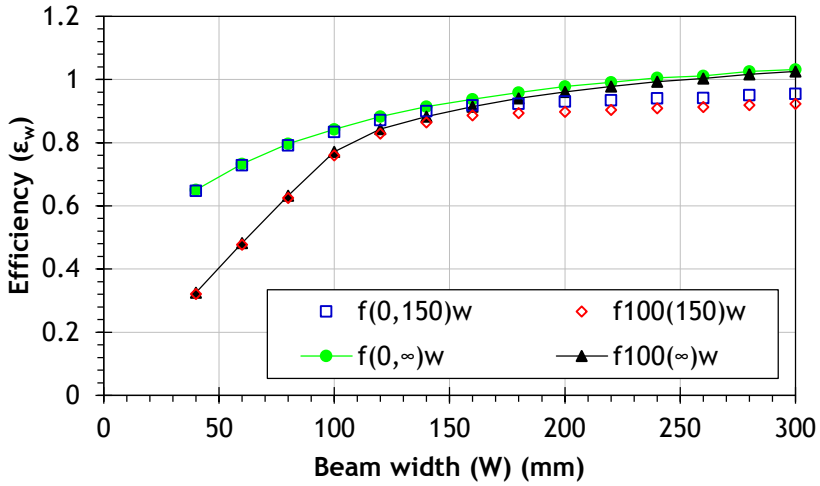

Figure 6.4: The efficiency values for $f(0,150)$, $f_{100}(150)$, $f(0,\infty)$, and $f_{100}(\infty)$ calculated at the (a) centre and (b) periphery of the head phantom, and for (c) the weighted values using Head-360 protocol derived by MC simulations.

Figures 6.3 - 6.6 (b) show $\varepsilon_p(f(0{,}150))$, $\varepsilon_p(f_{100}(150))$, $\varepsilon_p(f(0,\infty))$, and $\varepsilon_p(f_{100}(\infty))$ values calculated at the periphery of the simulated phantoms using Head-200, Head-360, Body-200, and Body-360 protocols, respectively. In a similar manner to that at the centre of the phantoms, $\varepsilon_p(f(0{,}150))$ and $\varepsilon_p(f_{100}(150))$ values remained constant when the beams extended beyond the edges of the phantoms at 4% and 3% for the standard head and body phantoms, respectively. As at the centre, $\varepsilon_p(f(0,\infty))$ and $\varepsilon_p(f_{100}(\infty))$ values increased with W within all phantoms. $f(0{,}150)_p$ and $f_{100}(\infty)_p$ exceeded $CTDI_{\infty,p}$ values by up to 2% for W ≥ 180 mm within the standard body phantom, whereas values for the head phantom were lower than $CTDI_{\infty,p}$ values for all beam widths. $CTDI_{\infty,p}$ values were overestimated by $f(0,\infty)_p$ and $f_{100}(\infty)_p$ by up to 5% for the head and 11% for the body phantom.

The differences between $\varepsilon_p(f(0{,}150))$ and $\varepsilon_p(f_{100}(150))$ and between $\varepsilon_p(f(0,\infty))$ and $\varepsilon_p(f_{100}(\infty))$ for W ≤ 100 mm at the periphery of the phantoms were much larger than those at the centre. For W = 40 mm, $\varepsilon_p(f(0{,}150))$ was 44% higher than $\varepsilon_p(f_{100}(150))$ for the head and body phantoms, and the difference between $\varepsilon_p(f(0,\infty))$ and $\varepsilon_p(f_{100}(\infty))$ was 43% for both the phantoms (Figures 6.3 - 6.6 (b)). These differences fell with increasing W reaching 2% between $\varepsilon_p(f(0{,}150))$ and $\varepsilon_p(f_{100}(150))$, and 1% between $\varepsilon_p(f(0,\infty))$ and $\varepsilon_p(f_{100}(\infty))$ for W = 300 mm. The diameter of the phantoms influenced the differences at the centres of the phantoms, but had little effect at the periphery (Figures 6.3 - 6.6 (a - b)).

(a)

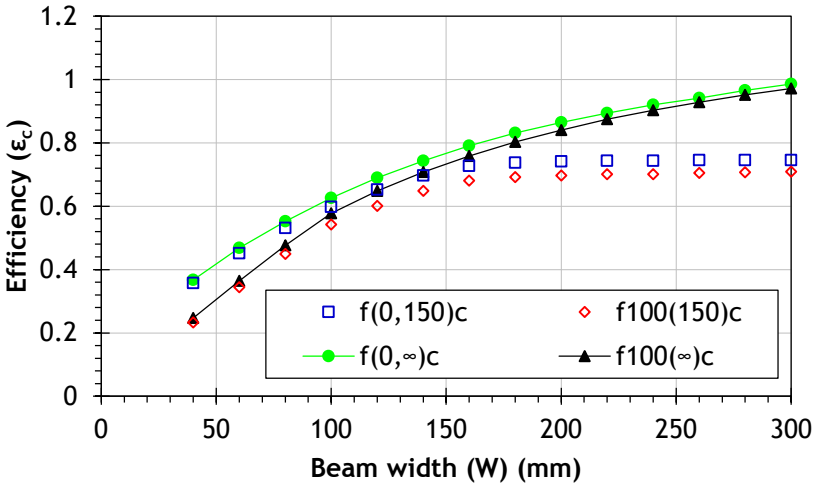

(b)

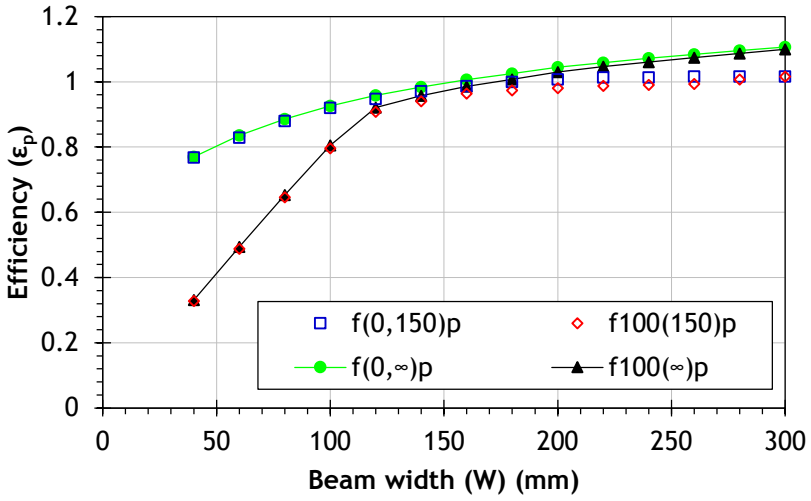

(c)

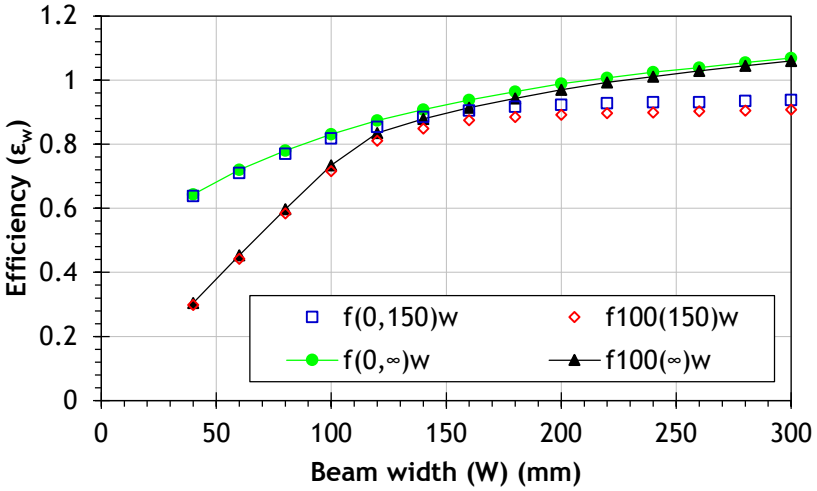

Figure 6.5: The efficiency values for $f(0,150)$, $f_{100}(150)$, $f(0,\infty)$, and $f_{100}(\infty)$ calculated at the (a) centre and (b) periphery of the body phantom, and for (c) the weighted values using Body-200 protocol derived by MC simulations.

(a)

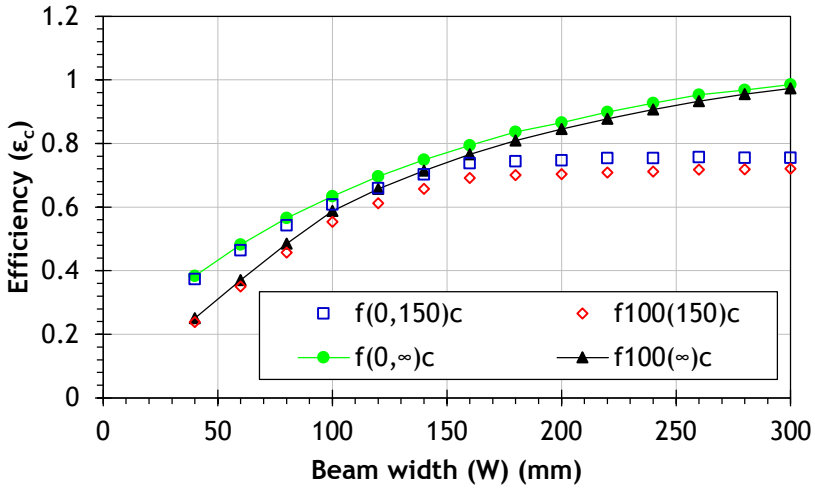

(b)

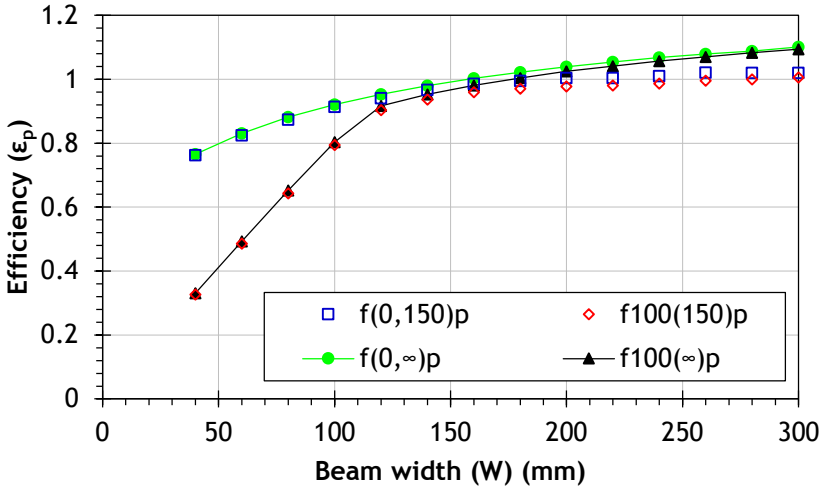

(c)

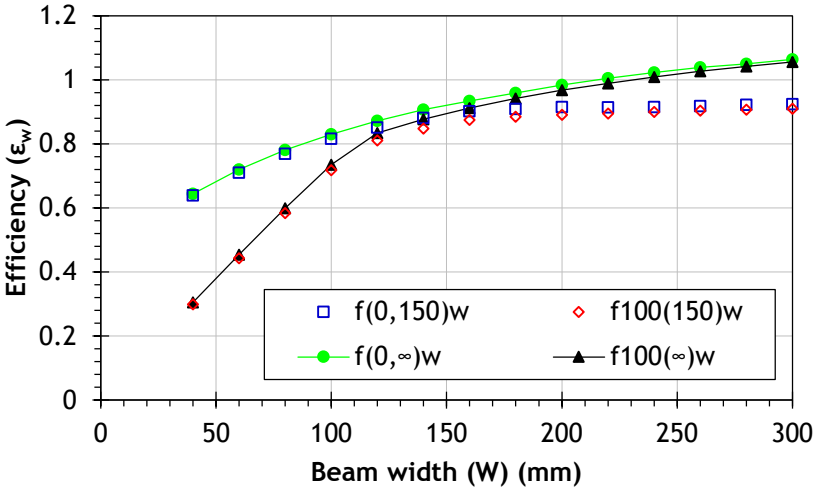

Figure 6.6: The efficiency values for $f(0,150)$, $f_{100}(150)$, $f(0,\infty)$, and $f_{100}(\infty)$ calculated at the (a) centre and (b) periphery of the body phantom, and for (c) the weighted values using Body-360 protocol derived by MC simulations.

Figures 6.3 - 6.6 (b) show that the difference between the contributions of the primary beam and scattered radiation to the cumulative dose at the peripheral axes under scatter equilibrium and non-equilibrium conditions was much lower than that at the central axis. For W = 300 mm, the differences between $\varepsilon_p(f(0{,}150))$ and $\varepsilon_p(f(0,\infty))$, and $\varepsilon_p(f_{100}(150))$ and $\varepsilon_p(f_{100}(\infty))$ were 6% and 10%, respectively, for the head phantoms (Figures 6.3 - 6.4 (b)), 8% and 10%, respectively, for the body phantoms (Figures 6.3 - 6.6 (b)).

The weighted values for $\varepsilon_w(f(0{,}150))$, $\varepsilon_w(f_{100}(150))$, $\varepsilon_w(f(0,\infty))$, and $\varepsilon_p(f_{100}(\infty))$ resulting from the values at the centre (Figures 6.3 - 6.6 (a)) and the periphery (Figures 6.3 - 6.6 (b)) of the phantoms simulated are shown in Figures 6.3 - 6.6 (c). From Figures 6.3 - 6.6, it can be seen that the scan mode (full or half) has a negligible effect on the efficiency values, where the differences between both the modes at the centre and periphery of the phantoms and the weighted values were all within 1%.

6.3.2 Experimental Measurements

Table 6.2 shows $CTDI_{100}$, $CTDI_{IEC}$, $f(0{,}150)$, $f_{100}(150)$ and $f(0,\infty)$ values measured experimentally using the clinical beam width of 198 mm and the Head-200 and Body-360 scanning protocols. $CTDI_{\infty}$ values for each scan were estimated by the application of correction factors (C_f) as in the previous chapter (Table 5.3) ($CTDI_{\infty} = C_f \times CTDI_{IEC}$). The efficiency values for all the dose indices including $CTDI_{100}$ and $CTDI_{IEC}$ were compared to the MC results. The efficiency values based on the experimental measurements agreed with the MC dose ratios within 3% (Figures 6.3 - 6.6). For all scanning protocols, $f(0,\infty)$ values were higher than those of the other approaches, and provided the closest dose quantities to $CTDI_{\infty}$ values. $f(0,\infty)_w$ values were within 3% and 1% of $CTDI_{\infty,w}$ values for the head and body scanning protocols, respectively.

Table 6.2: Experimental measurements (Exp) for $CTDI_{100}$, $CTDI_{IEC}$, $f_{100}(150)$, $f(0,150)$, and $f(0,\infty)$ for the head and body scanning protocols using the clinical beam width W = 198 mm. The correction factors used to estimate $CTDI_{\infty}$ values were derived from MC simulations and are given in parentheses.

		$CTDI_{100}$ [a]	$CTDI_{IEC}$ [a]	$f_{100}(150)$	$f(0,150)$	$f(0,\infty)$	$CTDI_{\infty}$
100 kV, 147 mAs				**Head scan (mGy)**			
Centre		1.72	3.06	3.40	3.51	3.68	4.01
Average periphery		1.62	2.84	3.23	3.21	3.32	3.32
Weighted (1/3 c + 2/3 p)		1.66	2.92	3.29	3.31	3.44	3.56
ε_c	Exp	0.43	0.76	0.85	0.87	0.91	
	MC	0.41	(1.31)	0.83	0.89	0.94	
ε_p	Exp	0.49	0.86	0.97	0.97	1.00	
	MC	0.47	(1.17)	0.94	0.97	1.00	
ε_w	Exp	0.47	0.82	0.92	0.93	0.97	
	MC	0.45	(1.22)	0.90	0.93	0.98	
125 kV, 264 mAs				**Body scan (mGy)**			
Centre		1.73	2.95	3.40	3.62	4.28	4.81
Average periphery		2.47	4.24	4.86	5.05	5.24	5.1
Weighted (1/3 c + 2/3 p)		2.21	3.81	4.38	4.57	4.92	4.95
ε_c	Exp	0.36	0.61	0.71	0.75	0.89	
	MC	0.35	(1.63)	0.70	0.75	0.87	
ε_p	Exp	0.48	0.83	0.95	0.99	1.03	
	MC	0.49	(1.20)	0.98	1.00	1.04	
ε_w	Exp	0.45	0.77	0.88	0.92	0.99	
	MC	0.44	(1.30)	0.89	0.92	0.98	

(a) $CTDI_{100}$ and $CTDI_{IEC}$ reported in the previous chapter.

6.3.3 The Use of Cumulative Dose Indices for CBCT Dosimetry

In recent years, CBCT dosimetry has received attention from the research community in relation to implementing an appropriate quality assurance (QA) and dosimetry system. The present study investigated the cumulative dose measurements under scatter equilibrium and non-equilibrium conditions. Results for $CTDI_{\infty}$ were used as standard values for comparison to examine the efficiency of the dose indices studied in reporting $CTDI_{\infty}$ values. It is recognised that $f(0,150)$ and $CTDI_{\infty}$ do not represent an exact comparison, since one is a measure of point dose and the other an integral of dose from a whole scan. However, the relationship between these variables is an important part of developing a coordinated approach to CBCT dosimetry. The MC results for the dose indices (Figures 6.3 - 6.6) indicated that $f(0,\infty)$, which has been proposed by (AAPM, 2010) and is equal to the peak value of a CBCT beam profile, provides a good method for estimating $CTDI_{\infty}$ values. However, the results at the periphery of the phantoms (Figures 6.3 - 6.6 (b)) showed that $f(0,\infty)_p$ and $f_{100}(\infty)_p$ overestimated $CTDI_{\infty,p}$ values for W ≥ 200 mm and W ≥ 220 mm, respectively, for the head phantom, and for W ≥ 160 mm and W ≥ 180 mm respectively, for the body phantom. These overestimations resulted in $f(0,\infty)_w$ and $f_{100}(\infty)_w$ values exceeding $CTDI_{\infty,w}$ values within both the phantoms, as the peripheral results have a higher weighting (2/3) than those at the centre (1/3) (Figures 6.3 - 6.6 (c)). This observation is in agreement with findings from a study conducted with W = 160 mm using a 320 detector row CT scanner (Aquilion ONE) (Geleijns et al., 2009). In their study, $f_{100}(150)_p$ at the periphery of a standard body phantom using 120 kV was a factor of 1.06 greater than $CTDI_{300,p}$, which was taken to represent $CTDI_{\infty,p}$.

The possible reasons for the overestimation may be: (1) the actual beam width, which is represented by the full width at half maximum (FWHM) at the periphery of the phantom, is less than the nominal beam width. For example, Figure 6.7 shows a FWHM for a beam of a nominal width of 200 mm at the peripheral axes of body and head phantoms. For the body phantom, FWHM = 170 mm at the side from which the x-ray source is incident and FWHM = 230 mm at the other side, and FWHM = 186 mm and

214 mm on either side of the head phantom. This variation in the beam width results from the beam divergence. The diameter of the phantom plays a major role in determining the magnitude of this variation, as this determines the distance of the measuring chamber from the isocentre. The differences between the actual width (FWHM) and the nominal width at the periphery, which is closer to the kV source, for all beam widths W = 40 – 300 mm were 7% and 15% for the head and body phantoms respectively. The main concept for estimating $f(0,\infty)$ and $f_{100}(\infty)$ values differs from that for $CTDI_{\infty}$. $f(0,\infty)$ and $f_{100}(\infty)$ are based on averaging the dose over arbitrary chamber lengths regardless of the beam width, whereas $CTDI_{\infty}$ is based on dividing the dose measured over arbitrary chamber lengths by the nominal beam width. The difference between the FWHM and the nominal width has been shown to have a significant influence on $CTDI_{\infty,p}$ values (Figures 6.3 - 6.6 (b)) (Geleijns et al., 2009). $f(0,\infty)$ and $f_{100}(\infty)$ measurements are also influenced by this difference when the FWHM of the beam at the peripheral axis is less than 20 mm and 100 mm, respectively, as the whole chambers were not exposed and the dose was averaged over the lengths. This influence disappears for wider beams, when the chambers were entirely within the FWHM of the beam.

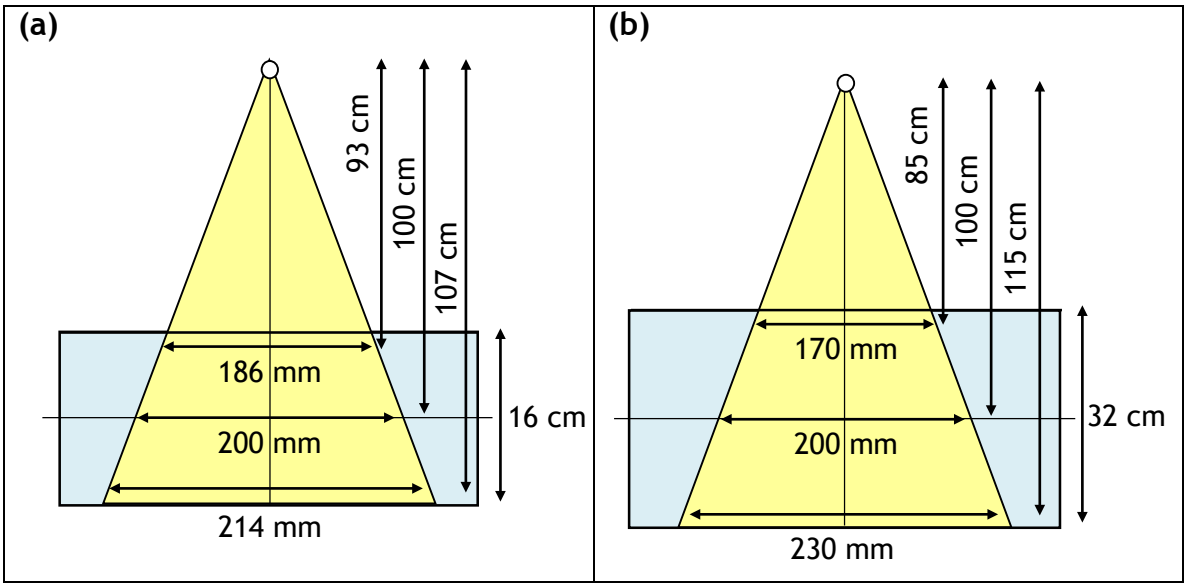

Figure 6.7: The actual beam width at the peripheral axes of (a) head and (b) body phantoms for a beam of a nominal width 200 mm.

In order to indicate the impact of using the nominal widths and the FWHM on the efficiency values, Figure 6.8 shows a comparison involving normalization of $f(0,\infty)_p$ and $f_{100}(\infty)_p$ values to $CTDI_{\infty,p}$ values calculated using the FWHM instead of the nominal width. The use of the FWHM of the beams studied increased $CTDI_{\infty,p}$ values by 7% and 15%, on average, for the head and body phantoms, respectively, and hence brought the efficiency values below unity (Figure 6.8).

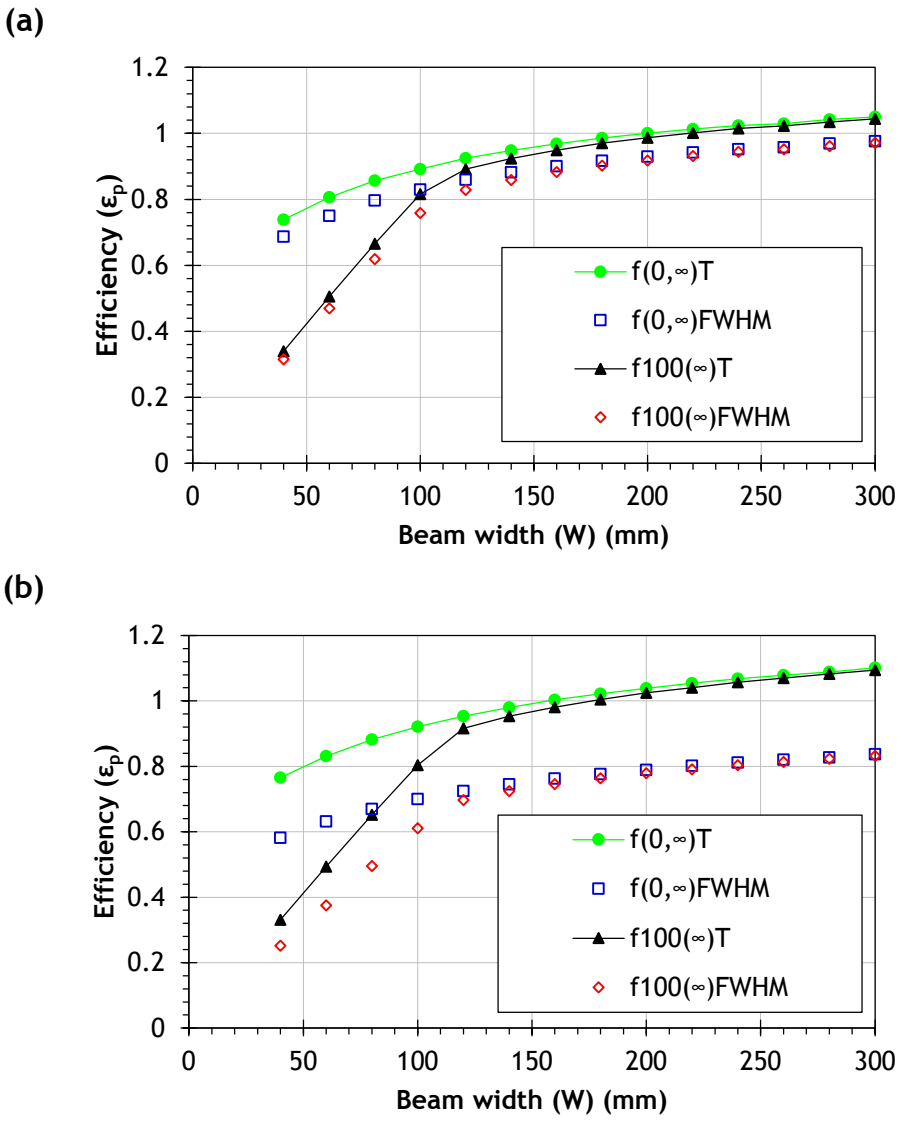

Figure 6.8: A comparison between the use of the nominal widths (T) and the FWHM of the beams to calculate $CTDI_{\infty,p}$ values within the head (a) and body (b) phantoms. T is used for the nominal width instead of W, so that it is not confused with the weighted values.

(2) The second possible reason for the overestimation is that the contribution of scattered radiation to the measurements made at the

peripheral axes is lower than to those at the centre. Figure 6.9 shows the contribution of the scattered radiation resulting from tails of the beam profiles at the centre and periphery of the phantoms. In both the phantoms, the scattered radiation at the centre is higher than that at the periphery, and this increases with increasing phantom diameter (Boone, 2009). The scatter to primary ratio (SPR) values at the periphery of the head and body phantoms were in the range (0.8 – 1.5) for x-ray tube potentials of (100 – 130 kV), whereas the SPR values were (3.0 – 13.0) at the centre of the phantoms for the same x-ray tube potentials (Tsai et al., 2003, Boone, 2009, Li et al., 2013b). Thus, the SPR values at the periphery were lower by factors of ~2 and ~7 than those at the centre of the head and body phantoms, respectively. When the incident beam becomes wider than the nominal width at the peripheral axis on the side away from the x-ray source (Figure 6.7), the beam intensity is lower because of attenuation in the phantom, so that it has less impact on the dose at the periphery. This means that by far the larger component of the dose measurements at the peripheral axes are from the primary beam which has a FWHM lower than the nominal width (Figure 6.7). These two points are considered to be the reasons why values for $f(0,\infty)_p$ and $f_{100}(\infty)_p$ at the periphery of the phantoms overestimated $CTDI_{\infty,p}$ values.

From Figure 6.9, it can be seen that the dose at the centre of the body phantom (Figure 6.9 (b)) was lower than that at the periphery. This is because of the large diameter of the phantom 32 cm, i.e. more attenuation of the primary beam. However, the dose at the centre of the head phantom (Figure 6.9 (a)) was higher than that at the periphery, and this is because of the build up of scattered radiation from the wider beam. For CT scans, it has been shown that the dose at the centre of the body phantom was lower than that at the periphery for all scan lengths, whereas the dose at the centre of the head phantom was higher for the scan lengths ≥ ~135 mm (ICRU, 2012).

(a)

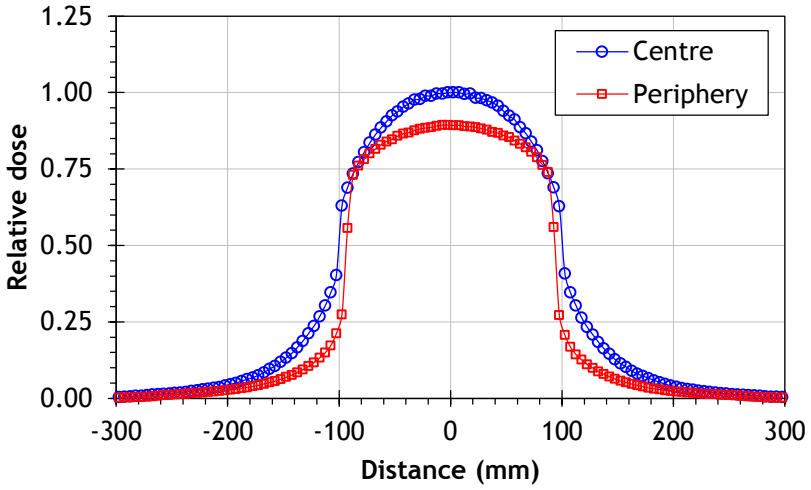

(b)

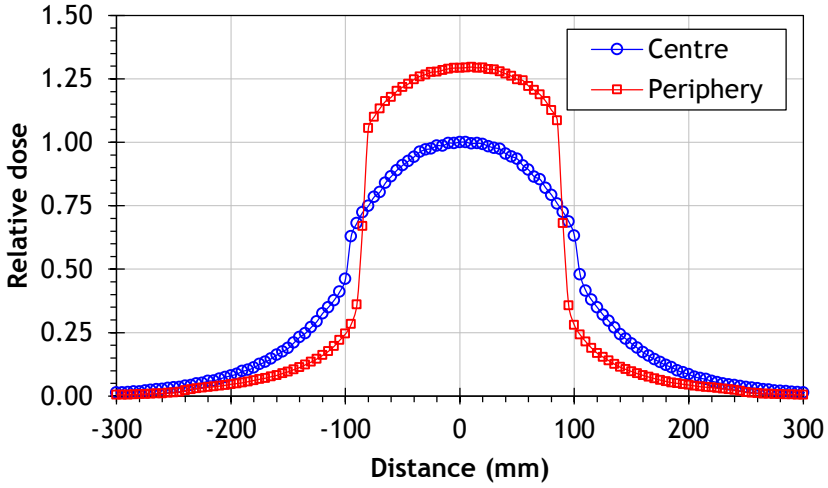

Figure 6.9: The beam profiles at the centre and periphery of the head (a) and body phantoms (b). The dose values are normalized with respect to the central value at $(z = 0)$ of the dose profile of the central axis.

6.3.4 The Small and Pencil Chambers for Cumulative Dose Measurements

The MC results showed that the differences between the small (20 mm) and pencil (100 mm) ionization chambers within the head and body phantoms were large for W < 120 mm, but the differences declined when wider beams were used (Figures 6.3 - 6.6). At the centres of the phantoms, the differences between $f(0,150)_c$ and $f_{100}(150)_c$ as the beam widths were increased stabilized after W = 100 mm, and after W = 120 mm at the periphery of the phantoms. This occurred because the 100 mm chamber was not exposed completely at W < 100 mm at the centre and < 120 mm at the periphery, whereas the 20 mm chamber was irradiated entirely at W >

20 mm. As the $f_{100}(150)$ and $f_{100}(\infty)$ measurements with the 100 mm chamber were averaging the dose over the chamber length, the length of the exposed part played a major role in determining the magnitudes of the measurements, as discussed in section 6.3.3. However, when the entire 100 mm chamber was irradiated, the differences were reduced, but the 20 mm chamber still gave a higher value (Figures 6.3 - 6.6).

Fahrig et al. (2006) and Dixon and Boone (2010) have stated that the use of the 100 mm chamber is inappropriate for cumulative dose measurements, which should equate to point dose measurements as proposed by (Dixon, 2003). However, results in the present study showed that the differences between measurements obtained with the 20 mm chamber and those of the 100 mm chamber were not significant for the weighted values being within 4% and 3% for the head and body phantoms, respectively (Figures 6.3 - 6.6 (c)). These findings were in agreement with other studies (Table 6.3), and support the suggestions proposed by (Amer et al., 2007, Geleijns et al., 2009, Li et al., 2014b) that the 100 mm chamber can be used for the cumulative dose measurements for CBCT provided beam width more than 120mm.

6.3.5 Scatter Equilibrium and Non-Equilibrium Conditions

The use of the infinitely long phantoms that provide the scatter equilibrium condition was proposed to measure the cumulative dose (AAPM, 2010). The findings in the present study showed that the cumulative dose for W ≤ 140 mm calculated with the 20 mm and 100 mm chambers within the infinitely long phantoms did not differ significantly from those calculated within the standard phantoms (Figures 6.3 - 6.6), but when wider beams were used, the differences became obvious. As expected, the largest differences between the cumulative dose calculated within the standard phantoms and those within the long phantoms were found at the centre of the body phantoms, as the diameter of the phantom enhances contributions from the scattered radiation to the measurements at the centre as discussed section 6.3.3.

Table 6.3: A comparison between dose ratios for the cumulative dose values calculated with the small (20 mm) and pencil (100 mm) chambers in standard and infinitely long head and body phantoms obtained in this study using MC and experimental measurements (Exp) and those published in other studies.

Investigator	Scanner	Method	Tube voltage (kV)	Scanning mode	Phantom	Beam width (mm)	$f(0,150)_x/f_{100}(150)_x$			$f(0,\infty)_x/f_{100}(\infty)_x$		
							$x = c$	$x = p$	$x = w$	$x = c$	$x = p$	$x = w$
(Li et al., 2014b)	Somatom Definition dual source	MC	100	Full Fan	Head	200	1.05	1.02	1.03	1.02	1.01	1.01
This study	OBI	Exp	100			198	1.03	0.99	1.01			
This study	OBI	MC	100			200	1.05	1.03	1.04	1.02	1.02	1.02
(Geleijns et al., 2009)	Toshiba Aquilion ONE	MC	120	Full Fan	Body	160			1.04			1.02
This study	OBI	MC	125			160			1.04			1.03
(Osei et al., 2009)	Varian On Board Imager	Exp	125	Full Fan	Body	206	1.08	1.03	1.03			
(Li et al., 2014b)	Somatom Definition dual source	MC	120			200	1.07	1.03	1.03	1.03	1.02	1.02
This study	OBI	MC	125			200	1.06	1.03	1.04	1.02	1.01	1.02
(Osei et al., 2009)	Varian OnBoard Imager	Exp	125	Half Fan	Body	206	1.07	1.04	1.05			
This study	OBI	Exp	125			198	1.06	1.04	1.04			
This study	OBI	MC	125			200	1.06	1.03	1.04			

Table 6.4: A comparison between dose ratios for the cumulative dose values calculated within standard and infinitely long head and body phantoms obtained in this study using MC and those published in other studies.

Investigator	Scanner	Method	Tube voltage (kV)	Phantom	Length of infinitely long phantom (mm)	Beam width (mm)	$f(0,150)_x/f(0,\infty)_x$			$f_{100}(150)_x/f_{100}(\infty)_x$		
							$x = c$	$x = p$	$x = w$	$x = c$	$x = p$	$x = w$
(Li et al., 2014b)	Somatom Definition dual source	MC	100	Head	900	140 - 240	0.98 - 0.91	1.0 - 0.95	0.99 - 0.94	0.97 - 0.88	0.99 - 0.93	0.98 - 0.92
This study	OBI	MC	100		600	140 - 240	0.98 - 0.90	0.99 - 0.95	0.98 - 0.94	0.97 - 0.87	0.99 - 0.94	0.98 - 0.92
(Geleijns et al., 2009)	Toshiba Aquilion ONE	MC	120	Body	700	160			0.98			0.96
This study	OBI	MC	125		900	160			0.97			0.96
(Li et al., 2014b)	Somatom Definition dual source	MC	120	Body	900	140 - 240	0.92 - 0.81	0.99 - 0.95	0.97 - 0.92	0.90 - 0.77	0.96 - 0.94	0.97 - 0.90
This study	OBI	MC	125		900	140 - 240	0.94 - 0.81	0.99 - 0.95	0.97 - 0.91	0.92 - 0.78	0.98 - 0.93	0.97 - 0.89

The influence of the infinitely long phantoms at the peripheral axes was minimal, as the contribution from scattered radiation to the peripheral measurements is much less. The differences between the cumulative dose $f(0,150)$ and $f_{100}(150)$ calculated within the standard body phantom and $f(0,\infty)$ and $f_{100}(\infty)$ calculated within the infinitely long phantoms (Figures 6.3 - 6.6) were in good agreement with other studies (Table 6.4).

6.4 Conclusion

The efficiencies of four dose indices $f(0,150)$, $f_{100}(150)$, $f(0,\infty)$, and $f_{100}(\infty)$ relative to $CTDI_{\infty}$ have been calculated in BEAMnrc and DOSXYZnrc codes using four different scanning protocols. $f(0,\infty)$ gave the highest dose values compared with the other approaches, and its values were the closet to $CTDI_{\infty}$ values, especially for wider beams. Dose values obtained with the 20 mm and 100 mm chambers for the cumulative dose measurements were substantially different for W < 120 mm, but the differences fell with increasing beam width and became approximately comparable. The need for infinitely long phantoms to be used for the cumulative dose measurements was not significant for W ≤ 140 mm, but such phantoms are required for wider beams to account for all the contributions arising from the primary beam and the scattered radiation that cannot be captured within the standard phantoms. The results of this study have been published in (Abuhaimed et al., 2015).

Chapter 7

The Use of $G_x(L)$ Function for CBCT Dosimetry

7.1 Introduction

The AAPM dosimetry method presented in Chapter 2 section 2.6.4 requires measuring cumulative dose within phantoms that are impractical for regular use in hospitals because they are long and heavy. This chapter investigates the use of a practical approach proposed by ICRU Report–87 to utilize the AAPM method, but avoid the difficulty of using the long phantoms (ICRU, 2012). This approach aims to keep the $CTDI_{100}$ dosimetry equipment. It is based on the application of a function called $G_x(L)$, which is measured within the ICRU/AAPM phantom shown in Figure 2.10 (b) of Chapter 2.

Li et al. (2013a) proposed a practical approach to avoid the use of long phantoms, which is suitable for stationary or moving table MSCT scans with beams of width ≤ 40 mm. This approach is based on the use of the $CTDI_{100}$, the efficiency of $CTDI_{100}$, and a function known as the approach to equilibrium function. Furthermore, Li et al. (2014b) proposed another practical approach for the stationary table mode employed for CBCT scans with beams of width 30 – 250 mm. This requires measurement of the cumulative dose using a small ionization chamber or a standard 100 mm long pencil ionization chamber within the standard PMMA phantoms, and the application of correction factors, which are equal to the ratios of the cumulative doses within infinitely long PMMA phantoms to those within the standard 150 mm long phantoms.

Dixon and Boone (2014) also introduced two methods to address the long phantom issue for scans obtained with the stationary table mode. The first method requires a single measurement of cumulative dose for a beam of full width at half maximum (FWHM) > 24 mm within a long phantom as described in (AAPM, 2010) TG – 111. Subsequently, the cumulative dose for

any beam width of interest can be evaluated by multiplying the cumulative dose measured by the ratio of the approach to equilibrium functions for the beam width of interest H(a') and for the measured beam width H(a), where H(a) and H(a') are calculated using theoretical equations based on a mathematical model (Dixon and Boone, 2010). The second method is based on the use of an analytical formula to evaluate the cumulative dose for a given scan by calculating the primary beam dose component in $CTDI_{100}$.

The $G_x(L)$ function was investigated in ICRU Report–87 using MSCT scanners. However, dosimetry of the moving table mode differs slightly from that of the stationary table mode, which is the basis for CBCT scans such as those used in IGRT, in perfusion scans, in dental scans, and with interventional radiology and cardiology C-arm equipment. This chapter describes an investigation into the extension of the $G_x(L)$ function to CBCT applications.

7.2 Materials and Methods

7.2.1 The $G_x(L)$ Function

Initially, the $G(L)$ function, proposed by ICRU, is defined as the ratio of the cumulative dose $D_L(0)$ at the middle (z = 0) of an infinitely long phantom, for a MSCT scan of length (L), to $CTDI_{vol}$ for the scan, as follows (ICRU, 2012):

$$G(L) = \frac{D_L(0)}{CTDI_{vol}} \tag{7.1}$$

Experimental measurements of the $G(L)$ function at the central axis of the ICRU/AAPM phantom at 120 kV reported in (ICRU, 2012) for three different MSCT scanners showed insignificant variations between the scanners. In addition, identical $G(L)$ functions were obtained for four different tube potentials 80, 100, 120 and 140 kV for one MSCT scanner. The $G(L)$ function, therefore, appeared to be independent of scan parameters such as tube potential, beam width, bowtie filter, SID, scanner table composition, and CT scanner model (ICRU, 2012). This independence occurs because the influence of scan parameters is cancelled out by the normalization of $D_L(0)$ with respect to $CTDI_{vol}$, and as a consequence, each phantom will have a

unique $G(L)$ function that can be used for any CT scanner depending only on phantom diameter and composition. This feature makes the ICRU approach efficient and practical in the clinical environment. When the $G(L)$ function is known, $D_L(0)$ can be estimated for any scan of specified scan length (L) as $D_L(0) = G(L) \times CTDI_{vol}$, where the $CTDI_{vol}$ is displayed on the console.

Although the $G(L)$ function was only investigated at the central axis of the ICRU/AAPM phantom, ICRU suggested that the use of the $G(L)$ function can be extended to the periphery of the phantom and hence the weighted value. It can also be employed with other phantoms of varying composition and diameter such as head or body phantoms made of PMMA or water (ICRU, 2012). Therefore, the $G(L)$ function of Eq.(7.1) can be redefined as:

$$G_x(L) = \frac{D_L(0)_x}{CTDI_{vol}} \tag{7.2}$$

where the x indicates the position of the measurement within a phantom, with $x = c$ for the centre or $x = p$ for the periphery, and $x = a$ for the weighted average measurements in the weighted function $G_a(L)$.

7.2.2 Modified Function for CBCT Scans

ICRU investigated and proposed the $G_x(L)$ function Eq.(7.2) for use with MSCT scanners with a moving table. The arrangement for CBCT usually uses a single rotation with a broader beam, a flat panel detector, and a stationary table. Therefore, the equivalent function should take the differences between conventional CT and CBCT scanners into account. The cumulative dose for CBCT scans at z = 0, which is equivalent to $D_L(0)_x$ in Eq.(7.2), is equal to $Nf(0)_{x,}$ called $Nf(0,\infty)_x$ in this project and presented in Chapter 2 section 2.6.4.

The standard dose quantity $CTDI_{vol}$ will be replaced by $CTDI_w$ in Eq.(7.2), since there is no table movement and so no pitch to take into account. The length of the scan (L) equates to the beam width (W), as this determines the axial extent of the scan along the z-axis, i.e. rotation axis (Dixon and Boone, 2010). Therefore, $G_x(L)$ transforms to a function of beam width (W),

i.e. $G_x(W)$, and an equation of similar form to Eq.(7.2) can be defined for CBCT scans as:

$$G_x(W) = \frac{Nf(0,\infty)_x}{CTDI_w} \quad (7.3)$$

The symbol (W) for the beam width of a CBCT scan should not be confused with (w) for the weighted CTDI ($CTDI_w$). Both $D_L(0)_x$ and $f(0,\infty)_x$ in the numerators of Eqs.(7.2) and (7.3) approach asymptotic values as the scan length (L) and the beam width (W), respectively, increase. This is because contributions from scatter originating further from the measurement point decline exponentially (ICRU, 2012, Dixon and Boone, 2010, Dixon and Boone, 2011). Therefore, $f(0,\infty)_x$ in Eq.(7.3) can be expressed as $f_W(0,\infty)_x$ in a manner similar to that for $D_L(0)_x$, but to avoid confusion with the weighted value (w), $f(0,\infty)_x$ notation has been used in this study.

However, the fact that $G_x(L)$ is a function of the scan length, whereas $G_x(W)$ is a function of the beam width means that Eqs.(7.2) and (7.3) are fundamentally different. This is because the denominators in the equations differ, $CTDI_{vol}$ for MSCT scans is independent of scan length L, whereas $CTDI_w$ for CBCT scans decreases with beam width W. The cumulative dose $D_L(0)_x$ in the $G_x(L)$ function Eq.(7.2) is normalized with respect to $CTDI_{vol}$. Thus, as the scan length (L) increases, $D_L(0)_x$ at the central and peripheral axes also increases, but approaches an equilibrium value at a length known as the equilibrium length (L_{eq}), after which further contributions from scattered radiation to $D_L(0)_x$ become negligible (AAPM, 2010). The asymptotic curve that describes the dependence of $D_L(0)_x$ on scan length, reaches 98% of the equilibrium cumulative dose $D_{eq}(0)_x$ at L_{eq}, and is known as the approach to equilibrium function (AAPM, 2010). The $G_x(L)$ function has a similar dependence on L to $D_L(0)_x$ as $CTDI_{vol}$ in the denominator is constant. In contrast to $G_x(L)$, the $G_x(W)$ function in Eq.(7.3) increases almost linearly with beam width. Although $f(0,\infty)_x$ values approach an equilibrium value in the same manner as $D_L(0)_x$ (Dixon and Boone, 2010), they are normalized with respect to the $CTDI_w$, which decreases with increasing beam width (Boone, 2007, Kyriakou et al., 2008). In order to obtain a function with a similar asymptotic behaviour to $G_x(L)$, $CTDI_w$ has

been measured with a reference beam width (W ≤ 40mm) and the $G_x(W)$ function in Eq.(7.3) redefined as:

$$G_x(W) = \frac{Nf(0,\infty)_x}{CTDI_{w,ref}} \quad (7.4)$$

where (ref) indicates the reference beam width used for $CTDI_w$. In this study, a beam of width 40 mm was used to calculate the $G_x(W)$ functions.

7.2.3 Monte Carlo for the $G_x(W)$ Functions

Two scanning protocols (head and body) were used to investigate the $G_x(W)$ function. These protocols were almost the same as the Head-360 and Body-360 listed in Chapter 5 Table 5.1. However, the tube potential was varied from 80 - 140 kV in increments of 20 kV, except that 125 kV was used instead of 120 kV for the body protocol as this is the potential used in the clinic. In addition, the beam widths studied were 40 – 500 mm. Parameters of the scanning protocols were used to generate PHSP files using BEAMnrc and then run in DOSXYZnrc as described in Chapter 4 section 4.4.2 to calculate values for $f(0,\infty)$ and $CTDI_{w,}$ for each protocol at each tube potential. DOSXYZnrc simulations used to calculate $f(0,\infty)$ and $CTDI_w$ were run until achieving a statistic uncertainty of <1% for each simulation.

Eight phantoms made of PMMA, polyethylene (PE), and water representing head and body phantoms (Table 7.1) were designed in DOSXYZnrc as described in Chapter 4 section 4.4.2. The four PMMA phantoms were designed with diameters equal to those of the standard PMMA phantoms, and diameters of the head and body water phantoms were those recommended by AAPM TG – 111 (AAPM, 2010). It has been shown that $CTDI_\infty$ calculated in a PE phantom of diameter 160 mm is comparable to that of a PMMA phantom of similar diameter (Zhou and Boone, 2008), thus this diameter was used for the PE head phantom, whereas the body PE phantom recommended by ICRU/AAPM is 300 mm in diameter (Figure 2.10 (b)). The short PMMA phantoms (150 mm) represented the standard phantoms used for dosimetry in hospitals and were used to calculate $CTDI_{100}$ values, and hence $CTDI_w$ values. The longer phantoms (600 mm) were considered to emulate the infinitely long phantoms, within which $f(0,\infty)_x$ values for the

different phantom compositions were calculated. Only a single rotation $N = 1$ was used, and the $G_x(W)$ function was evaluated at the middle of the central and peripheral axes of the phantom and for the weighted value. Therefore, the $G_x(W)$ function was calculated for the PMMA, PE and water head and body phantoms using Eq.(7.4) as:

$$G_c(W) = \frac{f(0,\infty)_{c,m}}{CTDI_{w,40}}$$

$$G_p(W) = \frac{f(0,\infty)_{p,m}}{CTDI_{w,40}} \quad (7.5)$$

$$G_a(W) = \frac{f(0,\infty)_{w,m}}{CTDI_{w,40}}$$

where (m) represents the composition of the phantom (PMMA, PE or water) used to calculate $f(0,\infty)_x$ values, and $f(0,\infty)_w$ is calculated in a manner similar to that used for $CTDI_w$, i.e. $\left(f(0,\infty)_w = 1/3\, f(0,\infty)_c + 2/3\, f(0,\infty)_p\right)$. Outputs from the DOSXYZnrc simulations were subsequently analyzed by a MATLAB code built in-house.

Table 7.1: Densities, chemical compositions, diameters, and lengths of the PMMA, PE, and water phantoms used in this investigation.

Phantom material	Density (ρ) (g/cm^3)	Chemical composition	Head diameter (mm)	Body diameter (mm)	Phantom length (mm)
PMMA	1.19	$C_5O_2H_8$	160	320	150 600
PE	0.97	C_2H_4	160	300	600
Water	1.0	H_2O	200	300	600

7.2.4 $CTDI_{100}$ and $f(0,\infty)_{PMMA}$ Experimental Measurements

The experimental set ups used for $CTDI_{100}$ and $f(0,\infty)_{PMMA}$ measurements were similar to those used in Chapter 5 section 5.2.3 for $CTDI_{100}$ measurements and Chapter 6 section 6.2.3 for $f(0,\infty)_{PMMA}$ measurements.

7.3 Results and Discussion

7.3.1 Study of the $G_x(W)$ Function as Dosimetry Variable for CBCT Assessment

Figures 7.1 - 7.3 show the $G_c(W)$, $G_p(W)$, and $G_a(W)$ functions for the PMMA, PE, and water head and body phantoms for CBCT scans. The functions increased with beam width, tending towards equilibrium values for beam widths above about 400 mm. There were differences in $G_c(W)$ and $G_p(W)$ functions with tube potential and these were larger for the body phantoms and increased with beam width. The results at the centre of the PE body phantom that represented the ICRU/AAPM phantom did not replicate the constant relationship with tube potential reported for MSCT scanners (ICRU, 2012). For the PMMA body phantom (Figure 7.1 (d – f)), the variations between tube potentials at the centre and periphery of the phantom for a beam of width 200 mm were in agreement with those for a CBCT scan of the same beam width obtained with a conventional CT scanner, a Somatom Definition dual source CT scanner, using MC simulations and the stationary table mode (Table 7.2) (Li et al., 2014b).

Table 7.2: A comparison between $G_c(W)$ and $G_p(W)$ functions obtained in the study for a beam of width 200 mm calculated within the PMMA body phantom as in Eq.(7.5) at 80 – 140 kV and those from (Li et al., 2014b).

Function	This study		(Li et al., 2014b)	
	Centre	Periphery	Centre	Periphery
G_x(W = 200) – 80 kV	0.94	1.46	0.88	1.78
G_x(W = 200) – 100 kV	1.04	1.44	0.94	1.75
G_x(W = 200) – 120/125 kV[(a)]	1.09	1.41	0.97	1.74
G_x(W = 200) – 140 kV	1.11	1.40	0.99	1.73

(a) 125 kV was used for the body phantoms in this study, whereas 120 kV was used in (Li et al., 2014b).

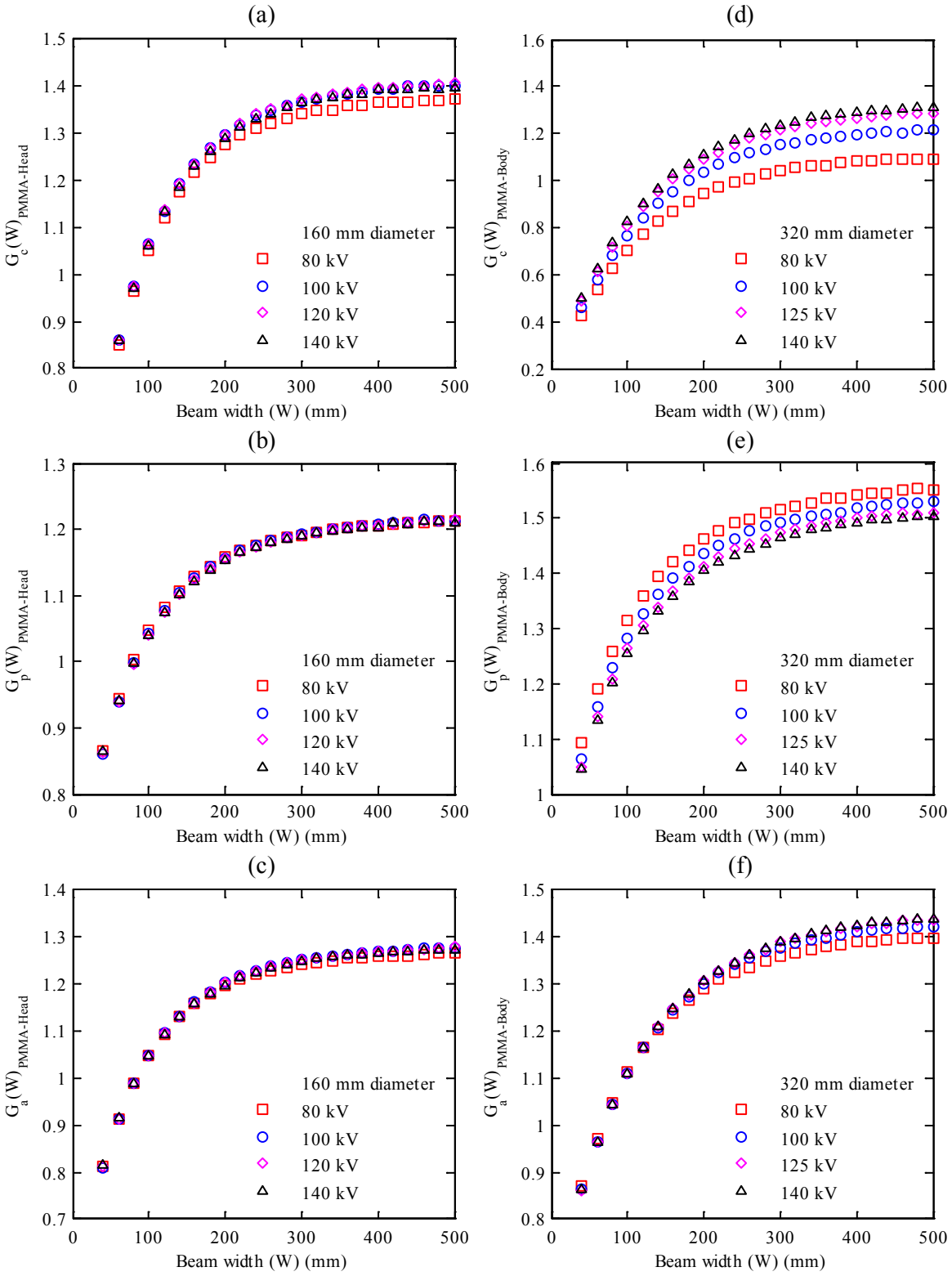

Figure 7.1: $G_c(W)$, $G_p(W)$, and $G_a(W)$ functions for $f(0,\infty)_{x,PMMA}$ values calculated within 600 mm long PMMA phantoms and normalized with respect to $CTDI_{w,40}$ values calculated within 150 mm long PMMA phantoms as in Eq.(7.5) using beams of width W = 40 – 500 mm. (a – c) for the head phantoms and (d – f) for the body phantoms (Table 7.1).

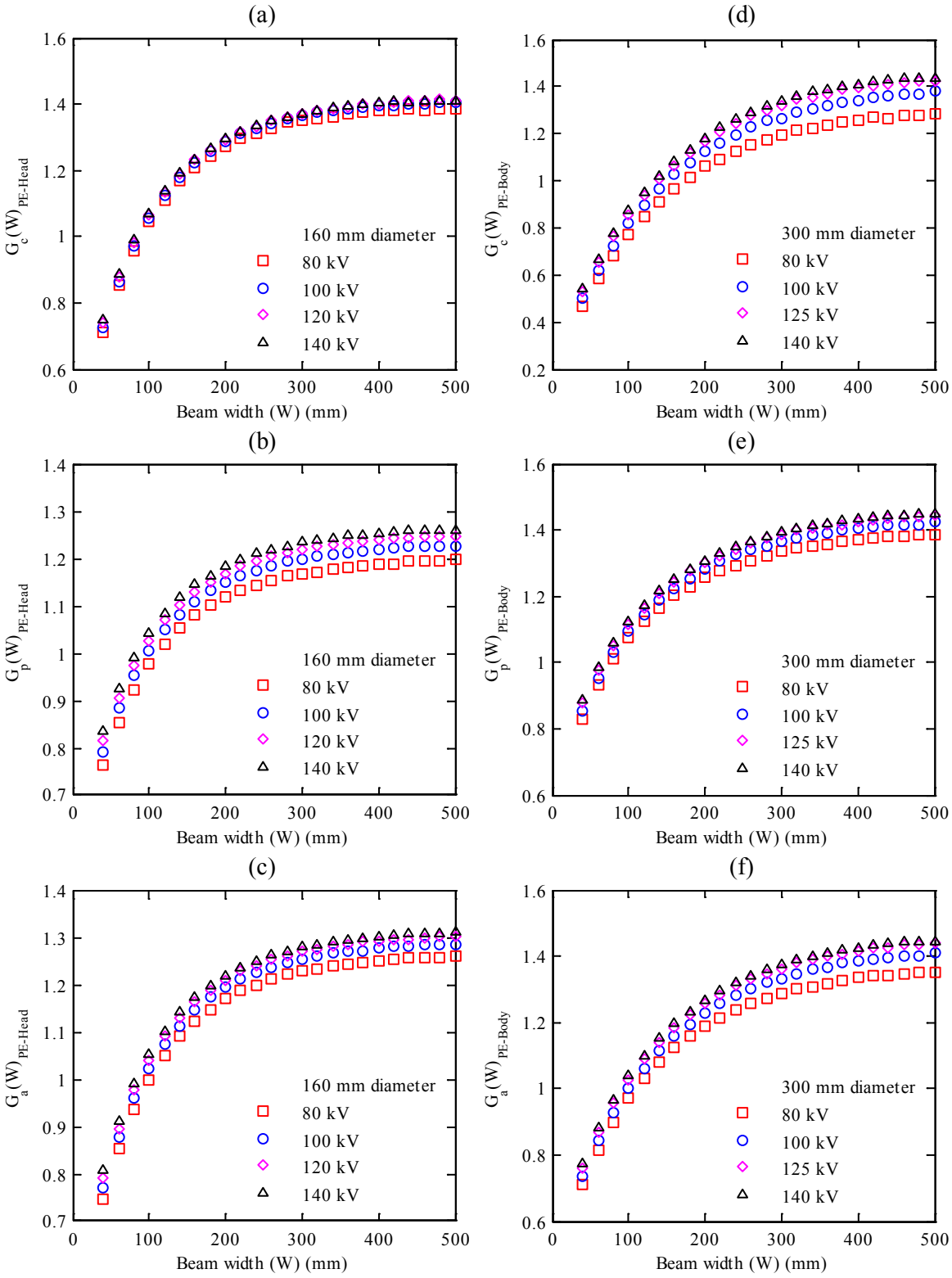

Figure 7.2: $G_c(W)$, $G_p(W)$, and $G_a(W)$ functions for $f(0,\infty)_{x,PE}$ values calculated within 600 mm long PE phantoms and normalized with respect to $CTDI_{w,40}$ values calculated within 150 mm long PMMA phantoms as in Eq.(7.5) using beams of width W = 40 – 500 mm. (a – c) for the head phantoms and (d – f) for the body phantoms (Table 7.1).

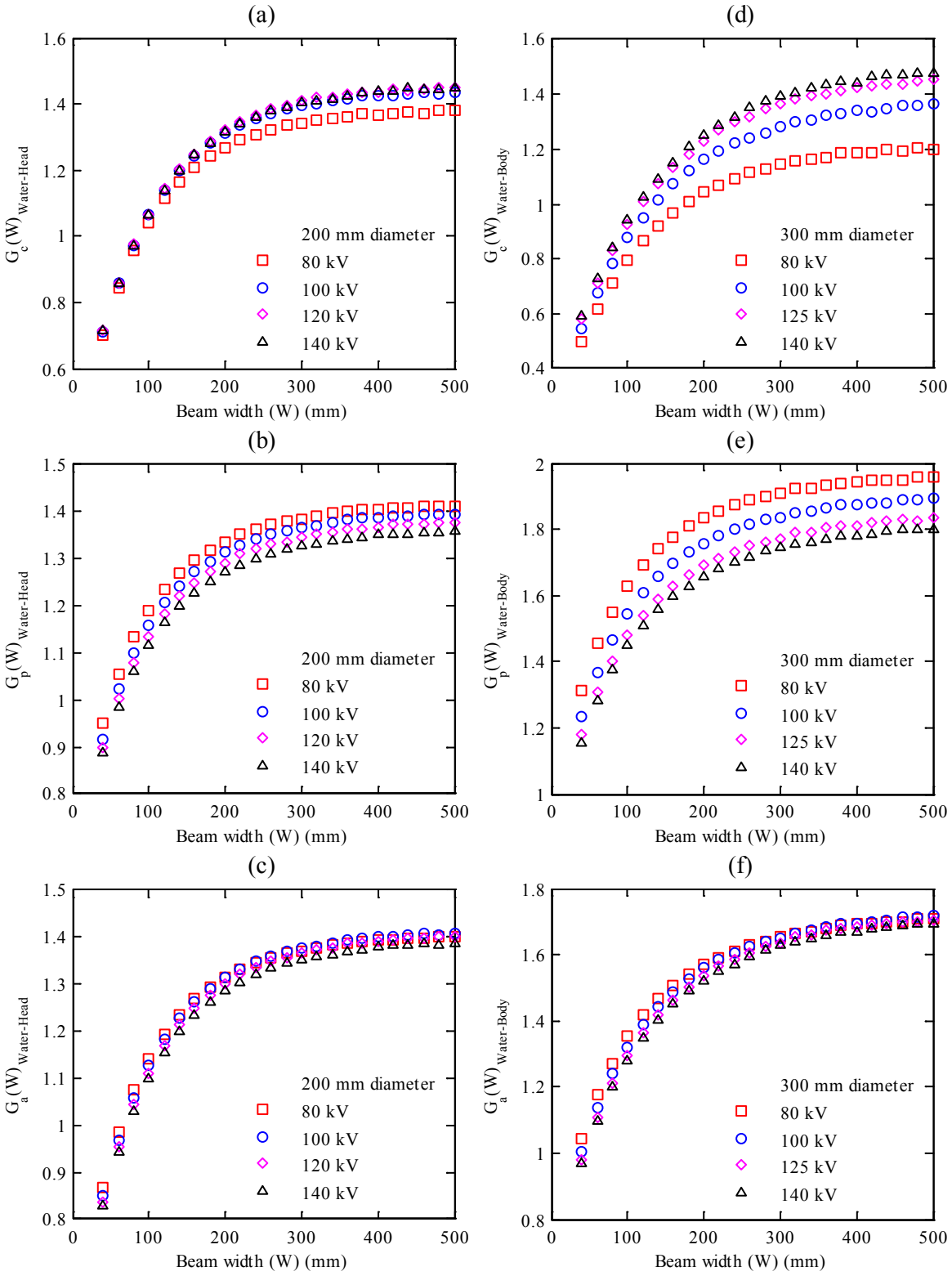

Figure 7.3: $G_c(W)$, $G_p(W)$, and $G_a(W)$ functions for $f(0,\infty)_{x,water}$ values calculated within 600 mm long water phantoms and normalized with respect to $CTDI_{w,40}$ values calculated within 150 mm long PMMA phantoms as in Eq.(7.5) using beams of width W = 40 – 500 mm. (a – c) for the head phantoms and (d – f) for the body phantoms (Table 7.1).

Although $f(0,\infty)_{c,m}$ and $f(0,\infty)_{p,m}$ values at 140 kV were larger than those for other tube potentials as would be expected, values for $G_c(W)$ and $G_p(W)$ varied in different ways depending on phantom composition. Values of $G_c(W)$ increased with tube potential for all phantoms, while those for $G_p(W)$ decreased with tube potential for the PMMA and water phantoms, so that the differences in $G_c(W)$ and $G_p(W)$ tended to cancel to some extent in the derivation of $G_a(W)$ (Figures 7.1 - 7.3). The influence of tube potential on values for the $G_x(W)$ functions within the PMMA body phantom was in agreement with that found for a conventional CT scanner (Table 7.2) (Li et al., 2014b), where $G_x(W)$ at 80 kV was lower at the centre of the phantom but larger than other tube potentials at the periphery. Whereas for the PE phantoms both $G_c(W)$ and $G_p(W)$ increased with tube potential (Figure 7.2). The variations resulted from the influence of tube potential on the dose level at the centre and periphery of each phantom. Figures 7.2 - 7.3 present measurements in phantoms made from PE and water, and can be compared with the standard PMMA phantoms in Figure 7.1. The reason for their contrasting behaviour relates to their different chemical compositions (Table 7.1), and the resulting energy dependence of the mass energy absorption coefficients, which determine the attenuation and distribution of energy absorption within the phantoms. Polyethylene contains only carbon and hydrogen atoms, whereas water and PMMA contain oxygen atoms. Considering changes in the attenuation as photon energy is reduced (<50 keV), the attenuation starts to rise more rapidly at slightly higher photon energies in PMMA and water due to the photoelectric absorption component than it does for PE. As a result, differences in $G_c(W)$ with tube potential are greater for PMMA (Table 7.1 (a and d)) and water (Figure 7.3 (a and d)), than for PE (Figure 7.2 (a and d)), while $G_p(W)$ values are greater for lower tube potentials for PE (Figure 7.2 (b and e)) than for PMMA and water, because the backscatter component is larger and the attenuation lower.

The beam qualities for the kV system used in this study are similar to those for conventional CT scanners, the half value layers (HVLs) at 125 kV and 100 kV being 8.7 mm and 7.55 mm Al, respectively. Moreover, the variations with tube potential found in this study are similar in form to those reported

for a CBCT scan obtained with a conventional CT scanner (Table 7.2), although slightly larger in magnitude. Therefore, it is likely that the variations found between the $G_x(W)$ functions (Figures 7.1 - 7.3) are not strongly influenced by the type of scanner CT or CBCT, but rather by use of the wider beams employed for CBCT scans. The main difference between the $G_x(W)$ Eq.(7.4) and $G_x(L)$ Eq.(7.2) functions is the use of beam width (W) instead of scan length (L). In a conventional CT scanner, $D_L(0)_x$ measurements at the centre and periphery of a phantom are built up from rotations of the same fan beam (≤ 40 mm) covering the specified length, and subsequently $D_L(0)_x$ values are normalized with respect to $CTDI_{vol}$ for the same beam width. However, in a CBCT scan, the beam is varied over a wide range of widths to measure $f(0,\infty)_{x,m}$ and subsequently normalized with respect to $CTDI_{w,ref}$ for a reference beam. The influence of scanning parameters at the centre and periphery of the phantom varies according to the change in geometry as the beam width increases from 40 mm to 500 mm. Photons near the edges of wider beams pass through the phantoms at oblique angles, and are therefore more heavily attenuated. This will change the relative magnitudes of doses measured at the centres and peripheries of the phantoms, as well as the path length through the phantoms contributing to the scatter. All of these factors will change with tube potential, which alters the photon energy distribution within the beams. Moreover, these differences will also vary with the attenuation and scattering properties of the phantom material. For a conventional CT scanner, the variation in beam geometry along the phantom is comparatively small, and normalization of $G_x(L)$ with respect to the $CTDI_{vol}$, which averages the dose over the x-y plane, is capable of eliminating most of the scan parameter differences. This view is supported by the lower differences found at W = 40 mm compared to those for wider beams, which increased with beam width (Figures 7.1 - 7.3). However, the $CTDI_w$ for the narrow reference beam that has been used for normalization of $G_x(W)$ Eq.(7.4) will not give the same averaging of the dose that occurs with the different widths of cone beams. Therefore, the differences in the geometry of the beams is considered to be the main reason for the discrepancy found between the results at different tube potentials obtained in the study at the centre of the PE body phantom (Figure 7.2 (d))

and those reported at the centre of the ICRU/AAPM phantom for a conventional CT scanner (ICRU, 2012).

The discrepancies between values of the proposed function $G_x(W)$ Eq.(7.4) for different tube potentials demonstrate an inherent weakness in its application for CBCT scans. These could be reduced by normalizing with respect to variables that take more account of the differences in scanning parameters and beam width such as:

(1) To normalize $f(0,\infty)_{x,m}$ with respect to $CTDI_{100,x}$ measured at the same position within the phantom (centre or periphery) instead of $CTDI_w$.

(2) To normalize every value of $f(0,\infty)_{x,m}$ with respect to $CTDI_{100,x}$ measured using the beam width (W) used for that $f(0,\infty)_{x,m}$ measurement instead of a reference beam width.

For the first factor, Figures 7.4 - 7.5 show $f(0,\infty)_{x,m}$ values calculated within head and body phantoms of different compositions for beams of width 40 – 500 mm normalized with respect to $CTDI_{100,x}$ obtained at the same position within the standard PMMA phantoms using a reference beam width of 40 mm. This factor reduced the variations with tube potential significantly at some positions, such as at the centre of the PMMA body phantom (Figure 7.5 (a)), but did not reduce the differences in others, such as for the periphery of the PE phantom (Figures 7.4 - 7.5 (d)). However, when the second factor was combined with the first, taking account of the different beam geometries, the variations with tube potential declined markedly at all positions for the head phantoms (Figure 7.6) and body phantoms (Figure 7.7). The application of the two factors appeared not only to cancel out the influence of the scanning parameters, but also the type of the scanner, since results for beams of width 40 – 240 mm calculated within the PMMA phantoms were in good agreement with those for a conventional CT scanner (Li et al., 2014b) (Figures 7.6 - 7.7 (a – b)), and the differences shown in Table 7.2 were eliminated. As the range of beam widths used in the present study was wider than that in (Li et al., 2014b) (30 – 250) mm, a discrepancy between the results outside this range was

anticipated as clearly seen in Figure 7.7 (a). The curves for $f(0,\infty)_{x,m}/CTDI_{100,x}$ (Figures 7.6 - 7.7) were entirely different from those for the $G_x(W)$ function (Figures 7.1 - 7.3), as expected from use of the same beam width to measure $f(0,\infty)_{x,m}$ and $CTDI_{100,x}$ as discussed in section 7.2.2.

Although the normalisation of $f(0,\infty)_{x,m}$ with respect to $CTDI_{100,x}$ measured at the same position and beam width (Figures 7.6 - 7.7) allowed the variations in the $G_x(W)$ functions with tube potential to be minimized (Figures 7.1 - 7.3), the use of $CTDI_{100,x}$ for beams of width > 100 mm does not provide a good practical solution as $CTDI_{100}$ values decline significantly when the primary beam width becomes wider than 100 mm as shown in Chapter 5 Figures 5.1 - 5.2. The influence of this decline on the $f(0,\infty)_{x,m}/CTDI_{100,x}$ values can be seen clearly in Figures 7.6 - 7.7 as the function starts to rise more rapidly at W > 100 mm. Therefore, this work recommends that a modification to the denominator of the $G_x(W)$ function Eq.(7.4) is proposed to achieve an equation that will tend to an asymptotic function for wide beams, in a similar manner to the $G_x(L)$ function, but still be independent of scan parameters.

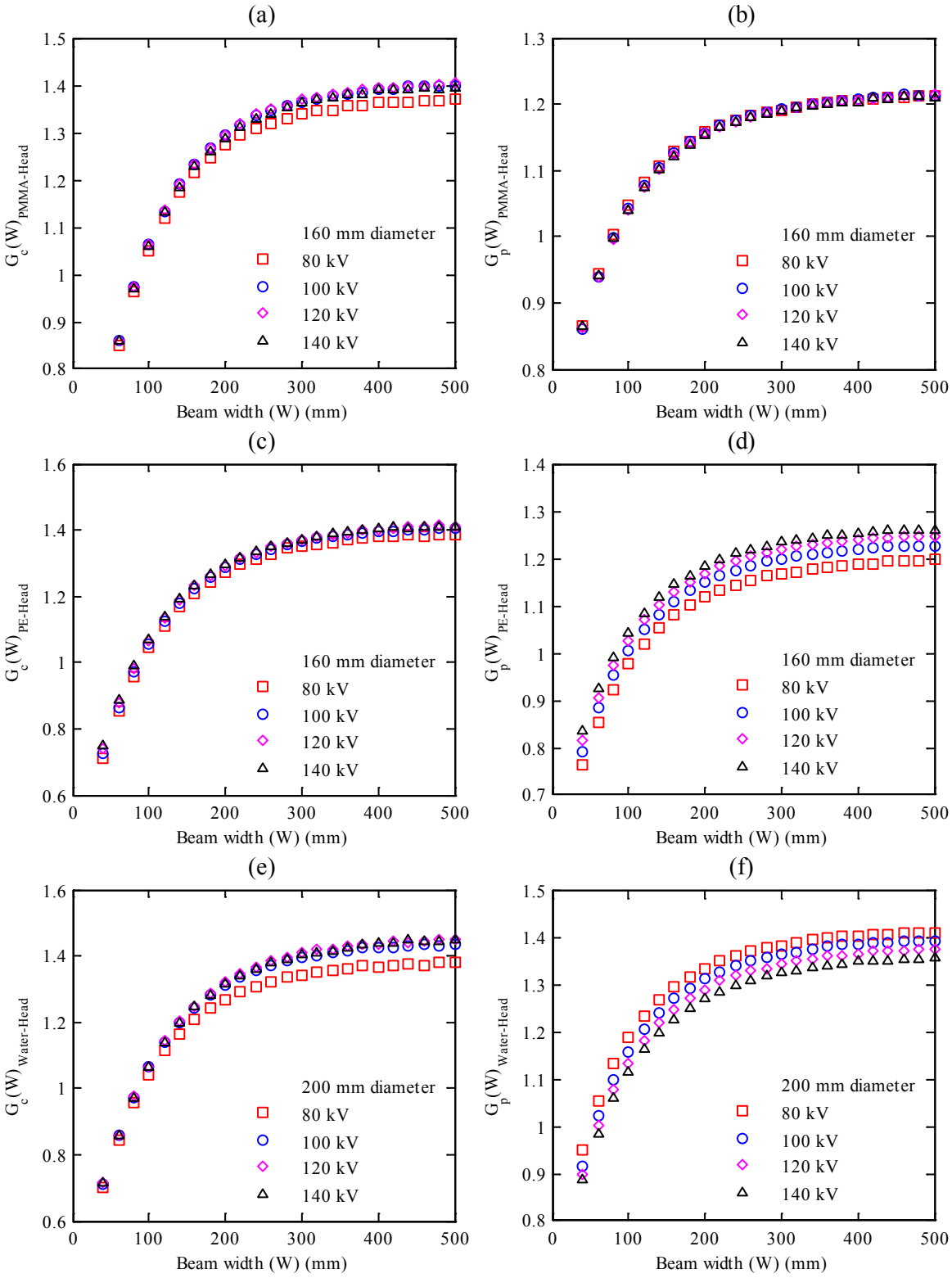

Figure 7.4: $f(0,\infty)_{x,m}$ values calculated within 600 mm long head phantoms of different compositions using beams of width W = 40 – 500 mm and normalized with respect to $CTDI_{100,x\text{-}40}$ measured at the same position within a 150 mm long PMMA head phantom (centre and periphery) using a reference beam of width W = 40 mm. (a – b) PMMA, (c – d) PE, and (e – f) water head phantoms (Table 7.1).

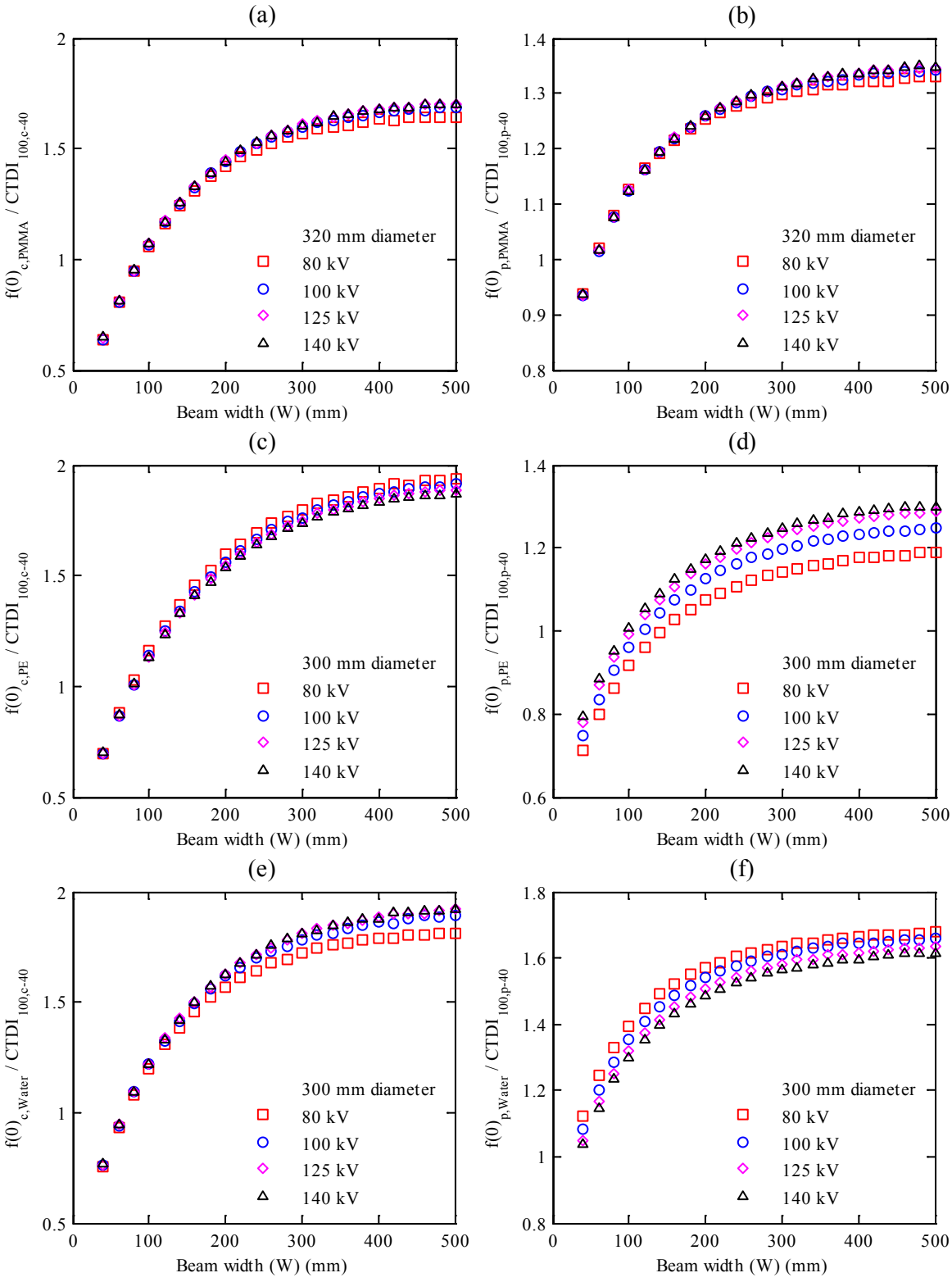

Figure 7.5: $f(0,\infty)_{x,m}$ values calculated within 600 mm long body phantoms of different compositions using beams of width W = 40 – 500 mm and normalized with respect to $CTDI_{100,x\text{-}40}$ measured at the same position within a 150 mm long PMMA body phantom (centre and periphery) using a reference beam of width W = 40 mm. (a – b) PMMA, (c – d) PE, and (e – f) water body phantoms (Table 7.1).

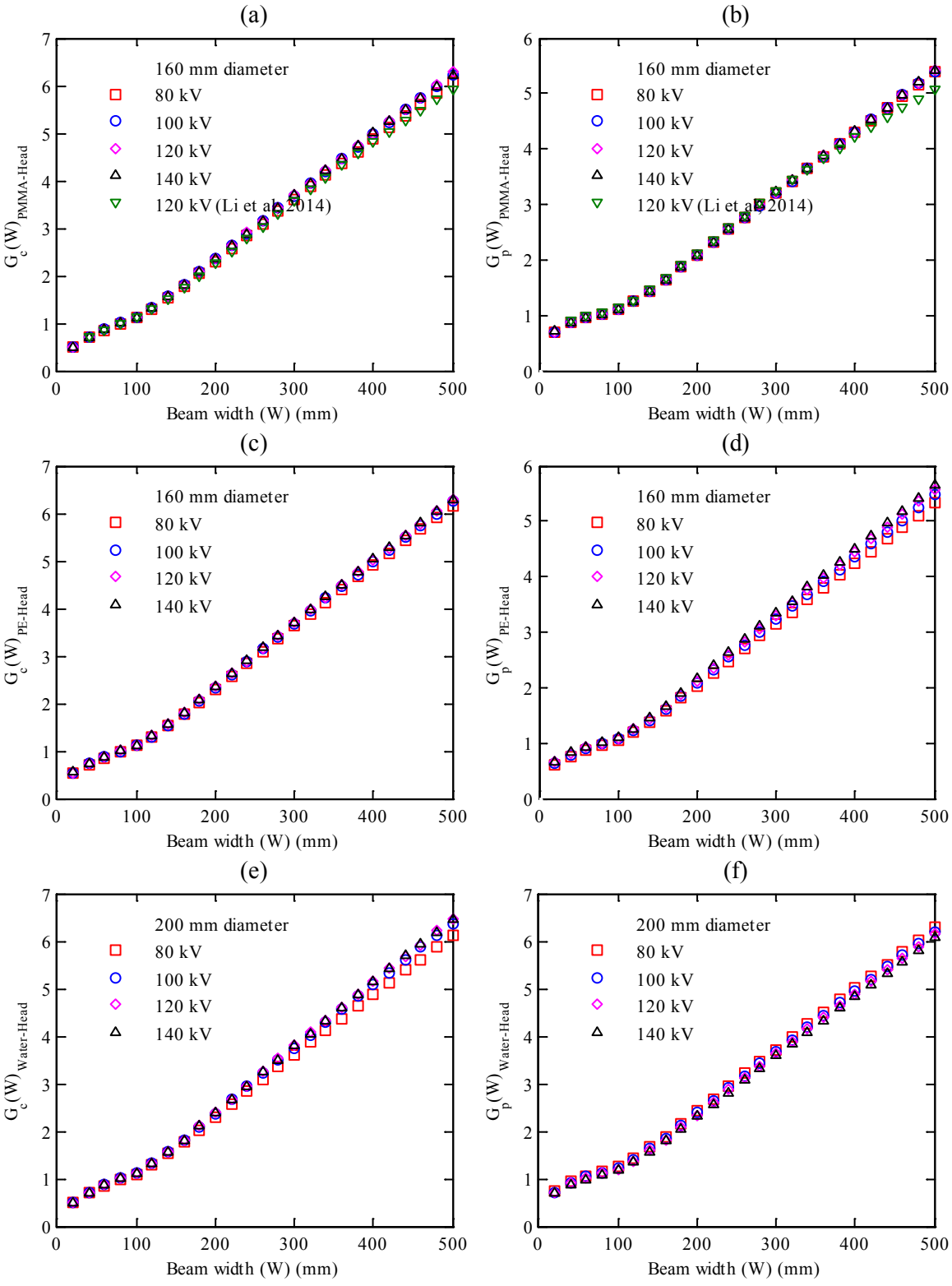

Figure 7.6: $f(0,\infty)_{x,m}$ values calculated within 600 mm long head phantoms of different compositions using beams of width W = 40 – 500 mm and normalized with respect to $CTDI_{100,x}$ measured at the same position within a 150 mm long PMMA head phantom (centre and periphery) and with the same beam widths. (a – b) PMMA, (c – d) PE, and (e – f) water head phantoms (Table 7.1).

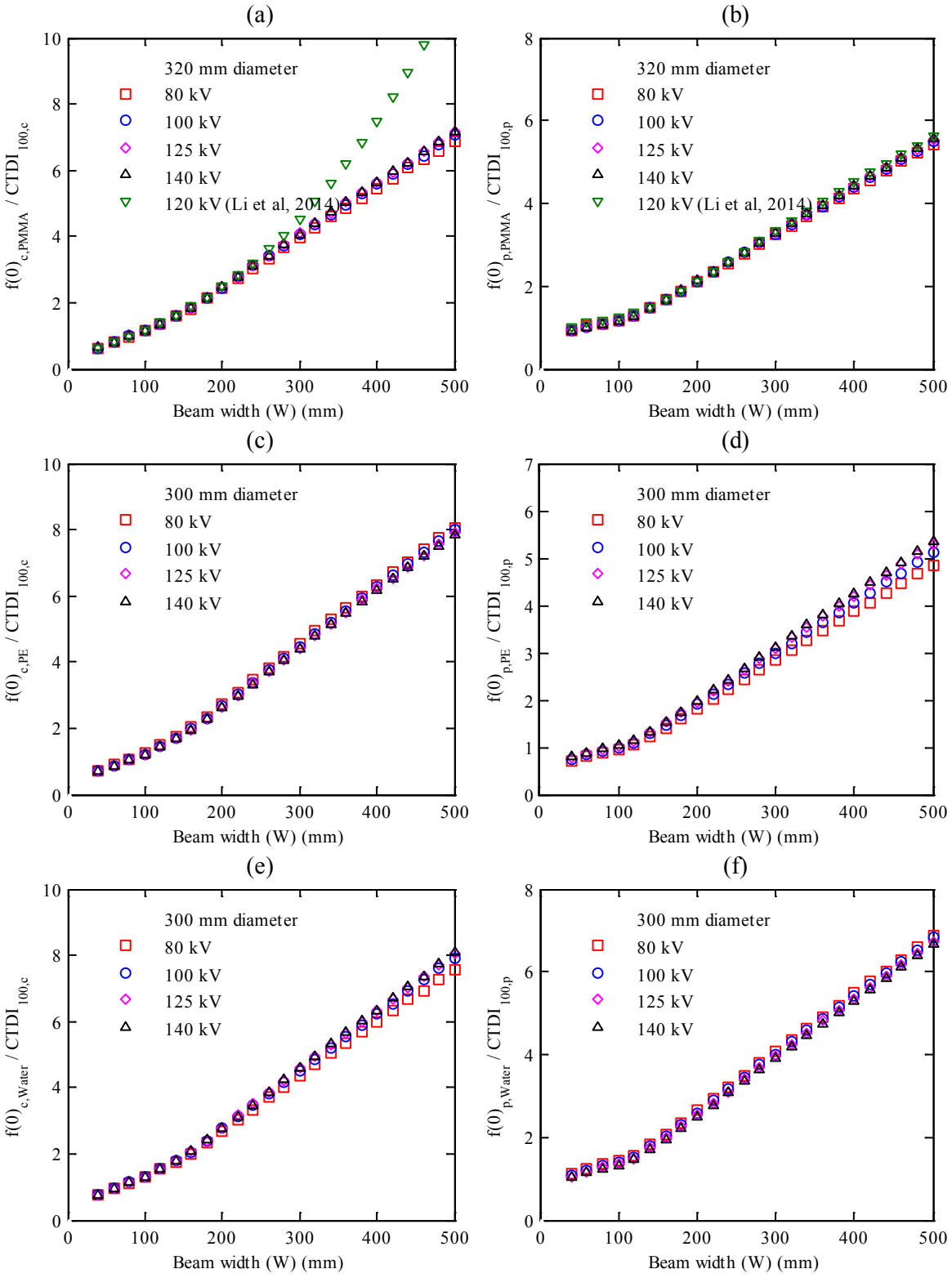

Figure 7.7: $f(0,\infty)_{x,m}$ values calculated within 600 mm long body phantoms of different compositions using beams of width W = 40 – 500 mm and normalized with respect to $CTDI_{100,x}$ measured at the same position within a 150 mm long PMMA body phantom (centre and periphery) and with the same beam widths. (a – b) PMMA, (c – d) PE, and (e – f) water body phantoms (Table 7.1).

7.3.2 Investigation of a Modified Function $G_x(W)_{100}$ for CBCT Scan Dosimetry

The main concept of the $G_x(L)$ and $G_x(W)$ functions is to evaluate the cumulative doses $D_L(0)_x$ and $f(0,\infty)_{x,m}$, while preserving the use of the CT dosimetry system, with the 100 mm pencil ionization chamber and the standard PMMA phantoms, which are available worldwide. Therefore, a modification should be applied to the denominator of the $G_x(W)$ function, $CTDI_{w,ref}$. taking into account the influence of the two factors discussed in section 7.3.1. The dose index $f_{100}(150)$ presented in Chapter 2 section 2.6.3 is based on evaluation of the dose in the middle of a scan of the standard PMMA phantoms averaged over the 100 mm length of a pencil ionization chamber. $f_{100}(150)$ is independent of wider beam widths, thus it is proposed for use in the denominator of a modified function $G_x(W)_{100}$ defined as:

$$G_x(W)_{100} = \frac{Nf(0,\infty)_x}{f_{100}(150)_x} \tag{7.6}$$

As $CTDI_{100}$ and $f_{100}(150)_x$ values are measured in the same manner, the MC results discussed in section 7.3.1 were re-analyzed to calculate $G_x(W)_{100}$ as:

$$\begin{aligned} G_c(W)_{100} &= \frac{f(0,\infty)_{c,m}}{f_{100}(150)_c} \\ G_p(W)_{100} &= \frac{f(0,\infty)_{p,m}}{f_{100}(150)_p} \\ G_a(W)_{100} &= \frac{f(0,\infty)_{w,m}}{f_{100}(150)_w} \end{aligned} \tag{7.7}$$

Figures 7.8 - 7.10 show the $G_x(W)_{100}$ functions calculated as described in Eq.(7.7) for the phantoms studied (Table 7.1). The functions show a weak dependency on tube potential with variations at some positions such as the periphery of the PE phantoms (Figure 7.9). However, the variations were much smaller than those found for the $G_x(W)$ functions (Figures 7.1 - 7.3) and did not vary significantly with beam width. The curves for the $G_x(W)_{100}$

functions were different from those for $G_x(L)$ and $G_x(W)$, because of the form of the $f_{100}(150)_x$ function in the denominator. $G_x(W)_{100}$ decreased steadily with beam width until ~150 mm after which the functions rose slightly. For beams of width < 150 mm, $f(0,\infty)_{x,m}$ was greater than $f_{100}(150)_x$, but differences between the values decreased with increasing beam width. Values of $f_{100}(150)_x$ were virtually constant for beams wider than 150 mm, as the outer parts of the beams did not interact with the phantom, whereas $f(0,\infty)_{x,m}$ values continued to rise approaching the equilibrium value $f_{eq}(0,\infty)_{x,m}$. This explains the slight increase in $G_x(W)_{100}$ for beams wider than 150 mm, especially at the centres of the phantoms. The relationship between the values for $f_{100}(150)_x$ and $f(0,\infty)_x$ have been discussed in detail in Chapter 6 Figures 6.3 - 6.6.

The $G_x(W)_{100}$ function described in Eq.(7.6) provides an option for CBCT scans, which is relatively independent of tube potential in the range 80 – 140 kV (Figures 7.8 - 7.10), that could be used for evaluating cumulative doses in long phantoms. This approach is well suited to CBCT applications such as those in radiotherapy, where the number of beam diameters and scanning parameters used is limited for the majority of examinations, and measurements of the $f_{100}(150)_x$ within standard dosimetry phantoms can readily be made for the beam widths used clinically. The $G_x(W)_{100}$ functions calculated within the PMMA phantoms were in good agreement with those calculated in (Li et al., 2014b) within the range 40 – 240 mm (Figure 7.8). Li et al. (2014b) used beams of width (30 – 250) mm, whereas a wider range was used in this study (40 – 500) mm. Thus, the discrepancy between the results outside this range was anticipated as explained earlier in section (7.3.1).

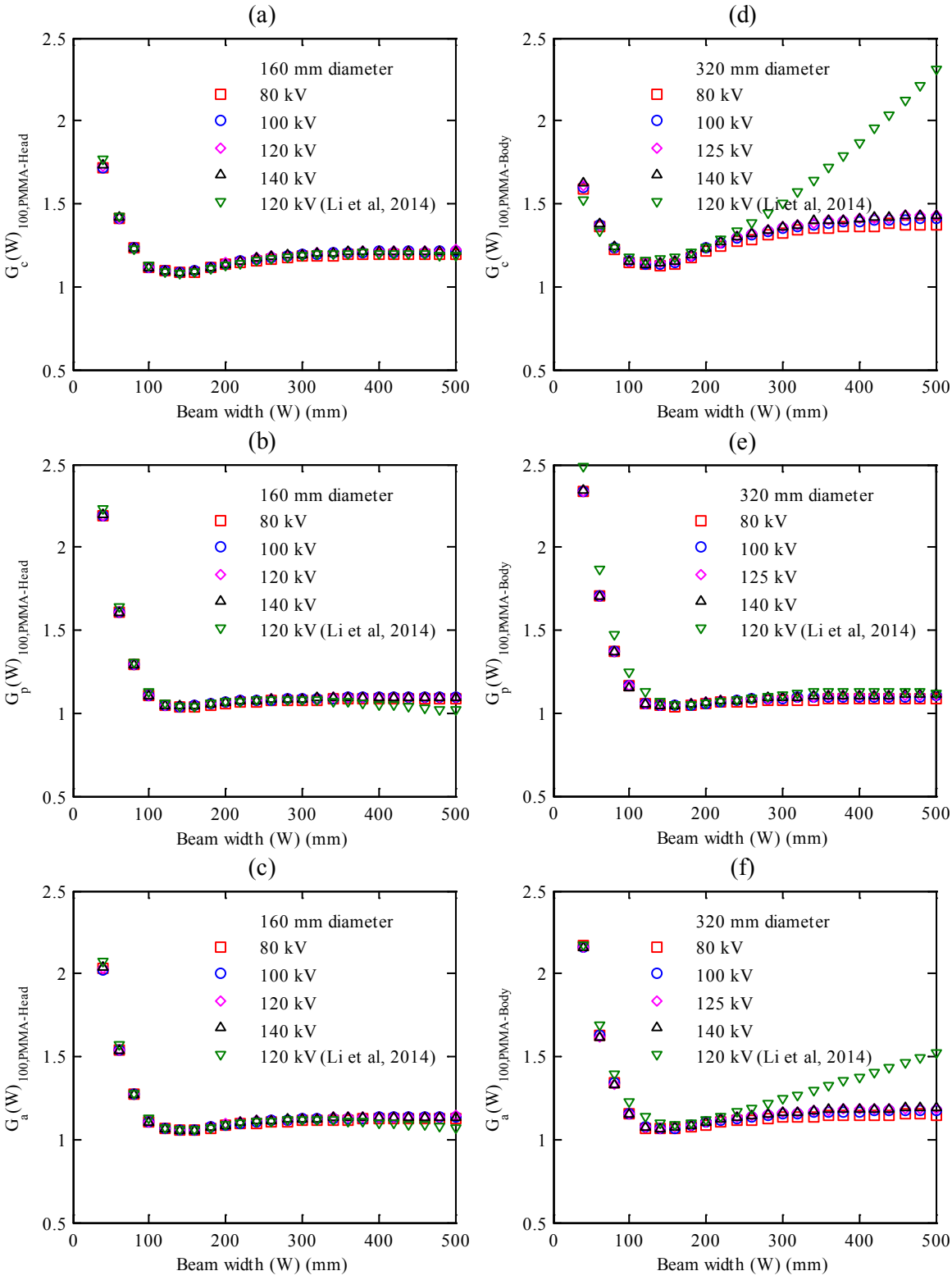

Figure 7.8: $G_c(W)_{100}$, $G_p(W)_{100}$, and $G_a(W)_{100}$ functions for $f(0,\infty)_{x,PMMA}$ values calculated within the 600 mm long PMMA phantoms for beams of width 40 – 500 mm and normalized with respect to $f_{100}(150)_x$ values calculated within the standard 150 mm long PMMA phantoms as in Eq.(7.7). (a – c) for the head phantoms and (d – f) for the body phantoms (Table 7.1). Results are compared with values reported in (Li et al., 2014b) at 120 kV.

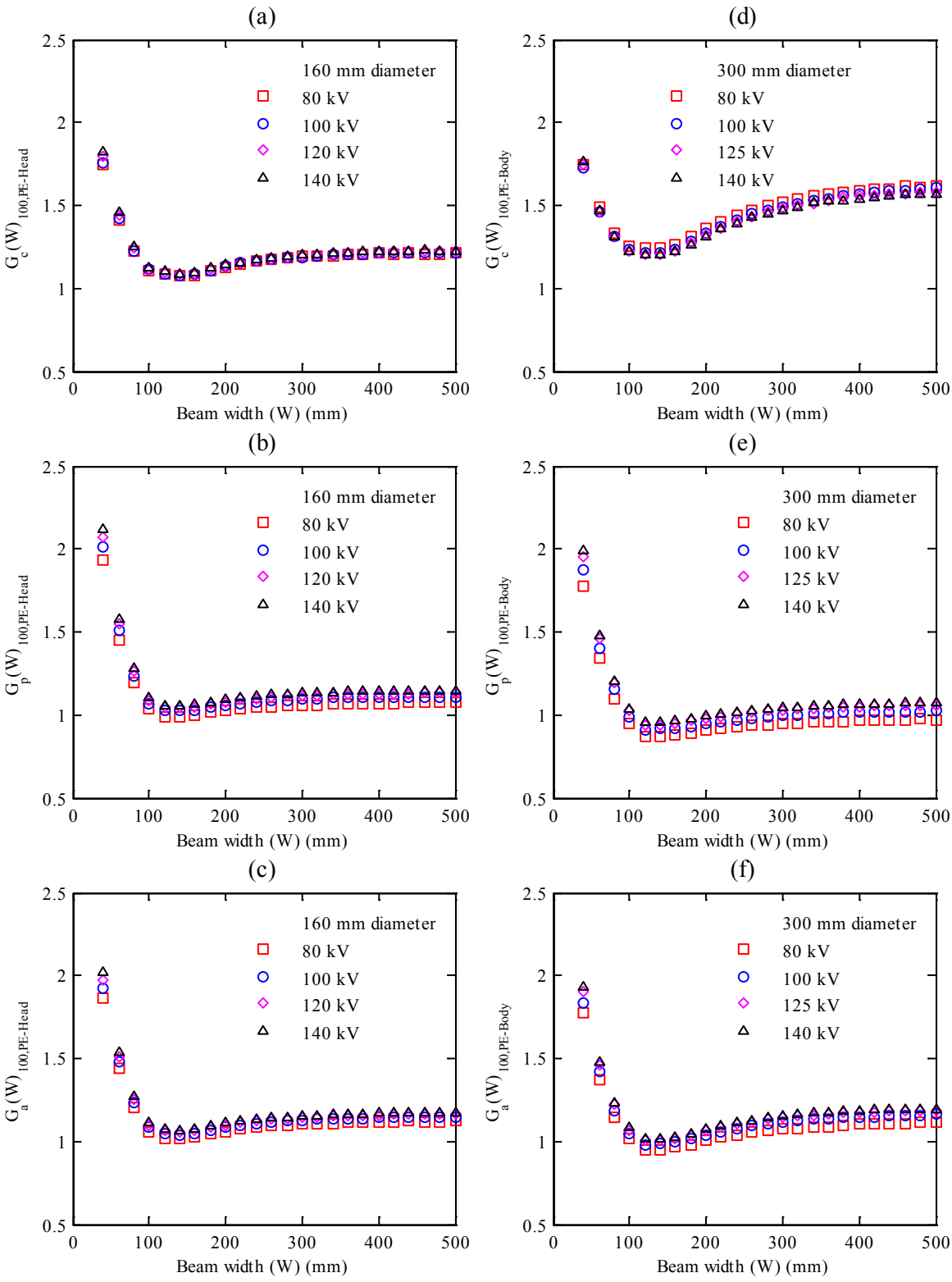

Figure 7.9: $G_c(W)_{100}$, $G_p(W)_{100}$, and $G_a(W)_{100}$ functions for $f(0,\infty)_{x,PE}$ values calculated within the 600 mm long PE phantoms for beams of width 40 – 500 mm and normalized with respect to $f_{100}(150)_x$ values calculated within the standard 150 mm long PMMA phantoms as in Eq.(7.7). (a – c) for the head phantoms and (d – f) for the body phantoms (Table 7.1).

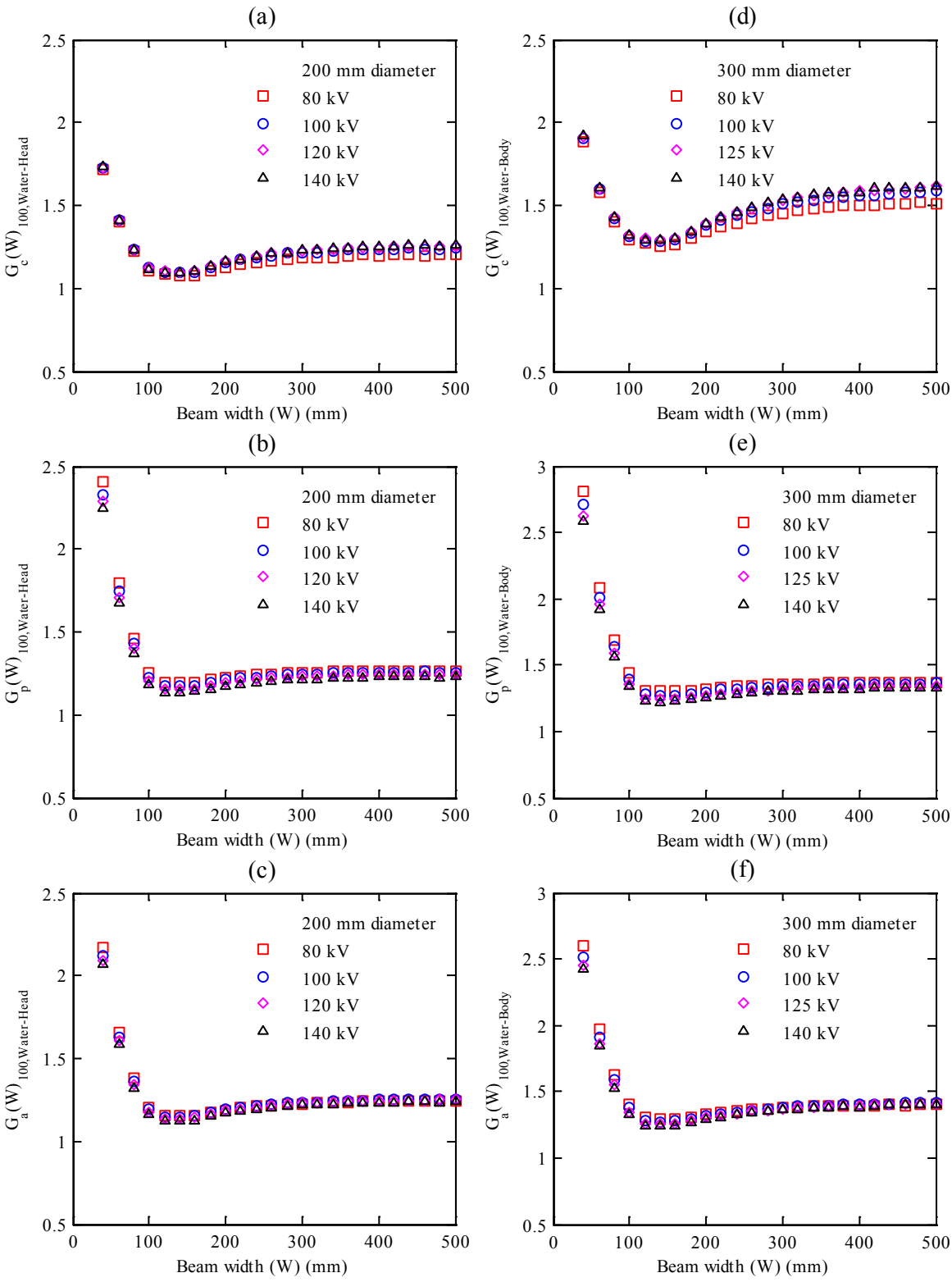

Figure 7.10: $G_c(W)_{100}$, $G_p(W)_{100}$, and $G_a(W)_{100}$ functions for $f(0,\infty)_{x,Water}$ values calculated within the 600 mm long water phantoms for beams of width 40 – 500 mm and normalized with respect to $f_{100}(150)_x$ values calculated within the standard 150 mm long PMMA phantoms as in Eq.(7.7). (a – c) for the head phantoms and (d – f) for the body phantoms (Table 7.1).

7.3.3 Derivation of Values of $G_x(W)_{100}$ for Use in CBCT Dosimetry

The $G_x(W)_{100}$ functions shown in Figures 7.8 - 7.10 were fitted to sixth-order polynomial equations in order to allow the functions to be calculated for different beam widths. As some of the $G_x(W)_{100}$ functions were complex such as those at the centre of the body phantoms (Figures 7.8 - 7.10 (d)), sixth-order equations were required to fit the $G_x(W)_{100}$ functions with high R^2 values. However, lower order polynomial equations can be obtained if only beams of width > 100 mm are considered. Coefficients of the fitted equations are given in Table 7.3, and these can be used to evaluate $f(0,\infty)_{x,m}$ for any beam width in the range 40 – 500 mm at tube potentials 80 – 140 kV within the PMMA, PE, or water, head and body phantoms used in this study (Table 7.1). All that is required are measurements of $f_{100}(150)_x$ within the standard PMMA phantoms for the beam width (W) being used. Subsequently, $f(0,\infty)_{x,m}$ is calculated as follows:

$$f(0,\infty)_{x,m} = G_x(W)_{100} \times f_{100}(150)_x \tag{7.8}$$

Table 7.4 shows experimental measurements for $f(0,\infty)_{x,PMMA}$ made within PMMA head and body phantoms of length 450 mm, and for $f_{100}(150)_x$ measured within the standard 150 mm long PMMA phantoms using the clinical beam width 198 mm. These measurements were used to evaluate the $G_x(W)_{100}$ function experimentally as in Eq.(7.7). The experimental values for the $G_x(W)_{100}$ function were, then, compared against those calculated by MC (Table 7.3). As shown in Table 7.4, the experimental and MC values for the $G_x(W)_{100}$ function were in good agreement, where the average differences within the head and body phantoms were 3.45% and 2.27%, respectively.

Table 7.3: Coefficients and R^2 of equations for $G_x(W)_{100}$ as a function of beam width W (in mm) for relationships shown in Figures 7.8 - 7.10. The functions were fitted to sixth-order polynomial equations for beams of width 40 – 500 mm at tube potentials 80 – 140 kV.

$$G_x(W)_{100} = P_1 W^6 + P_2 W^5 + P_3 W^4 + P_4 W^3 + P_5 W^2 + P_6 W + P_7$$

Coefficients	Head			Body		
	Centre	Periphery	Weighted	Centre	Periphery	Weighted
			PMMA			
P_1	2.721×10^{-15}	6.906×10^{-15}	5.459×10^{-15}	9.872×10^{-16}	6.396×10^{-15}	5.057×10^{-15}
P_2	-5.402×10^{-12}	-1.304×10^{-11}	-1.040×10^{-11}	-2.301×10^{-12}	-1.223×10^{-11}	-9.778×10^{-12}
P_3	4.339×10^{-09}	9.891×10^{-09}	7.975×10^{-09}	2.154×10^{-09}	9.429×10^{-09}	7.636×10^{-09}
P_4	-1.794×10^{-06}	-3.841×10^{-06}	-3.135×10^{-06}	-1.028×10^{-06}	-3.736×10^{-06}	-3.070×10^{-06}
P_5	3.982×10^{-04}	8.001×10^{-04}	6.618×10^{-04}	2.585×10^{-04}	7.980×10^{-04}	6.659×10^{-04}
P_6	-4.388×10^{-02}	-8.393×10^{-02}	-7.017×10^{-02}	-3.076×10^{-02}	-8.640×10^{-02}	-7.283×10^{-02}
P_7	2.947	4.484	3.956	2.483	4.728	4.183
R^2	0.99	0.99	0.99	0.98	0.99	0.99
			PE			
P_1	3.243×10^{-15}	5.916×10^{-15}	4.996×10^{-15}	1.360×10^{-15}	4.552×10^{-15}	3.768×10^{-15}
P_2	-6.347×10^{-12}	-1.124×10^{-11}	-9.556×10^{-12}	-3.016×10^{-12}	-8.814×10^{-12}	-7.400×10^{-12}
P_3	5.022×10^{-09}	8.587×10^{-09}	7.362×10^{-09}	2.711×10^{-09}	6.890×10^{-09}	5.879×10^{-09}
P_4	-2.046×10^{-06}	-3.360×10^{-06}	-2.909×10^{-06}	-1.255×10^{-06}	-2.772×10^{-06}	-2.407×10^{-06}
P_5	4.481×10^{-04}	7.050×10^{-04}	6.170×10^{-04}	3.090×10^{-04}	6.010×10^{-04}	5.314×10^{-04}

P_6	-4.885×10^{-02}	-7.417×10^{-02}	-6.551×10^{-02}	-3.611×10^{-02}	-6.562×10^{-02}	-5.861×10^{-02}
P_7	3.135	4.065	3.746	2.769	3.719	3.492
R^2	0.99	0.98	0.98	0.99	0.96	0.96
			Water			
P_1	2.830×10^{-15}	6.777×10^{-15}	5.397×10^{-15}	1.707×10^{-15}	6.711×10^{-15}	5.471×10^{-15}
P_2	-5.607×10^{-12}	-1.286×10^{-11}	-1.032×10^{-11}	-3.652×10^{-12}	-1.292×10^{-11}	-1.063×10^{-11}
P_3	4.493×10^{-09}	9.813×10^{-09}	7.955×10^{-09}	3.183×10^{-09}	1.004×10^{-08}	8.347×10^{-09}
P_4	-1.853×10^{-06}	-3.836×10^{-06}	-3.144×10^{-06}	-1.434×10^{-06}	-4.012×10^{-06}	-3.378×10^{-06}
P_5	4.102×10^{-04}	8.043×10^{-04}	6.671×10^{-04}	3.462×10^{-04}	8.649×10^{-04}	7.378×10^{-04}
P_6	-4.493×10^{-02}	-8.469×10^{-02}	-7.089×10^{-02}	-4.045×10^{-02}	-9.434×10^{-02}	-8.119×10^{-02}
P_7	2.975	4.637	4.064	3.051	5.301	4.756
R^2	0.98	0.99	0.99	0.96	0.99	0.99

Table 7.4: Experimental measurements of $f(0,\infty)_{x,PMMA}$ within PMMA head and body phantoms 450 mm in length and $f_{100}(150)_x$ in standard 150 mm long PMMA phantoms, using the clinical beam width 198 mm at 100 kV for the head and 125 kV for the body phantom. The $G_x(W)_{100}$ functions for PMMA were calculated from the experimental measurements (Exp) using Eq.(7.7) and from the fitted equations in (Table 7.3) derived from MC results. The $G_x(W)_{100}$ functions for PE and water were calculated from the fitted equations in (Table 7.3) as in Eq.(7.8). $\left[Difference\,(\%) = \left(G_x(W)_{100,PMMA,MC} - G_x(W)_{100,PMMA,Exp} \,/\, G_x(W)_{100,PMMA,Exp}\right) \times 100\right]$.

	Head phantom			Body phantom		
	Centre	Periphery	Weighted	Centre	Periphery	Weighted
			PMMA			
$f(0,\infty)_{x,PMMA,Exp}$ (mGy/100 mAs)	2.50	2.26	2.34	1.62	1.98	1.86
$f_{100}(150)_x$ (mGy/100 mAs)	2.32	2.18	2.22	1.29	1.84	1.66
$G_x(W)_{100,PMMA,Exp}$	1.08	1.04	1.06	1.26	1.08	1.12
$G_x(W)_{100,PMMA,MC}$	1.13	1.07	1.09	1.22	1.06	1.10
Difference (%)	4.63	2.88	2.83	-3.17	-1.85	-1.79
			PE			
$G_x(W)_{100,PE,MC}$	1.13	1.07	1.09	1.33	0.96	1.04
$f(0,\infty)_{x,PE,MC}$ (mGy/100 mAs)	2.63	2.33	2.42	1.71	1.76	1.74
			Water			
$G_x(W)_{100,Water,MC}$	1.15	1.20	1.18	1.37	1.29	1.31
$f(0,\infty)_{x,Water,MC}$	2.66	2.62	2.62	1.76	2.37	2.18

The experimental measurements for $f_{100}(150)_x$ were also used to assess $f(0,\infty)_{x,m}$ within the PE and water head and body phantoms using Eq.(7.8). Table 7.4 shows that the $f(0,\infty)_c$ value within the water head phantom was slightly larger than those in the PMMA and PE head phantoms, but all were within a factor of 1.06. $f(0,\infty)_c$ within the water and PE body phantoms were comparable within a factor of 1.02 and slightly larger than that for the PMMA body phantom. These findings were consistent with $CTDI_\infty$ values of (Zhou and Boone, 2008). For the periphery, however, values for $f(0,\infty)_p$ calculated within the water head and body phantoms were greater than those for the PMMA and PE phantoms. $f(0,\infty)_p$ for the water head and body phantoms were 16% and 20% larger, respectively, than those in the PMMA phantoms. These findings were also in agreement with those of (Zhou and Boone, 2008).

7.3.4 Capability of the $G_x(W)_{100}$ Functions for Different CT and CBCT Scanners

As mentioned previously, ICRU compared the $G_c(L)$ functions for three different conventional CT scanners and reported that the parameters of any scan are cancelled out by normalization to the $CTDI_{vol}$, and the effect of CT scanner model is also eliminated (ICRU, 2012). Li et al. (2014b) showed that their results obtained with a full 360° scan using a Somatom Definition dual source CT were in good agreement with those of a C-arm flat detector CT (Siemens Axiom Artis) acquired with a partial 200° scan without bowtie filters (Kyriakou et al., 2008), a Varian OBI system (Osei et al., 2009), and a Toshiba Aquilion ONE CT scanner (Geleijns et al., 2009). These investigations, including the (Li et al., 2014b) study as shown in Figure 7.8, were in good agreement with the results reported in the previous chapter (Tables 6.3 - 6.4). The results for CBCT scans acquired with a partial 200° scan were also found to be comparable to the those acquired with a full 360° scan in Chapter 5 (Figures 5.1 - 5.2) and Chapter 6 (Figures 6.3 - 6.6). Moreover, the efficiency values for $CTDI_{100}$ are comparable for a wide range of CT and CBCT scanners as shown in Chapter 5 (Table 5.4). Dixon and Boone (2010) compared the approach to equilibrium functions for two MSCT scanners (GE 16 channel and 64 channel scanners) and a CBCT scanner (256-

slice CT scanner) employed with the stationary table mode, and again reported good agreement in results between scanners.

These findings indicate that the effect of CT scanner is cancelled out when the effects of the scanning parameters are eliminated by using relative measurements, i.e. a dose ratio, of two dose indices measured with identical scanning parameters as discussed in sections 7.3.1 and 7.3.2. This may give a good indication for the suitability of utilizing the equations (Table 7.3) for different CT or CBCT scanners employed with wide beams 40 – 500 mm and the stationary table mode at 80 – 140 kV taking into account the dependence of the functions on diameter and composition of the phantom. The functions $G_x(L)$ and $G_x(W)_{100}$ have been derived to allow the new dosimetry quantities to be calculated from measurements made with the standard equipment. The main strength of the $G_x(L)$ function for MSCT scanners proposed by (ICRU, 2012) and the modified function $G_x(W)_{100}$ investigated in the present study is that they are relatively independent of scanning parameters including the tube potential. The functions enable the evaluation of $D_L(0)_x$ or $f(0,\infty)_{x,m}$ without the need for long phantoms of PMMA, PE, or water, which are heavy and difficult to handle in the scanning room and to transport between hospitals.

7.4 Conclusion

The aim of this study was to extend application of the $G_x(L)$ function, which can be used to derive the cumulative dose $D_L(0)_x$ in larger phantoms for standard MSCT scans (ICRU, 2012) to CBCT scans with stationary tables. The main difference is that the beam width (W) determines the length of the scan along the rotation axis (z-axis) rather than the number and pitch of the tube rotations. An analogous function $G_x(W)$ normalized with respect to the $CTDI_w$ of a narrow reference beam showed a dependence on tube potential that varied with phantom composition. This differed from results at the centre of the ICRU/AAPM PE body phantom reported for conventional CT scanners (ICRU, 2012). This is considered to be due to differences in geometry between the narrow fan beams used in MSCT scans and wide beams used for CBCT scans. A modified function $G_x(W)_{100}$, for which

cumulative doses $f(0,\infty)_{x,m}$ are normalized with respect to an alternative dose index $f_{100}(150)_x$ measured by a 100 mm ionization chamber with similar scan parameters and beam width at the same position within standard PMMA phantoms, was found to be relatively independent of beam quality over the range of tube potentials 80 – 140 kV. The $G_x(W)_{100}$ functions have been fitted to sixth-order polynomial equations, which can be utilized to evaluate $f(0,\infty)_{x,m}$ within infinitely long PMMA, PE and water head and body phantoms. These are valid for beam widths of 40 – 500 mm at 80 – 140 kV at the centres and peripheries of the phantoms. They allow cumulative doses in long phantoms to be evaluated from measurements of $f_{100}(150)_x$ at the centre and periphery of the standard PMMA phantoms for the beam of interest. It may be possible to apply the fitted equations to calculate cumulative doses for any CT or CBCT scan acquired with stationary table mode. Results of this study have been published in (Abuhaimed et al., 2015b).

Chapter 8

The Efficiency of $f(0,150)_{x,PMMA}$ and $f(0,150)_{x,PE}$ in Evaluating $f(0,\infty)_{x,m}$

8.1 Introduction

The suitability of using $CTDI_{100}$ dosimetry equipment for the estimation of $f(0,\infty)_{x,m}$ was investigated in the previous chapter through the use of $G_x(W)_{100}$ function. The $G_x(W)_{100}$ function has the potential to provide a practical approach to dosimetry avoiding the use of long phantoms. It is suitable for tube potentials of 80 – 140 kV, and serves as a correction factor applied to $f_{100}(150)_x$ for CBCT scans. This chapter presents an investigation of two other approaches that might be utilized to avoid the use of long phantoms: (1) to investigate the possibility of using a small chamber within the standard PMMA phantoms $f(0,150)_{x,PMMA}$ to evaluate $f(0,\infty)_{x,m}$ based on the AAPM method (AAPM, 2010). This approach is similar to the concept behind the $G_x(W)_{100}$ function. The only difference is in the use a small ionization chamber instead of the standard 100 mm pencil ionization chamber. (2) As the density of PE is lower than that for PMMA (Chapter 7 Table 7.1), and is widely available and low cost, the present study also investigated the suitability of using 150 mm long PE phantoms $f(0,150)_{x,PE}$ for assessment of cumulative dose $f(0,\infty)_{x,PE}$ within the long PE phantoms proposed by ICRU/AAPM shown in Chapter 2 Figure 2.10 (b). The relationships between results from the short and long phantoms studied using different scan parameters and beams of width 40 – 500 mm and tube potentials of 80 – 140 kV, were fitted to polynomial equations, from which conversion factors were derived to allow evaluation of the cumulative dose within a long phantom from a single measurement made within a standard PMMA phantom.

8.2 Materials and Methods

8.2.1 The Efficiency of $f(0,150)$

In order to investigate the possibility of making measurements with a small chamber within standard PMMA phantoms to evaluate cumulative doses measured under scatter equilibrium conditions in infinitely long phantoms $f(0,\infty)_{x,m}$, the cumulative dose values measured in 150 mm long phantoms $f(0{,}150)_{x,PMMA}$ were normalized with respect to $f(0,\infty)_{x,m}$. The MC calculations were performed for head and body phantoms. $f(0,\infty)_{x,m}$ values were calculated in phantoms made from PMMA, PE and water. The results are expressed in terms of the efficiency of the standard PMMA phantoms in recording $f(0,\infty)_{x,m}$ as (Li et al., 2014b):

$$\varepsilon(PMMA/m)_{x,kV} = \frac{f(0{,}150)_{x,PMMA}}{f(0,\infty)_{x,m}} \tag{8.1}$$

where $f(0{,}150)_{x,PMMA}$ and $f(0,\infty)_{x,m}$ were calculated with the same nominal beam widths (W), scan parameters, and positions within the phantoms.

The influence of the tube potential in the range studied on $\varepsilon(PMMA/m)_{x,kV}$ values was investigated by normalizing $\varepsilon(PMMA/m)_{x,80kV}$, $\varepsilon(PMMA/m)_{x,100kV}$ and $\varepsilon(PMMA/m)_{x,140kV}$ values with respect to those of $\varepsilon(PMMA/m)_{x,120kV}$ for the head phantom and $\varepsilon(PMMA/m)_{x,125kV}$ for the body phantom as follows:

$$Head = \frac{\varepsilon(PMMA/m)_{x,kV}}{\varepsilon(PMMA/m)_{x,120kV}} \quad , \quad Body = \frac{\varepsilon(PMMA/m)_{x,kV}}{\varepsilon(PMMA/m)_{x,125kV}} \tag{8.2}$$

The suitability of a 150 mm long PE phantom $\varepsilon(PE/PE)_{x,kV}$ for assessment of cumulative doses in the ICRU/AAPM phantom was investigated in a similar manner and results presented in the form:

$$\varepsilon(PE/PE)_{x,kV} = \frac{f(0,150)_{x,PE}}{f(0,\infty)_{x,PE}} \quad (8.3)$$

The scanning parameters employed to evaluate the efficiencies in Eqs.(8.1) and (8.3) were similar to those used for the $G_x(W)_{100}$ function in Chapter 7, Head-360 and Body-360 presented in section 7.2.3.

8.2.2 Conversion Factors for $f(0,\infty)_{x,m}$

From the efficiency values obtained in section 8.2.1, conversion factors $(C_f s)$ for the scan parameters employed were derived. The main purpose was to allow the evaluation of $f(0,\infty)_{x,m}$ for the infinitely long head and body phantoms from single measurements made within standard PMMA phantoms $f(0,150)_{x,PMMA}$. $(C_f s)$ were derived as:

$$C_f(PMMA/m)_{x,kV} = \frac{1}{\varepsilon(PMMA/m)_{x,kV}} = \frac{f(0,\infty)_{x,m}}{f(0,150)_{x,PMMA}} \quad (8.4)$$

Once $C_f(PMMA/m)_{x,kV}$ is known, the cumulative doses under scatter equilibrium conditions for a specific beam width and at a given tube potential can then be assessed as:

$$f(0,\infty)_{x,m} = C_f(PMMA/m)_{x,kV} \times f(0,150)_{x,PMMA} \quad (8.5)$$

8.2.3 Monte Carlo Calculations of the Efficiency

Parameters of the scanning protocols Head-360 and Body-360 were used to generate PHSP files using BEAMnrc and then run in DOSXYZnrc as described in section 4.4.2 to calculate the efficiency values as in Eqs.(8.1) and (8.3) for each protocol at each tube potential. The efficiency values were, then, used to derive the correction factors $C_f(PMMA/m)_{x,kV}$ as in Eq.(8.4). The

phantom compositions and diameters were similar to those employed for the $G_x(W)_{100}$ function listed in Table 7.1.

8.2.4 Experimental Measurements of $f(0,150)_{x,PMMA}$ and $f(0,\infty)_{x,PMMA}$

The accuracy of the correction factors derived from MC calculations in section 8.2.2 were evaluated by comparing the MC factors against those obtained from experimental measurements using the same scanning protocols Head-360 and Body-360. Moreover, in order to investigate the sensitively of the MC factors to the different scanning parameters and equipment factors namely the bowtie filter, the scan diameter, and the acquisition mode, further experimental measurements were made using the scanning protocols Head-200 and Body-200. The set ups used for $f(0,150)_{x,PMMA}$ and $f(0,\infty)_{x,PMMA}$ measurements were similar to those described in Chapter 4 section 4.4.1.3 for $f(0,150)_{x,PMMA}$ measurements and Chapter 6 section 6.2.3 for $f(0,\infty)_{x,PMMA}$ measurements.

8.3 Results and Discussion

8.3.1 The Efficiency of $f(0,150)_{x,PMMA}$

Figure 8.1 shows the efficiency values $\varepsilon(PMMA/m)_{x,kV}$ calculated using Eq.(8.1) at 120 kV for head phantoms and at 125 kV for body phantoms. $\varepsilon(PMMA/PMMA)_{x,kV}$ values at the central and peripheral axes declined as the beam width increased (Figure 8.1 (a and d)). The central $\varepsilon(PMMA/PMMA)_{c,kV}$ values for the head phantom were greater than those for the body, and the peripheral $\varepsilon(PMMA/PMMA)_{p,kV}$ ones were almost identical for the head and body phantoms, but higher than those at the centre. The variations in results at the centres of the phantoms arose from the differences in phantom diameters. There was less attenuation of the primary beam in the head phantom, so the scatter formed a proportionately smaller component of the measurement at the centre.

In addition, Dixon and Boone (2011) showed that the scatter tails in the dose profile from a beam of width 28 mm at the centre of a PMMA body

phantom extended to ±200 mm, i.e. 400 mm along the rotation axis (z-axis). Therefore, the scatter tails extend beyond the length of the standard phantoms, thus $f(0{,}150)_{x,PMMA}$ will not capture the entire absorbed dose that would be deposited in a longer phantom even for a narrow beam (Figure 8.1 (a and d)). The extents of the scatter tails, although related to the nominal beam width, are influenced by factors such as tube potential, phantom composition and diameter, the position within the phantom at which the measurements are made, and the use of a bowtie filter (Boone, 2009, ICRU, 2012, Li et al., 2014a). This, therefore, affects the scatter to primary ratio (SPR) values, which were discussed in Chapter 6 section 6.3.3 (Boone, 2009). The variations in SPR values and the inability of the standard phantoms to detect the whole scatter tails determine the variations in $\varepsilon(PMMA/PMMA)_{x,kV}$ values between the central and peripheral axes and between the phantoms.

The relationship between $\varepsilon(PMMA/PMMA)_{x,kV}$ and beam width can be divided into three regions (Figure 8.1 (a and d)): (1) The first region extended from narrow beam widths up to ~150 mm. In this region, the whole primary beam was within the phantom length. Therefore, both $f(0{,}150)_{x,PMMA}$ and $f(0,\infty)_{x,PMMA}$ values increased with beam width, although the contribution from scattered radiation to $f(0,\infty)_{x,PMMA}$ increased more rapidly than that to $f(0{,}150)_{x,PMMA}$. (2) The second region began at beam widths > 150 mm, when the beam extended beyond the length of the standard PMMA phantoms, so that a part of the primary beam did not contribute to the scattered radiation. As a result, $f(0{,}150)_{x,PMMA}$ values were virtually constant, as further increases in beam width made a negligible contribution to measurements at z = 0. In contrast, $f(0,\infty)_{x,PMMA}$ continued to rise, and so $\varepsilon(PMMA/PMMA)_{x,kV}$ declined at both the centre and periphery of the phantoms. (3) The third region began when further increases in beam width led to minimal contributions to $f(0,\infty)_{x,PMMA}$ values. This occurred when the beam width approached the equilibrium value (a_{eq}), at which further increases in beam width made a negligible contribution to $f(0,\infty)_{x,PMMA}$ as the scattered radiation did not reach the middle of the phantom $(z = 0)$ (AAPM, 2010, Dixon and Boone, 2010). The equilibrium beam width, which depends on the phantom diameter and the

position within the phantom, is larger than 400 mm (AAPM, 2010, ICRU, 2012). Since the increase in $f(0,\infty)_{x,PMMA}$ in this region was much lower compared to the second region, the decline in $\varepsilon(PMMA/PMMA)_{x,kV}$ was less and values became virtually constant.

Li et al. (2014b) studied $\varepsilon(PMMA/PMMA)_{x,kV}$ values for a Somatom Definition dual source CT scanner using MC simulations. The efficiency values were investigated for standard and 900 mm long head and body PMMA phantoms of the same diameters used in this study. The scan parameters were a tube potential of 120 kV, a full 360° rotation scan, head and body bowtie filters, and beams ranging in width from 30 mm to 250 mm. As shown in (Figure 8.1 (a and d)), $\varepsilon(PMMA/PMMA)_{x,kV}$ values from this study are in good agreement with those of (Li et al., 2014b) within ±1.53% and ±0.56% at the centre and periphery of the head phantom with variations of the mean of 0.72% and 0.10%, respectively, and within ±1.56% and ±0.55% for the body phantom with variations in the mean of 0.88% and 0.28%, respectively. Although the kV systems (CT and CBCT scanners) and the lengths of the long phantoms were different in the two studies, the differences are minor.

(Figure 8.1 (b and e)) and (Figure 8.1 (c and f)) show the efficiency values for $\varepsilon(PMMA/PE)_{x,kV}$ and $\varepsilon(PMMA/Water)_{x,kV}$, respectively. Although there are similarities in form with results comparing measurements in standard PMMA phantoms, there are substantial differences. $\varepsilon(PMMA/PMMA)_{x,kV}$ results were for phantoms of similar diameter and composition, and so were only influenced by differences in the lengths of the phantoms. However, the $\varepsilon(PMMA/PE)_{x,kV}$ and $\varepsilon(PMMA/Water)_{x,kV}$ values are from comparisons of phantoms with different diameters, compositions, and lengths. Differences in diameter will affect attenuation of the transmitted beam reaching the centre, while differences in phantom material will alter the mass attenuation coefficients and mass energy-absorption coefficients, and hence both the attenuation and the extent of the scatter tails (Zhou and Boone, 2008, Boone, 2009).

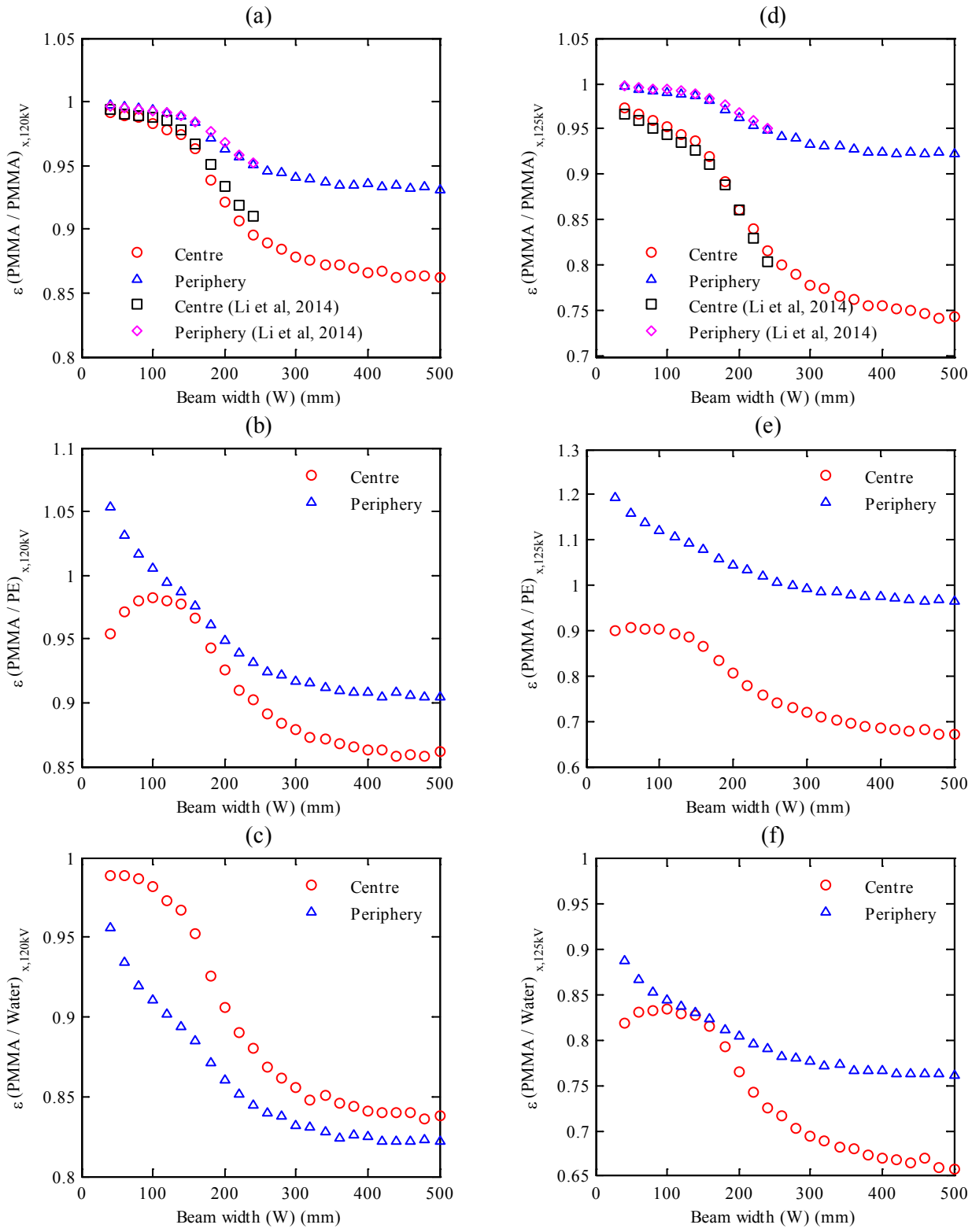

Figure 8.1: The efficiency values calculated as in Eq.(8.1) for (a) $\varepsilon(PMMA/PMMA)_{x,120kV}$ (b) $\varepsilon(PMMA/PE)_{x,120kV}$ and (c) $\varepsilon(PMMA/Water)_{x,120kV}$ at the centre and periphery of the head phantoms at 120 kV, and (d – f) for the body phantoms at 125 kV. $\varepsilon(PMMA/PMMA)_{x,kV}$ values for the head and body phantoms (a and d) were compared to those of (Li et al., 2014b) obtained within PMMA phantoms using a Somatom Definition dual source CT scanner at 120 kV and beams of width 30 – 250 mm.

PMMA has a higher attenuation than both PE and water, and the standard PMMA body phantom has a larger diameter than those proposed for other phantoms (Table 7.1). Differences in the primary radiation transmitted to the centres of the phantoms are apparent in the lower ratios for narrow beams (Figure 8.1 (b - c and e - f)). The scatter component in measurements at the centres increased with beam width, thus the influence of attenuation of the primary beam on the dose level at the centre then declined and the efficiency values increased accordingly up to beam widths of the order of 100 mm. Thereafter, the efficiency versus beam width relationships became similar to those from comparisons of PMMA phantoms (Figure 8.1 (a and d)) and followed similar relationships in the second and third regions. The peripheral measurements for narrow beams were affected by the different intensities incident on the phantom surfaces, resulting from the different compositions, and hence the scattering properties. The ratios between PMMA and other materials declined with beam width more than the PMMA ratios. The lower ratio for the periphery than the centre for the water head phantom was a result of the large difference in PMMA and water phantom diameters, as well as the composition (Figure 8.1 (c) and Table 7.1).

8.3.2 The Efficiency of $f(0,150)_{x,PE}$

Comparisons were made between shorter and longer PE phantoms, as PE might present an alternative for standard hospital dosimetry phantoms. Figure 8.2 (a - b) shows $\varepsilon(PE/PE)_{x,kV}$ values at the centre and periphery of the head and body phantoms as a function of beam width calculated as in Eq.(8.3). Because $\varepsilon(PE/PE)_{x,kV}$ values were only affected by the difference in phantom lengths, the trends for $\varepsilon(PE/PE)_{x,kV}$ were similar to those for $\varepsilon(PMMA/PMMA)_{x,kV}$ (Figure 8.1 (a and d)). $\varepsilon(PE/PE)_{x,kV}$ values also exhibited the three regions observed for $\varepsilon(PMMA/PMMA)_{x,kV}$. However, $\varepsilon(PE/PE)_{x,kV}$ values within the head at 120 kV and body at 125 kV were lower than those for $\varepsilon(PMMA/PMMA)_{x,kV}$ at the same tube potentials by up to 1% and 3% at the centre and periphery of the head phantom, respectively, and 6% and 7% within the body phantom, respectively (Figure 8.2 (c - d)). The variations between $\varepsilon(PE/PE)_{x,kV}$ and

$\varepsilon(PMMA/PMMA)_{x,kV}$ values were found to increase with beam width beyond 150 mm, i.e. the length of the short phantoms. This is caused by the increased build-up of scattered radiation within the infinitely long PE phantom with increasing beam width due to the lower density compared to PMMA (ICRU, 2012). PE phantoms have broader dose spread functions, i.e. longer scatter tails (Boone, 2009), so that the decline in $\varepsilon(PE/PE)_{x,kV}$ with beam width is greater than for $\varepsilon(PMMA/PMMA)_{x,kV}$. This means that the dose underestimation with standard PMMA phantoms will be less than with short PE phantoms, thus the current PMMA phantoms provide a better option for dosimetry.

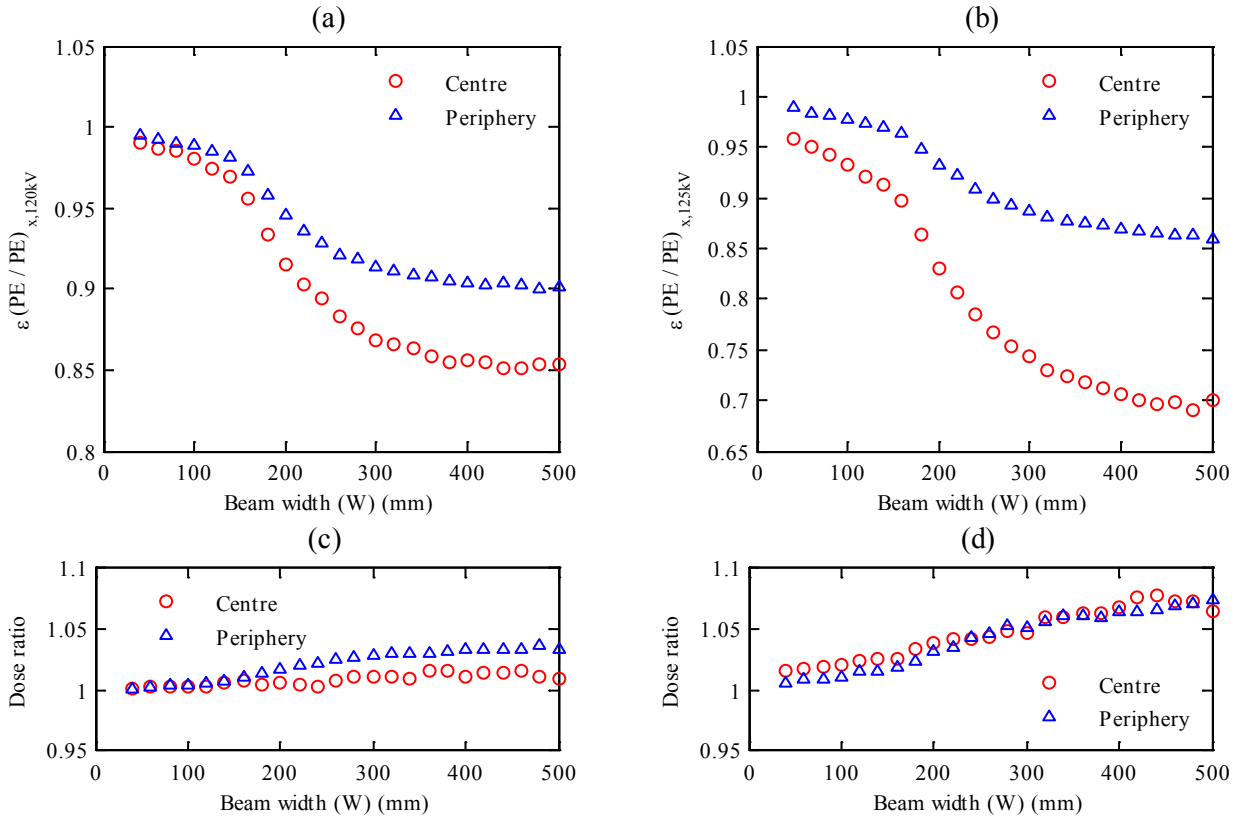

Figure 8.2: The efficiency values for $\varepsilon(PE/PE)_{x,kV}$ calculated as in Eq.(8.3) within (a) head phantoms at 120 kV and (b) body phantoms at 125 kV. (c – d) The dose ratios for $\varepsilon(PMMA/PMMA)_{x,kV}$ values normalised with respect to $\varepsilon(PE/PE)_{x,kV}$ values at the same tube potential and position within (c) head and (d) body phantoms.

8.3.3 The Influence of Tube Potential on the Efficiency Values

Figures 8.3 and 8.48.3 show the influence of tube potential on the efficiency values at the centre and periphery of the head and body phantoms. Differences in efficiency with tube potential were less for

$\varepsilon(PMMA/PMMA)_{x,kV}$, where the composition is the same, but larger for phantoms of different compositions $\varepsilon(PMMA/PE)_{x,kV}$ and $\varepsilon(PMMA/Water)_{x,kV}$. The influence of tube potential was greater within the body phantoms (Figure 8.4) than the head phantoms (Figure 8.3). These variations resulted from the difference in diameters and compositions of the head and body phantoms and in the scatter tails with tube potentials 80 – 140 kV (Boone, 2009). For $\varepsilon(PMMA/PMMA)_{x,kV}$, the efficiency values for 80 kV were larger by up to 4.8% than for other tube potentials, but the differences between the values for 100 – 140 kV were within ±1%, which is in agreement with results of (Li et al., 2014b).

The differences in efficiency values $\varepsilon(PMMA/PMMA)_{x,kV}$ with tube potential were similar at the centres and peripheries of the phantoms and increased with beam width, with the variations for the body phantom being slightly larger. The increase of the differences with beam width resulted from the build-up of scattered radiation. Differences in efficiency ratios for phantoms of different dimensions and compositions were larger, being up to ±10.5% for $\varepsilon(PMMA/PE)_{x,kV}$ and ±6.9% for $\varepsilon(PMMA/Water)_{x,kV}$ within the head and body phantoms. These larger variations were caused by the differences between the properties of the phantoms. For the peripheral measurements, values for $\varepsilon(PMMA/PE)_{p,kV}$ at 80 kV were larger for both head and body phantoms, while values for $\varepsilon(PMMA/Water)_{p,kV}$ at 140 kV were larger. Ratios at the centres of the body phantoms $\varepsilon(PMMA/PE)_{c,kV}$ and $\varepsilon(PMMA/Water)_{c,kV}$ were the reverse of the periphery. This is linked to the higher photoelectric component in the attenuation of 80 kV x-rays in water than in PMMA, and in PMMA than in PE (Hubbell and Seltzer, 2004, Berger et al., 2010). However, the trends in $\varepsilon(PMMA/PE)_{c,kV}$ and $\varepsilon(PMMA/Water)_{c,kV}$ for the head phantom did not show the same patterns, but the variations in dose within these phantoms are much smaller than the body phantoms.

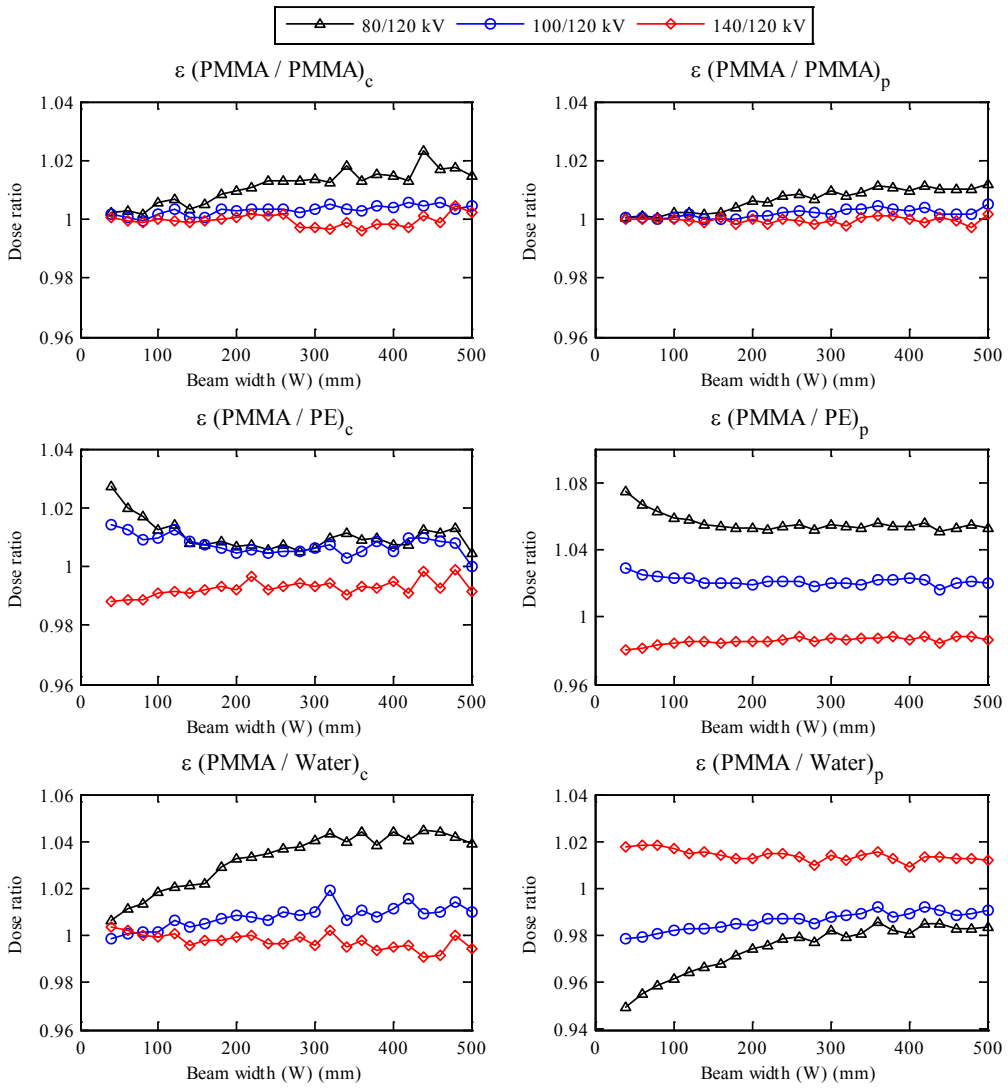

Figure 8.3: The influence of tube potential on the efficiency values $\varepsilon(PMMA/PMMA)_{x,kV}$, $\varepsilon(PMMA/PE)_{x,kV}$, and $\varepsilon(PMMA/Water)_{x,kV}$ at the centre (c) and periphery (p) of the head phantoms. The efficiency values calculated at 80, 100 and 140 kV were normalized with respect to those for 120 kV.

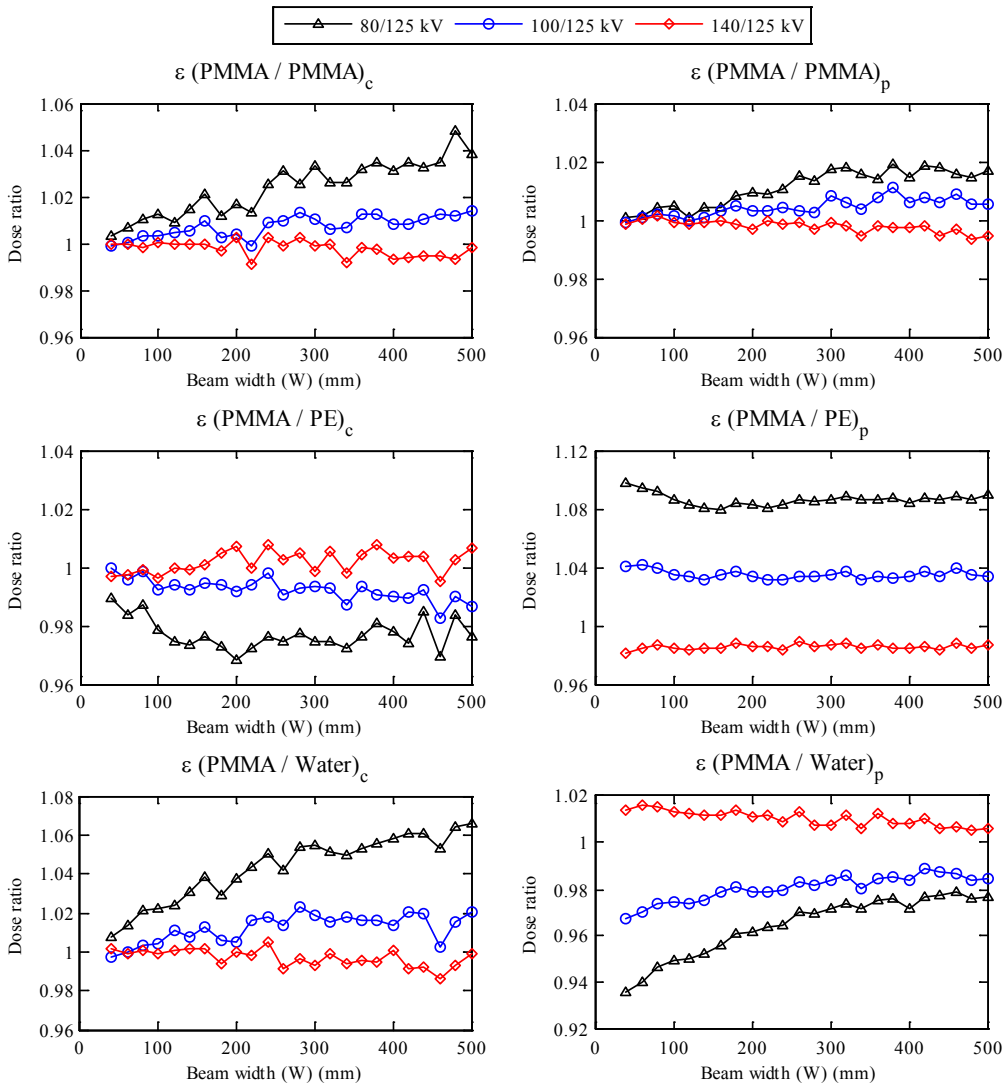

Figure 8.4: The influence of tube potential on the efficiency values $\varepsilon(PMMA/PMMA)_{x,kV}$, $\varepsilon(PMMA/PE)_{x,kV}$, and $\varepsilon(PMMA/Water)_{x,kV}$ at the centre (c) and periphery (p) of the body phantoms. The efficiency values calculated at 80, 100 and 140 kV were normalized with respect to those for 125 kV.

8.3.4 Sensitivity of Conversion Factors for the kV System and Scan Parameters

Conversion factors derived from MC calculations are provided in Tables 8.1 - 8.3.

Table 8.4 compares experimental measurements of $f(0{,}150)_{x,PMMA}$ and $f(0,\infty)_{x,PMMA}$ using the scanning protocols Head-200, Head-360, Body-200, and Body-360. The $f(0,\infty)_{x,m}$ values evaluated by using the Tables 8.1 - 8.3 and Eq.(8.5). The differences between $f(0,\infty)_{x,PMMA}$ values measured experimentally and those evaluated by application of the conversion factors using Eq.(8.5) were within ±2.9% and ±2.5% for the head and body phantoms, respectively (

Table 8.4). Although the MC calculations employed phantoms 600 mm in length and the experimental measurements were in 450 mm long phantoms, the differences between the experimental and calculated $f(0,\infty)_{x,PMMA}$ values were small. This is consistent with the recommendation of (AAPM, 2010), where the length of the infinitely long phantom is required to be ≥450 mm to provide the scatter equilibrium condition for cumulative dose measurements. The results provide further confirmation that in practice 600 mm PMMA phantoms can be replaced by ones 450 mm in length. The use of four standard 150 mm long phantoms to create a 600 mm length would potentially leave an air gap in the middle parallel to the direction of the incidents x-rays, which could produce anomalous results, whereas a 450 mm long phantom made from three standard ones avoids this issue. The differences between the values for $f(0,\infty)_{x,PMMA}$, $f(0,\infty)_{x,PE}$ and $f(0,\infty)_{x,Water}$ at the centres of head and body phantoms, and the peripheries of PMMA and water phantoms given in

Table 8.4 were in agreement with results reported by (Zhou and Boone, 2008, Li et al., 2013b).

Table 8.1: Coefficients for fitted equations to calculate the conversion factors $C_f(PMMA/PMMA)_{x,kV}$ to covert $f(0,150)_{x,PMMA}$ measurements made within the standard PMMA head and body phantoms to $f(0,\infty)_{x,PMMA}$ within infinitely long PMMA head and body phantoms as in Eq.(8.5). The conversion factors are suitable for beams of width 40 – 500 mm at tube potentials of 80 – 140 kV.

$$C_f = P_1 W^6 + P_2 W^5 + P_3 W^4 + P_4 W^3 + P_5 W^2 + P_6 W + P_7$$

$$Head - C_f(PMMA/PMMA)_{x,kV}$$

	80 kV		100 kV		120 kV		140 kV	
Coefficients	**Centre**	**Periphery**	**Centre**	**Periphery**	**Centre**	**Periphery**	**Centre**	**Periphery**
P_1	-7.785×10^{-16}	-3.793×10^{-16}	-9.064×10^{-16}	-4.597×10^{-16}	-9.411×10^{-16}	-3.897×10^{-16}	-8.206×10^{-16}	-4.657×10^{-16}
P_2	1.248×10^{-12}	6.029×10^{-13}	1.437×10^{-12}	7.181×10^{-13}	1.485×10^{-12}	6.250×10^{-13}	1.312×10^{-12}	7.352×10^{-13}
P_3	-7.426×10^{-10}	-3.560×10^{-10}	-8.476×10^{-10}	-4.170×10^{-10}	-8.715×10^{-10}	-3.722×10^{-10}	-7.818×10^{-10}	-4.314×10^{-10}
P_4	1.965×10^{-07}	9.365×10^{-08}	2.230×10^{-07}	1.081×10^{-07}	2.281×10^{-07}	9.848×10^{-08}	2.076×10^{-07}	1.129×10^{-07}
P_5	-2.134×10^{-05}	-1.012×10^{-05}	-2.422×10^{-05}	-1.156×10^{-05}	-2.461×10^{-05}	-1.063×10^{-05}	-2.265×10^{-05}	-1.222×10^{-05}
P_6	1.002×10^{-03}	4.564×10^{-04}	1.134×10^{-03}	5.245×10^{-04}	1.144×10^{-03}	4.913×10^{-04}	1.088×10^{-03}	5.605×10^{-04}
P_7	0.9899	0.9957	0.9901	0.9948	0.9910	0.9954	0.9910	0.9946

$$Body - C_f(PMMA/PMMA)_{x,kV}$$

	80 kV		100 kV		125 kV		140 kV	
Coefficients	**Centre**	**Periphery**	**Centre**	**Periphery**	**Centre**	**Periphery**	**Centre**	**Periphery**
P_1	-1.298×10^{-15}	-2.901×10^{-16}	-1.587×10^{-15}	-3.892×10^{-16}	-1.498×10^{-15}	-3.560×10^{-16}	-1.522×10^{-15}	-3.574×10^{-16}
P_2	2.126×10^{-12}	4.664×10^{-13}	2.581×10^{-12}	6.359×10^{-13}	2.457×10^{-12}	5.837×10^{-13}	2.477×10^{-12}	5.861×10^{-13}
P_3	-1.304×10^{-09}	-2.808×10^{-10}	-1.579×10^{-09}	-3.896×10^{-10}	-1.512×10^{-09}	-3.595×10^{-10}	-1.516×10^{-09}	-3.602×10^{-10}
P_4	3.608×10^{-07}	7.597×10^{-08}	4.391×10^{-07}	1.080×10^{-07}	4.219×10^{-07}	1.001×10^{-07}	4.216×10^{-07}	9.983×10^{-08}
P_5	-4.197×10^{-05}	-8.511×10^{-06}	-5.263×10^{-05}	-1.276×10^{-05}	-5.037×10^{-05}	-1.181×10^{-05}	-5.031×10^{-05}	-1.164×10^{-05}
P_6	2.153×10^{-03}	4.160×10^{-04}	2.827×10^{-03}	6.592×10^{-04}	2.719×10^{-03}	6.321×10^{-04}	2.734×10^{-03}	6.172×10^{-04}
P_7	0.9871	0.9964	0.9785	0.9933	0.9813	0.9933	0.9805	0.9939

Table 8.2: Coefficients of fitted equations to calculate the conversion factors $C_f(PMMA/PE)_{x,kV}$ to covert $f(0,150)_{x,PMMA}$ measurements made within the standard PMMA head and body phantoms to $f(0,\infty)_{x,PE}$ within infinitely long PE head and body phantoms as in Eq.(8.5). The conversion factors are suitable for beams of width 40 – 500 mm at tube potentials of 80 – 140 kV.

$$C_f = P_1 W^6 + P_2 W^5 + P_3 W^4 + P_4 W^3 + P_5 W^2 + P_6 W + P_7$$

$Head - C_f(PMMA/PE)_{x,kV}$

	80 kV		100 kV		120 kV		140 kV	
Coefficients	Centre	Periphery	Centre	Periphery	Centre	Periphery	Centre	Periphery
P_1	-4.650×10^{-16}	-4.884×10^{-16}	-4.307×10^{-16}	-5.701×10^{-16}	-5.628×10^{-16}	-5.002×10^{-16}	-3.823×10^{-16}	-5.040×10^{-16}
P_2	6.672×10^{-13}	8.054×10^{-13}	6.231×10^{-13}	9.317×10^{-13}	8.005×10^{-13}	8.263×10^{-13}	5.370×10^{-13}	8.280×10^{-13}
P_3	-3.149×10^{-10}	-5.106×10^{-10}	-2.906×10^{-10}	-5.826×10^{-10}	-3.802×10^{-10}	-5.218×10^{-10}	-2.346×10^{-10}	-5.190×10^{-10}
P_4	3.686×10^{-08}	1.568×10^{-07}	2.798×10^{-08}	1.746×10^{-07}	4.902×10^{-08}	1.573×10^{-07}	1.073×10^{-08}	1.547×10^{-07}
P_5	1.022×10^{-05}	-2.534×10^{-05}	1.267×10^{-05}	-2.677×10^{-05}	1.053×10^{-05}	-2.407×10^{-05}	1.559×10^{-05}	-2.325×10^{-05}
P_6	-2.008×10^{-03}	2.695×10^{-03}	-2.398×10^{-03}	2.614×10^{-03}	-2.386×10^{-03}	2.366×10^{-03}	-2.735×10^{-03}	2.244×10^{-03}
P_7	1.088	0.8088	1.112	0.8528	1.1290	0.8851	1.1490	0.9077

$Body - C_f(PMMA/PE)_{x,kV}$

	80 kV		100 kV		125 kV		140 kV	
Coefficients	Centre	Periphery	Centre	Periphery	Centre	Periphery	Centre	Periphery
P_1	-1.202×10^{-15}	-4.025×10^{-16}	-1.226×10^{-15}	-3.559×10^{-16}	-1.169×10^{-15}	-5.269×10^{-16}	-1.449×10^{-15}	-4.838×10^{-16}
P_2	1.924×10^{-12}	6.739×10^{-13}	1.968×10^{-12}	6.242×10^{-13}	1.863×10^{-12}	8.876×10^{-13}	2.298×10^{-12}	8.094×10^{-13}
P_3	-1.125×10^{-09}	-4.372×10^{-10}	-1.159×10^{-09}	-4.202×10^{-10}	-1.080×10^{-09}	-5.751×10^{-10}	-1.344×10^{-09}	-5.214×10^{-10}
P_4	2.766×10^{-07}	1.385×10^{-07}	2.890×10^{-07}	1.361×10^{-07}	2.592×10^{-07}	1.790×10^{-07}	3.367×10^{-07}	1.616×10^{-07}
P_5	-2.099×10^{-05}	-2.329×10^{-05}	-2.281×10^{-05}	-2.280×10^{-05}	-1.685×10^{-05}	-2.831×10^{-05}	-2.813×10^{-05}	-2.556×10^{-05}
P_6	7.761×10^{-05}	2.643×10^{-03}	5.196×10^{-05}	2.556×10^{-03}	-5.470×10^{-04}	2.815×10^{-03}	1.341×10^{-04}	2.620×10^{-03}
P_7	1.1460	0.6870	1.139	0.7315	1.1560	0.7617	1.1470	0.7803

Table 8.3: Coefficients for the fitted equations to calculate the conversion factors $C_f(PMMA/Water)_{x,kV}$ to covert $f(0,150)_{x,PMMA}$ measurements made within standard PMMA head and body phantoms to $f(0,\infty)_{x,Water}$ within infinitely long water head and body phantoms as in Eq.(8.5). The conversion factors are suitable for beams of width 40 – 500 mm at tube potentials of 80 – 140 kV.

$$C_f = P_1 W^6 + P_2 W^5 + P_3 W^4 + P_4 W^3 + P_5 W^2 + P_6 W + P_7$$

$$Head - C_f(PMMA/Water)_{x,kV}$$

	80 kV		100 kV		120 kV		140 kV	
Coefficients	**Centre**	**Periphery**	**Centre**	**Periphery**	**Centre**	**Periphery**	**Centre**	**Periphery**
P_1	-5.643×10^{-16}	-7.835×10^{-16}	-7.507×10^{-16}	-8.907×10^{-16}	-8.374×10^{-16}	-8.207×10^{-16}	-7.737×10^{-16}	-7.727×10^{-16}
P_2	8.694×10^{-13}	1.318×10^{-12}	1.164×10^{-12}	1.478×10^{-12}	1.305×10^{-12}	1.372×10^{-12}	1.190×10^{-12}	1.291×10^{-12}
P_3	-4.764×10^{-10}	-8.562×10^{-10}	-6.549×10^{-10}	-9.458×10^{-10}	-7.432×10^{-10}	-8.866×10^{-10}	-6.671×10^{-10}	-8.328×10^{-10}
P_4	1.017×10^{-07}	2.698×10^{-07}	1.534×10^{-07}	2.933×10^{-07}	1.799×10^{-07}	2.778×10^{-07}	1.572×10^{-07}	2.605×10^{-07}
P_5	-3.481×10^{-06}	-4.324×10^{-05}	-1.086×10^{-05}	-4.638×10^{-05}	-1.484×10^{-05}	-4.453×10^{-05}	-1.193×10^{-05}	-4.184×10^{-05}
P_6	-5.984×10^{-04}	3.795×10^{-03}	-1.699×10^{-05}	4.107×10^{-03}	3.152×10^{-04}	4.061×10^{-03}	2.188×10^{-04}	3.903×10^{-03}
P_7	1.0320	0.9997	1.025	0.9599	1.0150	0.9362	1.0120	0.9201

$$Body - C_f(PMMA/Water)_{x,kV}$$

	80 kV		100 kV		125 kV		140 kV	
Coefficients	**Centre**	**Periphery**	**Centre**	**Periphery**	**Centre**	**Periphery**	**Centre**	**Periphery**
P_1	-1.093×10^{-15}	-5.884×10^{-16}	-1.380×10^{-15}	-6.676×10^{-16}	-1.203×10^{-15}	-6.76×10^{-16}	-1.674×10^{-15}	-7.497×10^{-16}
P_2	1.757×10^{-12}	1.015×10^{-12}	2.190×10^{-12}	1.157×10^{-12}	1.966×10^{-12}	1.15×10^{-12}	2.677×10^{-12}	1.272×10^{-12}
P_3	-1.030×10^{-09}	-6.788×10^{-10}	-1.278×10^{-09}	-7.751×10^{-10}	-1.177×10^{-09}	-7.65×10^{-10}	-1.588×10^{-09}	-8.358×10^{-10}
P_4	2.508×10^{-07}	2.211×10^{-07}	3.188×10^{-07}	2.517×10^{-07}	2.990×10^{-07}	2.46×10^{-07}	4.122×10^{-07}	2.667×10^{-07}
P_5	-1.658×10^{-05}	-3.676×10^{-05}	-2.576×10^{-05}	-4.154×10^{-05}	-2.428×10^{-05}	-4.07×10^{-05}	-3.936×10^{-05}	-4.345×10^{-05}
P_6	-1.023×10^{-03}	3.384×10^{-03}	-3.284×10^{-04}	3.823×10^{-03}	-2.269×10^{-04}	3.844×10^{-03}	6.570×10^{-04}	4.029×10^{-03}
P_7	1.2700	1.1140	1.265	1.062	1.2580	1.024	1.2410	1.003

Table 8.4: Experimental measurements for $f(0,150)_{x,PMMA}$ and $f(0,\infty)_{x,PMMA}$ performed at the centre (c) and periphery (p) of standard and 450 mm long PMMA head and body phantoms using the scanning protocols Head-200, Head-360, Body-200, and Body-360. The $f(0,150)_{x,PMMA}$ values were used to estimate $f(0,\infty)_{x,m}$ within the head and body PMMA, PE and water phantoms using the conversion factors given in Tables 8.1 – 8.3 and Eq.(8.5). $\left[Difference\ (\%) = \left(f(0,\infty)_{MC} - f(0,\infty)_{Exp} / f(0,\infty)_{Exp}\right) \times 100\right]$.

	C_{f-MC}	$f(0,150)_{x,PMMA,Exp}$ mGy/100 mAs	$f(0,\infty)_{x,PMMA,Exp}$ mGy/100 mAs	$f(0,\infty)_{x,m,MC}$ mGy/100 mAs	Difference (%)
Partial Head 200° scan - 100 kV					
C-PMMA	1.076	2.39	2.50	2.57	2.87
	1.069[a]			2.55	2.24
C-PE	1.068			2.55	
C-Water	1.088			2.60	
P-PMMA	1.034	2.18	2.26	2.25	-0.24
	1.032[a]			2.25	-0.46
P-PE	1.029			2.24	
P-Water	1.174			2.56	
Full Head 360° scan - 100 kV					
C-PMMA	1.076	2.53	2.65	2.72	2.73
	1.069[a]			2.70	2.11
C-PE	1.068			2.70	
C-Water	1.088			2.75	
P-PMMA	1.034	2.27	2.34	2.35	0.33
	1.032[a]			2.34	0.10
P-PE	1.029			2.34	
P-Water	1.174			2.66	

		Partial Body 200° scan – 125 kV			
C-PMMA	1.153	1.59	1.83	1.83	0.20
	1.157[(a)]			1.84	0.55
C-PE	1.235			1.96	
C-Water	1.299			2.07	
P-PMMA	1.036	2.30	2.35	2.38	1.42
	1.032[(a)]			2.37	0.99
P-PE	0.953			2.19	
P-Water	1.239			2.85	
		Full Body 360° scan – 125 kV			
C-PMMA	1.153	1.37	1.62	1.58	-2.48
	1.157[(a)]			1.59	-2.13
C-PE	1.235			1.69	
C-Water	1.299			1.78	
P-PMMA	1.036	1.91	1.98	1.98	-0.04
	1.032[(a)]			1.97	-0.46
P-PE	0.953			1.82	
P-Water	1.239			2.37	

(a) Conversion factor calculated from the efficiency values provided in (Li et al., 2014b), which were obtained at 120 kV using a Somatom Definition dual source CT scanner.

Table 8.4 shows good agreement between experimental results with a 450 mm phantom and evaluations of $f(0,\infty)_{x,PMMA}$ from shorter phantoms with the same conversion factors for partial 200° scans, demonstrating that the conversion factors can also be applied to partial scans. This means that the conversion factors were relatively insensitive to the bowtie filter, the scan diameter, and the acquisition mode. The efficiency values of (Li et al., 2014b) shown in (Figure 8.1 (a and d)), which were calculated for a Somatom Definition dual source CT scanner at 120 kV, were used to derive conversion factors using Eq.(8.4), and results using these were again in excellent agreement with those derived in this study. Thus the conversion factors appear insensitive to differences in scanner type and scan parameters. These findings are consistent with the discussion presented for the $G_x(W)_{100}$ function in Chapter 7 section 7.3.4. This insensitivity, therefore, provides an efficient method for developing generic coefficients, which may be suitable for a range of scanners.

8.4 Conclusion

The capability of using a small chamber within standard PMMA head and body phantoms $f(0{,}150)_{x,PMMA}$ for reporting the cumulative dose within infinitely long PMMA, PE and water phantoms $f(0,\infty)_{x,m}$ has been studied using MC calculations. The efficiency values were investigated using head and body scanning protocols over a wide range of beam widths from 40 – 500 mm and tube potentials of 80 – 140 kV. The relationships between efficiencies for shorter phantoms of the same composition $\varepsilon(PMMA/PMMA)_{x,kV}$ and $\varepsilon(PE/PE)_{x,kV}$ were similar in form, exhibiting three distinct regions, a slow decline, followed by a rapid decline and then a levelling off. $\varepsilon(PMMA/PMMA)_{x,kV}$ values were larger than those for $\varepsilon(PE/PE)_{x,kV}$, due to differences in density. However, $\varepsilon(PMMA/PE)_{x,kV}$ and $\varepsilon(PMMA/Water)_{x,kV}$ values were also affected by differences in phantom diameters and compositions, which influenced both the attenuation and proportion of scattered photons. $\varepsilon(PE/PE)_{x,kV}$ values were lower than those for $\varepsilon(PMMA/PMMA)_{x,kV}$. Thus, the use of the standard PMMA phantoms to

estimate $f(0,\infty)_{x,kV}$ provides a better option than the short PE phantoms. Tube potential had a minor influence on the efficiency values for $\varepsilon(PMMA/PMMA)_{x,kV}$, but variations were more significant for $\varepsilon(PMMA/PE)_{x,kV}$ and $\varepsilon(PMMA/Water)_{x,kV}$. The results indicated that $f(0{,}150)_{x,PMMA}$ underestimated $f(0,\infty)_{x,m}$ values significantly for wider beams such as those used for CBCT scans. Therefore, it is necessary to use long phantoms (≥450 mm) to measure cumulative doses for such scans, or the use of conversion factors. Based on the efficiency values calculated, conversion factors have been derived at the centre and periphery of the phantoms for each tube potential to allow evaluation of $f(0,\infty)_{x,m}$ from single measurements of $f(0{,}150)_{x,PMMA}$. Based on comparisons shown in this study and those reported in the previous chapter, the conversion factors only showed a weak dependency on scanner type, and may be suitable for application to different CT and CBCT scanners. Results of this study have been published in (Abuhaimed et al., 2015c).

Chapter 9

Dose Indices and Organ Doses

9.1 Introduction

Investigations into the dose indices (DIs) proposed for CBCT dosimetry have been described for phantoms of homogenous compositions and arbitrary diameters in Chapters 5 - 8. An aim in the development of DIs in standard phantoms has been to provide a measurement more akin to doses received by organs and tissues in the region of a scan (McCollough et al., 2011). But since organs are at different depths and inhomogeneous compositions, and the radiation fields may only cover parts of particular organs, they are regarded as dosimetry quantities and not associated with the doses actually received by the exposed organs. If this link could be improved, it would allow clinicians and physicists to be more aware of dose levels delivered to organs within the scanning field, which would be helpful in establishing a better link between the benefits of imaging and the potential risks. The DIs recorded in patient records for such exposures, would then be seen as giving a more direct assessment of doses from imaging exposures required by the Ionising Radiation (Medical Exposure) Regulations 2000, Regulation 7(8) (IRMER, 2000). In order to assess how closely the various DIs based on different concepts can provide assessments of doses to radiosensitive organs, this chapter presents a study, which has been made for CBCT scans employed in the clinic for image guided radiation therapy (IGRT). The study has used MC simulations on the International Commission on Radiological Protection ICRP-110 adult male and female reference computational phantoms (ICRP, 2009) to evaluate organ doses (ODs). The investigation aimed to assess whether any of the DIs for CBCT scans can themselves give clinicians reasonable indications of doses to specific organs adjacent to those being treated to help inform their risk / benefit judgements.

9.2 Materials and Methods

9.2.1 Dose Indices

The various DIs investigated in the previous Chapters 5 – 8 were compared to ODs. Seven DIs were studied in this investigation:

1- DI1: $CTDI_{100}$, presented in Chapter 2 section 2.4.

2- DI2: $CTDI_{IEC}$, presented in Chapter 2 section 2.6.5.

3- DI3: $f_{100}(150)$, presented in Chapter 2 section 2.6.3.

4- DI4: $f(0{,}150)$, presented in Chapter 2 section 2.6.2.

5-DIs 5 - 7: $f(0,\infty)_m$, presented in Chapter 2 section 2.6.4, where DI5: $f(0,\infty)_{PMMA}$, DI6: $f(0,\infty)_{PE}$, and DI7: $f(0,\infty)_{Water}$.

All the DIs were measured at the middle of the central axis (DI_c) and four peripheral axes (DI_p), from which a weighted DI (DI_w) is evaluated to account for the dose distribution over the x-y plane in a manner similar to that used for $CTDI_w$ as:

$$DI_w = \frac{1}{3} DI_c + \frac{2}{3} DI_p \tag{9.1}$$

where DI_p is the average of four measurements at the peripheral axes ($DI_p = 1/4 \sum_{i=1}^{4} DI_{p,i}$).

9.2.2 The Scanning Protocols

Three pre-configured scanning protocols, head, thorax, and pelvis, which are commonly employed in IGRT procedures, were studied, and parameters of these protocols are given in Chapter 2 Table 2.1.

9.2.3 Dose Indices Measurements

The seven DIs were measured in the previous chapters using the head and body scanning protocols studied in this chapter. Values for DI1 and DI2 were measured in Chapter 5 and given in Table 5.3. Whereas, values for D3 and D4 were presented in Chapter 6 Table 6.2, and DIs 5 – 7 were given in Chapter 7 Table 7.4. Parameters of the head protocol were similar to those for the head scan (Table 2.1), and parameters of the body protocol were similar to those for the thorax and pelvis scans (Table 2.1).

9.2.4 Monte Carlo Simulations for Organ Doses

The use of MC simulation is considered as an efficient method for evaluation of ODs with a high level of accuracy, and facilitates the time-consuming experimental measurements that involve using dosimeters within human-like phantoms such as anthropomorphic phantoms. MC simulations based on different MC systems such as EGSnrc have been utilized extensively to estimate ODs from CBCT scans employed in IGRT procedures using CT images of different phantoms or real patients as shown in Chapter 2 Table 2.2. BEAMnrc and DOSXYZnrc were used to calculate ODs in three dimensions (3D) in terms of absorbed dose. Two simulations were run in BEAMnrc using fields of size 264 × 198 mm^2 for the head scan and 478 × 198 mm^2 for the body scans, thorax and pelvis. The simulations were run with the same MC parameters used in Chapter 4 section 4.4.2. The PHSP files were recorded at a SSD of 75 cm, which subsequently were used in DOSXYZnrc as kV sources.

ODs were evaluated in DOSXYZnrc using the ICRP-110 phantoms, which were based on whole body CT scans acquired for real patients, but by necessity represent a reference person of average build (ICRP, 2009). The main characteristics of the phantoms are given in Table 9.1. Each phantom is provided by the ICRP in a 3D matrix with a size of 254 × 127 × 222 and 299 × 137 × 348 for the male and female phantoms, respectively. Each cell of these matrixes contains a unique number (ID) between 1 – 141, which represents a pre-defined organ or tissue. Each ID number is assigned to one of 53 different mediums, which were defined with different elemental

compositions and densities to simulate the organs and tissues. DOSXYZnrc format, however, also takes the form of a 3D matrix, but it consists of voxels of specific sizes, and each voxel is assigned with a certain medium as described in Chapter 3 section 3.7.2. Thus, the first step required is to convert the ICRP-110 phantoms to DOSXYZnrc format. A MATLAB-based code was developed, and the phantoms were converted using the same voxel size used for the ICRP CT scans, 2.137 × 2.137 × 8.0 mm^3 for the male and 1.775 × 1.775 × 4.84 mm^3 for the female. The mediums assigned for the DOSXYZnrc voxels were based on the elemental compositions and density values used in the ICRP-110 report (ICRP, 2009). All the mediums were defined in DOSXYZnrc using PEGS4 code. Figure 9.1 shows the coronal and sagittal views of the phantoms converted to DOSXYZnrc format, which were in agreement with those given in the ICRP-110 report (ICRP, 2009).

Table 9.1: The main characteristics of the ICRP-110 male and female reference computational phantoms used in this study. The organ and tissue masses are reported in detail in ICRP-110 report (ICRP, 2009).

Property	Male	Female
Age (year)	38	43
Height (m)	1.76	1.63
Mass (kg)	73.0	60.0
Slice thickness (voxel height, mm)	8.0	4.84
Voxel in-plane resolution (mm)	2.137	1.775
Voxel volume (mm3)	36.54	15.25
Number of columns	254	299
Number of rows	127	137
Number of slices	222	348

All the scans simulated were acquired at a SID of 100 cm, thus the distance between the PHSP files and the isocentre in DOSXYZnrc was set to 25 cm. For both the phantoms, the centre of the head scan ($z = 0$) was positioned at the middle of the head, and centre of the thorax and pelvic scans at the middle of the lung and pelvis, respectively. 4 × 10^9 and 8 × 10^9 histories were run for the male and female phantoms, respectively, to obtain a statistical uncertainty of <1% for voxels of all organs and tissues located within the scan field. ISOURCE = 8 of DOSXYZnrc code was employed with

projection numbers and gantry rotation set to the values listed in Table 2.1. The HOWFARLESS technique was not employed as it can only be utilized for homogeneous phantoms (Walters and Kawrakow, 2007).

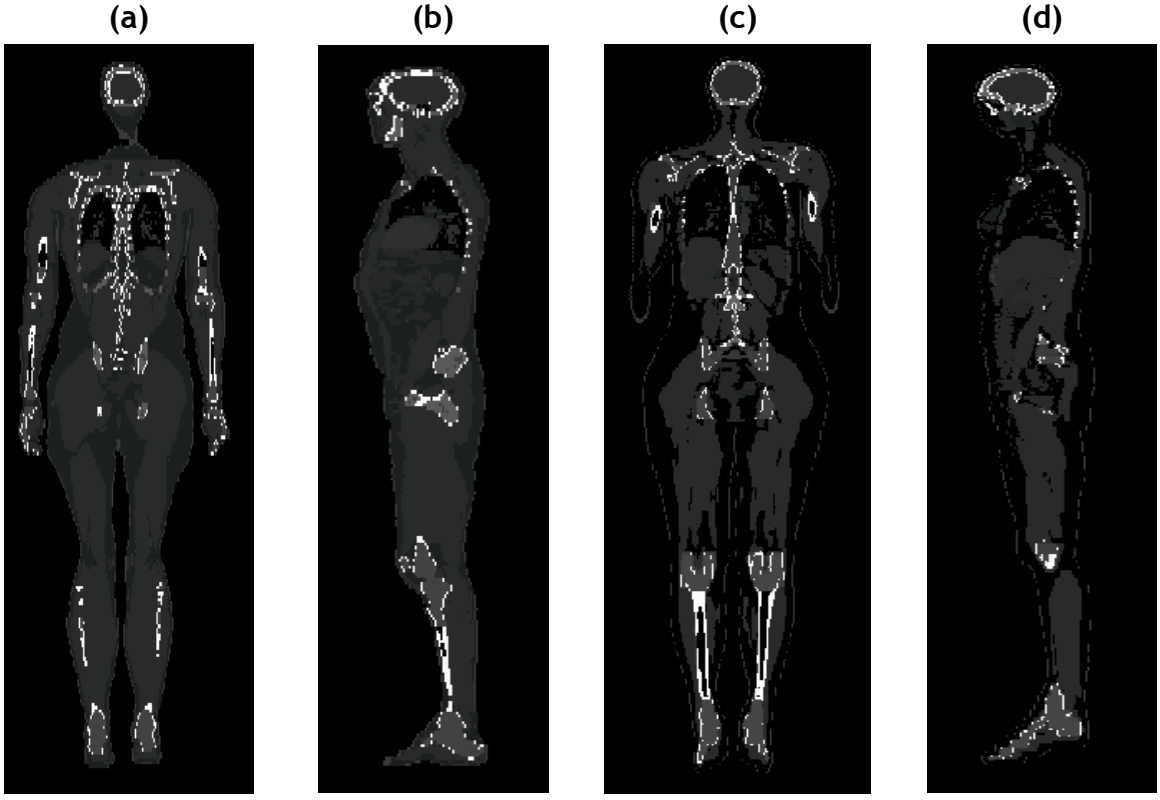

Figure 9.1: The coronal and sagittal views of the ICRP-110 (a–b) male and (c–d) female reference computational phantoms converted to DOSXYZnrc format.

In order to evaluate the absorbed dose for each organ and tissue in 3D efficiently, a MATLAB-based code was developed to analyze the outputs of the DOSXYZnrc simulations in (.3ddose) format. As each organ and tissue was defined with an ID number, three 3D matrixes were created for each simulation. The first matrix was based on the ICRP file, where each cell contains an ID number. The second and third matrixes were based on the (.3ddose) file, where each voxel of the second matrix contains an absorbed dose value, and a statistical uncertainty value in the third matrix. These matrixes were linked together in the MATLAB code. The first step was to specify coordinates of the voxels that carried the same ID number in the first array, and the second step was to obtain the mean absorbed dose (D_{MC}) and the mean statistical uncertainty value for each ID number from the second and third matrixes based on the coordinates specified in the first step.

The mean absorbed dose (D_{MC}) for each organ and tissue is calculated from either a single or multiple ID numbers as described in the ICRP-110 (ICRP, 2009), depending on whether the tissue comprises a single volume or separate regions. For example, the dose for the brain is represented by an ID number of 61, while that for the salivary glands is calculated from ID numbers of 120 and 121, which represent the left and right salivary glands, respectively. For organs and tissues evaluated from a single ID number, the mean absorbed dose (D_{MC}) was calculated as the mean value over all voxels assigned with the same ID number, such as the brain which consists of 37794 and 81192 voxels for the male and female, respectively. However, for organs and tissues with multiple ID numbers, i.e. consisting of several separate regions of tissues, (D_{MC}) was calculated as the weighted absorbed dose as each ID number had different voxels number (VN):

$$D_{MC} = \frac{\sum_{i=1}^{n} D_{MC,i}\, VN_i}{\sum_{i=1}^{n} VN_i} \tag{9.2}$$

where n is number of the ID numbers used to calculate the dose for a given organ or tissue, and $D_{MC,i}$.is the mean absorbed dose for each ID number. For example, $n = 2$ was used for the salivary glands with VN being 2228 and 2229 for the left and right salivary glands for the female, respectively.

Once (D_{MC}) was calculated for each organ and tissue, it was converted from the MC output $(Gy/incident\ particle)$ to the standard unit (Gy) using the calibration factors (F_{MC}) determined in Chapter 4 section (4.5) as:

$$OD = D_{MC} \times F_{MC} \times mAs \tag{9.3}$$

The statistical uncertainty $S(N)$, which was discussed in Chapter 3 section 3.8, for each organ and tissue was also calculated as the mean value over all voxels assigned with the same ID number. However, the standard deviation and the statistical uncertainly values for organs and tissues with multiple ID numbers were also calculated as weighted values using:

$$S(N) = \sqrt{\sum_{i=1}^{n} \left(\frac{VN_i}{(\sum_{i=1}^{n} VN_i)} \, x_i \right)^2} \quad (9.4)$$

where x_i is the $S(N)$ for each ID number.

The MATLAB code used to analyse (.3ddose) files was validated by comparing doses for some organs against known values calculated manually and by using STATDOSE code. The ability of each DI to assess ODs, was defined in terms of the difference between each DI_w and the calculated ODs as:

$$Difference\ (\%) = \left(1 - \frac{OD}{DI_w}\right) \times 100 \quad (9.5)$$

9.3 Results and Discussion

9.3.1 Organ Doses from the CBCT Scans

The dose values for organs and tissues located within the field of the primary beam for each scan are listed in Tables 9.2 - 9.4. Although the scanning protocols were the same for the male and female phantoms, ODs were different being greater for the female in the majority of organs. The disparities arose from differences in length, weight, gender, and diameter between the phantoms (Table 9.1), and were in agreement with ones reported in other studies conducted for CT (Zhang et al., 2012a) and dental CBCT scans (Morant et al., 2013, Zhang et al., 2013b). For pelvic scans, for example, the colon dose in the female was more than double that in the male. This resulted partly because the primary beam was more attenuated in the thicker male phantom and partly because a larger part of the colon for the female was within the scan field because of the shorter length (Table 9.1). For both the phantoms, dose to the right eye from the head scan was larger than to the left eye by ~17%, because of the asymmetric gantry rotation, which began at 90° to left of the phantom and rotated through 200° beneath the head to the 290° position with a 20° extra rotation on right of the phantom (Table 9.2).

Table 9.2: Calculated mean absorbed doses in organs and tissues of the ICRP-110 reference male and female phantoms in (mGy) from the head scan protocol

	OD (mGy)			
Organ / Tissue	**Male**		**Female**	
	Head scan			
Bone-marrow (red)	3.8	(1.2 – 6.4)	5.38	(1.69 - 9.07)
Extrathoracic (ET) region	2.3	(1.6 – 3.0)	3.64	(2.85 - 4.44)
Oral mucosa	2.3	(1.5 – 3.2)	3.41	(2.56 - 4.26)
Brain	3.0	(1.4 – 4.7)	3.39	(1.41 - 5.36)
Salivary glands	4.5	(3.9 – 5.1)	5.35	(4.75 - 5.94)
Eyes	1.1	(1.0 – 1.2)	1.09	(0.99 - 1.19)
Eye lens	0.9	(0.9 – 1.0)	1.01	(1.00 - 1.03)
Lymph nodes	5.8	(3.9 – 7.8)	7.83	(6.18 - 9.49)
Skin	3.3	(0.8 – 5.8)	3.57	(0.62 - 6.51)

Table 9.3: Calculated mean absorbed doses in organs and tissues of the ICRP-110 reference male and female phantoms in (mGy) from the thorax scan protocol

	OD (mGy)			
Organ / Tissue	**Male**		**Female**	
	Thorax scan			
Bone-marrow (red)	6.6	(4.5 – 8.8)	8.1	(6.0 – 10.2)
Lung	7.6	(6.3 – 8.9)	9.7	(8.4 – 11.0)
Stomach	3.4	(0.9 – 6.0)	2.7	(0.1 – 5.5)
Breast	7.5	(7.4 – 7.7)	9.9	(9.4 – 10.5)
Gall bladder	1.2	(0.8 – 1.7)	1.5	(1.2 – 1.9)
Lymph nodes	2.8	(0.8 – 6.4)	3.3	(1.0 – 7.6)
Heart	10.0	(8.3 – 11.7)	12.6	(11.0 – 14.1)
Pancreas	1.2	(0.9 – 1.5)	0.9	(0.6 – 1.2)
Spleen	3.4	(1.9 – 4.9)	3.4	(1.6 – 5.2)
Thymus	11.2	(8.8 – 13.6)	13.2	(12.4 – 14.0)
Oesophagus	6.1	(3.5 – 8.8)	7.9	(4.5 – 11.3)
Liver	3.2	(1.1 – 5.3)	4.0	(0.7 – 7.3)
Thyroid	2.5	(1.8 – 3.2)	3.3	(2.0 – 4.6)
Skin	2.0	(0.6 – 4.7)	2.7	(0.4 – 5.7)
Spinal cord	3.0	(0.3 – 5.7)	3.7	(0.2 – 7.1)

Table 9.4: Calculated mean absorbed doses in organs and tissues of the ICRP-110 reference male and female phantoms in (mGy) from the pelvic scan protocol

	OD (mGy)			
Organ / Tissue	**Male**		**Female**	
	Pelvic scan			
Bone-marrow (red)	29.1	(22.3 – 35.8)	34.0	(28.3 – 39.7)
Lymph nodes	12.8	(5.9 – 31.5)	13.7	(4.2 – 31.5)
Kidneys	1.3	(1.0 – 1.6)	2.3	(1.8 – 2.9)
Colon	10.7	(8.6 – 12.8)	26.9	(20.8 – 33.0)
Prostate / Uterus	32.4	(30.1 – 34.6)	36.6	(33.5 – 39.7)
Small intestine	14.3	(0.7 – 29.4)	24.2	(4.4 – 44.1)
Gonads (Testes / Ovary)	3.4	(2.8 – 4.0)	35.8	(34.7 – 37.0)
Urinary Bladder	41.6	(32.7 – 50.6)	46.4	(36.0 – 56.8)
Rectum	36.6	(35.7 – 37.5)	37.6	(35.8 – 39.5)
Skin	9.8	(5.5 – 25.0)	11.5	(4.8 – 27.8)

The statistical uncertainties in the dose calculations within each voxel for the majority of tissues were between 0.1% and 0.6%, with those for the lymph nodes and the skin being 1.8 – 2.5% and 2.7 – 3.8%, respectively, for scans of the thorax and pelvis. The skin and lymph nodes of the phantoms were divided into four regions: head, arms, trunk, and legs (ICRP, 2009), some of which were only partially irradiated in scans of the trunk. The statistical uncertainties for the male colon and kidney from the pelvic scan were relatively large, being 1.2% and 1.6%, respectively, and were larger than those for the female. This was related to the difference in the male and female phantom voxel sizes and the irradiated parts due to the differences in the phantoms.

Results of this study have been compared with those from a study by (Montanari et al., 2014), which was based on MC simulations on CT scans for 25 adult brain and 25 prostate cancer patients. They calculated ODs resulting from head and pelvic CBCT scans using the same OBI system and scanning protocols. The mAs value used for the pelvic scan (686.4 mAs) was different from that in this study (1056 mAs), thus 686.4 mAs was used to calculate ODs from the pelvic scan for the comparison. Doses for some organs in the present study are compared in Table 9.5 and show good agreement.

Table 9.5: A comparison between organ doses (ODs) calculated in this study using ICRP-110 adult male phantom and those from (Montanari et al., 2014) using the same OBI system and scanning parameters.

Organ	This study OD (mGy)	(Montanari et al., 2014) OD (mGy)
	Head scan	
Brain	3.0 (1.4 – 4.7)	2.7 (1.9 – 3.3)
Eyes	1.1 (1.0 – 1.2)	0.93 (0.3 – 2.4)
	Pelvic scan	
Prostate	21.0 (19.6 – 22.5)	20.4 (11.6 – 30.6)
Rectum	23.8 (23.2 – 24.4)	21.8 (14.4 – 28.8)
Bladder	27.1 (21.2 – 32.9)	21.3 (11.5 – 31.5)

9.3.2 Correlation between Dose Indices and Organ Doses

Table 9.6 shows values for the DIs studied using the scanning parameters listed in Table 2.1. The DI1:$CTDI_{w,100}$ was substantially lower than other indices, since the full width of the cone beam was not captured in the 100 mm length of the measurement, although the result was divided by the full beam width.

Table 9.6: Values for DI_w in (mGy) for the DIs described in section 9.2.1 (DI1:$CTDI_{w,100}$, DI2:$CTDI_{w,IEC}$, DI3:$f_{100}(150)_w$, DI4:$f(0,150)_w$, DI5:$f(0,\infty)_{w,PMMA}$, DI6: $f(0,\infty)_{w,PE}$, and DI7: $f(0,\infty)_{w,Water}$) using the three scanning protocols studied.

Protocol	DI1	DI2	DI3	DI4	DI5	DI6	DI7
Head	1.66	2.92	3.29	3.31	3.59	3.59	3.88
Thorax	2.21	3.81	4.38	4.57	4.82	4.56	5.74
Pelvis	8.84	15.25	17.50	18.29	19.25	18.20	22.93

Figures 9.2 - 9.4 show the difference values for the DIs calculated as in Eq.(9.5) to give an indication of their potential ability to evaluate ODs resulting from the scans studied. Since there were variations between ODs in the phantoms (Tables 9.2 - 9.4), the difference values varied. The relationship between the DIs and ODs varied for different scanning protocols:

The head scan (Figure 9.2): With the exception of DI1:$CTDI_{w,100}$, for which results are plotted on a separate bar chart at the end, generally the DIs overestimated doses to eyes and eyes lens and underestimated doses to bone marrow, salivary gland and lymph nodes for both the phantoms. Doses to the male ET region, oral mucosa, and brain were overestimated, but were overestimated and underestimated differently by DIs for the female phantom. The skin dose for both the phantoms were overestimated by some DIs, but underestimated by the other DIs. The best evaluation by the DIs was obtained for skin and brain within ±22% for the male and female phantoms, and the largest differences were for lymph node dose up to 100% for the male and 168% for the female. All the DIs apart from DI1:$CTDI_{w,100}$ overestimated the doses to the eyes and eye lenses by 62 – 76%, as might be expected since the eyes were only exposed indirectly to x-rays that had first passed through the head. DI5: $f(0,\infty)_{w,PMMA}$ was larger than the eye lens and skin doses by 74% and 7%, respectively, for the male and by 72% and 1%, respectively, for the female. This was in agreement with a dose study for CT neuro-perfusion scans using different MC adult phantoms and scanners employed with different tube potentials (Zhang et al., 2013a), where the differences ranged from -9% to 66% for the eyes lens and from -14% to 33% for the skin. DI1:$CTDI_{w,100}$, underestimated doses to the bone marrow, brain, salivary glands, lymph nodes, and skin significantly for both the phantoms by up to 372%. In general, the difference values between ODs and the DIs for the male phantom were lower than those for the female one.

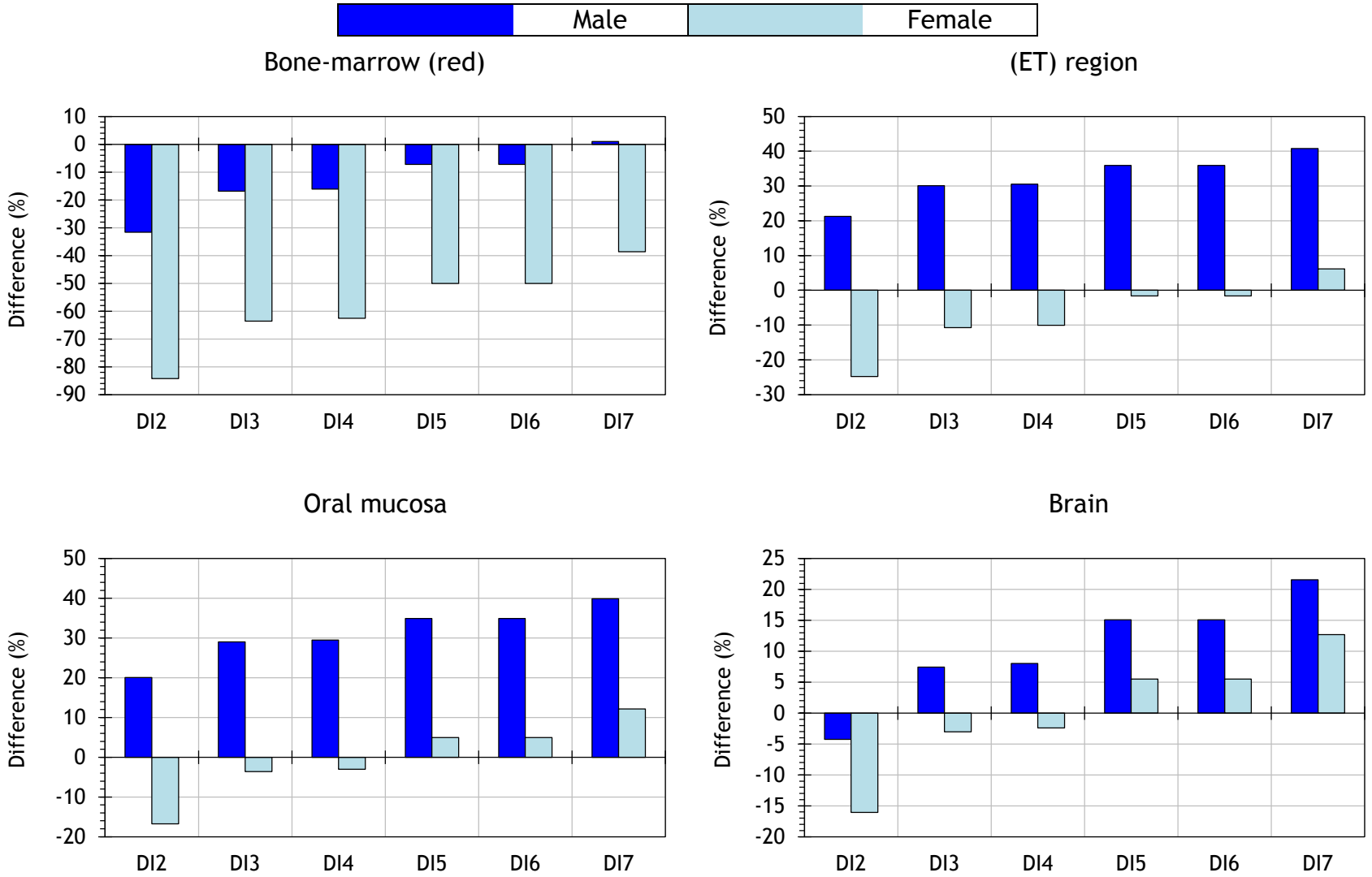
Male
Female
Bone-marrow (red)
(ET) region
Oral mucosa
Brain
Difference (%)
DI2
DI3
DI4
DI5
DI6
DI7

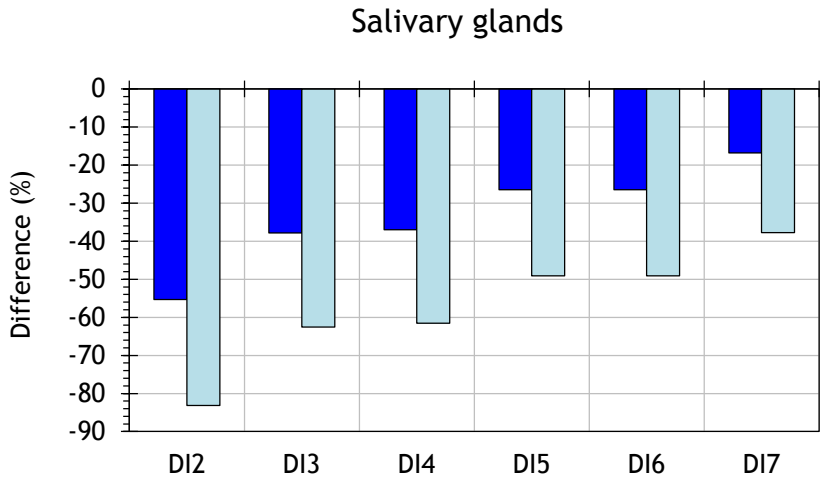
Salivary glands
Difference (%)
0
-10
-20
-30
-40
-50
-60
-70
-80
-90
DI2
DI3
DI4
DI5
DI6
DI7

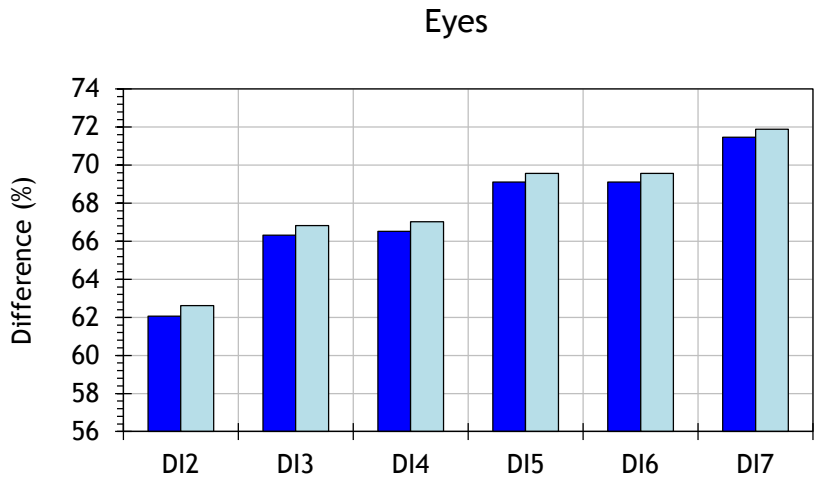
Eyes
Difference (%)
74
72
70
68
66
64
62
60
58
56
DI2
DI3
DI4
DI5
DI6
DI7

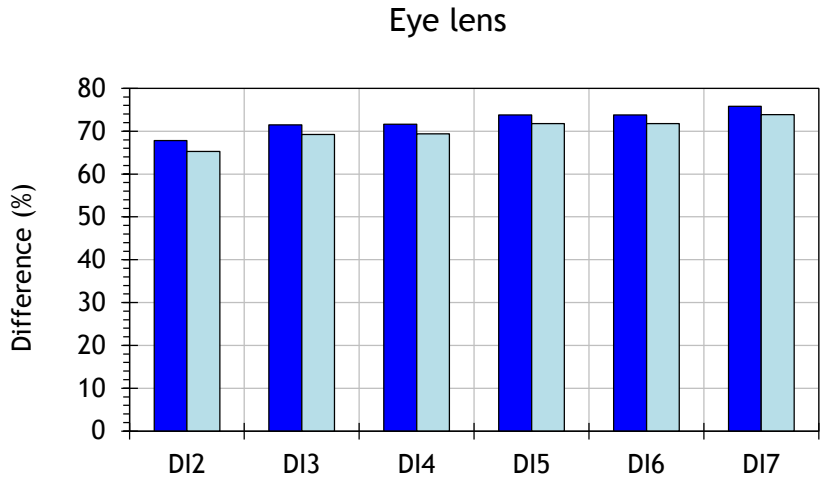
Eye lens
Difference (%)
80
70
60
50
40
30
20
10
0
DI2
DI3
DI4
DI5
DI6
DI7

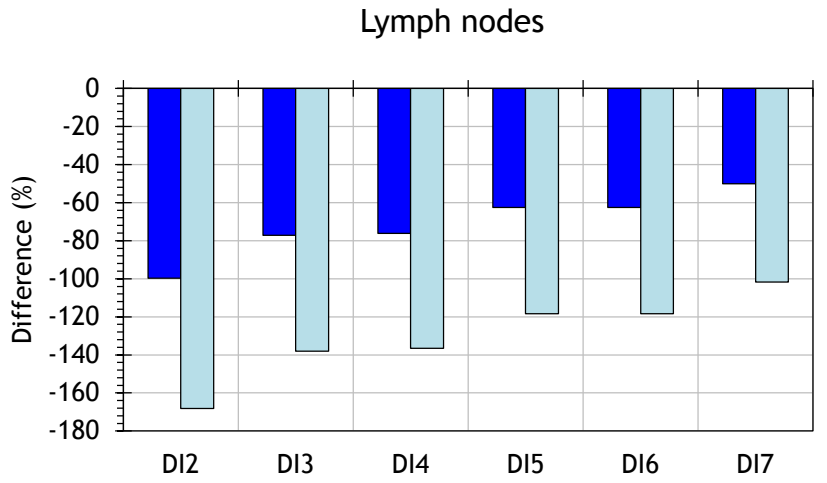
Lymph nodes
Difference (%)
0
-20
-40
-60
-80
-100
-120
-140
-160
-180
DI2
DI3
DI4
DI5
DI6
DI7

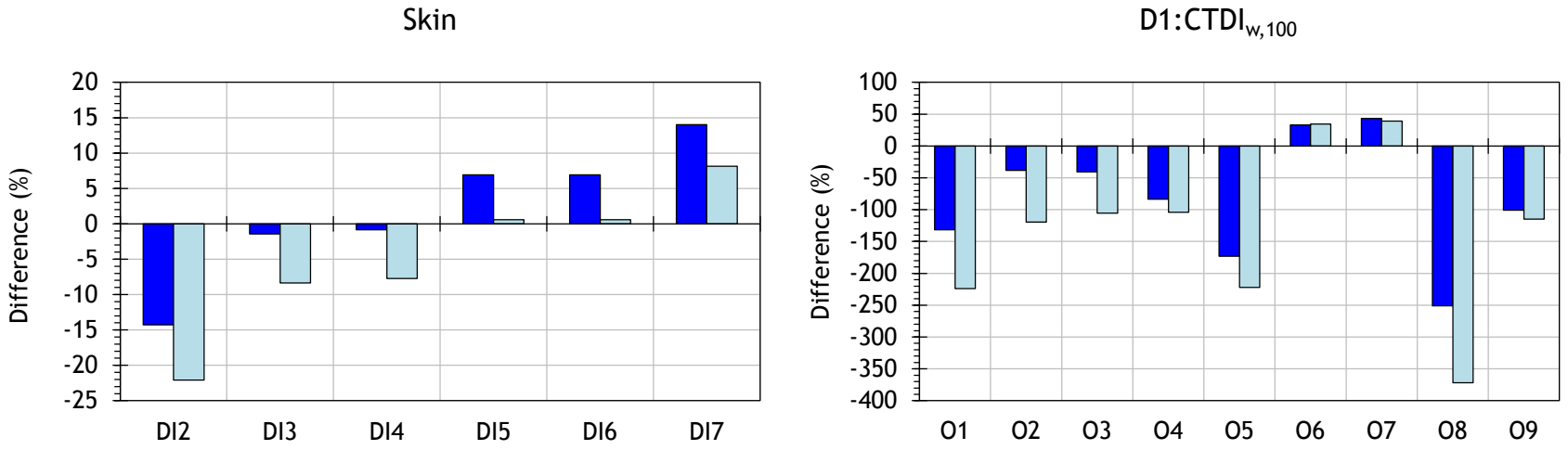

Figure 9.2: The ability of the DIs to evaluate organ doses listed in Table 9.2 in terms of the difference as in Eq.(9.5) for the head scan using the ICRP-110 reference male and female phantoms. (DI1:$CTDI_{w,100}$, DI2:$CTDI_{w,IEC}$, DI3:$f_{100}(150)_w$, DI4:$f(0,150)_w$, DI5:$f(0,\infty)_{w,PMMA}$, DI6: $f(0,\infty)_{w,PE}$, and DI7: $f(0,\infty)_{w,Water}$). The difference values for DI1:$CTDI_{w,100}$ were shown separately due to the large differences. O1: Bone marrow (red) followed by O2: (ET) region, and etc.

The thorax scan (Figure 9.3): Most DIs other than DI1:$CTDI_{w,100}$ overestimated doses to the stomach, lymph nodes, spleen, liver, thyroid, spinal cord and skin by less than 50% and pancreas and gall bladder by up to 84%. Doses to the bone marrow, lung, breast, and oesophagus were underestimated by between 7% and 161%, and some DIs underestimated dose to the heart and thymus by over 200%. The difference values between the male and female scans for each organ were less than those for the head scan (Figure 9.2). The lowest differences found between the DIs and ODs were for the male stomach and spleen within 44% and for the female liver within 31%, and the largest differences were for thymus doses up to 194% for the male and 246% for the female. Overall, differences between the IDs and ODs were lower for the male than the female, as with the head scan. DI1:$CTDI_{w,100}$ underestimated doses for organs significantly such as the bone marrow, lung, breast, heart thymus and oesophagus for both the phantoms by 178 – 497%.

The pelvic scan (Figure 9.4): Doses evaluated by most DIs for lymph nodes, colon, small intestine and skin, other than DI1:$CTDI_{w,100}$, were within ±50% of the ODs. The DIs overestimated doses for the lymph nodes, kidney and skin, but underestimated those for the bone marrow, prostate, uterus, urinary bladder, and rectum. Doses for the colon, small intestine and gonads were overestimated by the DIs for the male but underestimated for the female. The best estimation was obtained for the male small intestine within 38% and the female lymph nodes within 40%, and the largest differences were for urinary bladder doses up to 77% and 204% for the male and female, respectively. The differences between the DIs and ODs were lower for the male phantom than for the female one, as for the head and thorax scans, and most of the female organs 7/10 were underestimated. The $CTDI_{w,100}$ values were much lower than most of the ODs, and underestimated them by up to 371% and 425% for the male and female, respectively.

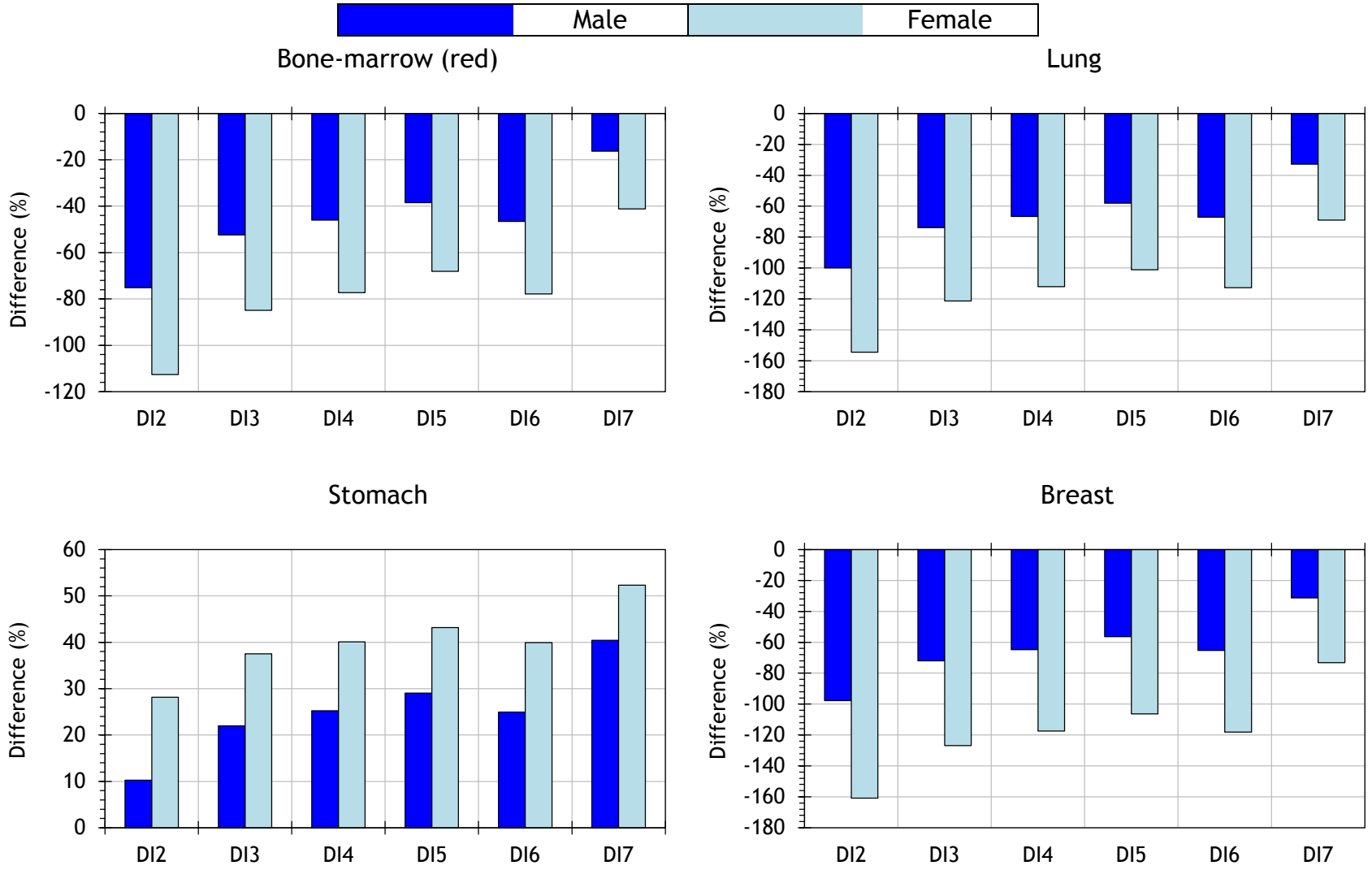
Male
Female
Bone-marrow (red)
Lung
Stomach
Breast
Difference (%)
0
-20
-40
-60
-80
-100
-120
-140
-160
-180
60
50
40
30
20
10
DI2
DI3
DI4
DI5
DI6
DI7

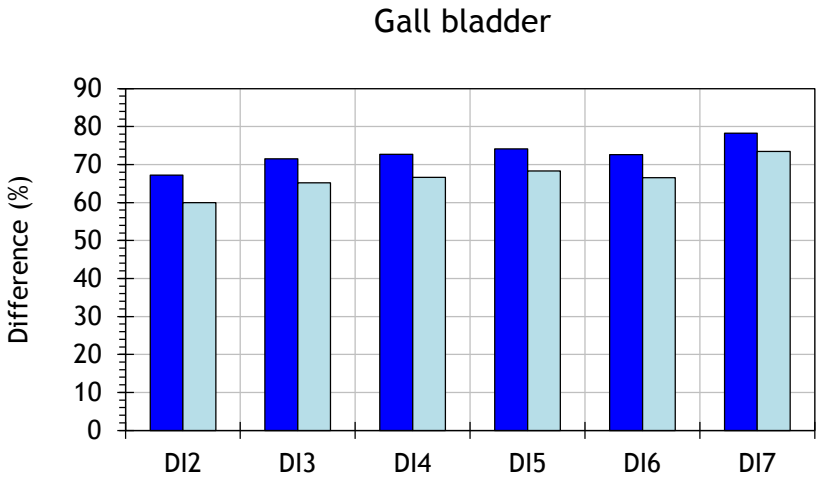
Gall bladder
Difference (%)
90
80
70
60
50
40
30
20
10
0
DI2
DI3
DI4
DI5
DI6
DI7

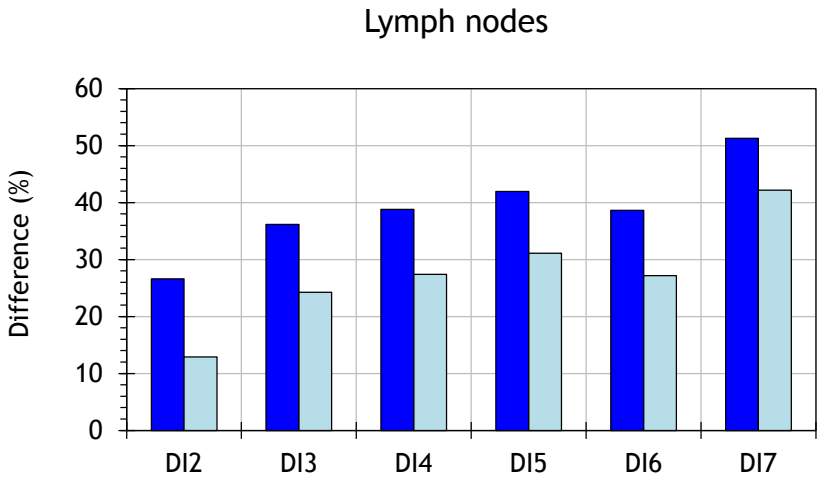
Lymph nodes
Difference (%)
60
50
40
30
20
10
0
DI2
DI3
DI4
DI5
DI6
DI7

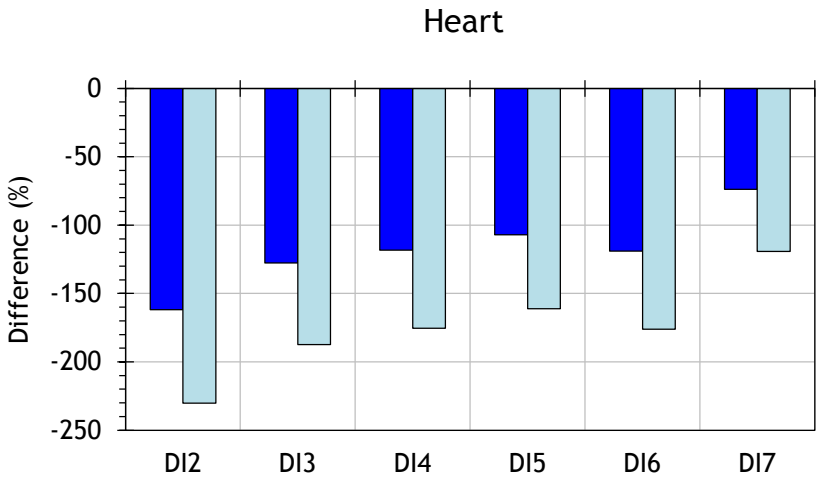
Heart
Difference (%)
0
-50
-100
-150
-200
-250
DI2
DI3
DI4
DI5
DI6
DI7

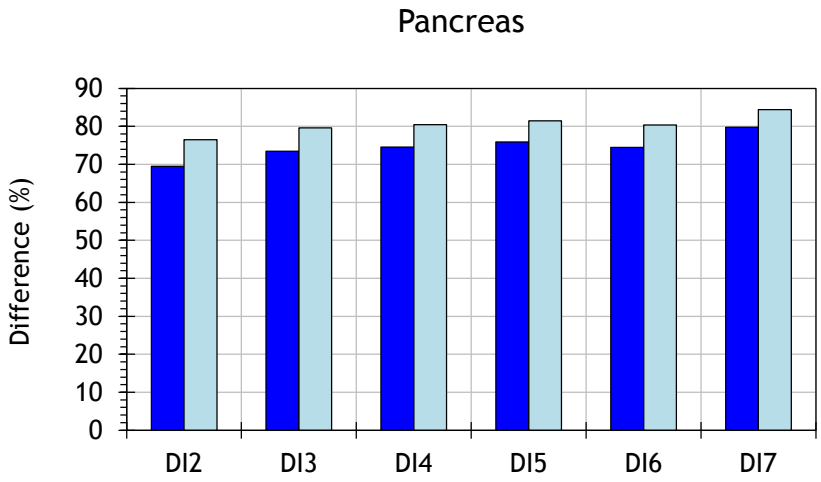
Pancreas
Difference (%)
90
80
70
60
50
40
30
20
10
0
DI2
DI3
DI4
DI5
DI6
DI7

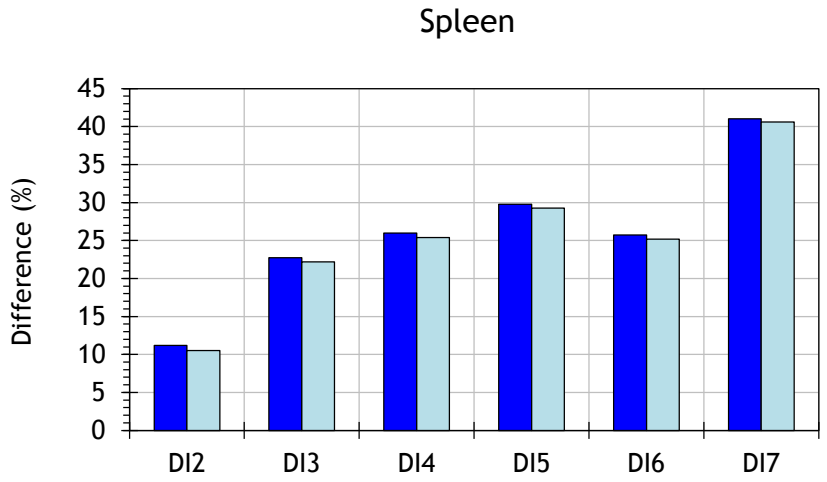
Spleen
Difference (%)
45
40
35
30
25
20
15
10
5
0
DI2
DI3
DI4
DI5
DI6
DI7

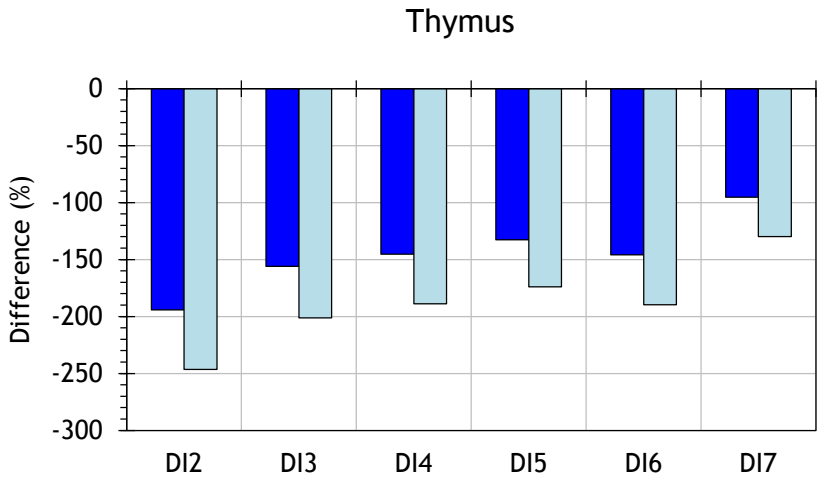
Thymus
Difference (%)
0
-50
-100
-150
-200
-250
-300
DI2
DI3
DI4
DI5
DI6
DI7

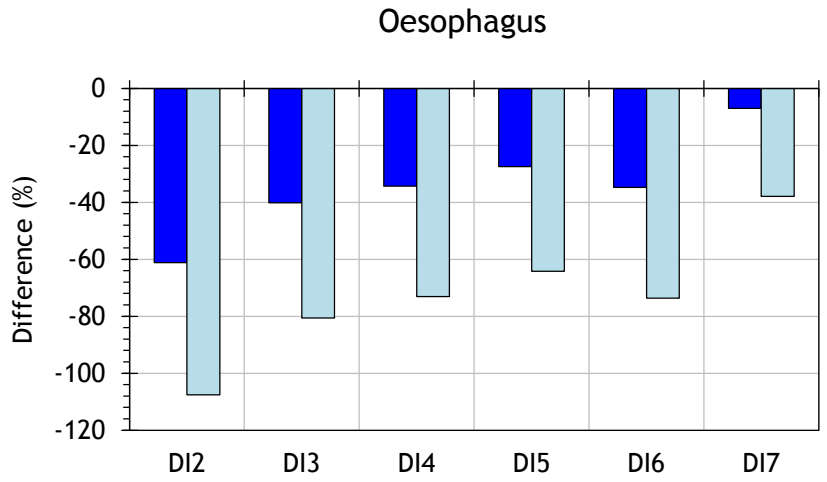
Oesophagus
Difference (%)
0
-20
-40
-60
-80
-100
-120
DI2
DI3
DI4
DI5
DI6
DI7

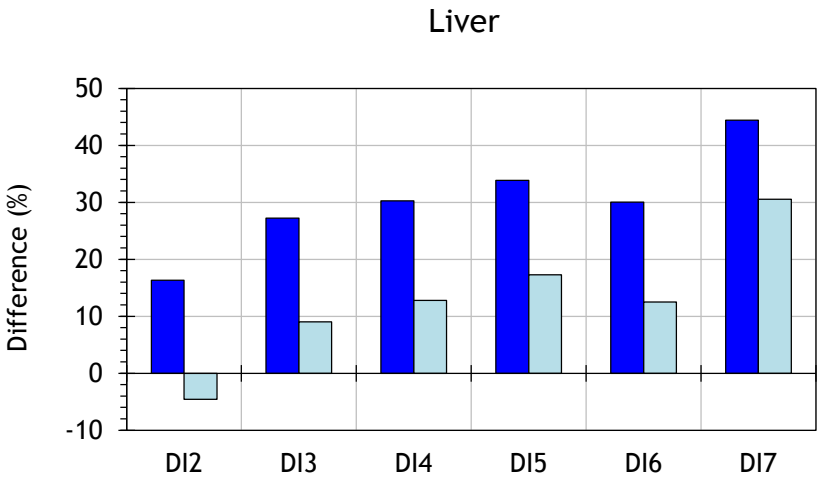
Liver
Difference (%)
50
40
30
20
10
0
-10
DI2
DI3
DI4
DI5
DI6
DI7

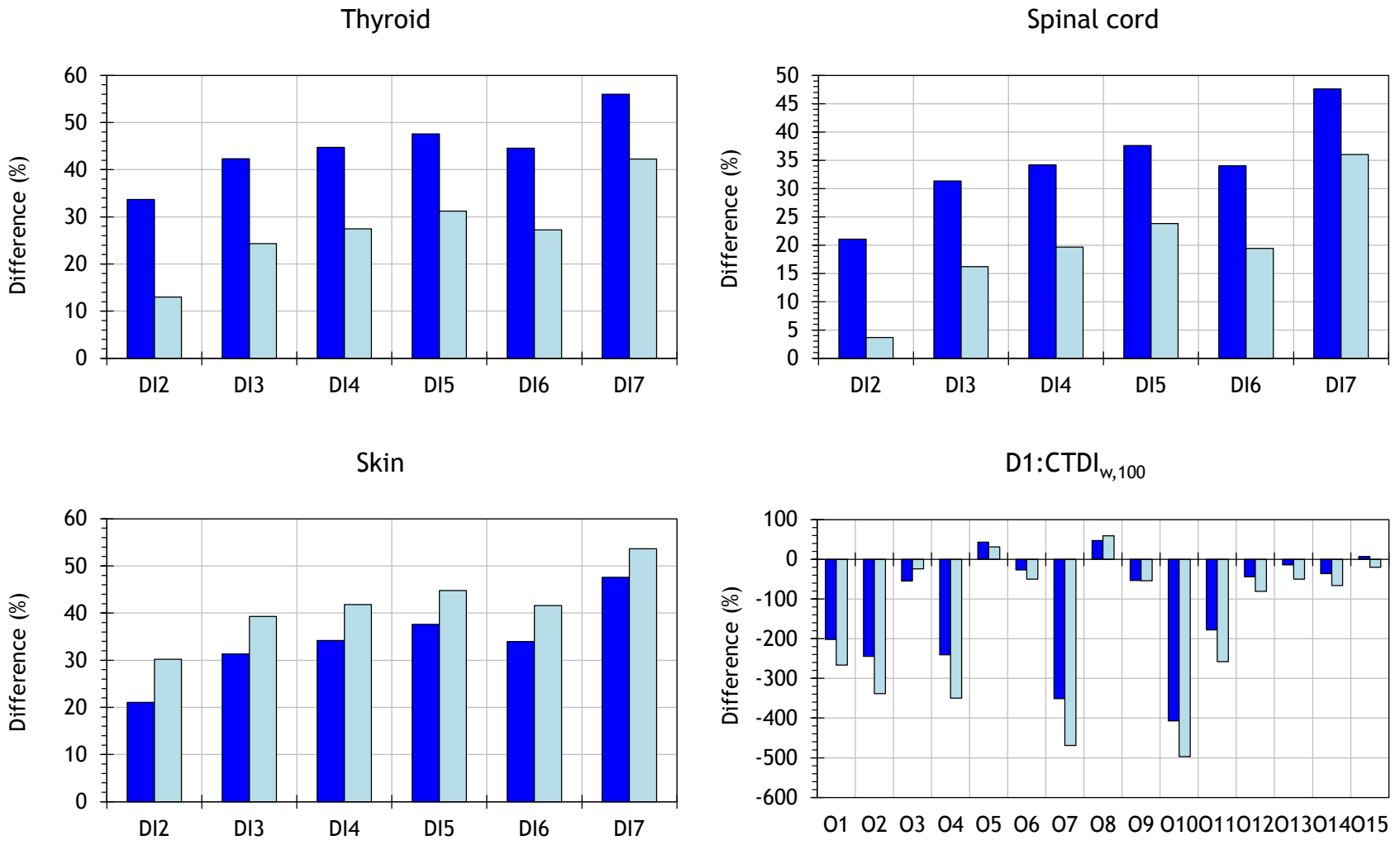

Figure 9.3: The ability of the DIs to evaluate organ doses listed in Table 9.3 in terms of the difference as in Eq.(9.5) for the thorax scan using the ICRP-110 reference male and female phantoms. (DI1:$CTDI_{w,100}$, DI2:$CTDI_{w,IEC}$, DI3:$f_{100}(150)_w$, DI4:$f(0,150)_w$, DI5:$f(0,\infty)_{w,PMMA}$, DI6: $f(0,\infty)_{w,PE}$, and

DI7: $f(0,\infty)_{w,Water}$). The difference values for DI1:CTDI$_{w,100}$ were shown separately due to the large differences. O1: Bone marrow (red) followed by O2: Lung, and etc.

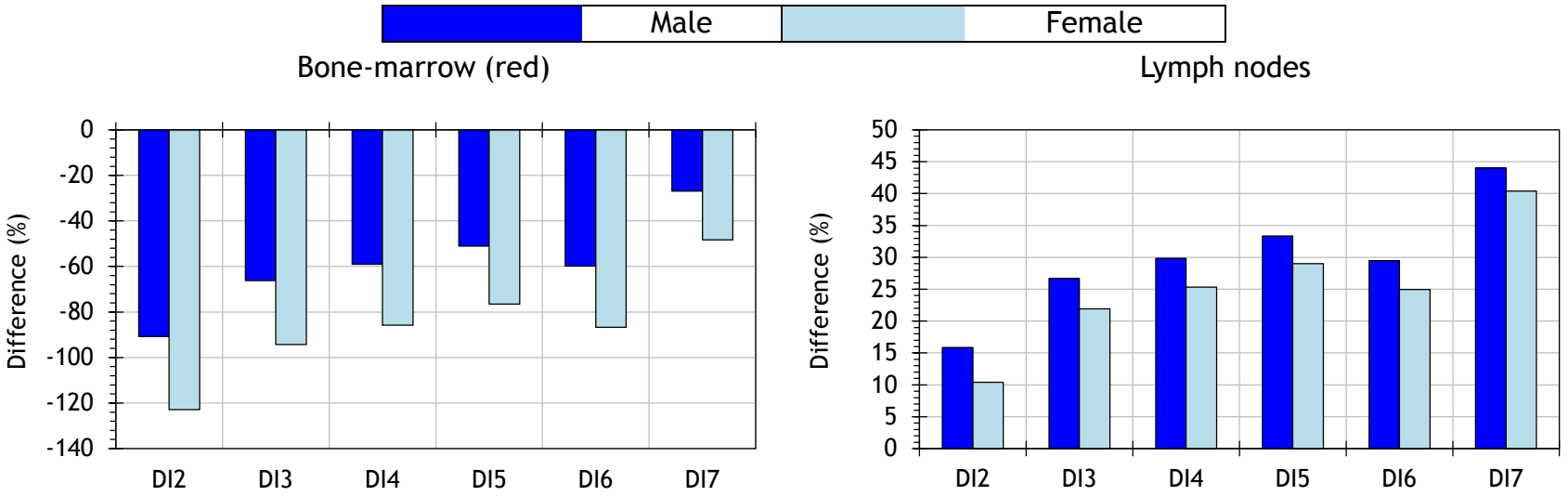

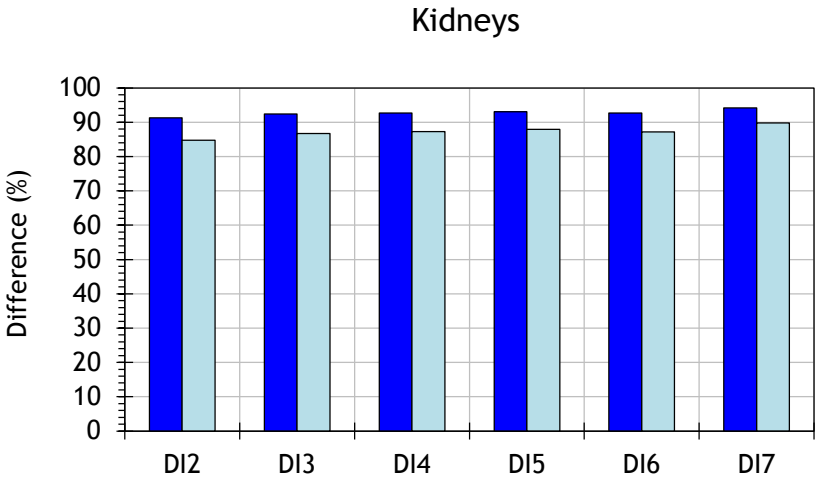
Kidneys
Difference (%)
100
90
80
70
60
50
40
30
20
10
0
DI2
DI3
DI4
DI5
DI6
DI7

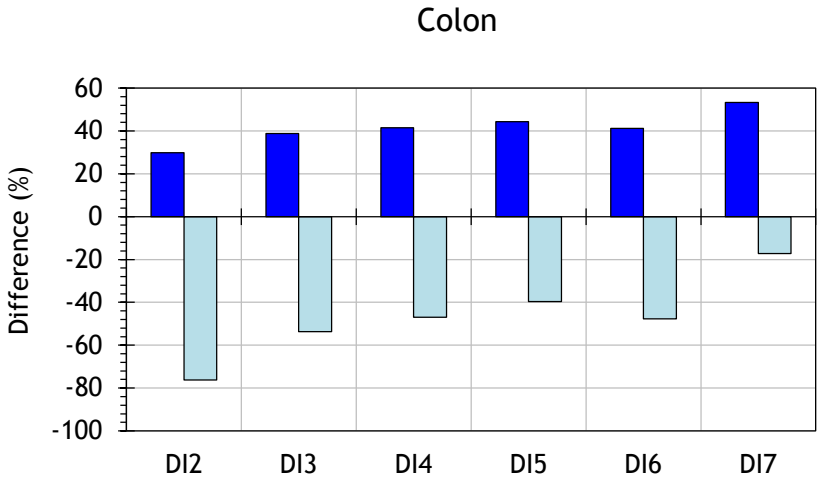
Colon
Difference (%)
60
40
20
0
-20
-40
-60
-80
-100
DI2
DI3
DI4
DI5
DI6
DI7

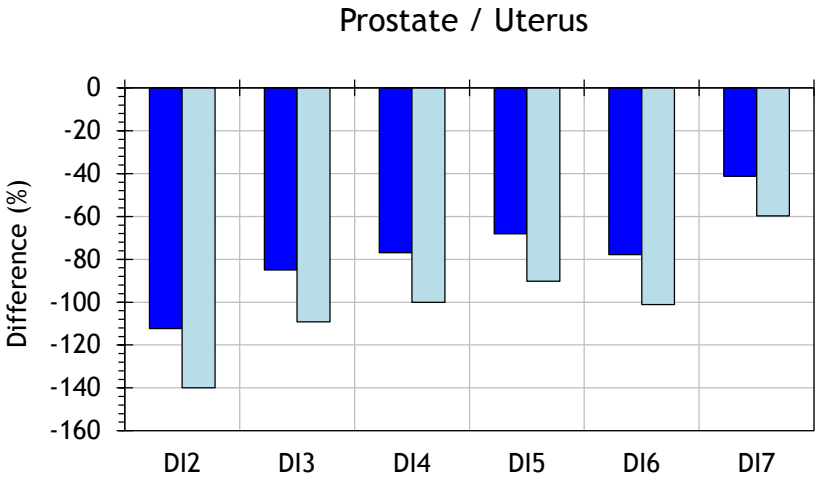
Prostate / Uterus
Difference (%)
0
-20
-40
-60
-80
-100
-120
-140
-160
DI2
DI3
DI4
DI5
DI6
DI7

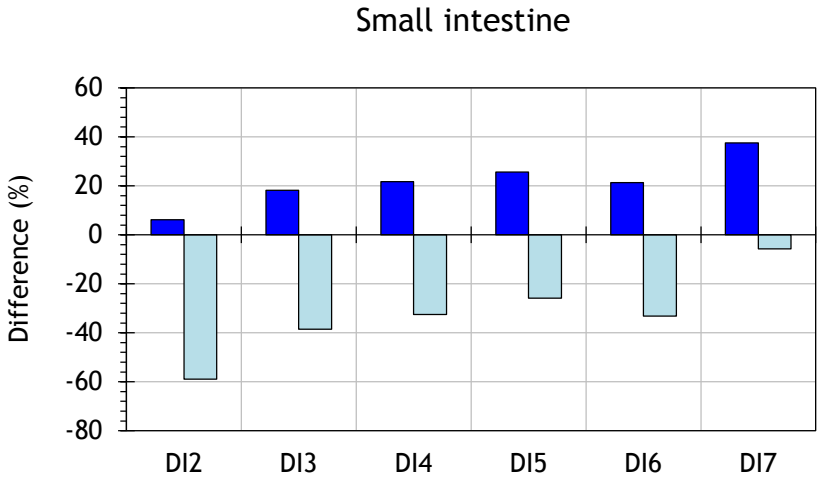
Small intestine
Difference (%)
60
40
20
0
-20
-40
-60
-80
DI2
DI3
DI4
DI5
DI6
DI7

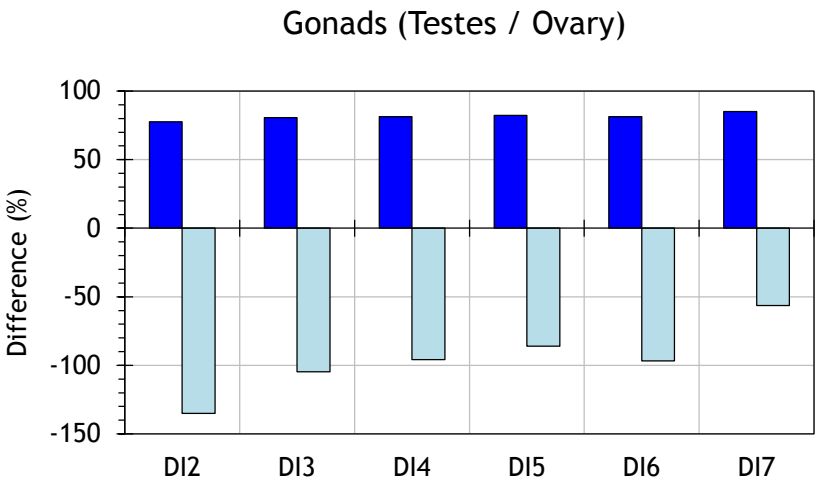
Gonads (Testes / Ovary)
Difference (%)
100
50
0
-50
-100
-150
DI2
DI3
DI4
DI5
DI6
DI7

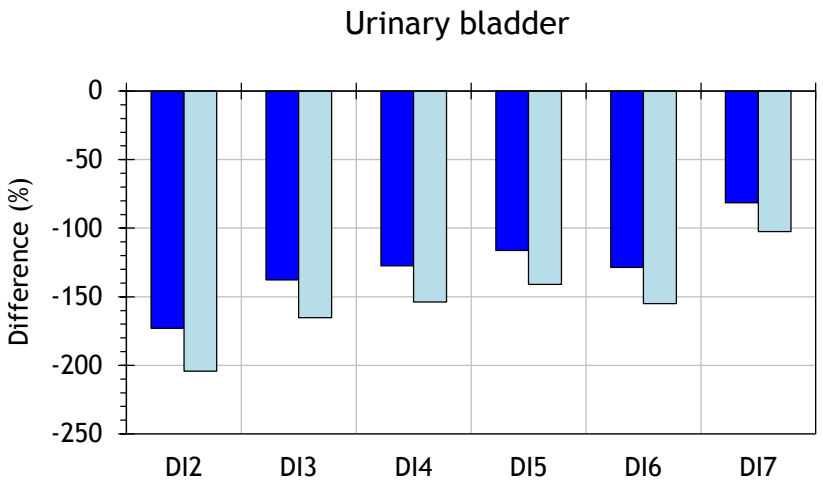
Urinary bladder
Difference (%)
0
-50
-100
-150
-200
-250
DI2
DI3
DI4
DI5
DI6
DI7

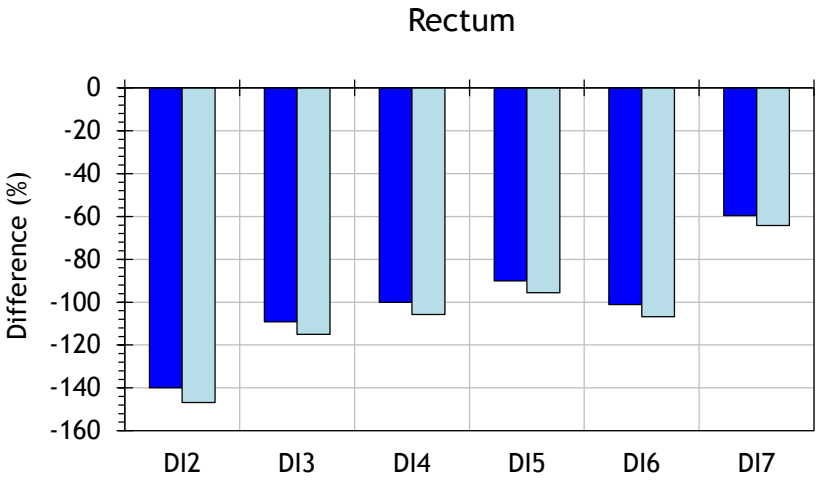
Rectum
Difference (%)
0
-20
-40
-60
-80
-100
-120
-140
-160
DI2
DI3
DI4
DI5
DI6
DI7

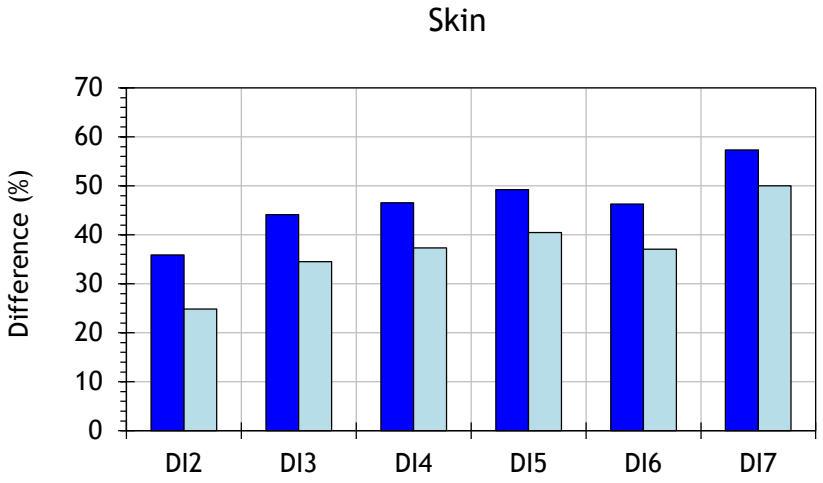
Skin
Difference (%)
70
60
50
40
30
20
10
0
DI2
DI3
DI4
DI5
DI6
DI7

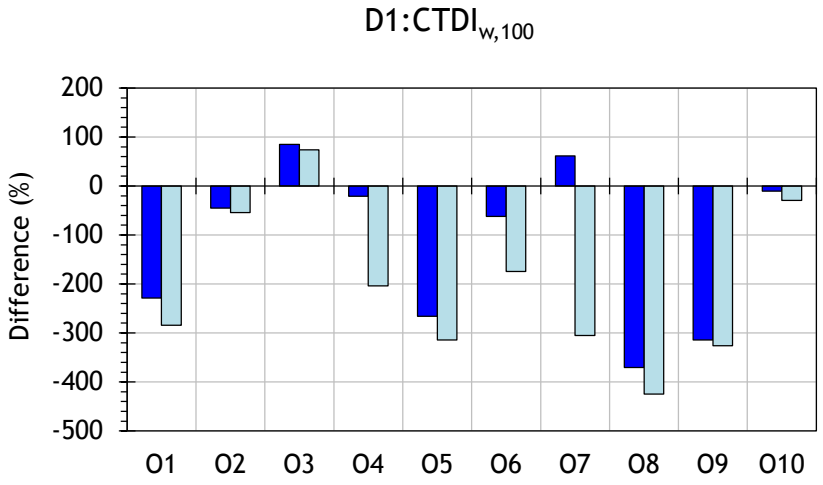

Figure 9.4: The ability of the DIs to evaluate organ doses listed in Table 9.4 in terms of the difference as in Eq.(9.5) for the pelvic scan using the ICRP-110 reference male and female phantoms. (DI1:$CTDI_{w,100}$, DI2:$CTDI_{w,IEC}$, DI3:$f_{100}(150)_w$, DI4:$f(0,150)_w$, DI5:$f(0,\infty)_{w,PMMA}$, DI6: $f(0,\infty)_{w,PE}$, and DI7: $f(0,\infty)_{w,Water}$). The difference values for DI1:$CTDI_{w,100}$ were shown separately due to the large differences. O1: Bone marrow (red) followed by O2: Lymph nodes, and etc.

In general the differences between DI1: $CTDI_{w,100}$ and ODs was larger than for the other IDs (Figures 9.2 - 9.4), thus it was not included in the general discussion. The purpose of the DIs is to provide practical measures that can be used to evaluate scanner performance that have a link to the dose within the body of a patient (Kalender, 2014). Doses to radiosensitive organs determine the risk from radiation and it has become clear in recent years that any assessment of risk should be based on doses to individual patients (McCollough et al., 2011, AAPM, 2011). It would be helpful to have more direct links between the measured dose quantities and ODs, in order to improve the knowledge and understanding of radiation professionals in healthcare. The uncertainties in any assessment of organ doses are large by their very nature (Martin, 2007), being based on simulations involving reference phantoms, which cannot represent even subtle differences between individuals, let alone large differences in body size and shape. It is apparent that even differences between the heads of reference male and female phantoms can give different doses, of the order of ±100% (Figure 9.2), thus it would be a vain hope that any DI could achieve an accurate evaluation for ODs. It is apparent from the analyses of differences between the DIs and ODs (Figures 9.2 - 9.4) that some DIs could provide values for doses to organs within the scan field. This would provide the radiotherapy clinician with an indication of the doses that are being delivered by imaging to other organs in the region of the body close to the radiotherapy target volume.

From the results (Figures 9.2 - 9.4), it is apparent that the DIs give assessments for doses to a number of organs in the reference phantom within about ±50%, which is similar to the uncertainty in the dose calculations for many organs (Martin, 2007). Doses to more distributed tissues such as the skin, lymph nodes and bone marrow had high uncertainties and are difficult to visualize in terms of doses to organs within the field. Doses to some organs were deviated by much more than 50%, such as the heart, pancreas, breast, gall bladder and thymus in the thorax scans, and the kidneys, prostate, bladder, rectum and gonads in the pelvic scans. However, focussing on the more exposed organs and those known to have a higher associated stochastic risk, Table 9.7 shows the differences

between ODs and some of the DIs, DI2:$CTDI_{w,IEC}$, DI3: $f_{100}(150)_w$, DI4: $f(0{,}150)_w$, and DI6: $f(0,\infty)_{w,PE}$, where DI6 represented measurements within the ICRU/AAPM phantom. The DIs underestimated doses to the lungs and female breast, but doubling these DIs would give values close to the ODs. Thus multiplying the dose index by two provides a possible option and is included in Table 9.7. Moreover, DI3: $f_{100}(150)_w$ and DI4: $f(0{,}150)_w$ could be taken as a reasonable indication of doses to selected organs for each type of scan.

Table 9.7: The differences between some of the DIs, DI2:$CTDI_{w,IEC}$, DI3: $f_{100}(150)_w$, DI4: $f(0,150)_w$, and DI6: $f(0,\infty)_{w,PE}$ and some organs of the ICRP-110 reference male and female phantoms, which have a higher associated stochastic risk.

Phantom	Male				Female			
DIs	DI2	DI3	DI4	DI6	DI2	DI3	DI4	DI6
	Deviation (%)				Deviation (%)			
Organ	**Head scan**							
Brain	-4	7	8	15	-16	-3	-2	-5
Salivary glands	-55	-38	-37	-26	-38	-63	-62	-49
	Thorax scan							
Breast					-161	-127	-117	-118
Breast (DIs × 2)					-30	-13	-9	45
Lung	-100	-74	-67	-67	-154	-121	-112	-113
Lung (DIs × 2)	0	13	17	58	-27	-11	-6	47
Stomach	10	22	25	25	28	38	40	40
Liver	16	27	30	30	-5	9	13	13
Thyroid	34	42	45	45	13	24	27	27
	Pelvic scan							
Colon	30	39	41	62	-76	-54	-47	-48

For some superficial organs such as eyes and breast, the use of DIs at the peripheries of the phantoms (DI_p) decreases the differences between DIs and ODs. Figure 9.5 shows a comparison between using the weighted and peripheral values of the DIs to estimate the breast dose for the female phantom. Differences between DI_p and breast dose were reduced by 4 – 24% compared to the DI_w. However, the reduction between DI_p and the eyes dose was lower, where the differences were by up to 4%. This is related to

that the differences between the dose at the centre and periphery of the head phantoms, which are lower than those for the body phantoms.

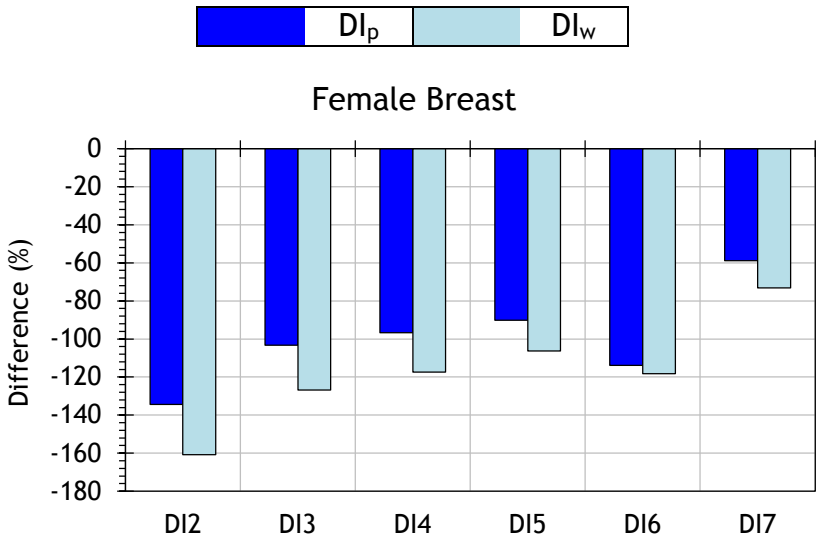

Figure 9.5: A comparison between using the dose at the periphery of the phantoms (DI_p) and the weighted values (DI_w) of the DIs studied to estimate the breast dose for the female phantom.

9.4 Conclusion

The ability of seven DIs to provide a surrogate index for ODs resulting from three CBCT scans has been investigated using the ICRP-110 male and female reference computational phantoms. The ability of each DI to assess ODs, was defined in terms of the difference between DI_w and the calculated ODs. With the exception of DI1:$CTDI_{100,w}$, lower differences were found for the head scan compared to the thorax and pelvis, where the differences for both the phantoms ranged from -168% to 76% for the head scan, from -246% to 84% for the thorax scan, and from -204% to 94% for the pelvic scan. The differences for the male phantom were smaller than those for the female phantom, and DI1:$CTDI_{100,w}$, underestimated most of the ODs for all the scanning protocols by up to 497%. By comparing the DIs to the dose of each organ resulting from the three scanning protocols, DI2:$CTDI_{w,IEC}$ and DIs 5 - 7: $f(0,\infty)_{w,m}$ had slightly lower differences. The DIs can give a reasonable measure of doses to the brain and salivary glands for head scans, the breast, lung, stomach, liver and thyroid for thorax scans, and the colon for scans of the pelvis. Multiplication of the DIs by a factor of 2 is proposed for

assessment of doses to the lungs and female breast for scans of the thorax. For practical application, any of the DIs 2 - 7 could be used to give an indication of doses to more exposed and more radiosensitive organs. Results of this study have been submitted for publication.

Chapter 10

Conclusion and Future Work

10.1 Conclusion

EGSnrc-based user codes BEAMnrc and DOSXYZnrc were employed to simulate the OBI system. The MC technique was utilized to investigate the performance of various methods for dosimetry of CBCT scans, which are presented in Chapters 5 – 9. The main aims of these studies were (1) to compare dose indices based on different approaches in terms of their suitability for CBCT dosimetry, and (2) to facilitate utilizing the AAPM approach which is based on heavy and long phantoms, and takes into account almost all the radiation contributing to patient doses.

This project investigated various aspects with the aim of contributing effectively to the body of knowledge on CBCT dosimetry. The efficiency of $CTDI_{100}$ and $CTDI_{IEC}$ were discussed (Chapter 5). This was followed by another investigation that looked into different methods proposed for CBCT dosimetry and is based on the cumulative dose concept (Chapter 6). As the AAPM method is based on evaluating the cumulative dose within long and heavy phantoms, alternative methods to simplify the AAPM method were studied. A function called $G_x(W)_{100}$, which was shown to be relatively independent of the tube potential, was proposed (Chapter 7). The use of small phantoms and developing correction factors were investigated (Chapter 8). The dose indices based on the different methods investigated in Chapters 5 - 8 were compared against organ doses resulting from three CBCT scans, head, thorax and pelvis to assess which method gives the best estimations for organ doses (Chapter 9). Based on these investigations, various recommendations and conclusions can be presented from this project:

10.1.1 Approaches for CBCT Dosimetry

Since the advent of CBCT, different dosimetric approaches have been proposed. Although almost all the different international organizations agreed on the failure of $CTDI_{100}$ in providing a satisfactory dose descriptor for CBCT scans, no standard approach has been agreed globally and as a result it is difficult to progress developments in measurement equipment and techniques. Each dose index has advantages and disadvantages, which make choosing a dosimetric method for CBCT scans difficult. However, a comparison between the dose indices can be provided, from which a dose index based on a specific approach is recommended in this project. This recommendation aims to contribute to the literature, which may help the scientific community and international organizations in reaching consensus on CBCT dosimetry methods. In order to compare the approaches based on a scientific ground, three main factors can be considered: (1) The efficiency of the approach as a dose descriptor to report $CTDI_{\infty}$ for CBCT scans.

(2) The simplicity of the application of the approach in the clinical environment in terms of availability of the measuring instruments, simplicity of the technique, and the number of the scans required to accomplish a QA assessment, i.e. the QA time.

(3) The ability of the approach for evaluating organ doses resulting from the scans.

Table 10.1 shows a comparison between the different dose indices studied in Chapters 5 - 6 taking into account the first and second factors. Considering the first factor, Figure 10.1 illustrates the ability of each approach to report the $CTDI_{\infty,w}$ values, i.e. the efficiency. All the approaches were strongly dependent on the beam width with the exception of the $CTDI_{IEC}$. However, for the beams of width W > 100 mm, the other approaches were able to provide values larger than those of $CTDI_{IEC}$ and so closer to $CTDI_{\infty}$. The highest values were obtained with $f(0,\infty)$ (Figure 10.1). Moreover, it can be seen that values for $f(0{,}150)$ and $f_{100}(150)$ became virtually constant for beam widths W > 150 mm.

By taking the second factor into account and based on the comparison presented in (Table 10.1), measurements of $f(0,150)$ and $f_{100}(150)$ require lower numbers of acquisitions compared to those required for $CTDI_{IEC}$, and hence a shorter time is required for the QA work. Moreover, $f(0,150)$ and $f_{100}(150)$ are measured within the standard PMMA phantoms, thus there is no need to use the long phantoms required for $f(0,\infty)$ and $f_{100}(\infty)$ measurements. Therefore, from this point of view, the dose indices $f(0,150)$ and $f_{100}(150)$ seem to be more practical for routine application in the clinic than the other approaches.

Considering the third factor, which considers the performance of the different dose indices in terms of predicting organ doses, Figures 10.2 - 10.3 show ranges between the maximum underestimation and overestimation values obtained for each dose index investigated in Chapter 9. The range in Figure 10.2 covers all organs studied for each scanning protocol presented in Figures 9.2 - 9.4 Chapter 9, whereas only the radiosensitive organs selected in Table 9.7 Chapter 9 are considered in Figure 10.3 . Note that, DI1:$CTDI_{100,w}$ was not included into the plots due to its larger deviations as discussed previously. The IEC (DI2) and AAPM (DIs 5 - 7) approaches were closest to respective organ doses in more cases, although deviations were variable (Figures 9.2 - 9.4). However, these approaches are considered the least practical in the clinical environment as shown in Table 10.1. The DIs that could be more readily assessed and are more practical for use in the clinic environment are DI3: $f_{100}(150)_w$ and DI4: $f(0,150)_w$. As shown in Figures 10.2 - 10.3, generally, the maximum underestimation and overestimation of these DIs are comparable to those for the other approaches. DI3: $f_{100}(150)_w$ and DI4: $f(0,150)_w$ could provide an estimate that is good enough, bearing in mind the overall accuracy, to give operators and clinicians a reasonable indication of the doses delivered to the designated organs within the scan field.

The comparisons between the different approaches presented in Table 10.1 and Figures 10.1 - 10.3 show that all the approaches investigated in this project, except $CTDI_{100}$, are comparable and suitable for CBCT dosimetry. However, based on the three factors considered earlier, and on the fact

that most of CBCT scans are conducted with a beam of width greater than 80 mm, this project recommends the $f(0,150)$ approach, as the best dose index for CBCT dosimetry. $f(0,150)_w$ values for W ≥ 80 mm were higher than $CTDI_{IEC,w}$ and $f_{100}(150)_w$ values for the head and body phantoms (Figure 10.1). $f(0,150)_w$ values for W ≥ 80 ranged from 0.79 to 0.95 of $CTDI_{\infty,w}$ values within the head phantom, and from 0.77 to 0.92 within the body phantom. Moreover, $f(0,150)_w$ values were approximately stable for W > 150 mm at ~0.94 and ~0.92 of $CTDI_{\infty,w}$, on average, for the head and body phantoms, respectively. These underestimations, however, can be overcome by the application of correction factors. Although $f(0,\infty)_w$ and $f_{100}(\infty)_w$ values were higher than those of $f(0,150)_w$, the $f(0,150)$ approach is more practical in the clinical environment in terms of the handling and availability of equipment and the QA measurement time, and deviations of DI4: $f(0,150)_w$ were comparable to those for the other approaches.

This project suggests that if a small chamber is unavailable, the $f_{100}(150)$ approach can also be employed instead of the $f(0,150)$ approach. $f_{100}(150)$ was shown to be practical and has most of the $f(0,150)$ advantages. The efficiency values for $f_{100}(150)$ were lower than those for $f(0,150)$ as discussed in detail in Chapter 6. However, the differences between the efficiency values were constant for the beam width > 150 mm at ~3% and ~ 2% for the head and body phantoms, respectively.

Table 10.1: A comparison between five different methods for CBCT dosimetry and the standard $CTDI_{100}$. The dose ratios were calculated with beams of width W = 40 – 300 mm.

		$CTDI_{100}$	$CTDI_{IEC}$	$f(0,150)$	$f_{100}(150)$	$f(0,\infty)$	$f_{100}(\infty)$
Chamber length (mm)		100	100, 300	20	100	20	100
Phantom type		Standard	Standard Free in air	Standard	Standard	Long	Long
Number of measurements		5	7, 8, 9,etc [(a)]	5	5	5	5
Affected by the nominal beam width (W)		Yes	No	Yes	Yes	Yes	Yes
Availability of equipment worldwide		Yes	Yes	Yes	Yes	No	No
ε_c	Head	0.74 – 0.28	0.76 ± 0.01	0.50 – 0.90	0.30 – 0.85	0.51 – 1.01	0.30 – 1.00
	Body	0.58 – 0.24	0.60 ± 0.01	0.36 – 0.75	0.23 – 0.72	0.37 – 0.99	0.25 – 0.97
ε_p	Head	0.84 – 0.32	0.86 ± 0.01	0.73 – 0.99	0.34 – 0.97	0.74 – 1.05	0.34 – 1.04
	Body	0.82 – 0.34	0.83 ± 0.01	0.76 – 1.02	0.33 – 1.02	0.77 – 1.11	0.33 – 1.10
ε_w	Head	0.80 – 0.31	0.82 ± 0.01	0.65 – 0.95	0.32 – 0.92	0.65 – 1.03	0.32 – 1.03
	Body	0.75 – 0.31	0.76 ± 0.01	0.64 – 0.94	0.30 – 0.91	0.64 – 1.07	0.30 – 1.06

(a) Number of the measurements required for $CTDI_{IEC}$ is based on the beam width and length of the ionization chamber.

(a)

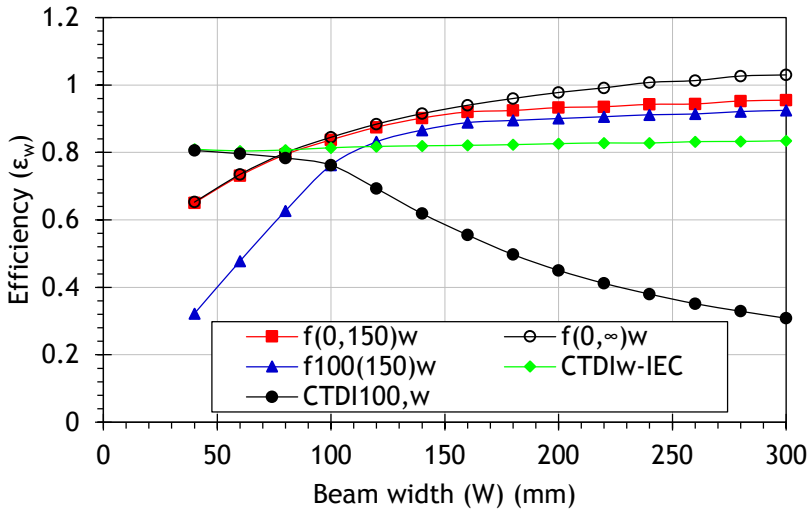

(b)

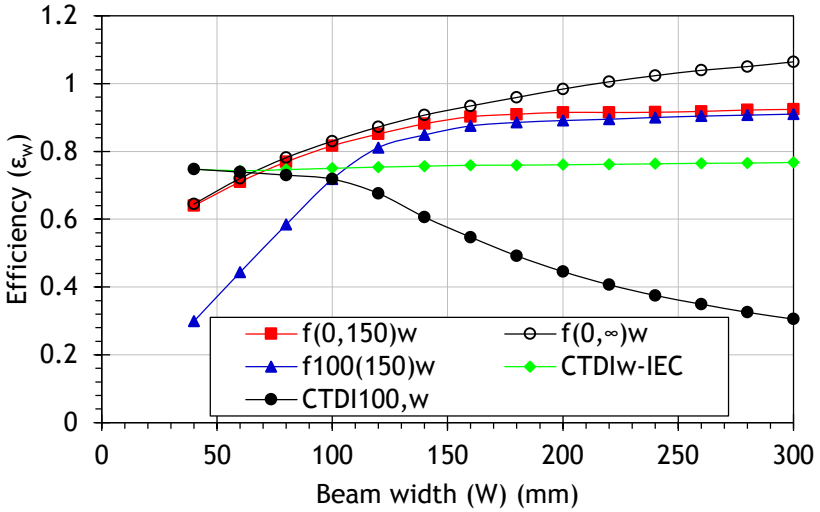

Figure 10.1: A comparison between the weighted efficiency values (ε_w) for four different dose indices for CBCT dosimetry and $CTDI_{100}$ for (a) head and (b) body phantoms. For clarity, $f_{100}(\infty)_w$ values were not added to the figure, but they are presented in Figures 6.3 - 6.6 (c) of Chapter 6.

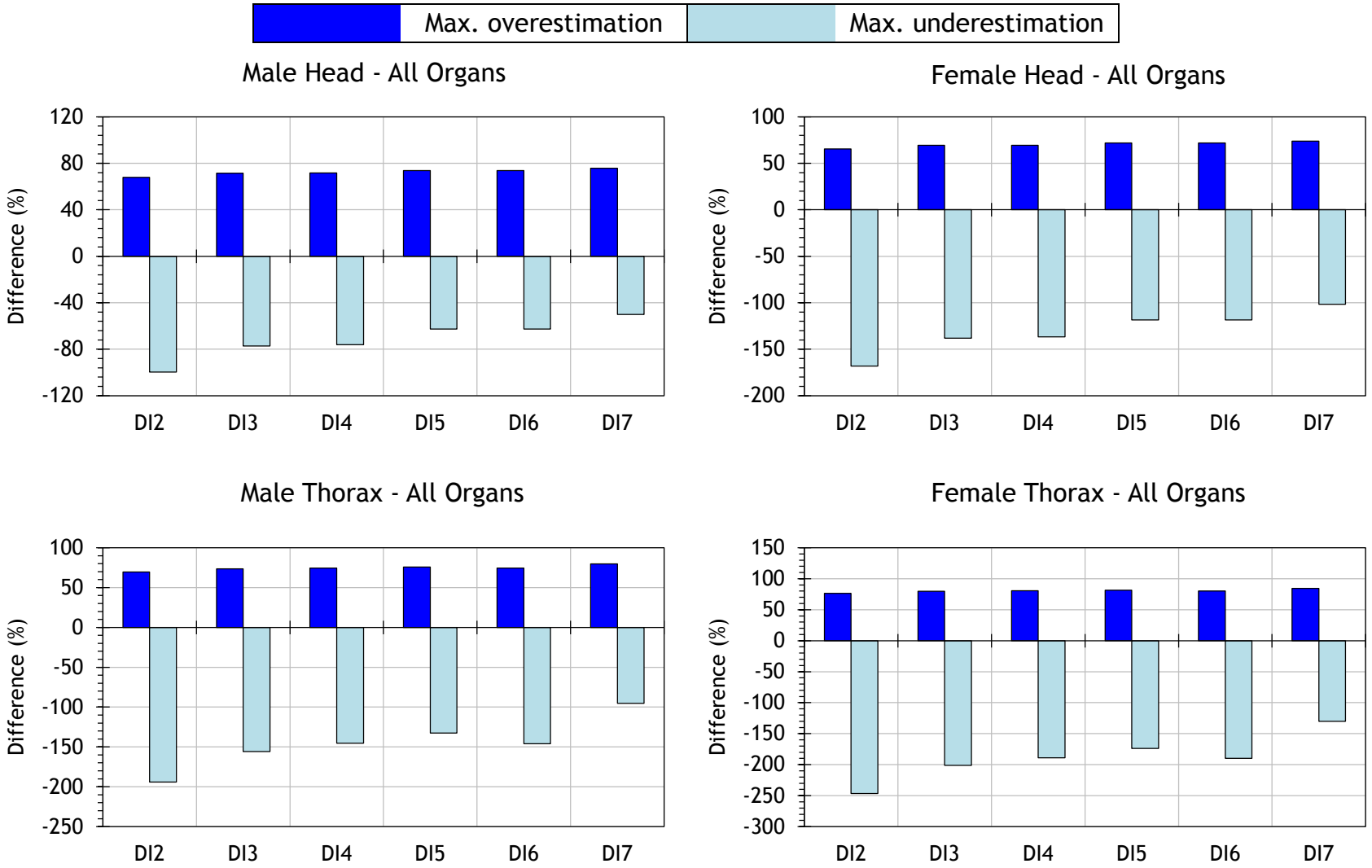
Max. overestimation
Max. underestimation
Male Head - All Organs
Female Head - All Organs
Male Thorax - All Organs
Female Thorax - All Organs
Difference (%)
DI2
DI3
DI4
DI5
DI6
DI7

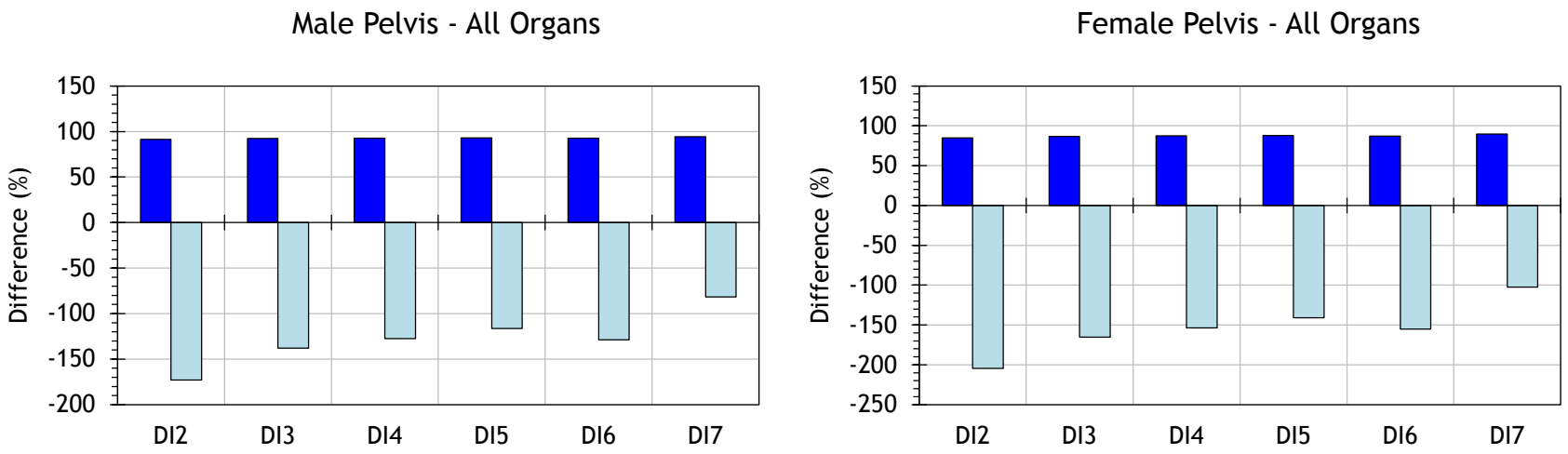

Figure 10.2: The maximum underestimation and overestimation for each DI in evaluating organ doses resulting from head, thorax, and pelvic scans on the ICRP-110 male and female reference computational phantoms. (DI2:$CTDI_{w,IEC}$, DI3:$f_{100}(150)_w$, DI4:$f(0,150)_w$, DI5:$f(0,\infty)_{w,PMMA}$, DI6: $f(0,\infty)_{w,PE}$, and DI7: $f(0,\infty)_{w,Water}$).

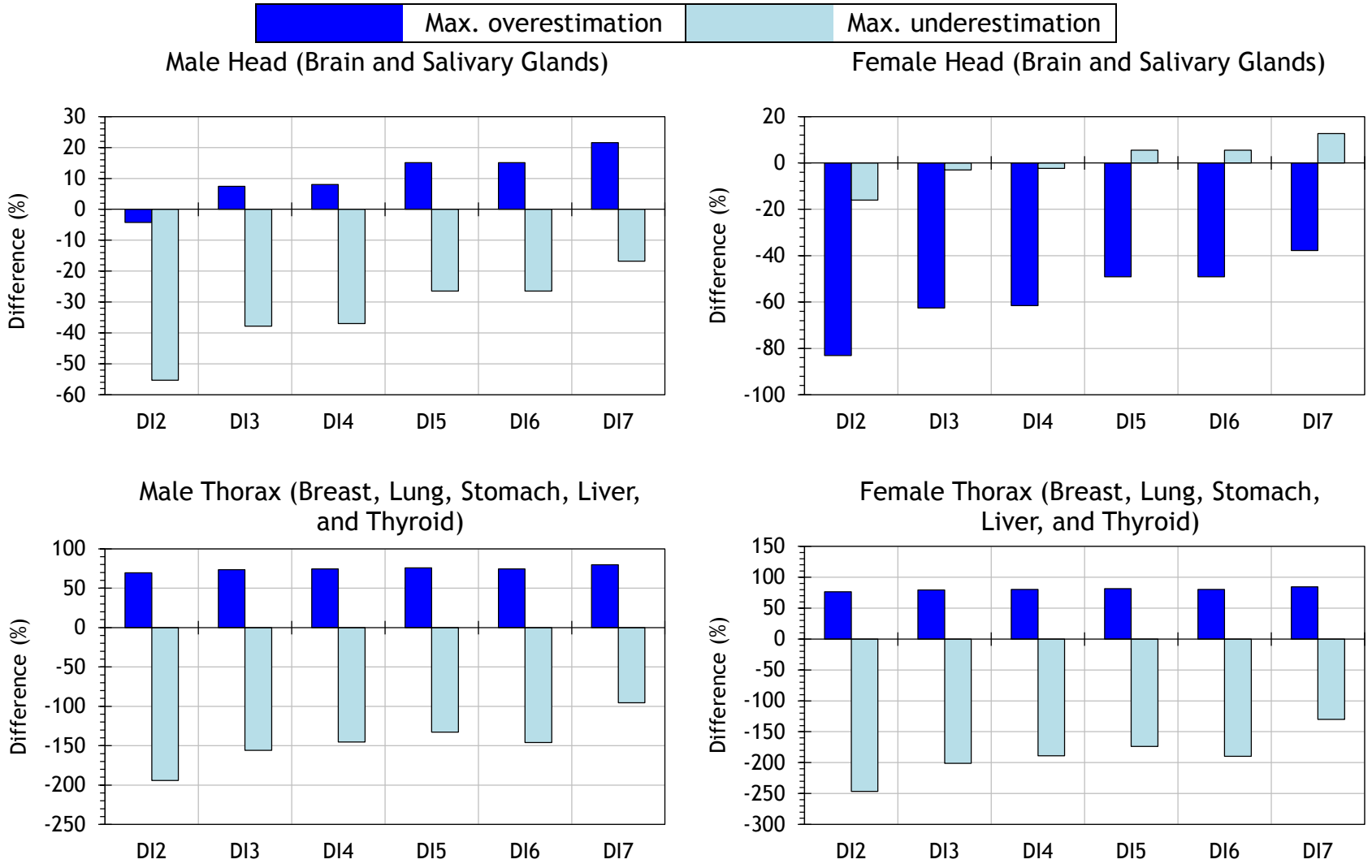
Max. overestimation
Max. underestimation
Male Head (Brain and Salivary Glands)
Female Head (Brain and Salivary Glands)
Male Thorax (Breast, Lung, Stomach, Liver, and Thyroid)
Female Thorax (Breast, Lung, Stomach, Liver, and Thyroid)
Difference (%)
DI2
DI3
DI4
DI5
DI6
DI7

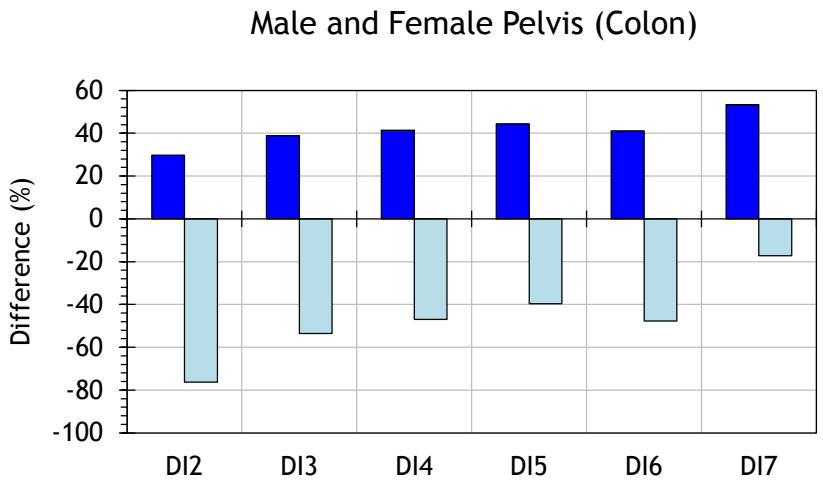

Figure 10.3: The maximum underestimation and overestimation for each DI in evaluating doses for some of radiosensitive organs resulting from head (Brain and Salivary Glands), thorax (Breast, Lung, Stomach, Liver, and Thyroid), and pelvic (Colon) scans on the ICRP-110 male and female reference computational phantoms. (DI2:$CTDI_{w,IEC}$, DI3:$f_{100}(150)_w$, DI4:$f(0,150)_w$, DI5:$f(0,\infty)_{w,PMMA}$, DI6: $f(0,\infty)_{w,PE}$, and DI7: $f(0,\infty)_{w,Water}$).

10.1.2 The Use of CBCT in Radiotherapy

As mentioned previously in the introduction and Chapter 2 section 2.7.6, there is a hope to acquire a CBCT scan on a daily basis and include the imaging dose within the treatment dose. This is because the cumulative dose resulting from daily scans is non-negligible. For example, if a CBCT scan is acquired on a daily basis using the scanning protocols used in Chapter 9 for a patient undergoing a treatment of 40 fractions, i.e. the maximum number of fractions, by the end of the treatment course, the cumulative organ doses resulting from the head scan will be in the range of 0.04 - 0.23 Gy, and in the range of 0.05 - 0.45 Gy and 0.05 – 1.66 Gy for thorax and pelvic scans, respectively. These ranges are in the same order of those reported by (Spezi et al., 2012, Nelson and Ding, 2014) as discussed in Chapter 2 section 2.7.6. At the present time, the current protocols in our centre requires a daily CBCT scan for SABR patients, while a weekly CBCT scan is taken for patients undergoing other treatment modalities such as IMRT and VMAT. Typically, most of SABR patients are treated with a few fractions 5 – 6, whereas 5 – 6 weeks are required for IMRT and VMAT patients. Thus, 5 CBCT scans can be considered as the average number of the scans acquired during the treatment course. As a result, the range of the cumulative organ doses for 5 scans will be 0.01 – 0.03 Gy, 0.01 – 0.06 Gy, and 0.01 – 0.21 Gy for the head, thorax, and pelvic scans, respectively.

Requirements for adjustment of these ranges will depend on the perceived need in the future to record more accurate data on patient doses for imaging procedures linked to treatment. They become important when decisions are made about optimization of clinical protocols for treatment. This involves balancing different objectives including:

- Increasing the frequency of CBCT scans to achieve optimal dose delivery to the target for each treatment fraction.
- Ensuring that the numbers of scans performed do not contribute more dose to surrounding tissues than is justified by the improvement in treatment.

- Choosing the optimal level of image quality to provide the information needed for organ delineation, while keeping the CBCT scan doses to a minimum.

Dose information may also be required if in the future doses from imaging are taken into account in determination of the treatment dose.

10.1.3 Facilitating the Use of Long Phantoms

The use of long phantoms such as the ICRU/AAPM phantom to measure $f(0,\infty)$ is impractical in the clinical environment. The $G_x(W)_{100}$ function proposed in Chapter 7 and the correction factors provided in Chapter 8 are considered to be practical ways to facilitate use of the long phantom dosimetry quantities. The $G_x(W)_{100}$ functions are utilized with $CTDI_{100}$ dosimetry equipment, and the correction factors can be employed with the standard PMMA phantoms and a small chamber. The $G_x(W)_{100}$ function was shown to have minimal variations with the tube voltage for all phantom compositions. The correction factors only showed a weak dependence on the tube voltage when the dose index was measured within short and long phantoms of a similar composition. The difference in the phantom compositions, however, was found to play a significant role in the influence of tube potential on the correction factors. Therefore, the use of the $G_x(W)_{100}$ function appears to be a better option for performing measurements in long phantoms compared to the use of correction factors.

10.1.4 Suitability Results of this Project to Other kV Systems

The results in this project and those from various studies published in the literature, which were conducted with different kV systems, have been shown to be in good agreement, based on results presented in Chapters 5 – 8. This agreement gives an indication that the efficiency values, the $G_x(W)_{100}$ function and the correction factor given in the chapters, may be relatively independent of the kV system, i.e. scanner, as only small variations were observed between the different systems. In addition, it is anticipated that deviations of the dose indices studied from organ doses

resulting from the different scans will be of the same order for other kV systems (Turner et al., 2010, Zhang et al., 2013a).

10.2 Future Work

Further to the different investigations presented in this study, various aspects may be studied in the future. One of these studies might be related to the displayed value $CTDI_w$, which is given on console of the Varian OBI system. This value is based on the measurement obtained with a reference narrow beam width of 20 mm and the standard PMMA head and body phantoms. This value was measured for each scanning protocol used for the CBCT scans, and is given prior to each scan. The main aim of this value is to compare between different scanners and scanning protocols under a reference condition. This value can be utilized by linking the displayed value to organ doses resulting from the different CBCT scans. This could provide the practitioners with an estimate of the organ doses received by patients undergoing the scans.

Although comparisons between results obtained from this project and other studies showed a minimal influence for the kV system, the majority of the studies used for the comparisons were conducted with CT scanners. Therefore, one area suggested for more work might be the study of another CBCT scanner used in IGRT procedures such the Elekta XVI system as this project was based on simulating the Varian OBI system. Thus, sensitivity of the efficiency values for the dose indices studied, the $G_x(W)_{100}$ function, and the ability of the dose indices in evaluating organ doses for other kV systems might be investigated. This will assist the scientific community in obtaining generic $G_x(W)_{100}$ functions and correction factors suitable for most of the kV systems covering CT and CBCT scanners employed with wide beams.

Another future work might be developing conversion factors from one of the dose indices studied in the project to organ doses resulting from CBCT scans under different conditions. This requires covering a wide range of patient sizes. The conversion factors resulting from these different sizes, then, could be tabulated so that patient-specific organ doses resulting from

a given scan are estimated with a reasonable level of accuracy. These conversion factors would allow clinicians to be more aware of dose levels absorbed by the patients during a scan acquired using certain parameters, which would be helpful in establishing a better link between the benefits of imaging and the potential risks. However, the main challenge is that when the isocentre of the CBCT scan is set at the centre of a tumour at a distance of (x, y) from the original isocentre (0, 0). In this case, the ioscentre is different for each patient as it is patient-dependent. The influence of shifting the isocentre on the patient doses has been investigated in several studies such as (Chow, 2009, Nelson and Ding, 2014) as discussed in Chapter 2 section 2.7.7.

List of References

AAPM 2007a. The management of imaging dose during image-guided radiotherapy. Report of the American Association of Physicists in Medicine (AAPM) Task Group No. 75. *Med Phys,* 34**,** 4041-4063.

AAPM 2007b. Issues associated with clinical implementation of Monte Carlo-based photon and electron external beam treatment planning. Report of the American Association of Physicists in Medicine (AAPM) Task Group No. 105. *Med Phys,* 34**,** 4818-53.

AAPM. 2010. *Comprehensive methodology for the evaluation of radiation dose in x-ray computed tomography. Report of the American Association of Physicists in Medicine (AAPM) Task Group No. 111* [Online]. Available: https://www.aapm.org/pubs/reports/RPT_111.pdf [Accessed 23/09/ 2015].

AAPM. 2011. *Size-Specific Dose Estimates (SSDE) in Pediatric and Adult Body CT Examinations. Report of the American Association of Physicists in Medicine (AAPM) Task Group No. 204* [Online]. Available: https://www.aapm.org/pubs/reports/RPT_204.pdf [Accessed 23/09/ 2015].

AAPM. 2015a. *Dosimetry Phantoms and the implementation of AAPM Report Number 111. The American Association of Physicists in Medicine (AAPM) Task Group No. 200* [Online]. Available: http://aapm.org/org/structure/default.asp?committee_code=TG200 [Accessed 23/09/ 2015].

AAPM. 2015b. *Modeling and Accounting for the Imaging Guidance Radiation Doses to Radiotherapy Patients in Treatment Planning. The American Association of Physicists in Medicine (AAPM) Task Group No. 180* [Online]. Available: http://aapm.org/org/structure/default.asp?committee_code=TG180 [Accessed 23/09/ 2015].

ABUHAIMED, A., MARTIN, C. J., SANKARALINGAM, M. & GENTLE, D. J. 2015. A Monte Carlo investigation of cumulative dose measurements for cone beam computed tomography (CBCT) dosimetry. *Phys Med Biol,* 60**,** 1519-1542.

ABUHAIMED, A., MARTIN, C. J., SANKARALINGAM, M. & GENTLE, D. J. 2015b. Investigation of practical approaches to evaluating cumulative dose for cone beam computed tomography (CBCT) from standard CT dosimetry measurements: a Monte Carlo study. *Phys Med Biol,* 60**,** 5413-5438.

ABUHAIMED, A., MARTIN, C. J., SANKARALINGAM, M. & GENTLE, D. J. 2015c. Evaluation of cumulative dose for cone beam computed tomography (CBCT) scans within phantoms made from different compositions using Monte Carlo simulation. *J Appl Clin Med Phys,* (In Press).

ABUHAIMED, A., MARTIN, C. J., SANKARALINGAM, M., GENTLE, D. J. & MCJURY, M. 2014. An assessment of the efficiency of methods for measurement of the computed tomography dose index (CTDI) for cone beam (CBCT) dosimetry by Monte Carlo simulation. *Phys Med Biol,* 59**,** 6307-26.

AGOSTINELLI, S., ALLISON, J., AMAKO, K. A., APOSTOLAKIS, J., ARAUJO, H., ARCE, P., ASAI, M., AXEN, D., BANERJEE, S. & BARRAND, G. 2003. GEANT4—a simulation toolkit. *Nuclear instruments and methods in physics research section A: Accelerators, Spectrometers, Detectors and Associated Equipment,* 506**,** 250-303.

ALAEI, P., DING, G. & GUAN, H. 2010. Inclusion of the dose from kilovoltage cone beam CT in the radiation therapy treatment plans. *Med Phys,* 37**,** 244-8.

ALAEI, P. & SPEZI, E. 2012. Commissioning kilovoltage cone-beam CT beams in a radiation therapy treatment planning system. *J Appl Clin Med Phys,* 13**,** 19-33.

ALAEI, P., SPEZI, E. & REYNOLDS, M. 2014. Dose calculation and treatment plan optimization including imaging dose from kilovoltage cone beam computed tomography. *Acta Oncol,* 53**,** 839-44.

ALI, E. S. & ROGERS, D. W. 2007. Efficiency improvements of x-ray simulations in EGSnrc user-codes using bremsstrahlung cross-section enhancement (BCSE). *Med Phys,* 34**,** 2143-54.

ALI, E. S. M. & ROGERS, D. W. O. 2008. Benchmarking EGSnrc in the kilovoltage energy range against experimental measurements of charged particle backscatter coefficients. *Phys Med Biol,* 53**,** 1527-43.

AMER, A., MARCHANT, T., SYKES, J., CZAJKA, J. & MOORE, C. 2007. Imaging doses from the Elekta Synergy X-ray cone beam CT system. *Br J Radiol,* 80**,** 476-482.

ARCHAMBAULT, J. P. & MAINEGRA-HING, E. 2015. Comparison between EGSnrc, Geant4, MCNP5 and Penelope for mono-energetic electron beams. *Phys Med Biol,* 60**,** 4951-62.

AUKETT, R. J., BURNS, J. E., GREENER, A. G., HARRISON, R. M., MORETTI, C., NAHUM, A. E. & ROSSER, K. E. 2005. Addendum to the IPEMB code of practice for the determination of absorbed dose for x-rays below 300 kV generating potential (0.035 mm Al-4 mm Cu HVL). *Phys Med Biol,* 50**,** 2739-48.

BABCOCK, K., CRANMER–SARGISON, G. & SIDHU, N. 2008. Increasing the speed of DOSXYZnrc Monte Carlo simulations through the introduction of nonvoxelated geometries. *Med Phys,* 35**,** 633-644.

BAZALOVA, M., ZHOU, H., KEALL, P. J. & GRAVES, E. E. 2009. Kilovoltage beam Monte Carlo dose calculations in submillimeter voxels for small animal radiotherapy. *Med Phys,* 36**,** 4991-4999.

BERGER, M. J., HUBBELL, J. H., SELTZER, S. M., CHANG, J., COURSEY, J. S., SUKUMAR, R., ZUCKER, D. S. & OLSEN, K. 2010. *XCOM: Photon Cross Section Database (version 1.5)* [Online]. National Institute of Standards and Technology, Gaithersburg, MD. Available: http://www.nist.gov/pml/data/xcom/index.cfm [Accessed 23/09/ 2015].

BOONE, J. M. 2007. The trouble with CTD100. *Med Phys,* 34**,** 1364-71.

BOONE, J. M. 2009. Dose spread functions in computed tomography: a Monte Carlo study. *Med Phys,* 36**,** 4547-54.

BRENNER, D. J. 2005. Is it time to retire the CTDI for CT quality assurance and dose optimization? *Med Phys,* 32**,** 3225-3226.

BRENNER, D. J. & HALL, E. J. 2007. Computed Tomography — An Increasing Source of Radiation Exposure. *N Engl J Med,* 357**,** 2277-2284.

BROCHU, F. M., BURNET, N. G., JENA, R., PLAISTOW, R., PARKER, M. A. & THOMAS, S. J. 2014. Geant4 simulation of the Elekta XVI kV CBCT unit for accurate description of potential late toxicity effects of image-guided radiotherapy. *Phys Med Biol,* 59**,** 7601-7608.

BUJOLD, A., CRAIG, T., JAFFRAY, D. & DAWSON, L. A. Image-guided radiotherapy: Has it influenced patient outcomes? Semin Radiat Oncol, 2012. Elsevier, 50-61.

CHENG, H. C., WU, V. W., LIU, E. S. & KWONG, D. L. 2011. Evaluation of Radiation Dose and Image Quality for the Varian Cone Beam Computed Tomography System. *Int J Radiat Oncol Biol Phys,* 80**,** 291-300.

CHOW, J. C. 2009. Cone-beam CT dosimetry for the positional variation in isocenter: A Monte Carlo study. *Med Phys,* 36**,** 3512-3520.

COMARE. 2014. *Committee on Medical Aspects of Radiation in the Environment: Patient radiation dose issues resulting from the use of CT in the UK, Report: 16* [Online]. Public Health England. Available: https://www.gov.uk/government/uploads/system/uploads/attachment_data/file/343836/COMARE_16th_Report.pdf [Accessed 23/09/ 2015].

DENG, J., CHEN, Z., ROBERTS, K. B. & NATH, R. 2012. Kilovoltage Imaging Doses in the Radiotherapy of Pediatric Cancer Patients. *Int J Radiat Oncol Biol Phys,* 82**,** 1680-1688.

DING, A., GU, J., TROFIMOV, A. V. & XU, X. 2010a. Monte Carlo calculation of imaging doses from diagnostic multidetector CT and kilovoltage cone-beam CT as part of prostate cancer treatment plans. *Med Phys,* 37**,** 6199-6204.

DING, G. X. & COFFEY, C. W. 2009. Radiation Dose From Kilovoltage Cone Beam Computed Tomography in an Image-Guided Radiotherapy Procedure. *International Journal of Radiation Oncology*Biology*Physics,* 73**,** 610-617.

DING, G. X. & COFFEY, C. W. 2010. Beam characteristics and radiation output of a kilovoltage cone-beam CT. *Phys Med Biol,* 55**,** 5231-48.

DING, G. X., DUGGAN, D. M. & COFFEY, C. W. 2007. Characteristics of kilovoltage x-ray beams used for cone-beam computed tomography in radiation therapy. *Phys Med Biol,* 52**,** 1595-615.

DING, G. X., DUGGAN, D. M. & COFFEY, C. W. 2008a. Accurate patient dosimetry of kilovoltage cone-beam CT in radiation therapy. *Med Phys,* 35**,** 1135-44.

DING, G. X., DUGGAN, D. M., COFFEY, C. W., DEELEY, M., HALLAHAN, D. E., CMELAK, A. & MALCOLM, A. 2007a. A study on adaptive IMRT treatment planning using kV cone-beam CT. *Radiother Oncol,* 85**,** 116-125.

DING, G. X. & MALCOLM, A. W. 2013. An optically stimulated luminescence dosimeter for measuring patient exposure from imaging guidance procedures. *Phys Med Biol,* 58**,** 5885-97.

DING, G. X. & MUNRO, P. 2013. Radiation exposure to patients from image guidance procedures and techniques to reduce the imaging dose. *Radiother Oncol,* 108**,** 91-98.

DING, G. X., MUNRO, P., PAWLOWSKI, J., MALCOLM, A. & COFFEY, C. W. 2010b. Reducing radiation exposure to patients from kV-CBCT imaging. *Radiother Oncol,* 97**,** 585-592.

DING, G. X., PAWLOWSKI, J. M. & COFFEY, C. W. 2008b. A correction-based dose calculation algorithm for kilovoltage x rays. *Med Phys,* 35**,** 5312-5316.

DIXON, R. L. 2003. A new look at CT dose measurement: beyond CTDI. *Med Phys,* 30**,** 1272-80.

DIXON, R. L. & BALLARD, A. C. 2007. Experimental validation of a versatile system of CT dosimetry using a conventional ion chamber: Beyond CTDI[sub 100]. *Med Phys,* 34**,** 3399-3413.

DIXON, R. L. & BOONE, J. M. 2010. Cone beam CT dosimetry: A unified and self-consistent approach including all scan modalities---With or without phantom motion. *Med Phys,* 37**,** 2703-2718.

DIXON, R. L. & BOONE, J. M. 2011. Analytical equations for CT dose profiles derived using a scatter kernel of Monte Carlo parentage with broad applicability to CT dosimetry problems. *Med Phys,* 38**,** 4251-4264.

DIXON, R. L. & BOONE, J. M. 2014. Stationary table CT dosimetry and anomalous scanner-reported values of CTDIvol. *Med Phys,* 41**,** 011907-6.

DOWNES, P., JARVIS, R., RADU, E., KAWRAKOW, I. & SPEZI, E. 2009. Monte Carlo simulation and patient dosimetry for a kilovoltage cone-beam CT unit. *Med Phys,* 36**,** 4156-4167.

DUFEK, V., HORAKOVA, I. & NOVAK, L. 2011. Organ and Effective Doses from Verification Techniques in Image-Guided Radiotherapy. *Radiat Prot Dosimetry,* 147**,** 277-280.

DUNN, W. L. & SHULTIS, J. K. 2011. *Exploring Monte Carlo Methods,* Elsevier.

DZIERMA, Y., NUESKEN, F., OTTO, W., ALAEI, P., LICHT, N. & RUBE, C. 2014. Dosimetry of an in-line kilovoltage imaging system and implementation in treatment planning. *Int J Radiat Oncol Biol Phys,* 88**,** 913-9.

FADDEGON, B. A., KAWRAKOW, I., KUBYSHIN, Y., PERL, J., SEMPAU, J. & URBAN, L. 2009. The accuracy of EGSnrc, Geant4 and PENELOPE Monte Carlo systems for the simulation of electron scatter in external beam radiotherapy. *Phys Med Biol,* 54**,** 6151-63.

FAHRIG, R., DIXON, R., PAYNE, T., MORIN, R. L., GANGULY, A. & STROBEL, N. 2006. Dose and image quality for a cone-beam C-arm CT system. *Med Phys,* 33**,** 4541-4550.

FAZEL, R., KRUMHOLZ, H. M., WANG, Y., ROSS, J. S., CHEN, J., TING, H. H., SHAH, N. D., NASIR, K., EINSTEIN, A. J. & NALLAMOTHU, B. K. 2009. Exposure to low-dose ionizing radiation from medical imaging procedures. *N Engl J Med,* 361**,** 849-57.

FLETCHER, C. L. & MILLS, J. A. 2008. An assessment of GafChromic film for measuring 50 kV and 100 kV percentage depth dose curves. *Phys Med Biol,* 53, N209-18.

FORD, R. L. & NELSON, W. R. 1978 The EGS code system-version 3 Report SLAC-210 (Stanford, CA: Stanford Linear Accelerator Center).

GELEIJNS, J., SALVADO ARTELLS, M., DE BRUIN, P. W., MATTER, R., MURAMATSU, Y. & MCNITT-GRAY, M. F. 2009. Computed tomography dose assessment for a 160 mm wide, 320 detector row, cone beam CT scanner. *Phys Med Biol,* 54, 3141-59.

GIADDUI, T., CUI, Y., GALVIN, J., CHEN, W., YU, Y. & XIAO, Y. 2012. Characteristics of Gafchromic XRQA2 films for kV image dose measurement. *Med Phys,* 39, 842-850.

GIADDUI, T., CUI, Y., GALVIN, J., YU, Y. & XIAO, Y. 2013. Comparative dose evaluations between XVI and OBI cone beam CT systems using Gafchromic XRQA2 film and nanoDot optical stimulated luminescence dosimeters. *Medical Physics,* 40, 062102-12.

GU, J., BEDNARZ, B., XU, X. & JIANG, S. B. 2008. Assessment of patient organ doses and effective doses using the VIP-Man adult male phantom for selected cone-beam CT imaging procedures during image guided radiation therapy. *Radiat Prot Dosimetry,* 131, 431-443.

HALL, E. J. & BRENNER, D. J. 2008. Cancer risks from diagnostic radiology. *Br J Radiol,* 81, 362-78.

HIRAYAMA, H., NAMITO, Y., BIELAJEW, A. F., WILDERMAN, S. J. & NELSON, W. R. 2005. The EGS5 code system. SLAC Report number: SLAC-R-730, KEK Report number: 2005-8.

HUBBELL, J. H. & SELTZER, S. M. 2004. *Tables of X-Ray Mass Attenuation Coefficients and Mass Energy-Absorption Coefficients from 1 keV to 20 MeV for Elements Z = 1 to 92 and 48 Additional Substances of Dosimetric Interest* [Online]. Radiation and Biomolecular Physics Division, PML, NIST. Available: http://www.nist.gov/pml/data/xraycoef/ [Accessed 23/09/ 2015].

HYER, D. E. & HINTENLANG, D. E. 2010. Estimation of organ doses from kilovoltage cone-beam CT imaging used during radiotherapy patient position verification. *Med Phys,* 37**,** 4620-4626.

HYER, D. E., SERAGO, C. F., KIM, S., LI, J. G. & HINTENLANG, D. E. 2010. An organ and effective dose study of XVI and OBI cone-beam CT systems. *J Appl Clin Med Phys,* 11**,** 181-197.

IAEA 2011. Status of Computed Tomography Dosimetry for Wide Cone Beam Scanners. The International Atomic Energy Agency (IAEA) Human Health Reports 5. [Online]. Available: http://www-pub.iaea.org/MTCD/Publications/PDF/Pub1528_web.pdf. [Accessed 23/09/ 2015].

ICRP 2009. Adult Reference Computational Phantoms. The International Commission on Radiological Protection (ICRP) Publication 110. *Ann. ICRP 39 (2).*

ICRU 2012. The International Commission on Radiation Units and Measurements (ICRU) Report No. 87: radiation dose and image-quality assessment in computed tomography. *J ICRU,* 12**,** 1-149.

IEC 2001. Particular requirements for the safety of x-ray equipment for computed tomography. The International Electrotechnical Commission (IEC), Medical Electrical Equipment.

IEC 2010. Amendment 1 to IEC 60601–2–44: 2009 Medical electrical equipment :part 2–44. Particular requirements for the basic safety and essentiell performance of x-ray equipment for computed tomography Committee Draft (CD) 62B/804/CD. The International Electrotechnical Commission (IEC).

IRMER. 2000. *THE IONISING RADIATION (MEDICAL EXPOSURE) REGULATIONS (IRMER) 2000. Department of Health* [Online]. Available: https://www.gov.uk/government/uploads/system/uploads/attachment_data/file/227075/IRMER_regulations_2000.pdf [Accessed 23/09/ 2015].

ISLAM, M. K., PURDIE, T. G., NORRLINGER, B. D., ALASTI, H., MOSELEY, D. J., SHARPE, M. B., SIEWERDSEN, J. H. & JAFFRAY, D. A. 2006. Patient dose

from kilovoltage cone beam computed tomography imaging in radiation therapy. *Med Phys,* 33**,** 1573-1582.

JAFFRAY, D. A. & SIEWERDSEN, J. H. 2000. Cone-beam computed tomography with a flat-panel imager: initial performance characterization. *Med Phys,* 27**,** 1311-23.

JAFFRAY, D. A., SIEWERDSEN, J. H., WONG, J. W. & MARTINEZ, A. A. 2002. Flat-panel cone-beam computed tomography for image-guided radiation therapy. *Int J Radiat Oncol Biol Phys,* 53**,** 1337-1349.

JAN, S., BENOIT, D., BECHEVA, E., CARLIER, T., CASSOL, F., DESCOURT, P., FRISSON, T., GREVILLOT, L., GUIGUES, L. & MAIGNE, L. 2011. GATE V6: a major enhancement of the GATE simulation platform enabling modelling of CT and radiotherapy. *Phys Med Biol,* 56**,** 881-901.

JAN, S., SANTIN, G., STRUL, D., STAELENS, S., ASSIE, K., AUTRET, D., AVNER, S., BARBIER, R., BARDIES, M. & BLOOMFIELD, P. 2004. GATE: a simulation toolkit for PET and SPECT. *Phys Med Biol,* 49**,** 4543-61.

KALENDER, W. A. 2014. Dose in x-ray computed tomography. *Phys Med Biol,* 59**,** R129-50.

KAN, M. W., LEUNG, L. H., WONG, W. & LAM, N. 2008. Radiation dose from cone beam computed tomography for image-guided radiation therapy. *Int J Radiat Oncol Biol Phys,* 70**,** 272-279.

KAWRAKOW, I. 2000a. Accurate condensed history Monte Carlo simulation of electron transport. I. EGSnrc, the new EGS4 version. *Med Phys,* 27**,** 485-498.

KAWRAKOW, I. 2000b. Accurate condensed history Monte Carlo simulation of electron transport. II. Application to ion chamber response simulations. *Med Phys,* 27**,** 499-513.

KAWRAKOW, I. 2006. *The Monte Carlo Simulation of Radiation Transport* [Online]. Available: https://www.aapm.org/meetings/06SS/documents/kawrakow_MonteCarlo_color.pdf [Accessed 23/09/ 2015].

KAWRAKOW, I. 2013. The dose visualization tool dosxyz show. Ionizing Radiation Standards National Research Council of Canada, Ottawa. NRCC Report PIRS-0624.

KAWRAKOW, I., MAINEGRA-HING, E. & ROGERS, D. W. O. 2006. EGSnrcMP: the multi-platform environment for EGSnrc. Ionizing Radiation Standards National Research Council of Canada, Ottawa. NRCC Report PIRS-877.

KAWRAKOW, I., MAINEGRA-HING, E., ROGERS, D. W. O., TESSIER, F. & WALTERS, B. R. B. 2013. The EGSnrc Code System: Monte Carlo Simulation of Electron and Photon Transport. Ionizing Radiation Standards National Research Council of Canada, Ottawa. NRCC Report PIRS-701.

KAWRAKOW, I., ROGERS, D. W. O. & WALTERS, B. R. B. 2004. Large efficiency improvements in BEAMnrc using directional bremsstrahlung splitting. *Med Phys,* 31**,** 2883-2898.

KAWRAKOW, I. & WALTERS, B. 2006. Efficient photon beam dose calculations using DOSXYZnrc with BEAMnrc. *Med Phys,* 33**,** 3046-3056.

KIM, S., SONG, H., MOVSAS, B. & CHETTY, I. J. 2012. Characteristics of x-ray beams in two commercial multidetector computed tomography simulators: Monte Carlo simulations. *Med Phys,* 39**,** 320-329.

KIM, S., SONG, H., SAMEI, E., YIN, F. F. & YOSHIZUMI, T. T. 2011. Computed tomography dose index and dose length product for cone-beam CT: Monte Carlo simulations. *J Appl Clin Med Phys,* 12**,** 84-95.

KIM, S., YOSHIZUMI, T., TONCHEVA, G., YOO, S., YIN, F. F. & FRUSH, D. 2010a. Estimation of computed tomography dose index in cone beam computed tomography: MOSFET measurements and Monte Carlo simulations. *Health Phys,* 98**,** 683-91.

KIM, S., YOSHIZUMI, T. T., FRUSH, D. P., TONCHEVA, G. & YIN, F.-F. 2010b. Radiation Dose From Cone Beam CT in a Pediatric Phantom: Risk Estimation of Cancer Incidence. *American Journal of Roentgenology,* 194**,** 186-190.

KIM, S., YOSHIZUMI, T. T., TONCHEVA, G., YOO, S. & YIN, F. F. 2008. Comparison of radiation doses between cone beam CT and multi detector CT: TLD measurements. *Radiat Prot Dosimetry,* 132**,** 339-345.

KLEVENHAGEN, P. B. A. W. P. O. T. I. W. T. F. M. S. C., AUKETT, R. J., HARRISON, R. M., MORETTI, C., NAHUM, A. E. & ROSSER, K. E. 1996. The IPEMB code of practice for the determination of absorbed dose for x-rays below 300 kV generating potential (0.035 mm Al - 4 mm Cu HVL; 10 - 300 kV generating potential). *Phys Med Biol,* 41**,** 2605-25.

KOIVUNORO, H., SIISKONEN, T., KOTILUOTO, P., AUTERINEN, I., HIPPELAINEN, E. & SAVOLAINEN, S. 2012. Accuracy of the electron transport in mcnp5 and its suitability for ionization chamber response simulations: A comparison with the egsnrc and penelope codes. *Med Phys,* 39**,** 1335-44.

KYRIAKOU, Y., DEAK, P., LANGNER, O. & KALENDER, W. A. 2008. Concepts for dose determination in flat-detector CT. *Phys Med Biol,* 53**,** 3551-66.

LÉTOURNEAU, D., WONG, J. W., OLDHAM, M., GULAM, M., WATT, L., JAFFRAY, D. A., SIEWERDSEN, J. H. & MARTINEZ, A. A. 2005. Cone-beam-CT guided radiation therapy: technical implementation. *Radiother Oncol,* 75**,** 279-286.

LI, X., ZHANG, D. & LIU, B. 2011. A practical approach to estimate the weighted CT dose index over an infinite integration length. *Phys Med Biol,* 56**,** 5789-803.

LI, X., ZHANG, D. & LIU, B. 2012. Estimation of the weighted CTDI∞ for multislice CT examinations. *Med Phys,* 39**,** 901-905.

LI, X., ZHANG, D. & LIU, B. 2013a. Calculations of two new dose metrics proposed by AAPM Task Group 111 using the measurements with standard CT dosimetry phantoms. *Med Phys,* 40**,** 081914-8.

LI, X., ZHANG, D. & LIU, B. 2013b. Monte Carlo assessment of CT dose equilibration in PMMA and water cylinders with diameters from 6 to 55 cm. *Med Phys,* 40**,** 031903-10.

LI, X., ZHANG, D. & LIU, B. 2014a. Longitudinal dose distribution and energy absorption in PMMA and water cylinders undergoing CT scans. *Med Phys,* 41, 101912-11.

LI, X., ZHANG, D., YANG, J. & LIU, B. 2014b. A study of the short- to long-phantom dose ratios for CT scanning without table translation. *Med Phys,* 41, 091912-10.

MA, C.-M. & ROGERS, D. W. O. 2013. BEAMDP Users Manual. . Ionizing Radiation Standards National Research Council of Canada, Ottawa. NRCC Report PIRS-0509(C)revA.

MAIGNE, L., PERROT, Y., SCHAART, D. R., DONNARIEIX, D. & BRETON, V. 2011. Comparison of GATE/GEANT4 with EGSnrc and MCNP for electron dose calculations at energies between 15 keV and 20 MeV. *Phys Med Biol,* 56, 811-27.

MAINEGRA-HING, E. & KAWRAKOW, I. 2006. Efficient x-ray tube simulations. *Med Phys,* 33, 2683-2690.

MARTIN, C. J. 2007. Effective dose: how should it be applied to medical exposures? *Br J Radiol,* 80, 639-647.

MARTIN, C. J., GENTLE, D. J., SOOKPENG, S. & LOVELAND, J. 2011. Application of Gafchromic film in the study of dosimetry methods in CT phantoms. *J Radiol Prot,* 31, 389-409.

MCCOLLOUGH, C. H., LENG, S., YU, L., CODY, D. D., BOONE, J. M. & MCNITT-GRAY, M. F. 2011. CT dose index and patient dose: they are not the same thing. *Radiology,* 259, 311-316.

MCGOWAN, H. C. E., FADDEGON, B. A. & MA, C.-M. 2013. STATDOSE for 3D dose distributions. Ionizing Radiation Standards National Research Council of Canada, Ottawa. NRCC Report PIRS-0509(F).

MCMILLAN, K., MCNITT-GRAY, M. & RUAN, D. 2013. Development and validation of a measurement-based source model for kilovoltage cone-beam CT Monte Carlo dosimetry simulations. *Medical Physics,* 40, 111907-9.

MCNITT-GRAY, M. F. 2002. AAPM/RSNA Physics Tutorial for Residents: Topics in CT. Radiation dose in CT. *Radiographics,* 22**,** 1541-53.

MIDGLEY, S., MILLAR, R. & DUDSON, J. 1998. A feasibility study for megavoltage cone beam CT using a commercial EPID. *Phys Med Biol,* 43**,** 155-69.

MIFTEN, M., GAYOU, O., REITZ, B., FUHRER, R., LEICHER, B. & PARDA, D. S. 2007. IMRT planning and delivery incorporating daily dose from mega-voltage cone-beam computed tomography imaging. *Med Phys,* 34**,** 3760-7.

MONTANARI, D., SCOLARI, E., SILVESTRI, C., GRAVES, Y. J., YAN, H., CERVINO, L., RICE, R., JIANG, S. B. & JIA, X. 2014. Comprehensive evaluations of cone-beam CT dose in image-guided radiation therapy via GPU-based Monte Carlo simulations. *Phys Med Biol,* 59**,** 1239-53.

MORANT, J. J., SALVADO, M., HERNANDEZ-GIRON, I., CASANOVAS, R., ORTEGA, R. & CALZADO, A. 2013. Dosimetry of a cone beam CT device for oral and maxillofacial radiology using Monte Carlo techniques and ICRP adult reference computational phantoms. *Dentomaxillofac Radiol,* 42**,** 92555893-9.

MORI, S., ENDO, M., NISHIZAWA, K., TSUNOO, T., AOYAMA, T., FUJIWARA, H. & MURASE, K. 2005. Enlarged longitudinal dose profiles in cone-beam CT and the need for modified dosimetry. *Med Phys,* 32**,** 1061-9.

NELSON, A. P. & DING, G. X. 2014. An alternative approach to account for patient organ doses from imaging guidance procedures. *Radiother Oncol,* 112**,** 112-8.

NELSON, W. R., HIRAYAMA, H. & ROGERS, D. W. O. 1985. The EGS4 code system Report SLAC-265 (Stanford, CA: Stanford Linear Accelerator Center).

NOBAH, A., ALDELAIJAN, S., DEVIC, S., TOMIC, N., SEUNTJENS, J., AL-SHABANAH, M. & MOFTAH, B. 2014. Radiochromic film based dosimetry of image-guidance procedures on different radiotherapy modalities. *J Appl Clin Med Phys,* 15**,** 229-239.

OSEI, E. K., SCHALY, B., FLECK, A., CHARLAND, P. & BARNETT, R. 2009. Dose assessment from an online kilovoltage imaging system in radiation therapy. *J Radiol Prot,* 29**,** 37-50.

PALM, A., NILSSON, E. & HERRNSDORF, L. 2010. Absorbed dose and dose rate using the Varian OBI 1.3 and 1.4 CBCT system. *J Appl Clin Med Phys,* 11**,** 229-240.

PAWLOWSKI, J. M. & DING, G. X. 2011. A new approach to account for the medium-dependent effect in model-based dose calculations for kilovoltage x-rays. *Phys Med Biol,* 56**,** 3919-34.

PAWLOWSKI, J. M. & DING, G. X. 2014. An algorithm for kilovoltage x-ray dose calculations with applications in kV-CBCT scans and 2D planar projected radiographs. *Phys Med Biol,* 59**,** 2041-58.

PEARCE, M. S., SALOTTI, J. A., LITTLE, M. P., MCHUGH, K., LEE, C., KIM, K. P., HOWE, N. L., RONCKERS, C. M., RAJARAMAN, P., CRAFT, A. W., PARKER, L. & BERRINGTON DE GONZÁLEZ, A. 2012. Radiation exposure from CT scans in childhood and subsequent risk of leukaemia and brain tumours: a retrospective cohort study. *Lancet,* 380**,** 499-505.

PELOWITZ, D. B. 2008. MCNPX User's Manual. Los Alamos National Security (LANS).

PERISINAKIS, K., DAMILAKIS, J., TZEDAKIS, A., PAPADAKIS, A., THEOCHAROPOULOS, N. & GOURTSOYIANNIS, N. 2007. Determination of the weighted CT dose index in modern multi-detector CT scanners. *Phys Med Biol,* 52**,** 6485-95.

PERKS, J. R., LEHMANN, J., CHEN, A. M., YANG, C. C., STERN, R. L. & PURDY, J. A. 2008. Comparison of peripheral dose from image-guided radiation therapy (IGRT) using kV cone beam CT to intensity-modulated radiation therapy (IMRT). *Radiother Oncol,* 89**,** 304-10.

PLATTEN, D. J., CASTELLANO, I. A., CHAPPLE, C. L., EDYVEAN, S., JANSEN, J. T., JOHNSON, B. & LEWIS, M. A. 2013. Radiation dosimetry for wide-beam CT scanners: recommendations of a working party of the Institute of Physics and Engineering in Medicine. *Br J Radiol,* 86**,** 20130089.

POIRIER, Y., KOUZNETSOV, A., KOGER, B. & TAMBASCO, M. 2014. Experimental validation of a kilovoltage x-ray source model for computing imaging dose. *Med Phys,* 41**,** 041915-11.

QIU, Y., MOISEENKO, V., AQUINO-PARSONS, C. & DUZENLI, C. 2012. Equivalent doses for gynecological patients undergoing IMRT or RapidArc with kilovoltage cone beam CT. *Radiother Oncol,* 104**,** 257-62.

ROGERS, D. 2006. Fifty years of Monte Carlo simulations for medical physics. *Phys Med Biol,* 51**,** R287-301.

ROGERS, D. W. O., FADDEGON, B. A., DING, G. X., MA, C.-M., WE, J. & MACKIE, T. R. 1995. BEAM: A Monte Carlo code to simulate radiotherapy treatment units. *Med Phys,* 22**,** 503-524.

ROGERS, D. W. O., KAWRAKOW, I., SEUNTJENS, J. P., WALTERS, B. R. B. & MAINEGRA-HING, E. 2013a. NRC User Codes for EGSnrc. Ionizing Radiation Standards National Research Council of Canada, Ottawa. NRCC Report PIRS-702(revC).

ROGERS, D. W. O., WALTERS, B. & KAWRAKOW, I. 2013b. BEAMnrc Users Manual. Ionizing Radiation Standards National Research Council of Canada, Ottawa. NRCC Report PIRS-0509(A)revL.

RUAN, C., YUKIHARA, E. G., CLOUSE, W. J., GASPARIAN, P. B. & AHMAD, S. 2010. Determination of multislice computed tomography dose index (CTDI) using optically stimulated luminescence technology. *Med Phys,* 37**,** 3560-8.

SALVAT, F., FERNÁNDEZ-VAREA, J. M. & SEMPAU, J. 2011. PENELOPE-2011: A Code System for Monte Carlo Simulation of Electron and Photon Transport. NEA/NSC/DOC20115, Workshop Proceedings, Barcelona, Spain, 4-7 July 2011.

SARRUT, D., BARDIES, M., BOUSSION, N., FREUD, N., JAN, S., LETANG, J. M., LOUDOS, G., MAIGNE, L., MARCATILI, S., MAUXION, T., PAPADIMITROULAS, P., PERROT, Y., PIETRZYK, U., ROBERT, C., SCHAART, D. R., VISVIKIS, D. & BUVAT, I. 2014. A review of the use and potential of the GATE Monte Carlo simulation code for radiation therapy and dosimetry applications. *Med Phys,* 41**,** 064301-14.

SECO, J. & VERHAEGEN, F. 2013. *Monte Carlo techniques in radiation therapy*, CRC Press.

SHAH, A., AIRD, E. & SHEKHDAR, J. 2012. Contribution to normal tissue dose from concomitant radiation for two common kV-CBCT systems and one MVCT system used in radiotherapy. *Radiother Oncol,* 105**,** 139-44.

SHOPE, T. B., GAGNE, R. M. & JOHNSON, G. C. 1981. A method for describing the doses delivered by transmission x-ray computed tomography. *Med Phys,* 8**,** 488-95.

SIEWERDSEN, J. H. & JAFFRAY, D. A. 2001. Cone-beam computed tomography with a flat-panel imager: magnitude and effects of x-ray scatter. *Med Phys,* 28**,** 220-31.

SIEWERDSEN, J. H., WAESE, A. M., MOSELEY, D. J., RICHARD, S. & JAFFRAY, D. A. 2004. Spektr: A computational tool for x-ray spectral analysis and imaging system optimization. *Med Phys,* 31**,** 3057-3067.

SON, K., CHO, S., KIM, J. S., HAN, Y., JU, S. G. & CHOI, D. H. 2014. Evaluation of radiation dose to organs during kilovoltage cone-beam computed tomography using Monte Carlo simulation. *J Appl Clin Med Phys,* 15**,** 295-302.

SONG, W. Y., KAMATH, S., OZAWAL, S., AL ANI, S., CHVETSOV, A., LHANDARE, N., PALTA, J. R., LIU, C. & LI, J. G. 2008. A dose comparison study between XVI (R) and OBI (R) CBCT systems. *Med Phys,* 35**,** 480-486.

SPEZI, E., DOWNES, P., JARVIS, R., RADU, E. & STAFFURTH, J. 2012. Patient-specific three-dimensional concomitant dose from cone beam computed tomography exposure in image-guided radiotherapy. *Int J Radiat Oncol Biol Phys,* 83**,** 419-426.

STOCK, M., PALM, A., ALTENDORFER, A., STEINER, E. & GEORG, D. 2012. IGRT induced dose burden for a variety of imaging protocols at two different anatomical sites. *Radiother Oncol,* 102**,** 355-363.

TAPIOVAARA, M. & SIISKONEN, T. 2008. *PCXMC A Monte Carlo program for calculating patient doses in medical x-ray examinations* [Online].

Available: http://www.stuk.fi/palvelut/pcxmc-a-monte-carlo-program-for-calculating-patient-doses-in-medical-x-ray-examinations [Accessed 23/09/ 2015].

TEAM, X.-M. C. 2008. MCNP — A General Monte Carlo N-Particle Transport Code, Version 5.

TOMIC, N., DEVIC, S., DEBLOIS, F. & SEUNTJENS, J. 2010. Reference radiochromic film dosimetry in kilovoltage photon beams during CBCT image acquisition. *Med Phys,* 37**,** 1083-1092.

TSAI, H. Y., TUNG, C. J., HUANG, M. H. & WAN, Y. L. 2003. Analyses and applications of single scan dose profiles in computed tomography. *Med Phys,* 30**,** 1982-9.

TURNER, A. C., ZANKL, M., DEMARCO, J. J., CAGNON, C. H., ZHANG, D., ANGEL, E., CODY, D. D., STEVENS, D. M., MCCOLLOUGH, C. H. & MCNITT-GRAY, M. F. 2010. The feasibility of a scanner-independent technique to estimate organ dose from MDCT scans: using CTDIvol to account for differences between scanners. *Med Phys,* 37**,** 1816-1825.

VARIAN 2010. TrueBeam Technical Reference Guide. Volume: 2 Imaging.

WALTER, C., BODA-HEGGEMANN, J., WERTZ, H., LOEB, I., RAHN, A., LOHR, F. & WENZ, F. 2007. Phantom and in-vivo measurements of dose exposure by image-guided radiotherapy (IGRT): MV portal images vs. kV portal images vs. cone-beam CT. *Radiother Oncol,* 85**,** 418-423.

WALTERS, B., DING, G., KRAMER, R. & KAWRAKOW, I. 2009. Skeletal dosimetry in cone beam computed tomography. *Med Phys,* 36**,** 2915-2922.

WALTERS, B., KAWRAKOW, I. & ROGERS, D. W. O. 2013. DOSXYZnrc Users Manual. Ionizing Radiation Standards National Research Council of Canada, Ottawa. NRC Report PIRS 794.

WALTERS, B. R. & KAWRAKOW, I. 2007. A "HOWFARLESS" option to increase efficiency of homogeneous phantom calculations with DOSXYZnrc. *Med Phys,* 34**,** 3794-807.

WEN, N., GUAN, H., HAMMOUD, R., PRADHAN, D., NURUSHEV, T., LI, S. & MOVSAS, B. 2007. Dose delivered from Varian's CBCT to patients receiving IMRT for prostate cancer. *Phys Med Biol,* 52**,** 2267-76.

WOOD, T., MOORE, C., SAUNDERSON, J. & BEAVIS, A. 2015. Validation of a technique for estimating organ doses for kilovoltage cone-beam CT of the prostate using the PCXMC 2.0 patient dose calculator. *J Radiol Prot,* 35**,** 153-63.

ZHANG, D., CAGNON, C. H., VILLABLANCA, J. P., MCCOLLOUGH, C. H., CODY, D. D., ZANKL, M., DEMARCO, J. J. & MCNITT-GRAY, M. F. 2013a. Estimating peak skin and eye lens dose from neuroperfusion examinations: Use of Monte Carlo based simulations and comparisons to CTDIvol, AAPM Report No. 111, and ImPACT dosimetry tool values. *Med Phys,* 40**,** 091901-9.

ZHANG, G., MARSHALL, N., BOGAERTS, R., JACOBS, R. & BOSMANS, H. 2013b. Monte Carlo modeling for dose assessment in cone beam CT for oral and maxillofacial applications. *Med Phys,* 40**,** 072103-12.

ZHANG, Y., LI, X., SEGARS, W. P. & SAMEI, E. 2012a. Organ doses, effective doses, and risk indices in adult CT: Comparison of four types of reference phantoms across different examination protocols. *Med Phys,* 39**,** 3404-3423.

ZHANG, Y., YAN, Y., NATH, R., BAO, S. & DENG, J. 2012b. Personalized Assessment of kV Cone Beam Computed Tomography Doses in Image-guided Radiotherapy of Pediatric Cancer Patients. *Int J Radiat Oncol Biol Phys,* 83**,** 1649-54.

ZHOU, H. & BOONE, J. M. 2008. Monte Carlo evaluation of $CTDI_{\infty}$ in infinitely long cylinders of water, polyethylene and PMMA with diameters from 10mm to 500mm. *Med Phys,* 35**,** 2424-2431.